

NATIONAL AERONAUTICS AND SPACE ADMINISTRATION

Technical Report 32-1526

Volume X

The Deep Space Network

Progress Report

For May and June 1972

**CASE FILE
COPY**

**JET PROPULSION LABORATORY
CALIFORNIA INSTITUTE OF TECHNOLOGY
PASADENA, CALIFORNIA**

August 15, 1972

NATIONAL AERONAUTICS AND SPACE ADMINISTRATION

Technical Report 32-1526

Volume X

The Deep Space Network

Progress Report

For May and June 1972

JET PROPULSION LABORATORY
CALIFORNIA INSTITUTE OF TECHNOLOGY
PASADENA, CALIFORNIA

August 15, 1972

Preface

This report series presents progress on DSN supporting research and technology, advanced development and engineering, implementation, and operations which pertain to mission-independent or multiple-mission development as well as to support of flight projects. Each issue presents material in some, but not all, of the following categories in the order indicated.

Description of the DSN

Mission Support

- Interplanetary Flight Projects
- Planetary Flight Projects
- Manned Space Flight Project
- Advanced Flight Projects

Radio Science

Advanced Engineering

- Tracking and Navigational Accuracy Analysis
- Communications Systems Research
- Communications Elements Research
- Supporting Research and Technology

Development and Implementation

- Space Flight Operations Facility Development
- Ground Communications Facility Development
- Deep Space Instrumentation Facility Development
- DSN Projects and Systems Development

Operations and Facilities

- DSN Operations
- Space Flight Operations Facility Operations
- Ground Communications Facility Operations
- Deep Space Instrumentation Facility Operations
- Facility Engineering

In each issue, the part entitled "Description of the DSN" describes the functions and facilities of the DSN and may report the current configuration of one of the six DSN systems (tracking, telemetry, command, monitoring, simulation, and operations control).

The work described in this report series is either performed or managed by the Tracking and Data Acquisition organization of JPL for NASA.

Page Intentionally Left Blank

Contents

DESCRIPTION OF THE DSN

DSN Functions and Facilities	1
---	----------

N. A. Renzetti

End-to-End Medium Rate Telemetry System Test	5
---	----------

W. J. Kinder

NASA Code 311-03-42-91

MISSION SUPPORT

Interplanetary Flight Projects

Pioneer 6-9 Mission Support	10
--	-----------

A. J. Siegmeth

NASA Code 311-03-21-20

Helios Mission Support	14
---	-----------

P. S. Goodwin

NASA Code 311-03-21-50

Planetary Flight Projects

Mariner Mars 1971 Mission Support	20
--	-----------

G. P. Textor

NASA Code 311-03-21-40

Viking Mission Support	22
---	-----------

D. J. Mudgway

NASA Code 311-03-21-70

Pioneer 10 and G Mission Support	27
---	-----------

A. J. Siegmeth

NASA Code 311-03-21-20

Mariner Jupiter-Saturn 1977 Mission Support	35
--	-----------

D. J. Mudgway

NASA Code 311-03-21-90

Manned Space Flight Project

Apollo Mission Support	41
---	-----------

R. B. Hartley

NASA Code 311-03-21-80

Contents (contd)

Advanced Flight Projects

Pioneer Venus Mission Support	49
--	-----------

A. J. Siegmeth
NASA Code 311-03-21-20

RADIO SCIENCE

Radio Science Support	52
--	-----------

K. W. Linnes
NASA Code 311-03-21-60

ADVANCED ENGINEERING

Tracking and Navigational Accuracy Analysis

Preliminary Evaluation of Radio Data Orbit Determination Capabilities for the Saturn Portion of a Jupiter-Saturn-Pluto 1977 Mission	59
--	-----------

V. J. Ondrasik, C. E. Hildebrand, and G. A. Ransford
NASA Code 150-22-60-10

Determining the Mass and Ephemeris of Saturn by Radio Tracking of a Jupiter-Saturn-Pluto 1977 Spacecraft	76
---	-----------

V. J. Ondrasik, C. E. Hildebrand, and G. A. Ransford
NASA Code 150-22-60-10

Communications Systems Research

DSN Station Clock Synchronization by Maximum Likelihood VLBI	82
---	-----------

W. J. Hurd
NASA Code 150-22-12-04

Frame Synchronization in Time-Multiplexed PCM Telemetry With Variable Frame Length	96
---	-----------

U. Timor
NASA Code 150-22-15-29

L-Band Frequency Multipliers: Phase Noise, Stability, and Group Delay	104
--	------------

J. MacConnell and R. Meyer
NASA Code 150-22-14-24

A Minimization Algorithm for a Class of Functions	110
--	------------

L. R. Welch
NASA Code 150-22-12-04

Contents (contd)

Communications Elements Research

Tracking and Ground Based Navigation: Performance of Hydrogen Maser Cavity Tuning Servo	113
--	------------

S. Petty and C. Finnie
NASA Code 150-22-14-05

Tracking and Ground Based Navigation: A Description of the Weather Project	116
---	------------

M. S. Reid
NASA Code 150-22-66-20

Improved RF Calibration Techniques: System Operating Noise Temperature Calibrations	123
--	------------

M. S. Reid
NASA Code 150-22-66-20

Antenna Study: Performance Enhancement :	129
---	------------

P. D. Potter
NASA Code 150-22-13-12

Network Engineering and Implementation: S- and X-Band Feed System	135
--	------------

P. D. Potter
NASA Code 311-03-14-61

Error Analysis of Precision Calibrations of Perforated Plate Mesh Materials on a Tuned Reflectometer System	143
--	------------

T. Y. Otoshi
NASA Code 150-22-14-10

Supporting Research and Technology

DSN Research and Technology Support	149
--	------------

E. B. Jackson
NASA Code 150-22-12-05

DEVELOPMENT AND IMPLEMENTATION

DSIF Development

DSN/MSFN Antenna-Pointing and Tracking Implementation	153
--	------------

J. H. McInnis, Jr.
NASA Codes 311-03-14-21 and 312-03-12-00

The Use of an Interplex Modulation Technique for the Mariner Venus-Mercury 1973 Mission	157
--	------------

M. M. Whang
NASA Codes 311-03-14-21 and 312-03-12-00

Contents (contd)

Post-Detection Subcarrier Recording Subsystem	161
L. I. DeGennaro and G. B. Hamilton NASA Codes 311-03-42-45 and 312-03-31-45	
Performance Capabilities of the Data Decoder Assembly Through the Viking Era	164
C. R. Grauling and N. J. Jones NASA Codes 311-03-42-43 and 312-03-31-43	
S-Band Receiver Third-Order Loop Demonstration	168
R. B. Crow NASA Code 150-22-14-04	
Novel 70-MHz Limiting Amplifier	172
J. G. Leflang and R. N. MacClellan NASA Code 150-22-14-12	
Block IV Receiver Development	175
C. E. Johns NASA Code 150-22-14-29	
Programmed Oscillator Development	180
H. Donnelly and M. R. Wick NASA Code 311-03-14-21	
Experimental S- and X-Band Feed System Ellipsoid Reflector	186
H. R. Hoggan and W. J. Kissane NASA Code 312-03-31-46	
Improvements to Angle Data System Autocollimators	191
R. A. Zanteson NASA Code 150-22-65-20	
New Probes for Tracing Electrical Noise	194
C. Lundy NASA Code 312-03-31-45	
Repositioning of Parabolic Antenna Panels Onto a Shaped Surface	199
R. Levy NASA Code 150-22-65-20	

OPERATIONS AND FACILITIES

DSN Operations

DSN System Testing: A Critical Review of the Pioneer 10 Test Program	207
C. K. Stein NASA Code 311-03-42-91	

Contents (contd)

DSN Telemetry Predicts Generation and Distribution	210
---	------------

C. W. Harris and E. S. Burke

NASA Code 311-03-13-20

DSN Command System Performance Evaluation	213
--	------------

W. G. Stinnett

NASA Code 311-03-13-20

DSIF Operations

Accuracy of the Signal-to-Noise Ratio Estimator	217
--	------------

J. R. Lesh

NASA Code 311-03-14-52

Initial Acquisition Planning	236
---	------------

W. G. Meeks

NASA Code 311-03-21-40

Bibliography	243
-------------------------------	------------

DSN Functions and Facilities

N. A. Renzetti
Mission Support Office

The objectives, functions, and organization of the Deep Space Network are summarized. The Deep Space Instrumentation Facility, the Ground Communications Facility, and the Space Flight Operations Facility are described.

The Deep Space Network (DSN), established by the NASA Office of Tracking and Data Acquisition under the system management and technical direction of JPL, is designed for two-way communications with unmanned spacecraft traveling approximately 16,000 km (10,000 mi) from Earth to planetary distances. It supports, or has supported, the following NASA deep space exploration projects: *Ranger*, *Surveyor*, *Mariner Venus 1962*, *Mariner Mars 1964*, *Mariner Venus 67*, *Mariner Mars 1969*, *Mariner Mars 1971* (JPL); *Lunar Orbiter* and *Viking* (Langley Research Center); *Pioneer* (Ames Research Center); *Helios* (West Germany); and *Apollo* (Manned Spacecraft Center), to supplement the Manned Space Flight Network (MSFN).

The Deep Space Network is one of two NASA networks. The other, known as the Spaceflight Tracking and Data Network, is under the system management and technical direction of the Goddard Space Flight Center. Its function is to support manned and unmanned Earth-orbiting and lunar scientific and communications satellites. Although the DSN was concerned with unmanned lunar spacecraft in its early years, its primary objective now and into the future is to continue its support of planetary and interplanetary flight projects. It has been a development objec-

tive that the network capability be kept at the state of the art of telecommunications and data handling and that it support as many flight projects as possible with a minimum of mission-dependent hardware and software. It provides direct support of each project through that project's tracking and data system. This management element, in concert with the telecommunications and mission operations personnel of the project, is responsible for the design and operation of the hardware and software which are required for the conduct of flight operation. The organization and procedures necessary to carry out these activities are described in Ref. 1.

The DSN function, in supporting a flight project by tracking the spacecraft, is characterized by six DSN systems:

- (1) DSN Tracking System. Generates radio metric data; i.e., angles, one- and two-way doppler and range.
- (2) DSN Telemetry System. Receives, records, and retransmits engineering and scientific data generated in the spacecraft.
- (3) DSN Command System. Sends coded signals to the spacecraft in order to initiate spacecraft functions in flight.

- (4) DSN Monitor System. Instruments, transmits, records, and displays those parameters of the DSN that measure its performance.
- (5) DSN Simulation System. Provides computer-based facilities in order to test and train network functions and assist the flight project in carrying out similar functions for its Mission Operations System.
- (6) DSN Operations Control. Provides the hardware and software, personnel, real-time and non-real-time operational direction of the network, and primary interface with the flight projects Mission Operations personnel.

The facilities needed to carry out these functions have evolved in three technical areas: (1) the deep space stations and the telecommunications interface through the RF link with the spacecraft is known as the Deep Space Instrumentation Facility (DSIF); (2) the Earth-based point-to-point voice and data communications from the stations to the control center is known as the Ground Communications Facility (GCF); (3) the control center, both for network control function and mission control support, is known as the Space Flight Operations Facility (SFOF).

I. Deep Space Instrumentation Facility

A. Tracking and Data Acquisition Facilities

A world-wide set of deep space stations (DSSs) with large antennas, low-noise phase-lock receiving systems, and high-power transmitters provide radio communications with spacecraft. The DSSs and the deep space communications complexes (DSCCs) they comprise are given in Table 1.

Radio contact with a spacecraft usually begins when the spacecraft is on the launch vehicle at Cape Kennedy, and it is maintained throughout the mission. The early part of the trajectory is covered by selected network stations of the Air Force Eastern Test Range (AFETR) and the MSFN of the Goddard Space Flight Center.¹ Normally, two-way communications are established between the spacecraft and the DSN within 30 min after the spacecraft has been injected into lunar, planetary, or interplanetary flight. A compatibility test station at Cape Kennedy (discussed later) monitors the spacecraft continuously dur-

ing the launch phase until it passes over the local horizon. The deep space phase begins with acquisition by either DSS 51, 41, or 42. These and the remaining DSSs given in Table 1 provide radio communications to the end of the flight.

To enable continuous radio contact with spacecraft, the DSSs are located approximately 120 deg apart in longitude; thus, a spacecraft in deep space flight is always within the field-of-view of at least one DSS, and for several hours each day may be seen by two DSSs. Furthermore, since most spacecraft on deep space missions travel within 30 deg of the equatorial plane, the DSSs are located within latitudes of 45 deg north or south of the equator. All DSSs operate at S-band frequencies: 2110–2120 MHz for Earth-to-spacecraft transmission and 2290–2300 MHz for spacecraft-to-Earth transmission.

To provide sufficient tracking capability to enable useful data returns from around the planets and from the edge of the solar system, a 64-m (210-ft) diam antenna network will be required. Two additional 64-m (210-ft) diam antenna DSSs are under construction at Madrid and Canberra, which will operate in conjunction with DSS 14 to provide this capability. These stations are scheduled to be operational by the middle of 1973.

B. Compatibility Test Facilities

In 1959, a mobile L-band compatibility test station was established at Cape Kennedy to verify flight-spacecraft-DSN compatibility prior to the launch of the *Ranger* and *Mariner Venus* 1962 spacecraft. Experience revealed the need for a permanent facility at Cape Kennedy for this function. An S-band compatibility test station with a 1.2-m (4-ft) diam antenna became operational in 1965. In addition to supporting the preflight compatibility tests, this station monitors the spacecraft continuously during the launch phase until it passes over the local horizon.

Spacecraft telecommunications compatibility in the design and prototype development phases was formerly verified by tests at the Goldstone DSCC. To provide a more economical means for conducting such work and because of the increasing use of multiple-mission telemetry and command equipment by the DSN, a compatibility test area (CTA) was established at JPL in 1968. In all essential characteristics, the configuration of this facility is identical to that of the 26-m (85-ft) and 64-m (210-ft) diam antenna stations.

The JPL CTA is used during spacecraft system tests to establish the compatibility with the DSN of the proof test

¹The 9-m (30-ft) diam antenna station established by the DSN on Ascension Island during 1965 to act in conjunction with the MSFN orbital support 9-m (30-ft) diam antenna station was transferred to the MSFN in July 1968.

model and development models of spacecraft, and the Cape Kennedy compatibility test station is used for final flight spacecraft compatibility validation testing prior to launch.

II. Ground Communications Facility

The GCF provides voice, high-speed data, wideband data, and teletype communications between the SFOF and the DSSs. In providing these capabilities, the GCF uses the facilities of the worldwide NASA Communications Network (NASCOM)² for all long distance circuits, except those between the SFOF and the Goldstone DSCC. Communications between the Goldstone DSCC and the SFOF are provided by a microwave link directly leased by the DSN from a common carrier.

Early missions were supported by voice and teletype circuits only, but increased data rates necessitated the

²Managed and directed by the Goddard Space Flight Center.

use of high-speed circuits for all DSSs, plus wideband circuits for some stations.

III. Space Flight Operations Facility

Network and mission control functions are performed at the SFOF at JPL. The SFOF receives data from all DSSs and processes that information required by the flight project to conduct mission operations. The following functions are carried out: (1) real-time processing and display of radio metric data; (2) real-time and non-real-time processing and display of telemetry data; (3) simulation of flight operations; (4) near-real-time evaluation of DSN performance; (5) operations control, and status and operational data display; and (6) general support such as internal communications by telephone, intercom, public address, closed-circuit TV, documentation, and reproduction of data packages. Master data records of science data received from spacecraft are generated. Technical areas are provided for flight project personnel who analyze spacecraft performance, trajectories, and generation of commands.

Reference

1. *The Deep Space Network*, Space Programs Summary 37-50, Vol. II, pp. 15-17. Jet Propulsion Laboratory, Pasadena, Calif., Mar. 31, 1968.

Table 1. Tracking and data acquisition stations of the DSN

DSCC	Location	DSS	DSS serial designation	Antenna		Year of initial operation
				Diameter, m (ft)	Type of mounting	
Goldstone	California	Pioneer	11	26 (85)	Polar	1958
		Echo	12	26 (85)	Polar	1962
		(Venus) ^a	13	26 (85)	Az-El	1962
		Mars	14	64 (210)	Az-El	1966
—	Australia	Woomera	41	26 (85)	Polar	1960
Tidbinbilla	Australia	Weemala (formerly Tidbinbilla)	42	26 (85)	Polar	1965
		Ballima (formerly Booroomba)	43	64 (210)	Az-El	Under construction
		Johannesburg	51	26 (85)	Polar	1961
Madrid	Spain	Robledo	61	26 (85)	Polar	1965
		Cebreros	62	26 (85)	Polar	1967
		Robledo	63	64 (210)	Az-El	Under construction

^aA research-and-development facility used to demonstrate the feasibility of new equipment and methods to be integrated into the operational network. Besides the 26-m (85-ft) diam az-el-mounted antenna, DSS 13 has a 9-m (30-ft) diam az-el-mounted antenna that is used for testing the design of new equipment and support of ground-based radio science.

End-to-End Medium Rate Telemetry System Test

W. J. Kinder

DSN Engineering and Operations Office

An end-to-end test of the operational medium rate Telemetry System was conducted on May 23, 1972. The errors recorded seem to group themselves around three patterns: those errors associated with 360 computer time corrections, those errors concerned with Ground Communications Facility (GCF) transmission, and those errors apparent in the GCF/synchronizer/360 interface. Noise on the data-block-detected signal from the GCF decoder to the SFOF synchronizers is suspected. A recommendation is made for a facility test between the GCF and SFOF to be undertaken to validate the quality of the data-block-detected signal per transfer agreement and assembly specifications.

I. Introduction

Numerous instances have been reported involving the unreliable operation of the DSN Medium Rate Telemetry System during support of early phases of the *Pioneer 10* mission. The system includes the processing of coded and uncoded data at rates between 50 and 2500 bps. Specific anomalies observed have been the inability of the system to maintain frame synchronization for more than approximately 10 minutes without a data interruption or the appearance of "short blocks" i.e., incomplete high-speed data (HSD) blocks received at the Space Flight Operations Facility (SFOF). Since the causes of the problem(s) were not obvious, the DSN Tele-

metry Design Team recommended an end-to-end medium rate Telemetry System test. This test was conducted on May 23, 1972.

II. Test Configuration

As shown in Fig. 1, DSS 71 and CTA 21 were used in this test along with the 360/75 SFOF computer. The Simulation Conversion Assembly (at DSS 71) generated *Pioneer 10* fixed-pattern formats which were converted to RF signals for DSS 71 processing. Besides the normal telemetry original data record (ODR), DSS 71 had a Digital Instrumentation Subsystem (DIS) program and a

HSD ODR program in the spare Telemetry and Command Processor (TCP) that printed and logged the data as seen on the output of the Ground Communications Facility (GCF) data set and TCP. CTA 21 looked at DSS 71's data via a separate communication line from DSS 71/Goddard, with the same TCP ODR and DIS programs logging and printing errors for received HSD blocks. At JPL, the GCF monitored data-block-detected status on its Printer-Punch-Recorder (PPR). Also, as shown in Fig. 1, two data sets were used to drive all four synchronizers in the SFOF, using the signal from DSS 71. Synchronizers 2 and 4 were driven by the data-block-detected signal (all data mode) from the SFOF Communication Terminal, while synchronizers 1 and 3 were in the forced-check mode (derive sync from HSD block, i.e., internal synchronization). The GCF provided a hard copy test record from their PPR and the SFOF 360/75 printed alarm messages on teletypewriters (TTY), while also maintaining a digital log. The test was run at data rates of 1024 and 2048 bps in the convolutional coded mode.

III. Discussion

Condensed results of the test are shown in Table 1. Each anomalous event and time is shown in comparison with: (1) what the synchronizers and 360/75 received; (2) what the GCF received (PPR); (3) what CTA 21 recorded (DIS TCP programs); and, finally, (4) what DSS 71 transmitted (DIS TCP programs). For a scheduled 8-hour test, over seven hours of test data were obtained and recorded. The error events exhibited in this test seem to group themselves around the following patterns; namely, those errors associated with 360 time corrections (events 10, 12, 13, 15), those errors concerned with GCF transmission (1, 2, 3, 4, 5, 6, 7, 8, 9, 16, 18, 19) and those errors spawned in the GCF/synchronizer/360 interface (11, 14, 17).

Concerning the first error pattern, 360/75 time corrections, the facility representative provided the following information. The time tags on the telemetry data received in the SFOF via HSD can be in error due to noise on the HSD line or incorrect time tagging of the data at the DSS. If the time parameters in the HSD blocks exceed the specified limit, the time tag is considered to be in error and a corrected time tag is used if possible. Based on a re-examination of the DSIF data, events 12, 13, and 15 can be attributed to hits on the GCF HSD line while event 10 was due to a TCP outage at DSS 71 because of re-initialization.

In reference to the second group of errors, NASCOM performance is quoted as:

- (1) Undetected bit error rate: $< 10^{-10}$
- (2) Detected bit error rate:
 - 2 bits in 10^5 bits — one link
 - 4 bits in 10^5 bits — two links
 - 6 bits in 10^5 bits — three links
- (3) Errors occur in bursts of from 3 to 200 bits in an HSD block with an average burst length of 15 bits
- (4) Block throughput: $\geq 98\%$ (percent of error-free blocks)

The GCF representative, in analyzing the PPR data, concluded that the errors experienced during this test for the GCF were within specifications. The block throughput for the test was 99.37%. It should be noted that, contemporaneously with this end-to-end system test, the live *Pioneer F* track was exhibiting periodic frame sync loss while being processed in the same 360/75 computer as the test data.

Concerning the last group of errors, events 11, 14, and 17 were isolated to the GCF/synchronizer/360 interface. Two types of errors were noted; namely, the short block problem (11) and the independent operation of synchronizers 2 and 4 (14, 17). At time 17:52:44 the short blocks from all four synchronizers were due to a 360/75 loop condition which necessitated a manual reset/select action on the computer. Synchronizers 2 and 4 were driven by the data-block-detected signal from separate decoders in the GCF. Noise on this signal is suspected of causing errors in data format to be transferred to the 360/75. A patch-field condition existed such that the block-error-detected signal to the PPR could trigger the synchronizers with a false data-block-detected signal. However, at the time of the test, it was not clear that this was a problem. This has subsequently been corrected. This interference with the data-block-detected signals could also account for overlay blocks being received by the 360/75, although the SFOF printer may not be printing all occurrences of short blocks. At 2048 bps, the Telemetry System is using three of the four data blocks which are transferred to the 360 computer each second. At lower bit rates, the synchronizer interference problem could have gone undetected because of the discarding of filler blocks; only one of the four HSD blocks each second contained data.

IV. Conclusions

For a throughput of 99%, on the average for a single GCF link, one could expect one block in error for every 100 serviced. Although the incidence of GCF errors did not approach this average, errors were present. It should also be noted that during this test we processed over an

hour of 2048 coded data without incident while servicing real *Pioneer* data in the same 360 computer. A recommendation is made for a facility test between the GCF and SFOF to be undertaken to validate the quality of the data-block-detected signal per transfer agreement and assembly specification. A future end-to-end medium rate test is again planned.

Table 1. Medium Rate Telemetry System test data condensation

Event as alarmed in 360/75	Time of event	360/75 synchronizer behavior	GCF behavior		CTA 21 notation	DSS 71 notation
			Error in data-block-detected signal	Block errors detected		
1. Missed data block; sync lost	15:06:58	Blocks accountable	0	8	No errors	No errors
2. Missed data block; sync lost	15:08:55	Blocks accountable	2	2	HSD SN error at 150856	No errors
3. Missed data block	15:11:24	Blocks accountable	0	2	No errors	No errors
4. Missed data block	15:15:46	Blocks accountable	2	7	GCF error at 151548	No errors
5. Sync lost	15:16:17	Blocks accountable	2	7	No errors	No errors
6. Missed data block	15:34:56	Blocks accountable	2	2	GCF error at 153443	No errors
7. Sync lost	15:39:13	Blocks accountable	0	1	No errors	No errors
8. Missed data block	16:03:55	Blocks accountable	2	2	No errors	No errors
9. Missed data block; sync lost	16:28:26	Blocks accountable	0	1	No errors	No errors
10. Time correction started error	16:49:00	Blocks accountable	0	0	No errors	No errors
11. Missed data block; sync lost	17:52:46	Sync 2 missed block SN 1203; other blocks accounted for	0	0	No errors	No errors
12. Time correction started error	17:56:41	Blocks accountable	0	2	No errors	No errors
13. Time correction started error	18:03:29	Blocks accountable	0	2	No errors	No errors
14. Sync lost	18:07:58	Sync 4 block SN 10851 stopped; then started with SN 10852	0	2	No errors	No errors
15. Time correction started error	18:58:26	Blocks accountable	0	1	No errors	No errors
16. Missed data block; sync lost	19:08:13	Blocks accountable	2	2	No errors	No errors
17. Missed data block; sync lost	19:11:20	Sync 4 missed data block; other blocks accounted for	2	0	No errors	No errors
18. Sync lost	19:32:21	Blocks accountable	0	1	No errors	No errors
19. Missed data block; sync lost	19:58:07	Blocks accountable	2	2	No errors	No errors

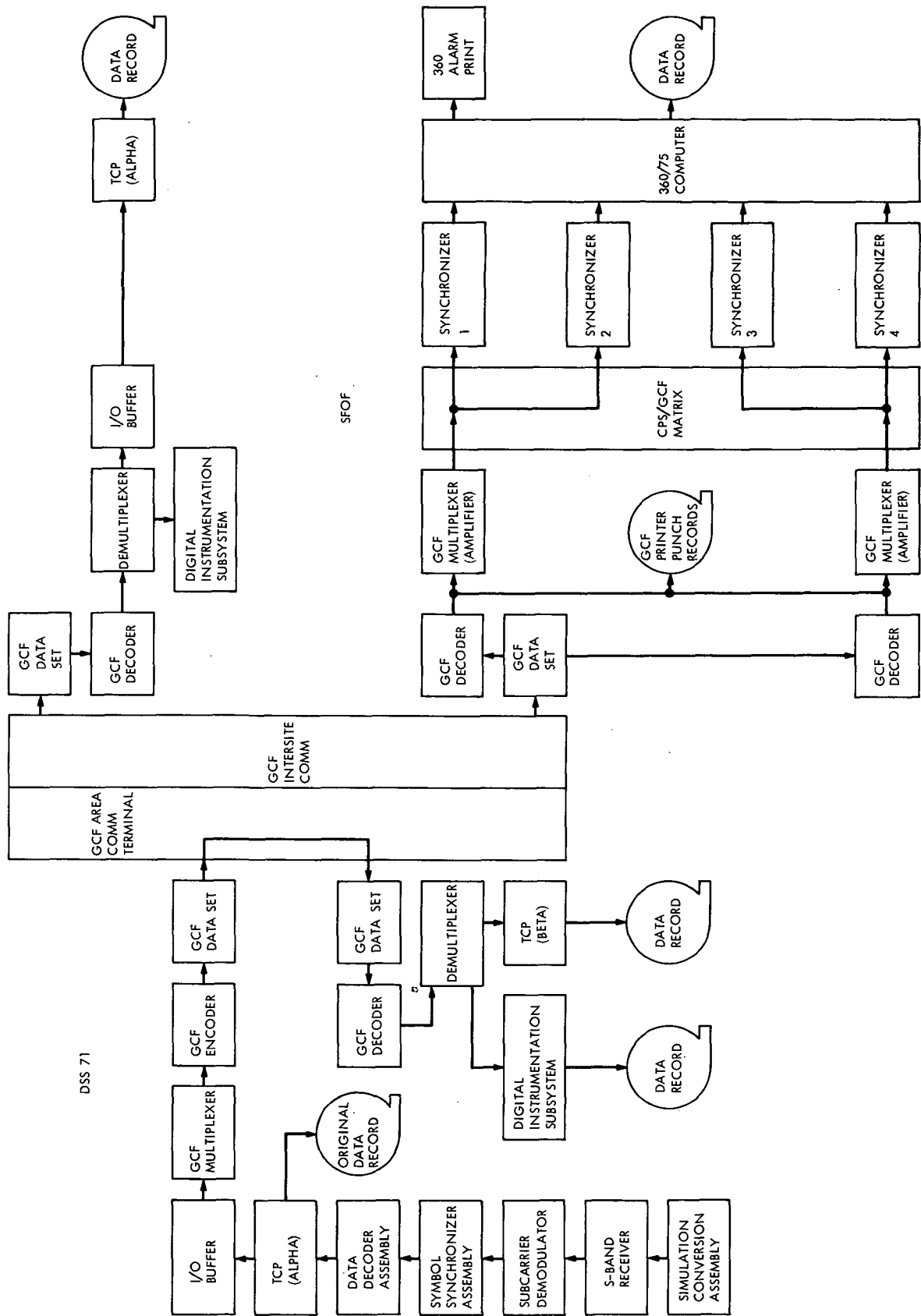


Fig. 1. Medium rate telemetry data flow

Pioneer 6-9 Mission Support

A. J. Siegmeth
Mission Support Office

To meet the specific scientific objectives of the Pioneer 10 and G missions, the importance of the simultaneous support of the still-active Pioneers 6-9 has increased. The Pioneer Project requires tracks during the radial- and spiral-type configurations of the Pioneer 8, 9, and 10 missions. Fields and particles data acquired by DSN will make possible the measurement of distribution gradients. This article gives the description of the radial and spiral configurations and opportunities, and the support requirements.

Since the successful launch of the *Pioneer 10* mission destined to fly by Jupiter, the importance of tracking the still-active *Pioneers 6-9* spacecraft in conjunction with *Pioneer 10* has considerably increased in order to meet some of the specific interplanetary objectives of the *Pioneer 10* and *G* missions. One of the most important aspects of the interplanetary objectives is the determination of the heliocentric radial dependence of the solar wind plasma's distribution function, the parameters of the interplanetary magnetic field, and the phenomena of solar energetic particles. Past experience has already shown that these radial gradient measurements are extremely suspect when observations are obtained only from a single spacecraft. The principal difficulties are the long-term, large-scale temporal variations of the desired measurables even over periods of many solar rotations (the Sun rotates around its axis once every 27 Earth days); thus, even long-term averaging techniques are completely inadequate in shedding light on the question of radial gradients.

Simultaneous observations by two spacecraft separated by a large heliocentric radial distance are required in order to meet these specific objectives. If one wants to determine

the parameters of the solar wind and magnetic field, the two spacecraft under surveillance must be aligned on the same solar radial, and, for the case of the solar energetic particles, the two spacecraft should be aligned along approximately the same interplanetary magnetic field line or spiral. Also, there have been several radial/spiral experiments performed in the past between various *Pioneer* and *Mariner* spacecraft, but the radial separation has not been sufficiently large to clearly define the gradients. In addition, the previous experiments were performed at the time when the Sun was much more active and the interplanetary medium correspondingly much more complex than it is in the present period.

Figure 1 displays the upcoming *Pioneer* radial/spiral configurations. These opportunities are listed in Table 1.

To obtain the expected results of a radial experiment, at which the Sun and two *Pioneer* spacecraft are located on the same solar radial, two weeks of simultaneous tracking surveillance is required. During this time temporal variations and signatures can be observed, and the solar winds plasma distribution function can be determined.

The solar energetic particles are traveling on an interplanetary magnetic field line which is represented by an Archimedian spiral. However, this model of the interplanetary magnetic field has not yet been validated, and it is probable that these field lines in distances larger than one astronomical unit are following a somewhat different geometry. The spiral line-up is highly dependent on the solar wind velocity. The given epochs were calculated for an average solar wind velocity of 400 km/s. Recent measurements made by the on-board instruments of the *Pioneer 6* spacecraft indicate solar wind velocities between 400 and 600 km/s. For this reason the Project requires at least daily passes for each of these missions for a duration of four weeks.

The *Pioneer 6* mission can be tracked approximately until September, 1972, from the 26-m-diam antenna stations. *Pioneer 9* will stay within the threshold of the 26-m

antennas up to the first quarter of 1974. *Pioneers 7* and *8* can operate only with the 64-m antenna at DSS 14. *Pioneer 10* will be supported continuously until July 1973 from the 26-m stations. The network plans to support the *Pioneer* radial/spiral experiments within the available resources and support constraints. It is generally possible to secure the required support from one or two of the seven available 26-m antenna stations. It is, nevertheless, very difficult to obtain the required support from the 64-m station at DSS 14 which has to support, besides the *Pioneer* spacecraft, the extended phase of the *Mariner Mars 1971* mission and numerous high-priority radio science experiments. Figure 2 depicts flight project requirements of DSS 14 (excluding the radio science experiments). This chart shows the required passes per week. It should be noted that this station has a capability of supporting approximately seven to nine passes per week. Therefore, many of the requirements are far above the available resources.

Table 1. Radial/spiral opportunities

Missions ^a	Experiment	Epoch	Required support window
<i>Pioneers 8 and 9</i>	Radial	5/21/72	For one month before and one month after epoch
<i>Pioneers 8 and 9</i>	Spiral	6/21/72	For two months before and two months after epoch
<i>Pioneers 9 and 10</i>	Radial	8/6/72	For one month before and one month after epoch
<i>Pioneers 9 and 10</i>	Spiral	12/28/72	For two months before and two months after epoch
<i>Pioneers 8 and 10</i>	Radial	10/20/72	For one month before and one month after epoch
<i>Pioneers 8 and 10</i>	Spiral	5/9/73	For two months before and two months after epoch
^a At least one daily pass is required for each mission.			

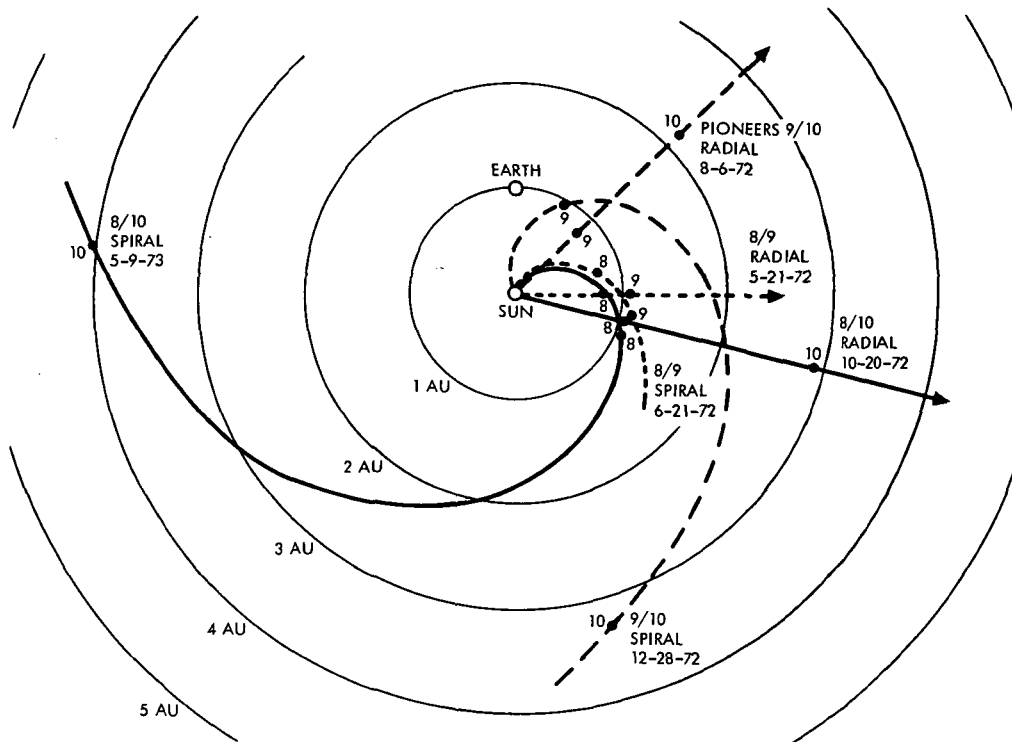


Fig. 1. Pioneer 8, 9 and 10 radial/spiral configurations

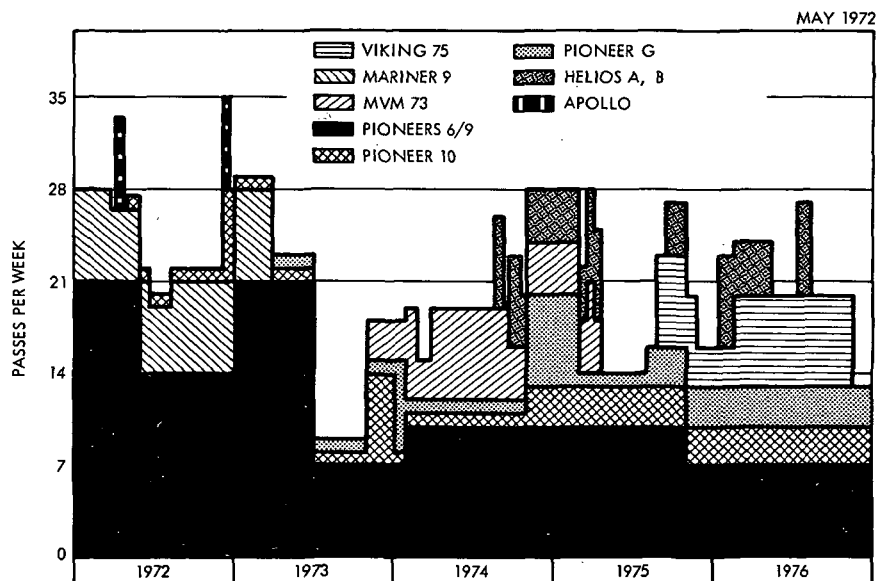


Fig. 2. DSS 14 flight project support requirements

Helios Mission Support

P. S. Goodwin
Mission Support Office

Project Helios, named after the ancient Greek Goddess of the Sun, is a joint undertaking by the Federal Republic of West Germany and the United States of America, who divide the project responsibilities. Each country has a Project Manager who is responsible for his own country's contribution as determined by the International Agreement. In addition, the two Project Managers act as co-Chairmen of the internationally structured Helios Joint Working Group Meetings which are held semi-annually and alternate between the two countries. The project objective is to launch two unmanned scientific satellites into heliocentric orbits that will come closer to the Sun than any known or planned spacecraft to date for the purpose of obtaining further knowledge about the Sun and its influence upon life on Earth. The plan is to launch the first spacecraft in mid-1974 and the second in late 1975.

Prior volumes of this series described the history and organization of this program, the spacecraft configuration and trajectory, its telecommunications system, and the results of prior Joint Working Group Meetings. This article deals with the activities and highlights of the Sixth Helios Joint Working Group Meeting which was held at JPL in April-May 1972.

I. Introduction

Volume II (Ref. 1, p. 19) of this report series described the *Helios* Project Management organization. It was noted that in addition to the line management organization within the United States and the Federal Republic of West Germany, the International Agreement established a Working Group structure wherein the U.S. and German Project Managers would act as co-Chairmen of semi-annual technical coordination meetings to be held alternately between the United States and West Germany. Initially, these meetings were held at the respective Project Headquarters at Goddard Space Flight Center, Greenbelt, Maryland, and at the Gesellschaft fuer Wel-

traumforschung (GfW) facility in Bonn-Bad Godesberg, West Germany. However, in recognition of the importance of the *Helios* Ground Data System, the co-Chairmen scheduled the Fifth *Helios* Joint Working Group (HJWG) Meeting (October 1971) to be held at Deutsche Forschungs und Versuchsanstalt fuer Luft-Und Raumfahrt (DFVLR), Oberpfaffenhofen, West Germany, which houses the German Space and Operations Center (GSOC). Likewise, the co-Chairmen scheduled the Sixth *Helios* Joint Working Group Meeting at the Jet Propulsion Laboratory, April 26 through May 3, 1972, in recognition of the Tracking and Data System (TDS) support being provided by JPL along with consultation in selected fields of spacecraft technology. The Laboratory appreciated this oppor-

tunity to host this international conference which was attended by 158 official representatives—including some 89 West Germans. In addition, the Sixth HJWG Meeting was supported by a large number of JPL attendees who actively participated in the proceedings. This article will, therefore, be devoted to the highlights of that meeting.

II. Technical Highlights of the Sixth *Helios* Joint Working Group Meeting

A. TDS Subgroup Meetings

1. **General.** Due to the scope of the agenda, the TDS Subgroup met independently on four different occasions during the course of the Sixth *Helios* Joint Working Group Meeting. In addition, individual TDS Subgroup members participated in a number of special splinter group sessions devoted to specific technical topics. The number and scope of these meetings is in itself evidence that *Helios* has progressed past the conceptual design phase and is now deeply engrossed in the detail design phase. Since the latter also involves the detail design of all interfacing elements, such as the DSN, it was fortunate from the TDS viewpoint that the Sixth HJWG Meeting was conducted at JPL. This permitted rapid access to DSN technical resources as the need arose during the conduct of the Working Group meeting. This need did arise on many occasions and the results are documented both in the official minutes (Ref. 2) and in the formal interface agreements documents. Because of this, the following paragraphs will only attempt to highlight the most significant TDS developments that occurred during the Sixth HJWG Meeting.

2. **Near-Earth trajectory.** During the Fifth HJWG Meeting, which was held in October 1971 at Oberpfaffenhofen, West Germany, it was officially announced that *Helios* would employ a *Titan/Centaur*/TE364-4 launch vehicle using a direct-ascent launch trajectory. At that meeting, the Performance, Trajectory and Guidance (PT&G) Working Group recommended that the launch phase perigee altitude be raised from 185 to 926 km (100 to 500 nmi) to avoid the possibility of the *Titan*'s second stage impacting land masses in either Europe or Africa (see Ref. 3, p. 22). As a result of this recommendation, action items were assigned to develop a new set of powered-flight launch trajectories using the 926-km (500-nmi) perigee altitude. This work was accomplished during the period between the Fifth and Sixth Joint Meetings. Analysis of the new trajectories disclosed several interesting phenomena: First, while the angular tracking and doppler rates were higher during the near-vertical ascent phase, these rates dropped very rapidly and came well within DSN tracking capabilities by the time the spacecraft be-

came visible to either the Madrid or Johannesburg, South Africa, DSSs. Second, the higher perigee altitude permits practically continuous spacecraft visibility from land-based stations, thereby eliminating the need for ships and aircraft. Third, starting in mid-July 1974, the daily launch windows experienced in the southern launch corridor (Fig. 1 of Ref. 4, p. 26) have a longer time duration than the corresponding daily launch window in the northern corridor. Partially offsetting these advantages is a fourth factor which is a degradation due to an increase in the space loss (signal strength attenuation) because of the higher perigee altitude. However, the full impact of the latter is not known at this time. Data were presented at the Sixth HJWG Meeting which state the Near-Earth Phase station capabilities. These data must now be processed by the *Helios* Project Office to determine the telecommunications link performance at the higher perigee altitude. However, preliminary calculations indicate that this penalty may not be too severe. Therefore, after reviewing all of the results of the Sixth HJWG Meeting, the U.S. and German co-Chairmen (Project Managers) accepted the PT&G recommendation to use the southern launch corridor for future studies and analyses—but with the provision that all spacecraft, experiment, and ground operational efforts/schedules should remain consistent with a July 1, 1974 launch readiness date (Page 4 of Ref. 2).

3. **Compatibility tests schedule.** As mentioned in the previous issue (Ref. 5), initial *Helios*/DSN compatibility tests were conducted at DSS 71, Cape Kennedy, during April 1972. For these tests, the project employed an Engineering Model (EM) spacecraft transponder, which, due to schedule conflicts, did not contain the (telemetry and command) Data Handling Unit. As a result, the telemetry and command modulation had to be simulated, using specially generated digital waveforms in order to measure the various transponder performance parameters. While these tests were meaningful in themselves, they did not establish true end-to-end telecommunications compatibility; therefore, it was suggested that additional compatibility tests be conducted prior to the availability of the Prototype Model (PM) spacecraft in the fall of 1973 (see Fig. 3 of Ref. 6, p. 31). However, in his opening remarks to the general session of the Sixth HJWG Meeting, the German co-Chairman specifically requested that the individual subgroups study the implications and ramifications of delaying the PM compatibility tests with the DSN until after similar tests have been conducted between the Prototype Model and the German network stations (Ref. 4, p. 23; Ref. 3, p. 18) in order to avoid the expense and schedule delay associated with bringing the Prototype Model to the U.S. for compatibility and environmental tests, returning it to Germany for German network com-

patibility tests, and then returning it to Cape Kennedy to serve as a backup for the Flight Spacecraft. Scheduling all German tests prior to the U.S. tests would eliminate one round trip across the Atlantic. Along with the other subgroups, the TDS Subgroup pondered this question in considerable detail. The TDS Subgroup concluded that a delay in the U.S. compatibility test program would result in no time being available for any fixes necessary between the Prototype and Flight Model Spacecraft—based on the assumption that the German network will not be able to support compatibility tests prior to December 1, 1973 and the Flight Spacecraft is to be launched on schedule in July 1974. The co-Chairmen (Project Managers) weighed this consideration against the fact that the Prototype availability schedule had been delayed to December 1, 1973, which means it cannot meet the October 1973 schedule for compatibility tests in either event. However, the co-Chairmen stated that consideration will be given to the feasibility of utilizing the Engineering Model Spacecraft for the October 1973 DSN tests and the November 1973 launch vehicle mating tests. If this proves to be infeasible, the next compatibility testing opportunity would be with the Prototype at Cape Kennedy in April 1974. The outcome of this feasibility study is not predictable at the present time.

4. Ground Data System. A considerable number of the detailed technical discussions conducted within the TDS Subgroup concerned the characteristics, interfaces and performance of the Ground Data System (GDS). For *Helios*, the Ground Data System comprises all Earth-based elements from the receipt of the spacecraft signal at the stations to the final delivery of the Experiment Data Records (EDRs) to the individual experimenters. It encompasses both the U.S. and German support effort. While the external TDS interfaces with the spacecraft and the experiments were discussed in the respective joint sessions, there were numerous internal interfaces to be discussed within the TDS Subgroup during the Sixth HJWG Meeting. Among these was the definition of the data flow (routing) between the stations and the Project for both the realtime (mission operations) and non-realtime (EDR) modes of operation. An important decision was reached that all data received by the DSSs, whether intended for realtime or non-realtime use, would be routed via the Mission Control and Computing Center (MCCC)¹ for the generation of Master Data Records (MDRs) prior to re-formatting and routing the data to the *Helios* Mission Support Area—whether the latter be located at JPL or in Germany. This is particularly important with respect to

the interface between the MCCC and the German Space Operations Center (GSOC) located at Oberpfaffenhofen, West Germany. This routing permits a consistent interface for both Mission Operations data and coordination activities between the U.S. and German supporting networks.

The establishment of a consistent interface has obvious advantages for the realtime conduct of the mission. The non-realtime advantages may not be quite so obvious. For one thing, a consistent interface permits the Ground Data System to allocate within itself the permissible error level that can be tolerated for each element of the system and still meet the experimenters' requirements regarding their data records. For another thing, it permits the Ground Data System to re-examine the classical definition of the division of content between the MDR and the EDR to ensure maximum effectiveness of available resources. Another advantage, though seemingly mundane, is that a consistent interface permits a bit-by-bit specification of the data in each high-speed data block sent over the Ground Communication System between the various elements of the GDS. Such specifications are necessary because these data blocks are processed by computers and a change in data block format necessitates a change in computer software programs and/or subroutines. Since GSOC plans to obtain its computer software via procurement contracts, it is necessary to have these specifications defined at an early date and for the specifications to come under change control to avoid unnecessary contract modification expenses. Toward this end, the telemetry data block format for the MCCC/GSOC interface was established during the Sixth HJWG Meeting, and, in addition, an action item was generated to similarly define the command data block format prior to the next Working Group Meeting. These are examples of the level of detailed technical discussion mentioned in *Section II-A-1*, above.

B. TDS/Spacecraft Telecommunications Joint Meeting

In addition to discussions on the results of the Engineering Model Compatibility Tests and the impact of the new *Helios* trajectory upon Near-Earth Phase coverage, the following topics were discussed in the joint TDS/Spacecraft Telecommunications Meeting:

1. Status of DSS Ground Data System to handle *Helios* telemetry. The DSN experience to date in processing *Pioneer 10* telemetry was of interest to *Helios* since the latter also uses convolutionally encoded telemetry. Unfortunately, only a limited amount of *Pioneer 10* data had been accumulated and analyzed with respect to DSN performance by the time of the Sixth *Helios* Joint Working Group Meeting. In addition, it is difficult to extrapolate

¹The Space Flight Operations Facility (SFOF) at JPL has been renamed the Mission Control and Computing Center (MCCC).

DSN performance regarding the *Pioneer 10* frame length of 384 bits (maximum) to the anticipated performance with the 1152-bit *Helios* frame length. Some 192-bit frame length *Pioneer 10* data had been analyzed which showed a decoding deficiency of between 0.3 and 1.2 dB over preflight predictions. A portion of this deficiency may be attributable to certain preflight calculations which did not consider all of the error sources that exist in an actual receiving station. To reduce this discrepancy, the DSN presented an improved analytical model of DSS telemetry performance for project use in their telecommunications link analyses. In addition, the DSN agreed to provide *Helios* with a complete set of computer simulations, which are presently being run, regarding DSN performance with respect to *Pioneer 10* telemetry, and also to provide the *Helios* Project selected computer simulations based on the *Helios* telemetry frame length, etc. Dissemination of this information is anticipated prior to the Seventh *Helios* Joint Working Group Meeting.

2. *Helios* link design calculations. The project reported that calculations performed since the Fifth HJWG Meeting indicated that a significant reduction in anticipated telemetry performance will be reflected in the next issue of the *Helios* Link Design Control Tables. This reduction, which can total 1.5 dB for the nominal case and as much as 5 dB for the adverse tolerance case, is attributable to both spacecraft and ground station factors. The spacecraft factors include a forced reduction in dc power available to the radio subsystem, plus a better understanding of the actual performance (measured values) of the various elements within the radio subsystem. The ground station factors include adjustments to the analytical model and the incorporation of actual measurement data as mentioned in *Section II-B-1*, above. In addition, it is anticipated that the next issue of the *Helios* Link Design Control Tables will incorporate the effects of the new 926-km (500-nmi)-perigee powered-flight trajectory mentioned in *Section II-A*, above. Because this new issuance of the Link Design Control Tables will be used to develop the standard sequence of *Helios* mission events, the DSN agreed to give the document an immediate but thorough review upon its issuance.

C. TDS/Mission Analysis and Operations Joint Meeting

In addition to the foregoing topics, which were also discussed during the joint TDS/Mission Analysis and Operations (MA&O) meeting, the following subjects were also discussed:

1. *Blind acquisition procedures.* The present spacecraft design incorporates a safety feature which shuts off the

spacecraft transmitter in the event of an overload to the spacecraft dc power supply. To re-establish the downlink, it is necessary to send a command to reactivate the transmitter. This may create operational problems, especially in the very early phases of the mission. This factor, plus the complex nature of the associated analyses, led to the establishment during the Sixth HJWG Meeting of a special task team to study the matter in detail. The task team is to be composed of representatives from the TDS and Spacecraft Subgroups, and will be chaired by an MA&O representative.

2. *Data flow.* A detailed discussion was held on the data flow from the DSS through the MCCC to GSOC for telemetry, and from GSOC via the MCCC to the DSS for command data. This discussion reaffirmed the TDS Subgroup's conclusion that the routing should not bypass the MCCC. During the Working Group sessions, splinter groups were able to establish the high-speed data line block format for telemetry flow from the MCCC to GSOC, and an action item was assigned to similarly develop the high-speed data line block formats for command data. In addition, the DSN provided a status report on the operation to date of the *Pioneer 10* Remote Information Center (Ames Research Center) interface with the MCCC. It was duly noted that due to software development delays, *Pioneer* operates in a combination mode: telemetry data bypassing the MCCC, while command data are routed via the MCCC.

3. *Early orbit determination.* Since *Helios* requires an early (10 hours after launch) orbit determination in order to properly structure the Step II maneuver, the DSN presented its recent experience in performing an early orbit determination for *Pioneer 10*. Since the *Pioneer 10* actual launch trajectory followed very close to preflight nominals, its orbit was determined to sufficient accuracy well within the time constraint required by *Helios*. However, it was pointed out that this rapid orbit determination was aided by the existence of the two-way coherent doppler data as opposed to the *Helios* case where the doppler would be non-coherent. Because of the inaccuracies associated with non-coherent doppler, it was recommended that MA&O attempt, during the design of the mission sequence, to obtain as much two-way coherent doppler data as possible during the early mission phases. It was pointed out that the lack of coherent two-way doppler can only be partially offset by data from the Near-Earth Phase Network.

4. *Documentation.* The interface between the Ground Data System and Mission Operations is heavily dependent upon documentation. This is due not only to the fact

that it is necessary to reduce these interfaces to specification form, but also because it is necessary to develop procedures whereby personnel conducting the mission can react quickly and in a predictable manner to both standard and non-standard events experienced during the course of the mission. Further, if one considers computer software programs to fall into the general category of documentation, then one might state that the Mission Analysis and Operations function is more heavily dependent upon documentation than are the other elements of the project. It is, therefore, not surprising that the *Helios* Ground and Operations System (HGOS) (see Ref. 1, p. 20) has been actively developing a Management Plan which is expected to be published in July 1972. This plan not only establishes what documents are to be produced but also establishes a schedule for their publication. The Management Plan not only encompasses such standard documents as the Support Instrumentation Requirements Document (SIRD), but also includes specialized documents required to meet *Helios* program objectives. The status of a few of the key documents was provided during the Working Group Meeting: The SIRD was issued in preliminary form in September 1971. This document is presently being updated to incorporate the launch vehicle requirements; Experiments 11, 12 and 13 requirements; and numerous other changes. It is anticipated that the final version of the SIRD will be published during the summer of 1972.

The *Helios* Software Requirements Documents for telemetry and command data processing received an extensive review at JPL during the week prior to the Sixth HJWG Meeting. These requirements were found to be technically feasible; therefore, once the review comments are incorporated, the document will be officially published.

Documents will also be generated covering the Mission Design, Mission Operations, and the interfaces between MA&O and the other elements of the project—particularly those interfaces between the U.S. and German efforts.

D. TDS/Experiment Joint Meeting

The *Helios* Ground Data System has two major interfaces with the experiments: A realtime interface, and a non-realtime interface. In practice, the realtime interface for the display of science data is considered part of the total Mission Operations display requirements upon the Ground Data System. The non-realtime interface is via the Experiment Data Record (EDR). With respect to the latter, the following important factors were discussed during the joint sessions.

The experimenters defined their telemetry accuracy requirements as follows:

Undetected bit error rate	1×10^{-5}
Frame deletion rate ^a	1×10^{-3}
Dropout rate ^a (after establishment of link between spacecraft and station)	4%
^a Frame deletion rate (1×10^{-3}) is based on data after dropout rate (4%).	

After reviewing these requirements, the TDS Subgroup concluded that on a selective basis it appeared that the Ground Data System can perform to these specifications provided there is sufficient signal strength in the spacecraft-to-ground link. As noted above, the latter needs further investigation.

The proposed science data processing plans of both the U.S. and German data centers were presented to the experimenters for their review. The plans satisfied the experimenters' requirements and were accepted.

For further details on this or any of the above-mentioned meetings, the reader is referred to the minutes of the Sixth *Helios* Joint Working Group Meeting (Ref. 2).

III. Conclusions

In the opinion of both the TDS Subgroup and Project Management, the Sixth *Helios* Joint Working Group Meeting was highly productive. Marked progress was made in defining many of the important interfaces. Some of these were resolved to the point where formal specifications can now be generated, while others require further study. In the latter instance, specific actions were assigned participants in order that schedule objectives can be met. In addition, the exchange of technical information during the Sixth HJWG Meeting provided an important base upon which to structure each country's future activities in support of *Helios*. While the actual accomplishment of project activities is achieved within the line management organization of the respective countries, such efforts would be hardly compatible if it were not for the coordination achieved through the mutual understanding derived from the semi-annual Joint Working Group Meetings. The Jet Propulsion Laboratory is, therefore, pleased to have been selected host for the Sixth HJWG Meeting and is looking forward to its participation during the Seventh HJWG Meeting, which is to be held October 25–31, 1972 at Porz-Wahn, West Germany.

References

1. Goodwin, P. S., "Helios Mission Support," in *The Deep Space Network Progress Report*, Technical Report 32-1526, Vol. II, pp. 18-27. Jet Propulsion Laboratory, Pasadena, Calif., Apr. 15, 1971.
2. *Project Helios Minutes of the Sixth Helios Joint Working Group Meeting at Jet Propulsion Laboratory, Pasadena, California, April 26-May 3, 1972*. Goddard Space Flight Center, Greenbelt, Md.
3. Goodwin, P. S., "Helios Mission Support," in *The Deep Space Network Progress Report*, Technical Report 32-1526, Vol. VII, pp. 17-24. Jet Propulsion Laboratory, Pasadena, Calif., Feb. 15, 1972.
4. Goodwin, P. S., "Helios Mission Support," in *The Deep Space Network Progress Report*, Technical Report 32-1526, Vol. III, pp. 20-28. Jet Propulsion Laboratory, Pasadena, Calif., June 15, 1971.
5. Goodwin, P. S., "Helios Mission Support," in *The Deep Space Network Progress Report*, Technical Report 32-1526, Vol. IX, pp. 33-34. Jet Propulsion Laboratory, Pasadena, Calif., June 15, 1972.
6. Goodwin, P. S., "Helios Mission Support," in *The Deep Space Network Progress Report*, Technical Report 32-1526, Vol. IV, pp. 22-31. Jet Propulsion Laboratory, Pasadena, Calif., Aug. 15, 1971.

Mariner Mars 1971 Mission Support

G. P. Textor

DSN Engineering and Operations Office

The Mariner Mars 1971 Extended Mission utilizes DSS 14, the 64-meter-diameter antenna station at Goldstone, California, for acquiring telemetry and radio metric data. The 26-meter-diameter antenna stations at Madrid, Spain and Goldstone, California, however, are playing an important part maximizing the quantity and quality of the data received at DSS 14. This article describes the role of the 26-meter-diameter antenna stations presently engaged in the Mariner Mars 1971 Extended Mission.

I. Introduction

Due to the current telecommunications performance margins, only the 64-meter-diameter antenna at DSS 14 can receive meaningful telemetry data from *Mariner 9*.¹ The data rate received can be increased by boresighting the *Mariner 9* high-gain antenna with the Earth, and by configuring DSS 14 in a "listen-only" mode, i.e., receiving but not transmitting. This mode allows data rates as high as 8.1 kbps to be received from *Mariner 9*, but prevents DSS 14 from commanding the spacecraft. In addition, without a transmitting station, the radio metric data ac-

quired is of little value. The 26-meter stations, DSS 62, DSS 11, and DSS 12, are being employed to perform the transmitting functions for command and radio metric data.

II. Command Support

While only DSS 14 can acquire the telemetry data from *Mariner 9*, the 26-meter stations are able to provide an uplink to the spacecraft and transmit commands. This capability was used early in the extended mission. On the days that DSS 14 was unavailable, DSS 62 was called upon to transmit commands that helped conserve attitude control gas. These commands were sent "in the blind," i.e., without confirming telemetry data.

¹A 26-meter station can receive low-rate telemetry when the high-gain antenna is boresighted with Earth, but the present command support is required prior to the boresighting maneuver.

Present command support from DSS 62 serves two purposes: (1) allows early transmission of a crucial command in the maneuver sequence, thus providing additional response time in the event of an anomaly; and (2) allows DSS 14 to be in a "listen-only" mode at the start of playback of scientific data from *Mariner 9*.

III. Uplink Support for Improved Metric Data

When a DSS is in a receive-only condition, the resulting doppler data from the spacecraft signal are called one-way doppler. These data do not have the precision necessary for good positional data because of errors introduced by drifts in the spacecraft exciter frequency. Normally the DSS transmits an S-band signal and the spacecraft transponder, by the use of coherent frequency multiplication, converts the signal to a higher frequency which is then transmitted back to Earth. This is a closed, two-way, phased-locked system which provides precision doppler.

Another way of obtaining high accuracy tracking information is to have a DSS in a two-way mode and a second station in a receive-only condition at the same time; the resultant mode of the second station is identified as three-way. Doppler data nearly as precise as two-way can be obtained from the three-way mode.

Metric data of at least three-way precision are required for the *Mariner* Occultation and Celestial Mechanics (CM) Experiments. The Occultation Experiment requires three-way data at entrance of occultation, and the CM Experiment requires three-way data 1 hour prior to and 1 hour after periapsis passage. Using the uplink signal from DSS 62, DSS 14 can receive three-way doppler during "enter occultation." However, the DSS 62 view period ends prior to the periapsis period, so either DSS 12 or DSS 11 (whichever is available) replaces DSS 62 in providing the uplink. DSS 14 can acquire the required metric data while maintaining a receive-only configuration for enhanced telemetry reception.

Viking Mission Support

D. J. Mudgway
Mission Support Office

A previous article identified the probable impact of changes to the scope of the DSN to Flight Project interfaces as far as Viking was concerned. In this article the outcome of the resulting changes is described in the areas of DSN configuration, interfaces, schedules, documentation, and organization in order to establish a background against which subsequent articles can report progress in each of these particular areas.

I. Introduction

Since the beginning of 1972, a substantial effort has been directed toward revising previously existing agreements for support of *Viking* in the context of the new definition of DSN/Flight Project Interfaces. The probable impact of this new definition was identified in a previous article (Ref. 1).

As a consequence of this effort, all major areas which were affected by the change have now been re-negotiated with the Flight Project, with the Office of Computing and Information Systems (OCIS), and with the DSN Facilities, and new agreements regarding interfaces, documentation, organization configuration, and support have been documented. This article describes the new situation in each of these areas in order to provide a background against which future articles will report continuing progress in DSN support for *Viking*.

II. Configuration

The DSN configuration for *Viking* is shown in general terms in Figs. 1 and 2. From a hardware and software point of view, Fig. 1 shows the Deep Space Stations connected via high-speed and wide-band circuits to the GCF Communications Terminal in Building 230 at JPL and then to the *Viking* Mission Control and Computing Complex in Buildings 230 and 264. This arrangement provides for the direct flow of all telemetry, tracking, and command activity between the DSSs and the *Viking* Flight Operations System (FOS) located in the *Viking* Mission Control and Computing Complex (VMCCC).

The DSN operations control function is also located in Building 230 and accesses its supporting data processing function via the GCF Communications Terminal as shown in the figure. The Network Control System (NCS) data processing function may be carried out at some location

yet to be determined other than Building 230. The addition of the NCS to the DSN in no way interferes with the flow of data between the DSSs and VMCCC or vice versa.

From an operations point of view, the DSN configuration for *Viking* appears to the Project as shown in Fig. 2. In this case the NCS operations control function is in series between the FOS and the DSS. All operations traffic to and from the DSSs will pass through this function which acts effectively as the prime operations interface between the DSN and the *Viking* Project. The NCS data processing function provides support to the operations function as described above.

This basically describes the DSN configuration for *Viking*. Detailed configurations at the functional level are presently being developed from these basic concepts in terms of each of the Network systems (telemetry, tracking, command, monitor and operations control, and test and training). These configurations will be described in subsequent reports.

III. Interfaces

The data processing and supporting facilities in Building 230, formerly included in the DSN and called the Space Flight Operations Facility, have now been designated as the Mission Control and Computing Center. In the *Viking* configuration this becomes the *Viking* Mission Control and Computing Center (VMCCC) and was recently established as a sixth system of the *Viking* Project. The other Project Systems are: Launch Vehicle System (LVS), *Viking* Orbiter System (VOS), *Viking* Lander System (VLS), Launch and Flight Operations System (LFOS), and Tracking and Data System (TDS). As a consequence, the TDS interfaces with the *Viking* Project are now defined as shown in Fig. 3. Each of the interfaces is described and controlled by an Interface Requirements Document (IRD), which is signed by the Manager of each of the interfacing systems and approved by the Project Manager. The status of each of these documents is described in Section V, below.

IV. Schedules

The *Viking* TDS level 3 schedule is the controlling schedule for all TDS planning in support of *Viking*. The division of responsibility for *Viking* support covered by the previous level 3 schedule, which included the SFOF support, has now been completed. Two level 3 schedules are now approved, one covering TDS support, the other

covering VMCCC support. These schedules are updated monthly and transmitted to the *Viking* Project Office for inclusion in the Project Monthly Review (PMR).

All milestones on the TDS schedule up to the current period have been completed on time. In addition to the level 3 schedule, the TDS is also committed to support the Project-wide PERT (program evaluation and review technique) reporting system. A TDS/PERT network has been developed and is updated twice monthly to reflect TDS activity in the context of Project-level progress.

V. Documentation

As of June 1972, the NASA Support Plan (NSP) for *Viking* has been approved and distributed after being completely revised to reflect the new interfaces.

The Interface Requirements Documents (IRDs) between the DSN Orbiter and DSN/Lander are currently being reviewed prior to final approval.

The DSN/VMCCC IRD is in the early stages of development and, since it is a new concept, will probably require a longer preparation and review cycle.

A new version of the DSN/Project Interface Design Handbook has been issued, which also reflects the change in DSN/Project interfaces.

By agreement with the Project Office, it was decided not to revise the TDS Functional Specification for *Viking* since it no longer matched the DSN organization described in Section VI. Instead, a new document called the DSN Support Plan for *Viking* has been created, which better suits the new DSN approach to inform the DSN facilities of the flight project requirements. This document summarizes and brings together all the agreements that have been made in a multitude of Project documents on such matters as configuration control, test and training, documentation, reporting interfaces, DSN capabilities, trouble and failure reporting, reviews, operations support, etc.

The facilities response to this document is in two parts as shown in Fig. 4. The Facilities Mission Preparation Plan responds to the DSN Support Plan with instructions and plans at the facility level for configuration, capability, testing, and schedules related to preparing the facilities for mission support.

The Facilities Mission Operation Plan describes the facility plans for operational support during the mission. These three documents supersede all previous mission-dependent documents and will be formalized in a revision to the DSN documentation system in the near future. The DSN Support Plan is undergoing final review at this time, while the facility responses are still in the early formative stages.

VI. Organization

The change in DSN responsibilities referred to above together with general consolidation of DSN manpower resources resulted in the deletion of the DSN Project Engineer function. The DSN Manager and Project Engineer functions are now combined, and as a consequence a new approach to DSN/Facility working relationships is required. The previous concept of a Capabilities Planning Team (CPT) has been dissolved and replaced with a DSN Support Team chaired by the DSN Manager and composed of an engineering and an operations representative from each of the facilities.

This team continues to exist for the life of the Project and provides continuous support from the planning phase through implementation, test, and operations. It is believed that this will afford a closer tie between the facilities implementation and operations support and the DSN commitments to the Project than we have had in the past.

The DSN Support Team for *Viking* has been established and has been in operation for several months. The team members are:

Chairman	D. J. Mudgway DSN Manager for <i>Viking</i>
DSIF Engineering	W. D. Brown
DSIF Operations	D. W. Johnston
GCF Engineer	J. P. McClure
GCF Operations	J. W. Capps
Network Central System	W. J. Kinder
DSN Operations	R. J. Amorose
<i>Viking</i> Project Representative	R. R. Peterson
VMCCC Representative	E. L. Pyle

Formal minutes of its regular meetings are prepared for a wide distribution throughout the Project and DSN.

VII. Conclusion

Most of the disruptions caused by the change in DSN/Flight Project interfaces have now been resolved and new and, in many cases, better interfaces and working relationships have been developed and put into effect. The DSN is now proceeding in the new environment described above, and progress toward *Viking* mission readiness will be reported in this context in subsequent issues.

Reference

1. Mudgway, D. J., "Viking Mission Support," in *The Deep Space Network Progress Report*, Technical Report 32-1526, Vol. VIII, pp. 20-23. Jet Propulsion Laboratory, Pasadena, Calif., Apr. 15, 1972.

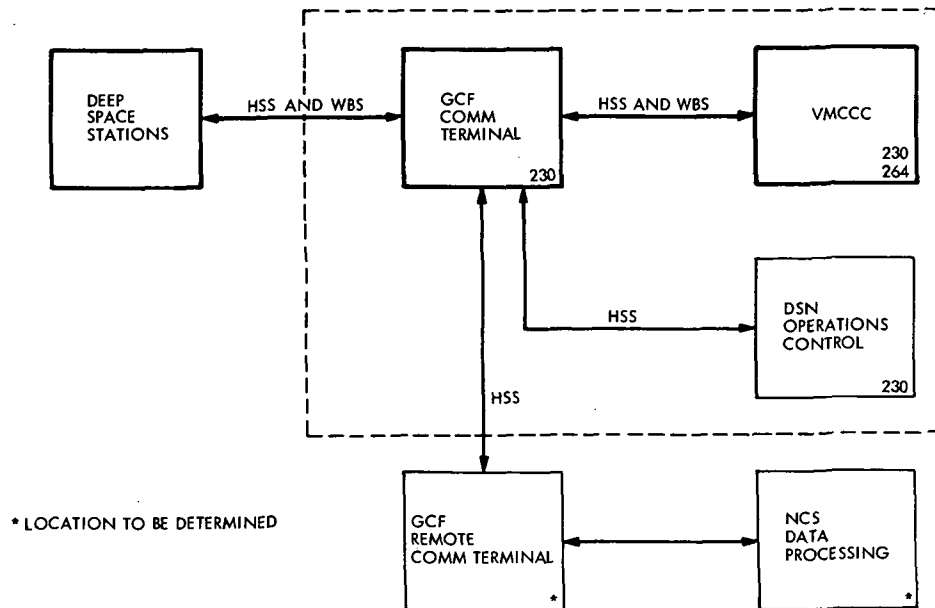


Fig. 1. DSN general hardware configuration

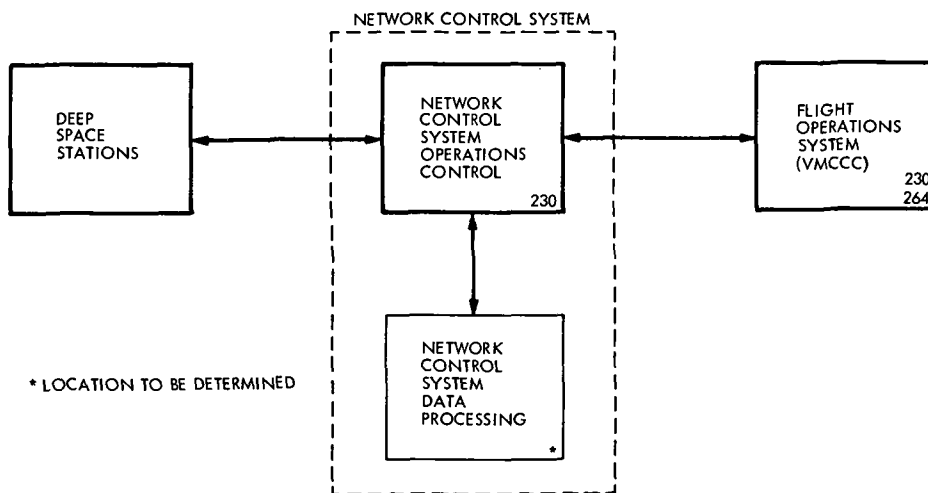


Fig. 2. DSN general operations configuration

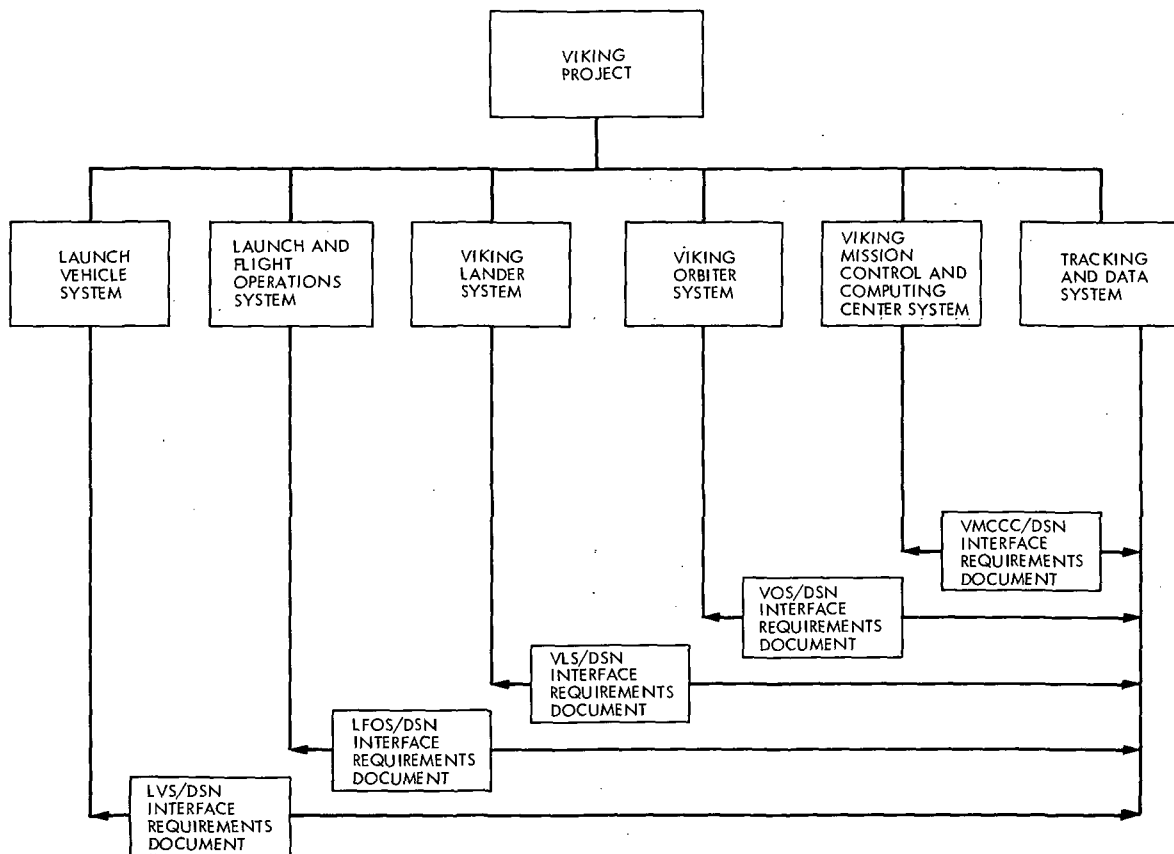
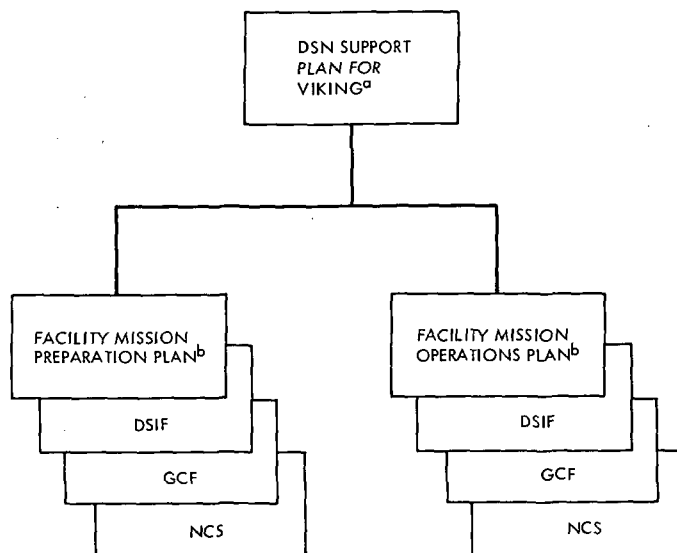


Fig. 3. TDS interfaces within Viking Project



^a PREPARED BY DSN MANAGER

^b PREPARED BY FACILITIES MANAGERS

Fig. 4. DSN/Facilities documentation for Viking

Pioneer 10 and G Mission Support

A. J. Siegmeth
Mission Support Office

The Deep Space Network (DSN) has already furnished more than four months of continuous data acquisition and command support for Pioneer 10, launched on March 3, 1972. After the description of the new DSN/Flight Project interface, a brief review is given on the qualitative and quantitative performance of DSN's data recovery support.

I. Pioneer 10 Cruise

The *Pioneer 10* spacecraft has been cruising for over four months toward the Planet Jupiter. It was successfully launched on March 3, 1972.

The DSN has furnished continuous tracking for the *Pioneer 10* mission using 26-m-diam antenna stations. During the midcourse maneuvers, data were obtained from the 64-m antenna at DSS 14 to enhance the telemetry signal-to-noise ratio. Most of the time the spacecraft operated on a telemetry bit rate of 2048 bps. All spacecraft telemetry was processed in real time, and for the Project's Mission Operations Team numerous digital display tables, teletype, and high-speed line printer formats were provided for configuration control and spacecraft health analysis. Based upon the mission plan and the analysis of the real-time telemetry information, the Operations Team has sent to the spacecraft over 5000 commands to obtain the best scientific data return. The Project initiated all commands using the DSN's Mark III-type automatic command system.

The DSN has also supported, via a high-speed data line interface, the *Pioneer* Remote Information Center (RIC),

which is located in the *Pioneer* Building at Ames Research Center, Moffett Field, California. This Remote Space Flight Control Facility is processing in real-time synchronized spacecraft telemetry data handled by the Central Processing System of the Space Flight Operations Facility (360/75 IBM computer). In addition, the DSN provided to the RIC the on-site-generated *Pioneer 10* telemetry high-speed data blocks as a backup.

In the non-real-time mode, the DSN generated, within 24 hours, *Pioneer 10* digital System Data Records (SDR) which contain not only all telemetry data received by the Central Processing System in real time, but also fill data obtained postflight from a digital Original Data Record (ODR) generated on-site. The *Pioneer* Project has received in biweekly batches the system data records from the DSN and converted them to experimenter data records (EDR). During June 1972, the DSN finished the software implementation of a master data record (MDR) capability. The MDR data tapes contain filled, time-cued, and merged spacecraft telemetry data.

During the first half of CY 1972, the DSN was engaged in extensive planning activities to modify the DSN/Flight

Project interface configuration. The Office of Space Sciences and the Office of Tracking and Data Acquisition of NASA Headquarters has reviewed the Planetary Mission Operations/DSN interface to bring the program control and budget functions more into line with management responsibilities. The Headquarters guidelines were asking for the development of a reasonably clear Network/Project interface in order to simplify technical management and also to assure that budgeting requirements of the two offices are well understood. Assurance was also sought for the coverage of all technical and operational requirements. In accordance with these guidelines, the Deep Space Network will have the responsibility of network control and monitoring. These functions will include network scheduling and performance monitoring, and will provide clean data streams (bit synchronized and identified) to Mission Operations. In addition, the network will accept commands from Mission Operations and will transmit them to the stations and spacecraft and will have a provision for recording of clean data streams of radio metric, telemetry, and command data. These data can be provided to Mission Operations as required. The network will also participate in the test and training activity of Mission Operations using simulated data streams generated by the missions. The same guidelines shifted all Mission Operations responsibilities to OSS funding and to the Flight Projects.

The funding, planning, and operations of the Space Flight Operations Facility (SFOF) at JPL, which also supports the *Pioneer* Mission Support Area, will be transferred to JPL's Office of Computing and Information Systems (OCIS). The Data System Division, operating under OCIS, will be responsible for taking over the Mission Operations support and computing functions by July 1, 1972. The Space Flight Operations Facility has been renamed the Mission Control and Computing Center (MCCC). The DSN will provide the telemetry, radio metric, and command verification data streams to the MCCC for the support of all planetary and interplanetary projects. Provisions will also be made to transmit automatic commands via high-speed data line to the DSSs. The DSN plans to add to the network a Network Control System (NCS). This system will have a network control area and a data processing area. The DSN started the development of the NCS, which will have the capabilities as recommended by NASA Headquarters guidelines. During the interim, the MCCC's Central Processing System (360/75) will support the Network Control System requirements.

Based upon the actual performance evaluation of the *Pioneer 10* telecommunications downlink, which carries

the spacecraft-generated telemetry signals to the Deep Space Stations, it was observed that the performance parameters were correlating well with the design goals established during *Pioneer 10* preflight planning. The actual performance residuals were well within a tolerance range of $\pm 1\frac{1}{2}$ dB. This is the root sum square (RSS) value of all combined favorable and adverse measurement tolerances of the flight and ground equipment operating the downlink telemetry channel.

To assess the actual performance of the *Pioneer 10* telecommunications downlink, the DSN measures regularly the following parameters: system-noise temperature (SNT), received carrier power P_c , symbol energy per bit versus receiver noise spectral density ratio (ST_s/N_o), symbol error rate (SER), and deletion rate (DLR).

Table 1 is a recently updated *Pioneer 10* Telecommunications Downlink Design Table. Figure 1 depicts the design and actual characteristics of the *Pioneer 10* sequential decoding capabilities. Based upon the contents of Table 1 and Fig. 1, downlink performance nomograms were charted which are illustrated in Fig. 2. These nomograms are based upon *Pioneer 10* downlink performance characteristics and represent actual and nominal conditions. If the reader wishes to use these graphic calculation aids, the following procedures can be followed:

- (1) Obtain cold sky SNT and antenna elevation readings from the DSS and using correction scales (C) and (H) to determine the deviation from the nominal SNT. This will be a positive or negative dB adjustment defining the actual SNT.
- (2) Obtain the actual downlink carrier power level from DSN monitoring format 24. Connect on both (A) scales this actual carrier power value with a horizontal line. At the appropriate telemetry bit rate, read out on the (F) scale the SNR related to an SNT of 33 K. Mark down this value.
- (3) Add or subtract the SNT dB adjustment as calculated in (1) to the 33 K SNR obtained from the (F) scale. This is the adjusted SNR. Read out the SER and DLR values corresponding with the adjusted SNR.
- (4) Obtain the measured signal-to-noise ratio (SNR) from Form 815 (which contains numbers of the digital display forms available from the DSN Network Control Area), and calculate a residual versus the adjusted SNR. The residual of these two values should be within $\pm 1\frac{1}{2}$ dB.

- (5) Obtain actual Earth/spacecraft range in kilometers from the RTLT displayed on Form 815.

$$\text{Range in million km} = 9 \times \text{RTLT (in minutes)}$$

or

$$\text{Range in million km} = \frac{3}{20} \times \text{RTLT (in seconds)}$$

The estimated Earth/spacecraft range and the predicted downlink carrier power can be obtained from the *Pioneer 10* and *G* telecommunications calculator.

- (6) Determine a residual between predicted P_c (5) and measured P_c (2).

If the reader wants to use the attached graphs for the 64-m DSS, the following corrections should be made:

$$\text{SNT 26 m (nominal)} = 33 \text{ K}$$

$$\text{SNT 64 m (nominal)} = 24 \text{ K}$$

The lower 64-m SNT results in a nominal SNR correction of +1.4 dB. Nominal antenna gain:

$$64 \text{ m: } 61.4 \text{ dBi}$$

$$26 \text{ m: } 53.3 \text{ dBi}$$

The 64-m versus 26-m antenna gain improvement factor is 8.1 dB; thus the received spacecraft power level should be increased by this factor. Therefore, the attached curves can be used with 64-m antennas, if one makes the proper SNT correction.

If during the spacecraft's 12-s-long rotational period the amplitude of the downlink power has a CONSCAN-type amplitude variation of more than 1 dB peak-to-peak, the following corrections should be made:

- (1) Obtain from the DSS the minimum and maximum downlink carrier power readings. Calculate the arithmetic mean of P_c and use this value. The computer-generated mean values are not always accurate unless several averaged readings are taken.
- (2) The signal-to-noise ratio estimator (SNORE) program-generated telemetry SNR as displayed on Format 815 is somewhat higher than the arithmetic mean corresponding with P_c . This reading should be lowered by approximately 0.5 dB at P_c variations of 5 dB peak-to-peak.
- (3) The SER and DLR readings are average values. All the symbol errors and deletions are generated only

during the low values of the time-varying SNR. For a 10-dB peak-to-peak, divide SER by approximately 3.3; for a 5-dB peak-to-peak, divide by 2.2; for a 3-dB peak-to-peak, divide by 1.5 to obtain correlation between the constant SNR scale (F) and DLR scale (D) readings.

To obtain the most accurate performance parameters from the *Pioneer* Form 815, and the DSN Monitoring Format 24 displayed on the digital monitors, it is necessary that the user understand the relationship between quantizing levels and errors, the statistical sampling time periods, and their impact on the displayed values. In other words, it is important to know how the on-site and CPS processors manipulate the raw measurement data.

The following example shows the typical steps of the downlink analysis.

- (1) Nominal 26-m SNT = 33 K (charts are based on this value)
 Actual cold sky DSS SNT = 24 K, (scale (G))
 Noise power improvement: +1.4 dB (scale (H))
 Elevation angle: 10 deg
 Noise degradation because of 10 deg elevation:
 -2.1 dB (scale (H))
 Resultant noise power correction: $-2.1 + 1.4 = -0.7 \text{ dB}$
- (2) Actual downlink carrier power, $P_c = -157.4 \text{ dBmW}$
 (place straight at this value on both (A) scales)
 CONSCAN amplitude $\sim 1 \text{ dB}$ peak-to-peak
 Telemetry bit rate: 512 bps
 33 K SNR = 1.3 dB (read on scale (F))
- (3) Adjusted SNR: $1.3 \text{ dB} - 0.7 \text{ dB} = 0.6 \text{ dB}$
 (predicted value of SNR)
 SER: 6% (read from scale (E) and compare with Format 815)
 DLR: 0.5% (read from scale (D) and compare with Format 815)
- (4) Actual SNR: 1.0 dB (Format 815) (use (I) and (K) scales)
 SNR residual: 0.4 dB
- (5) RTLT: 46 min
 Range: 415 million km

High-gain spacecraft antenna with ELA = 0.3 deg

Calculated downlink carrier power: -157.7 dBmW

(6) Predicted P_c from (5) -157.7 dBmW

Measured P_c from (2) -157.4 dBmW

P_c residual: +0.3 dB

To illustrate the quantitative support performance of *Pioneer 10*, it should be stated that DSN has delivered to the *Pioneer* Project continuous telemetry data packages which contain on a daily basis 98 to 99% of all data acquired by the stations. Our original commitment was to furnish at least 97% of the received data stream.

II. Planning and Preparations for the *Pioneer G* Launch Readiness

The second mission of the third-generation *Pioneers*, *Pioneer G*, will be launched during April 1973. The DSN plans to use the same network configuration and capabilities for *Pioneer G* which are already in operation for the support of *Pioneer 10*. This decision will be based upon the assumption that the *Pioneer G* and *Pioneer 10* telecommunications interfaces will be the same. The planning activities for *Pioneer G* are in progress and regular bi-weekly *Pioneer G* Operational Support and Planning Group meetings are held to identify, issue, or close out *Pioneer G*-oriented action items. The updating of the *Pioneer 10* documentation has been started.

Terms used in this article are defined as follows:

SNT = Cold-sky high-elevation angle system noise temperature measured during *Pioneer 10* pre-pass calibrations. Obtain from DSS.

P_T = Total transmitted power of *Pioneer 10*, nominal value: 39 dBmW (actual displayed on Format 808).

P_c = Received carrier power. With a nominal modulation index of 1.1, the carrier is 6.9 dB below the received total power P_r . P_c is measured by a DSS and displayed at MCCC in dBmW or in voltages. Use the DIS-generated (DSIF monitoring) value displayed on Format 24 whenever available. The P_c displayed on Format 815 is generated by the DSS/TCP. The engineering conversion of the TCP-generated value is based upon a linear approximation and it has a somewhat lower accuracy.

P_s = Received symbol power. It is 1 dB below P_r . It is not measured or displayed at the MCCC.

$\frac{ST_s}{N_0}$ = Symbol energy per bit versus receiver noise spectral density ratio. The DSS/TCP SNR program calculates this value from statistical values obtained from the symbol synchronizer assembly (SSA). The results of these calculations are displayed on Format 815 as the SNR of the demodulated symbol stream. It should be noted that the telemetry SNR is higher at the input of the DSIF receiver. This SNR degradation is caused by some additive noise originating from the carrier tracking loop, the subcarrier demodulator, and the symbol synchronizer. The measured values of the combined SNR degradations (also called demodulation efficiency) are included in the 810-5 document. The attached graphs are adjusted for this SNR degradation. Below SNR = 6 dB use scales (I) and (K) and convert the displayed SNR to an actual SNR.

SER = Symbol error rate. Parameters for this calculation are generated in the DSS/DDA/TCP and calculated and displayed by the SFOP/CPS. Format 815 displays SER and it is identified as BER (0.10000 = 10% and 0.0100 = 1%).

DLR = Deletion rate. A constraint caused by physical limitations of the sequential decoding processor. This value describes the percentage of the deleted telemetry frames versus the total number of received telemetry frames. Display Format 815 shows the actual DLR (0.10000 = 10% and 0.0100 = 1%). Because of statistical constraints, the DLRs displayed are only meaningful between 1% and 10%. The displayed numbers should be averaged for at least 30 min. The DDA can perform approximately 25,000 computations per second as an upper limit and at SER values >4%; some telemetry frames cannot be decoded and are deleted. The deletion rates displayed on the nomograms show the statistical decoding performance. The actual DDA performance will be somewhat improved when all decoders are equipped with the correct read-only memories (ROMs).

ELA = Earth look angle. Angle between the spacecraft spin axis and the spacecraft/Earth line.

RTLTL = Round-trip light time.

ROM = Read-only memory

Table 1. Pioneer 10 typical telecommunications downlink design

DSN/spacecraft range: 300 Mkm; spacecraft antenna: high-gain; DSS antenna: 26-m diam							
Item	Source	Parameter	Nominal	Unit	Tolerances		Notes
					Favorable	Adverse	
1	ARC	Transmitter power, spacecraft	39.0	dBmW	0.2	0.2	Telemetered value
2	ARC	Transmitting circuit losses	-2.0	dB	0.12	0.12	Includes antenna alignment loss
3	ARC	Transmitting antenna gain	31.8	dBi	0.4	0.4	High-gain antenna, ELA = 0 deg
4	—	Space loss	-268.9	dB	—	—	at 2292 MHz
5	DSN	Receiving antenna gain	53.3	dBi	0.6	0.6	26-m antenna
6	DSN/ARC	Polarization and antenna pointing	-0.5	dB	—	—	Spacecraft, DSN measurements
7	Σ 1-6	Total received power	-147.3	dBmW	0.76	0.76	RSS of tolerances
8	DSN	Receiver noise spectral density	-183.4	dBmW-Hz	0.4	0.4	N_0
<i>Carrier performance</i>							
9	ARC	Carrier modulation loss	-6.9	dB	—	—	$\theta = 1.1$ rad
10	DSN	Received carrier power	-154.2	dBmW	0.76	0.76	Measured by DSN
11	DSN	Carrier loop threshold bandwidth	10.8	dB	0.5	0.5	$2B_{l_0} = 12$ Hz
12	DSN	Required SNR in carrier loop	6.0	dB			Cycle slip constraint
13	8 + 11 + 12	Required minimum carrier power	-166.6	dBmW	0.9	0.9	Calculated
14	13-10	Margin	12.4	dB	0.9	0.9	RSS of tolerances
<i>Data channel performance</i>							
15	ARC	Data modulation loss	-1.0	dB	—	—	$\theta = 1.1$ rad, measured and calculated
16	7-15	Received symbol power	-148.3	dBmW	0.76	0.76	
17	DSN	Demodulation loss	-0.5	dB	0.2	0.2	810-5, measured and calculated
18	16 + 17	Effective symbol power	-148.8	dBmW	0.78	0.78	Calculated
19	—	Time per symbol	-33.1	dB-s	—	—	2048 symbols/s 1024 bps calculated
20	18 + 19	Effective ST_s (energy per bit)	-181.9	dBmW-s	—	—	
21	20-8	Effective ST_s/N_0	1.5	dB	0.4	0.4	Measured by DSN
22	ARC	Required ST_s/N_0	1.5	dB	—	—	24 SER = 4.6% 25 DLR = 0.01%
23	21-22	Margin	0	dB	0.9	0.9	RSS of tolerances

Measured by ARC

Spacecraft transmitter power (1)

Measured by DSN

Received carrier power, P_c (10)

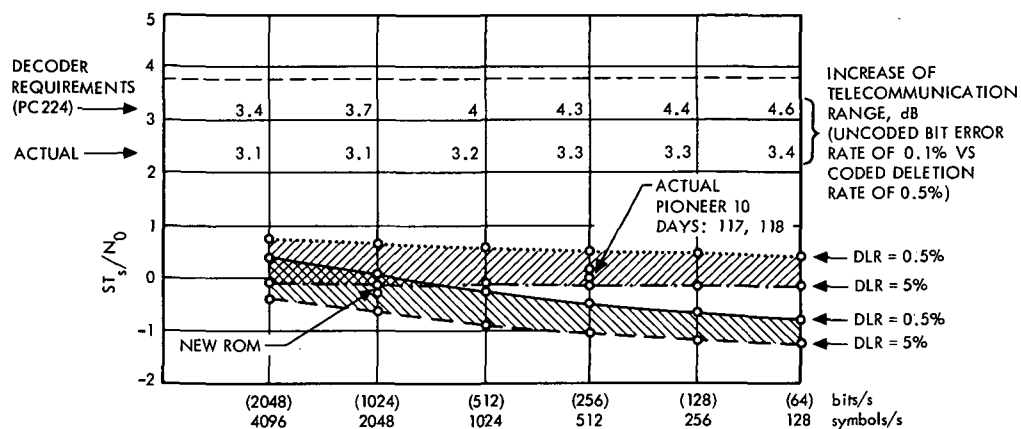
DSN cold sky system noise temperature, SNT (8)

Effective ST_s/N_0 (21)

Symbol error rate, SER (24)

Coded mode deletion rate, DLR (25)

Tolerances are one-sigma values



MODULATION INDEX = 1.1 rad, 25,000 COMPUTATIONS/s

THE PIONEER REQUIREMENTS VERSUS ACTUAL PERFORMANCE RESIDUALS OF ~0.3 TO 1.2 dB (2048 TO 64 bps) ARE CAUSED BY THE PHASE JITTER OF THE BEST ESTIMATE OF THE RECEIVED S-BAND CARRIER. THIS PHASE NOISE HAS SOME NON-WHITE GAUSSIAN COMPONENTS (1/F TYPE) AND IT IS A FUNCTION OF THE S/N RATIO IN THE $2BL_0 = 12$ -Hz CARRIER LOOP

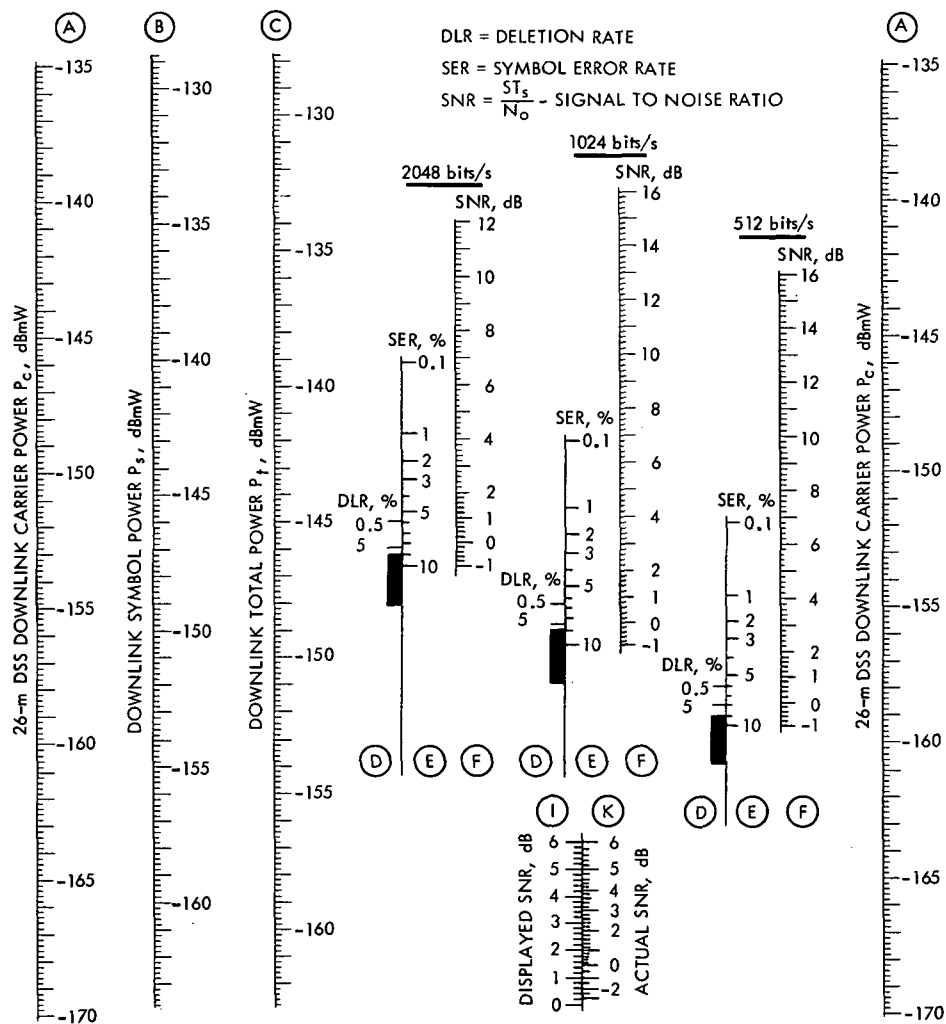
DLR = DELETION RATE

$2BL_0$ = TWO-SIDED NOISE BANDWIDTH OF THE CARRIER TRACKING PHASE-LOCKED LOOP AT THRESHOLD CONDITIONS

▨ SIMULATED AND ACTUAL SYSTEM PERFORMANCE

▨ DECODER REQUIREMENTS, PC224

Fig. 1. Pioneer 10 sequential decoding



MODULATION INDEX: 1.1, CODED MODE, CARRIER SUPPRESSION: 6.9 dB,
 SYMBOL POWER SUPPRESSION: 1 dB

26-m DSS SNT: 33 K (NOMINAL)

RECEIVER NOISE SPECTRAL DENSITY: -183.4 dBmW Hz

Fig. 2. Pioneer 10 downlink performance nomograms: (a) 2048, 1024, and 512 bps; (b) 256, 128, and 64 bps

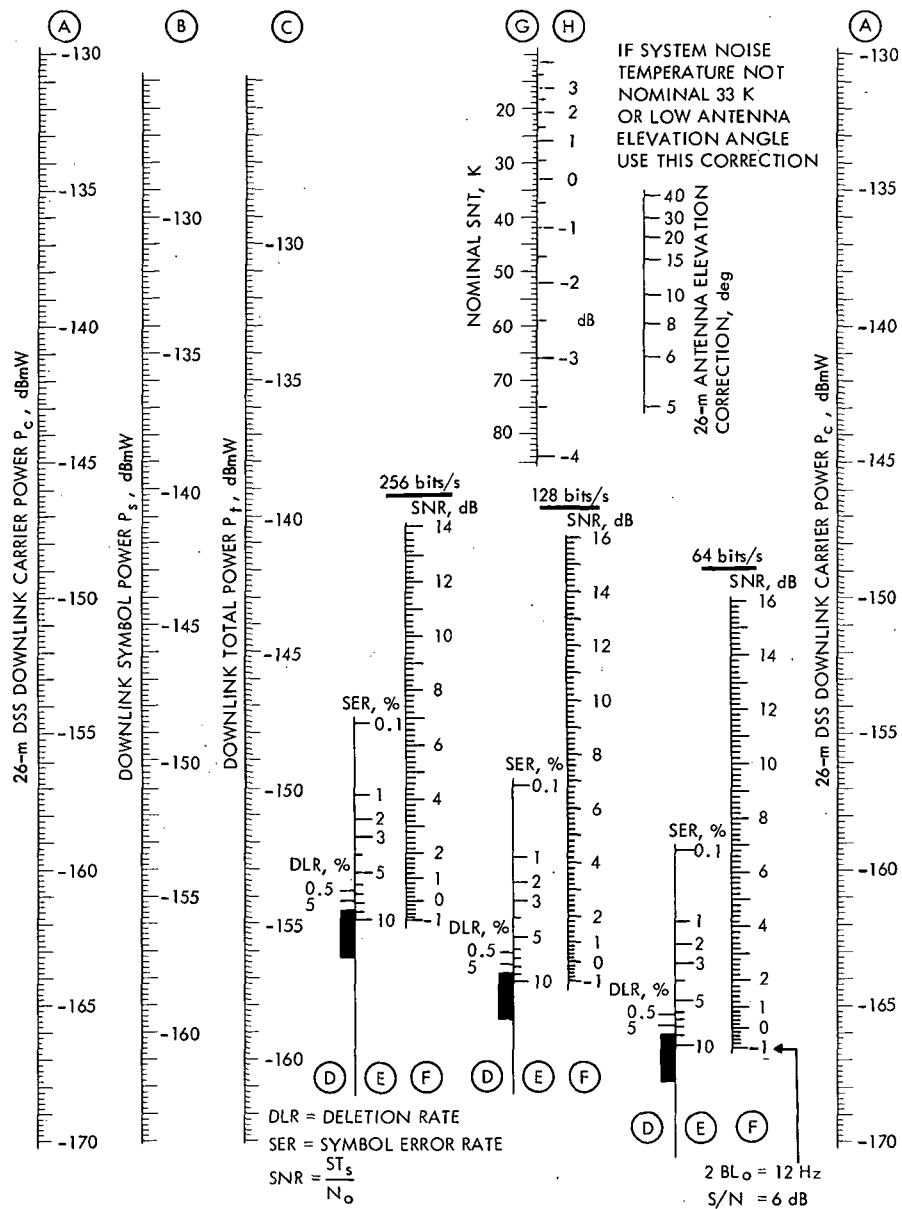


Fig. 2 (contd)

Mariner Jupiter-Saturn 1977 Mission Support

D. J. Mudgway
Mission Support Office

The Mariner Jupiter-Saturn 1977 Project has recently been formally established as a Flight Project. The mission calls for the launch of two Mariner-class spacecraft in 1977 to fly by Jupiter and Saturn. Flight times to Jupiter and Saturn are approximately 2 and 4 years, respectively. The primary scientific objectives of the missions are to explore Jupiter, Saturn, and their satellites, and to investigate the nature of the interplanetary medium. Engineering objectives include the demonstration of a Mariner-class of spacecraft in space for operational periods of 4 years, use of radio-isotope thermoelectric generators as the primary power source, and communications and navigational accuracy out to 10 AU.

Support from the 26-m-diameter antenna subnet is required intermittently during the long cruise periods with 64-m support covering the encounters. Navigation support will require S-X planetary ranging, S-X doppler, and differenced range versus integrated doppler (DRVID) and will be planned around complete "cycles" of data. The number of "cycles" per week will vary with the phases of the mission.

The Office of Computing and Information Systems (OCIS) organization will be responsible for the hardware, software, and simulation needed by the Mission Operations System (MOS) to carry out the mission. This article provides an introduction to the mission requirements as presently understood.

I. Introduction

The primary scientific objectives of the *Mariner Jupiter-Saturn 1977 (MJS77)* Project are to explore Jupiter, Saturn, and their satellites. Exploration of the planetary bodies encountered includes the study of their interaction with the interplanetary/interstellar medium, ionospheric and atmospheric characteristics, as well as planetary fields, trapped radiation, and radio emissions. Physical charac-

teristics of satellites, such as size, spin rate, ephemerides, surface configuration, etc., are also an important part of these objectives.

Interplanetary objectives include studies of energetic particles, solar wind characteristics, magnetic fields and particulate matter. Additional objectives are related to investigation of the boundary of the heliosphere and the interstellar medium.

The engineering objectives of this mission are to demonstrate the use of a *Mariner*-class of spacecraft in space for operational periods of 4 years, including the use of radioisotope thermoelectric generators (RTGs) as the primary spacecraft power source for long duration interplanetary missions.

A further engineering objective is to demonstrate interplanetary communications and navigational accuracy for distances out to 10 AU.

The material for this article was summarized from the comprehensive discussion of all aspects of MJS77 Mission Design contained in JPL Internal Document PD-618-4 (Ref. 1).

II. Mission Summary

Two identical *Mariner*-type spacecraft will be launched during the 1977 Jupiter-Saturn launch opportunity. Their flight paths will take them first to Jupiter and then on to Saturn. The mission has important scientific objectives related to each of the target planets, as many of the satellites as practical, and the interplanetary space between and beyond the planets. A *Mariner*-type spacecraft designed specifically for the outer planet missions will be launched by the *Titan/Centaur/Burner II* launch vehicle.

An MJS77 mission consists of a series of planetary encounters over intervals of several years. Time between planetary encounters is spent in traversing unexplored interplanetary regions progressively farther removed from the influence of the Sun. During the interplanetary portions of the mission, the science instruments will acquire data at a rate consistent with the combined retrieval capability of the project systems. The acquired data will be transmitted to Earth in real time on a nearly continuous coverage schedule. As a spacecraft approaches each planet, encounter operations associated with planetary science and approach guidance operations will begin. A trajectory correction will be performed at particular times prior to Jupiter closest approach. Optical measurements of the planetary satellites for approach guidance to the satellites will also be required.

About 2 months before Jupiter or Saturn closest approach, the imaging instrument will begin observations of the planets and their satellites. Measurement schedules of all science instruments will be varied as appropriate as the spacecraft nears each planet. Earth occultation is achieved for all planetary encounters. Flights encountering Jupiter must be compatible with the anticipated proton and electron environment.

The major characteristics of the two standard trajectories are summarized in Table 1, and heliocentric plots of the two trajectories are shown in Figs. 1 and 2.

III. Flight Phases

A flight phase is defined as a period during the flight when the mission operations of all the project systems are similar during that period. The MJS77 mission requires special considerations for each of the flight phases in terms of data retrieval and processing as well as spacecraft tracking and control functions.

A. Launch Phase

The *Titan/Centaur/Burner II* launch vehicle will inject first into an Earth parking orbit and then reignite to provide the mission injection velocity. The spacecraft will maintain communications via the S-band link and the launch vehicle telemetry system during the ascent. Following separation, deployment of all structural appendages will be completed prior to beginning celestial acquisition. Cruise science begins during the acquisition and a science roll sequence will occur. Upon completion of celestial acquisition, the spacecraft will be configured for cruise. DSN coverage during this phase consists of a 26-m subnet and a 64-m subnet.

B. Cruise Phase

The cruise flight phase is defined to include portions of a flight during which the spacecraft is in a relatively quiescent state. The purpose of cruise operations is to continuously acquire science data, monitor the engineering status of the spacecraft, and to accumulate radio metric data for navigation. The typical navigation tracking requirement will be 1 "cycle" of a DSN 64-m network tracking every 2 weeks as discussed in *Section IV-C*. The DSN coverage includes a full 26-m subnet and $\frac{1}{4}$ of a 64-m subnet until encounter minus 100 days when the 64-m coverage will increase to $\frac{3}{4}$ of the subnet. During the cruise phase, specific science and engineering sequences will be required, such as instrument mapping of the celestial sphere, instrument calibrations, and high-gain antenna mapping. Some of these sequences will require controlled turn maneuvers of the spacecraft for extended periods of time.

C. Trajectory Correction Maneuver Phase

At designated times during flight, the spacecraft will be required to perform trajectory correction maneuvers to improve navigation. The amount of DSN tracking required

will depend on the navigation data needed for the maneuver and will typically include a full 26-m and a full 64-m subnet. The mission operations activity will increase significantly during this period.

D. Encounter Phase

The encounter phase will begin about 40 days before the time of closest approach to the planet when the frequency of activities and observations becomes very high. It will last until 40 days following closest approach. DSN and MOS coverage will be increased to monitor the spacecraft operations. Observations will include high-resolution planetary imaging and observations with the non-TV instruments, atmospheric scans by the spectral instruments, and planetary fields and particles data acquisition from close range. As much of the scientific data as possible will be relayed in real time. However, there will be data rate limitations as the spacecraft approaches Jupiter and Saturn due to "hot target noise."

Following closest approach, an Earth occultation period will occur during which all data must be recorded for later playback when the downlink has been reestablished. The near-encounter phase will also include the closest approach observation of many of the planetary satellites.

IV. Telecommunications Requirements

The requirements for the MJS77 telecommunications system fall into four general areas:

- (1) Command data.
- (2) Telemetry data.
- (3) Radio metric data.
- (4) Radio science data.

The capability in each of these areas, except radio science, is discussed in the following paragraphs.

A. Command Data

Command reception will be provided via S-band throughout the mission at 4 bps. Command data will be received at the spacecraft uncoded. The command link will be inhibited when no uplink signal is present or when synchronization is lost.

Reception of commands via the spacecraft high-gain antenna requires the spacecraft to be Earth-oriented. Reception via the low-gain antenna requires the antenna cone angle to Earth to be less than 30 degrees.

When the spacecraft has acquired the uplink RF signal at S-band and is in the two-way mode, it will achieve synchronization with the command signal within 1 min after receipt of the first symbol of the command acquisition sequence.

B. Telemetry Data

Telemetry transmission will be provided at selected times throughout the mission via S- and X-band. Telemetry data generated in the spacecraft will be transmitted via a single channel per carrier. The transmitters of the spacecraft will, in general, share the downlink power between the RF carrier, the ranging channel, and the telemetry channel. The telemetry data sent simultaneously via the S- and X-band channels will be identical, with the capability existing to remove telemetry modulation from the S-band link.

All telemetry data transmitted from the spacecraft will be time-multiplexed together. Prior to time-multiplexing, the non-imaging data may be coded with an error-correcting binary code. All data transmitted from the spacecraft to Earth will be convolutional coded.

The spacecraft can transmit data at 16 different rates between 20 bps and 115 kbps to take advantage of the prevailing link capability at different phases of the mission.

C. Radio Metric Data

The telecommunications system will provide the capability for generation of radio metric data including single- and dual-frequency ranging at planetary distances for selected times throughout the mission. Single-frequency ranging will be provided with a 64-m station at S- or X-band. Dual-frequency ranging will be provided at S- and X-band with a 64-m station. The uplink will be at S-band only and the downlink at S- and X-band, or both. The capability to make range measurements required sharing the uplink and downlink power with other channels. As such, ranging performance is dependent on, and impacts with, carrier tracking, command, telemetry, and radio science performance.

For orbit determination purposes, solutions will be performed using radio metric data which are taken simultaneously from two stations. For this reason the MJS77 tracking coverage is based upon a "cycle" of data which consists of continuous horizon-to-horizon passes from DSSs 14, 43, 63, and 14 again, as illustrated in Fig. 3. Almost full doppler and range coverage is required from encounter minus 40 days to plus 40 days. Because of the

need for simultaneous data and large round trip light times, it is necessary that the quality of the three-way data be equivalent to current two-way data. This will probably require the use of hydrogen masers. The requirements on instrumentation-induced data noise and calibration capabilities for quantities affecting the data (e.g., station location and transmission media) are equally stringent. If the quality of the data can be made to satisfy the "design goals," the orbit determination result could possibly be significantly improved to yield better navigation accuracies of interest to the project.

V. Deep Space Network

The MJS77 mission will take advantage of the planned Deep Space Network (DSN) capability which is designed to support the NASA Mission Set planned for 1975-1980. It is expected that the spacecraft will incorporate additional capability to match the planned DSN performance improvements during the mission lifetime.

The DSN plans to support the MJS77 flight operations with the following facilities:

- (1) Deep Space Stations (DSSs), including a subnet of three 64-m antennas.
- (2) Data circuits to handle real-time radio metric, telemetry, and command data between Deep Space Stations and the Mission Operations Center. Data circuits will also be provided to handle real-time data between Remote Spacecraft Assembly Facilities and the Mission Operations Center.
- (3) A Network Control function to control the DSN, and to validate the DSN data.

- (4) A capability for participating in MJS77 simulation activities.
- (5) Compatibility Test Area 21 (CTA 21) at JPL and DSS 71 at the Air Force Eastern Test Range for supporting spacecraft and system compatibility tests.

VI. Interfaces

The DSN will interface with the MJS77 spacecraft via the standard RF telecommunications link, the design and control of which will be the subject of an RF Interface Control Document.

The DSN interface with the MJS77 Mission Operations System for real-time data will be via the GCF high-speed and wide-band data lines to the Mission Control and Computing Center.

For operations control purposes an additional interface will be established between DSN Operations Control and the corresponding flight operations control function in the MOS.

VII. Concluding Remarks

The basic outline for the MJS77 mission and requirements for DSN support have been described above. As the mission design progresses, DSN plans for management, documentation, network configuration and capabilities, interfaces, and mission support will be developed and implemented. Future articles will describe significant achievement in this process.

Reference

1. *Mariner Jupiter/Saturn 1977—Mission Requirements*, JPL Document PD-618-4, May 25, 1972 (JPL internal document).

Table 1. Example trajectories for the MJS77 mission

Parameter	Flight 1 JSI77	Flight 2 JST77
Launch:		
C_s	110	100
Launch date	8/17/77	9/4/77
Jupiter:		
Periapsis radius	$7.2 R_J$	$5.8 R_J$
Arrival date	5/25/79	4/18/79
Flight time	1.7 yr	1.6 yr
Satellites	Ganymede or Callisto	Io
Satellite distance	$\sim 20 \times 10^3$ km (or greater)	$\sim 50 \times 10^3$ km (or greater)
Occultations	Jupiter	Jupiter
Saturn:		
Periapsis radius	$3.2 R_s$	$2.3 R_s$
Arrival date	5/4/81	2/16/81
Flight time	3.7 yr	3.4 yr
Satellite encounter	Iapetus after Saturn	Titan before Saturn
Earth occultation	Saturn Iapetus	Saturn Titan

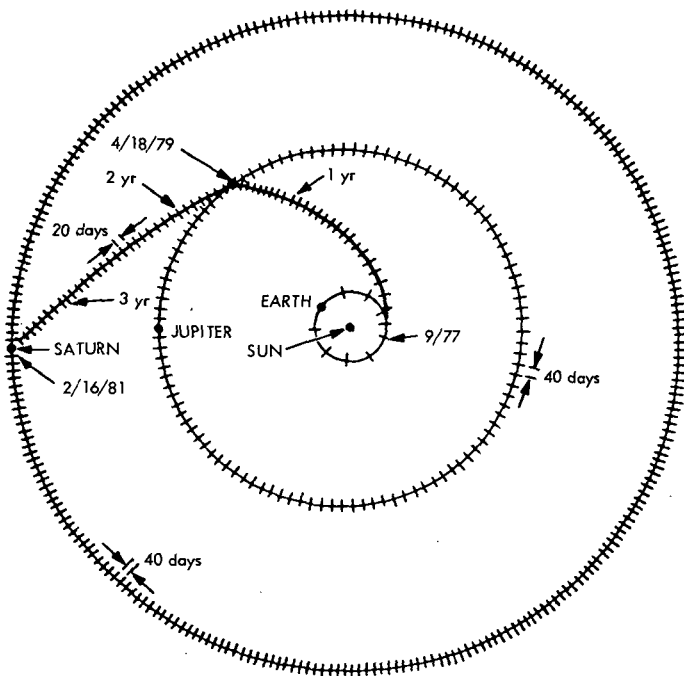


Fig. 1. JST77 heliocentric trajectory (ecliptic plane projection)

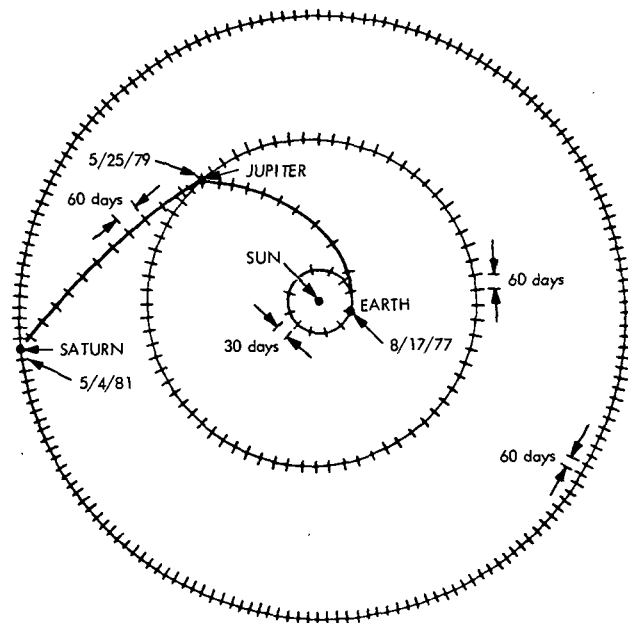


Fig. 2. JSI77 heliocentric trajectory (ecliptic plane projection)

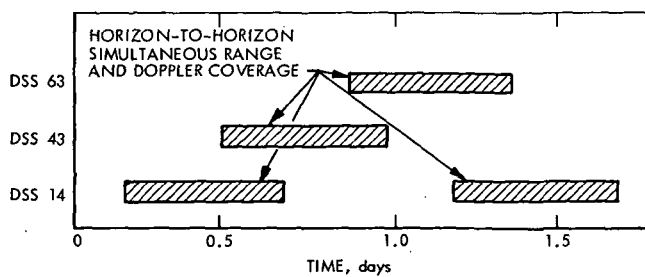


Fig. 3. A navigation "cycle" of data

Apollo Mission Support

R. B. Hartley

DSN Engineering and Operations Office

The support provided by the DSN to the Spaceflight Tracking and Data Network during the Apollo 16 mission is described. Support was provided by three 26-m- (85-ft-) antenna deep space stations, the 64-m- (210-ft-) antenna Mars Deep Space Station (DSS 14), the Ground Communications Facility, and the Space Flight Operations Facility. Pre-mission and mission activities of the DSN are discussed, and the mission is described.

I. Introduction

The DSN support provided to the Spaceflight Tracking and Data Network (STDN, previously termed the Manned Space Flight Network) has been described in Refs. 1-3 and in earlier issues of the JPL Space Programs Summary, Vol. II series. This article describes the support provided for the *Apollo 16* (AS-511) mission, the fifth manned lunar landing and the second of the new "J" type missions devoted almost exclusively to scientific objectives.

II. Mission Description

Apollo 16, the ninth manned *Apollo* spacecraft flown above the three-stage *Saturn V* launch vehicle, carried astronauts John Young (Commander), Charles Duke (Lunar

Module Pilot), and Ken Mattingly (Command Module Pilot). The mission goal was exploration of the Descartes highland region of the Moon. A secondary goal was to collect scientific data while in an extended lunar-orbit phase.

Launch from Cape Kennedy Pad 39A occurred at 17:54:00.65 GMT on April 16, 1972, at a launch azimuth of 72.03 deg. Translunar injection (TLI) over the Pacific Ocean occurred midway through the second revolution in the Earth parking orbit with a 5-min, 46-sec burn of the S-IVB stage engine. Following TLI, the Command Service Module (CSM) separated from the booster, docked with the unattended Lunar Module (LM), and extracted the LM from the S-IVB. The S-IVB was directed by ground command to crash on the Moon as an additional calibration of the seismometers left there by the *Apollo 12*, *14*,

and 15 missions. Unfortunately, an abnormal venting of helium gas from a stuck regulator caused trajectory disturbances, and the radio system on the S-IVB quit abruptly at 21:03:58 GMT on April 17, preventing an accurate determination of the crash location. The best estimate is that the crash occurred at 21:01:04 GMT on April 19 at lunar coordinates 1.83°N and 23.3°W, approximately 280 km northeast of the targeted location.

Midcourse correction 1 was deleted due to the accuracy of the TLI maneuver. Midcourse correction 2 was a short 2.1-sec burn of the Service Propulsion System (SPS) for a 3.81-m/sec (12.5 ft/sec) velocity change, which lowered the upcoming perilune from 216 km (117 nmi) to 133 km (71.7 nmi), within 0.5 km of the planned height. Midcourse corrections 3 and 4 were not required. During translunar cruise, the astronauts entered the LM twice to activate its radio system, allowing telemetry reception on Earth. The crew also worked at solving several minor problems, including an intermittent monitor on the television camera, a leaking water chlorinator, and a suspected gimbal lock on the Inertial Measurement Unit. The latter problem was resolved as being a false warning indication caused by an electrical transient.

Shortly before entering lunar orbit, the astronauts jettisoned a door covering the Scientific Instruments Module (SIM) of the Service Module. The SIM bay carries scientific instruments for observation of the Moon from lunar orbit. The instruments include a gamma ray spectrometer developed at JPL, an X-ray spectrometer, an alpha particle spectrometer, a mass spectrometer, a laser altimeter, a mapping camera, and a panoramic camera.

A successful lunar orbit insertion (LOI) burn of 374.3 sec, for a velocity change of 854 m/sec (2802 ft/sec), put the spacecraft into a 316- × 108-km (170.3- × 58.1-nmi) orbit. Two orbits later, a descent orbit insertion (DOI) burn lowered the spacecraft to a 107.5- × 20.2-km (58.5- × 10.9-nmi) orbit.

During lunar orbit 12, the CSM and LM separated, with astronauts Young and Duke in the LM preparing for descent to the lunar surface on orbit 13. When communication was re-established at the beginning of orbit 13, it was learned that the CSM had not executed a circularization burn that should have been completed while behind the Moon. During the checkout for the burn, a rate feedback signal was absent, and the engine gimbal position indicator showed yaw oscillations. Preparations for LM landing were immediately halted, and the two spacecraft went into formation flight, prepared to dock

and use the LM as a "lifeboat," as on *Apollo 13*, should the malfunction be serious and the backup system also become inoperative. Considerable resources were quickly gathered on the ground to study and simulate the problem. Within several hours, a decision was made to continue the mission and to use the backup SPS gimbal system for all SPS burns. The decision was based on the finding that, if the backup system were lost, the oscillating engine gimbal would still allow a desired maneuver to be safely, albeit crudely, executed. The delay, however, caused considerable modification to the rest of the mission.

The landing was planned for orbit 16, and this time the CSM came from behind the Moon in the proper circular orbit. The descent phase was normal, except that the LM high-gain steerable antenna, a perennial trouble source, was malfunctioning, and the LM was forced to transmit using its omni-antenna. The low signal levels caused data dropouts at all stations except DSS 14, the 64-m-antenna station of the DSN. Landing took place at 8°54'S and 15°30'E, only 262 m northwest of the planned site.

The original flight plan anticipated extravehicular activity (EVA) shortly after landing, but, because of the delayed landing, a sleep period was scheduled before the EVA. During the first EVA period, the astronauts deployed the lunar rover. As on *Apollo 15*, there were initially some problems with the rover; in this case, the rear steering was inoperative, but it later corrected itself. The astronauts set up the *Apollo* Lunar Surface Experiments Package (ALSEP), which contained a seismometer and several fields-and-particles experiments. Unfortunately, the commander tripped over the cable leading to an experiment designed to measure the flow of heat from the interior of the Moon. The cable was so severely damaged that repair was impractical, and the experiment was lost. The ALSEP transmitter was activated, and stations with 9-m (30-ft) antennas were reporting steady signal levels of -139 dBm. The crew also made one traverse using the rover.

After a sleep period, the crew began the second EVA, which consisted of several traverses primarily for geological exploration. Adjustments were also made to the ALSEP instruments. The rover navigation system experienced a partial failure, but it was not considered necessary for normal range traverses.

After another sleep period, the crew conducted a third EVA, which was of shorter duration than the others. In

addition to the geological exploration traverses, a "grand prix" exercise was conducted, with the rover operating at high speeds and making sharp turns to evaluate rover capabilities and the effect of the lunar soil upon maneuverability. At the end of the third EVA, the rover had traveled a total of 27.1 km; and the astronauts had collected approximately 97 kg (213 lb) of rocks.

Some 4 hr after the third EVA, the LM blasted off the lunar surface to rejoin the orbiting CSM. The liftoff was observed on Earth via the television camera on the rover. Rendezvous and docking were normal, except that television coverage was deleted. Television transmission requires the CSM to maintain a high S-band radiated power level, and the LM radiated power level was low due to the unusable high-gain antenna. Earlier in the mission, the strong CSM signal had interfered with the weak LM signal when received at DSS 14, and the television coverage was cancelled to insure high-quality LM data reception.

The original flight plan called for the LM to be jettisoned 4 hr after docking and for the CSM to conduct orbital science experiments for another 47 hr. Because of lingering concern for the SPS engine, the LM was retained until shortly before trans-Earth injection (TEI), and the duration of the orbital operations was reduced to approximately 22 hr. These changes caused the bistatic radar experiment to be reduced from two orbits (numbers 26 and 66) to one orbit (number 40). The planners also cancelled a CSM orbit-shaping burn that was necessary for the Particles-and-Fields Subsatellite (P&FS) to be released into a long-lifetime orbit. The P&FS, which had a planned lifetime of more than 1 yr, crashed on the Moon on May 29, 1972, only 35 days after release.

The LM was jettisoned 5 hr before TEI. Unfortunately, an attitude-control switch had been left in the wrong position, and the LM began to tumble at a rate of 3 deg/sec. Without attitude control, it was impossible to conduct the de-orbit burn for the planned lunar impact and the calibration of the ALSEP seismometers. Therefore, the LM remains in a lunar orbit that will eventually (early 1973) degrade, resulting in an unobserved lunar impact. The transmitter on the LM ceased due to battery depletion at 13:05:40 GMT on April 25 during lunar orbit 70.

The TEI maneuver, despite concerns over the SPS engine, was highly accurate, and midcourse correction 5 was a short burn for only a 1.04-m/sec (3.4 ft/sec) velocity change. An EVA was conducted during trans-Earth cruise

to retrieve exposed film and other scientific materials from the SIM bay. *Apollo 16* landed at 0°44'S and 156°12'W in the Pacific Ocean, approximately 300 km southeast of Christmas Island.

Table 1 shows the mission event times. The term "ground elapsed time" (GET) is actually a misnomer since the GET clocks were readjusted twice during the mission: First, the GET clock was advanced 11 min, 48 sec at 16:30 GMT on April 21; then, the clock was advanced 24 hr, 34 min, 12 sec at 04:08:01 GMT on April 25. These changes caused the GET of the mission events to correspond to the GET indicated in the flight plan, in spite of the delays caused by the SPS problems.

III. Requirements for DSN Support

A. 26-m-Antenna Stations

As was done with previous *Apollo* missions, DSSs 11, 42, and 61 were committed to support *Apollo 16* under direct STDN/MSC (Manned Spacecraft Center) control. Their responsibilities included two-way tracking of the CSM, LM, S-IVB, and Lunar Communications Relay Unit (LCRU), which transmits on a frequency of 2265.5 MHz and receives on the LM uplink frequency. The P&FS was also to be tracked, but was not to be activated until after LM impact, since the uplink and downlink frequencies for the two vehicles are identical.

Unlike previous *Apollo* missions, scheduling authority for the 26-m-antenna stations was retained by the DSN for the entire *Apollo 16* mission. This change was necessary because the DSN had assumed complete maintenance and operations responsibility for these 26-m-antenna stations (see Ref. 5).

B. DSS 14

The Mars station (DSS 14) was required to receive voice, telemetry, biomedical, and television data and to relay the data to the Goldstone prime STDN station (GDS). Specific requirements existed for low lunar orbit, touchdown, EVA television, and LM crash. Coverage was also desired for television during translunar coast.

C. Precision Doppler Data

As part of a continuing study (based at JPL) of potential lunar anomalies (mascons), DSS 14 was required to provide precision high-speed doppler recordings of the CSM and LM during low lunar orbits and of the LM during the descent phase and later during the crash.

Some results from the same experiment for *Apollo 14* are given in Ref. 4. The unexpected events during the mission modified this requirement: First, the extra time spent in low lunar orbit while the SPS engine problem was being studied provided considerable extra mascon data; second, the lack of an LM crash relieved DSS 14 of the coverage requirement. A related *Apollo* requirement was for high-speed strip-chart recordings of DSS 14 received signal strength during orbit 3 of the CSM and the crash of the LM.

D. Bistatic Radar Experiment

DSS 14 was required to conduct another bistatic radar experiment as had been done on *Apollo 14* and *15*. The experiment was originally scheduled for CSM orbits 26 and 66, but after the SPS problems the experiment was rescheduled to the single orbit 40. The experiment consists of receiving the CSM downlink signal, which has been reflected from the lunar surface, at DSS 14 in two orthogonal polarizations simultaneously. From the recorded signal characteristics, deductions can be made as to the nature of the lunar soil.

E. LCRU

A very late requirement was imposed for additional DSS 14 tracking of the LCRU after LM liftoff. The requirement, received on April 18 (during translunar cruise), was for 10 short daily passes from April 25 through May 4 to receive television signals from the LCRU until its batteries were depleted. Due to the unmanned, non-*Apollo* nature of the requirement and its severe impact on DSS 14 tracking of unmanned spacecraft and radioscience objects, the conflict was submitted to NASA Headquarters for resolution. The DSN was subsequently instructed to schedule the LCRU tracking, regardless of the impact on other activities. The LCRU was tracked daily until it ceased to operate on April 30 (see Table 3).

IV. DSN Pre-mission Preparations and Testing

A. 26-m-Antenna Stations

Because of power amplifier interlock tripoffs on past missions, the DSN undertook a reliability study shortly after the *Apollo 15* mission. This study resulted in a mechanical redesign of the transmitter power supply. This modification was made at each 26-m-antenna station before the *Apollo 16* mission. In addition, a particularly troublesome power amplifier at DSS 11 was completely replaced with a new unit direct from the manufacturer.

Between the *Apollo 15* and *16* missions, the method of processing pointing data at the stations was changed. Previously, the 29-point acquisition message from the Goddard Space Flight Center (GSFC) or the Manned Spacecraft Center (MSC) was entered into an STDN Univac 1218 computer, where it was reformatted for inputting to the Antenna Position Programmer (APP). After the *Apollo 15* mission, the Univac 1218 computer was removed, and a program was written for the existing DSN Antenna Pointing System (APS) computer to assume the reformatting function. The program was written using a specification (Ref. 5) from GSFC, the DSN's official *Apollo* contact, and the program operated perfectly when tested with GSFC.

Shortly before the mission, testing began with MSC, and the program developed serious problems. An investigation quickly revealed that MSC does not transmit 29-point acquisition messages formatted according to the GSFC specification; when an angle in the message is less than 10 deg, GSFC fills the unused digit position with a zero, whereas MSC fills the position with a teletype space. MSC claimed that they would be unable to meet the specification with the launch less than 1 wk away.

During a worldwide conference call, DSS 61 operations personnel mentioned that they had discovered that changes in only two computer words of the on-site program would enable the program to accept either format. The modifications were studied by the programmer at JPL and hastily tested at both DSS 61 and DSS 42. The changes were found to be sound, and the modified program was used during the mission. It is anticipated that the program will be rewritten before the *Apollo 17* mission to improve the input formatting and also to remove several operator inconveniences discovered during testing.

DSSs 11, 42, and 61 were placed under configuration control for the *Apollo 16* mission on April 4, 1972. They were placed on mission status by the STDN on April 3.

B. DSS 14

DSS 14 conducted normal pre-mission activities, including installation and tests of the bistatic radar equipment, as shown in Table 2.

V. DSN Operations During Mission

A. 26-m-Antenna Stations

DSSs 11, 42, and 61 successfully supported all phases of the *Apollo 16* mission. The problems experienced are

noted in Table 3. As can be seen, there were no power amplifier overcurrent or arc detector tripoffs.

B. DSS 14

Seven *Apollo* passes were tracked, as shown in Table 3. The station also tracked six LCRU passes. The station had originally been scheduled for ten LCRU tracks, but, on April 30, the signal could not be acquired, indicating a dead LCRU battery.

DSS 14 experienced a pointing problem on the first pass, beginning shortly after TLI. The spacecraft rose rapidly in the west, crossed the station meridian at a high elevation, reversed its apparent motion, and again set in the west. At the moment that the spacecraft crossed the station meridian going from west to east, the Antenna Pointing System (APS) malfunctioned. At first it was thought to be a predict problem, but post-mission study may show that the APS correctly interpolates forward from an hour angle of 359 to 0, but not in reverse. This is a unique problem because it is the first known spacecraft track at DSS 14 to cross the meridian in a reverse direction.

A significant problem occurred on April 19 and 20. With the CSM and LM both in the main beam of the DSS 14 antenna and the CSM and LM signal levels at -92 and -115, respectively, the LM signal received interference that caused an increased telemetry bit error rate. When the CSM signal was reduced, the bit error rate returned to normal. Assuming that a maser overload was at fault, DSS 14 switched masers and then retuned the backup maser. In so doing, gain on the backup maser was lost, and the station switched back to the prime maser. The immediate impact of the problem was to restrict

the allowable CSM signal level whenever it was in the vicinity of the LM. Therefore, it was necessary to cancel the planned television coverage of the CSM-LM docking maneuvers. This interference was not experienced on past missions because the LM usually transmits a high signal level using its high-gain steerable antenna.

DSS 14 supported the bistatic radar experiment successfully. The experiment was reduced from two lunar orbits to one orbit (number 40) because of the other mission problems.

C. GCF Participation

The GCF provided voice, teletype, and high-speed data circuits to support the DSN *Apollo* operations. In addition, JPL acts as the west coast switching center for the NASA Communications Network and handles many non-DSN circuits in support of *Apollo*. There were no known GCF anomalies, and GCF support was considered excellent.

D. SFOF Participation

The SFOF areas and equipment used for the *Apollo 16* mission included the Operations Area, the Network Analysis Area, the *Mariner* computer terminal area, and the Univac 1108 and IBM 360/75 computers. The SFOF support was limited to predict generation and some off-line monitoring. In contrast to previous *Apollo* missions, no problems were experienced with predict generation. Fourteen Probe Ephemeris Tapes were generated on the Univac 1108, and sixteen predict sets were generated for DSS 14 on the IBM 360/75. The SFOF support was excellent.

References

1. Hartley, R. B., "Apollo Mission Support," in *The Deep Space Network*, Space Programs Summary 37-64, Vol. II, pp. 7-11. Jet Propulsion Laboratory, Pasadena, Calif., Aug. 31, 1970.
2. Hartley, R. B., "Apollo Mission Support," in *The Deep Space Network Progress Report for January and February 1971*, Technical Report 32-1526, Vol. II, pp. 33-41. Jet Propulsion Laboratory, Pasadena, Calif., Apr. 15, 1971.
3. Hartley, R. B., "Apollo Mission Support," in *The Deep Space Network Progress Report for July and August 1971*, Technical Report 32-1526, Vol. V, pp. 29-38. Jet Propulsion Laboratory, Pasadena, Calif., Oct. 15, 1971.
4. Sjogren, W. L., et al., "S-Band Transponder Experiment," in *The Apollo 14 Preliminary Science Report*, NASA Document SP-272. National Aeronautics and Space Administration, Washington, D.C., 1971.
5. *MSFN/DSN Station Operating Interface Procedures for Support of Manned Apollo Missions*, MSFN Document 508.3. Goddard Space Flight Center, Greenbelt, Md., May 1971.

Table 1. Apollo 16 sequence of major events

Event	Ground elapsed time, hr:min:sec	Actual elapsed time, hr:min:sec	Date/Greenwich mean time, hr:min:sec
Launch	00:00:00	00:00:00	April 16/17:54:01
TLI ignition	02:33:34	02:33:34	April 16/20:27:35
TLI cutoff	02:39:20	02:39:20	April 16/20:33:21
First midcourse (deleted)	—	—	—
Second midcourse	30:39:00	30:39:00	April 18/00:33:01
LM comm test	33:00:00	33:00:00	April 18/02:54:01
Third midcourse (deleted)	—	—	—
LM comm test	53:31:00	53:31:00	April 18/23:25:01
Bistatic frequency check	57:19:39	57:19:39	April 19/03:13:40
Fourth midcourse (deleted)	—	—	—
SIM door jettison	69:59:00	69:59:00	April 19/15:53:01
LOI	74:28:27	74:28:27	April 19/20:22:28
S-IVB impact	75:07:03	75:07:03	April 19/21:01:04
DOI	78:33:44	78:33:44	April 20/00:27:45
Separation	96:13:31	96:13:31	April 20/18:07:32
Second separation	102:30:00	102:30:00	April 21/00:24:01
Power descent initiation	104:17:25	104:17:25	April 21/02:11:26
Touchdown	104:29:35	104:29:35	April 21/02:23:36
Begin EVA 1	119:05:48	118:54:00	April 21/16:48:01
End EVA 1	126:16:48	126:05:00	April 21/23:59:01
Begin EVA 2	142:51:15	142:39:27	April 22/16:33:28
End EVA 2	150:14:41	150:02:53	April 22/23:56:54
Bistatic radar begin (orbit 40)	151:28:21	151:16:33	April 23/01:10:34
Bistatic radar end	152:41:15	152:29:27	April 23/02:23:28
Begin EVA 3	165:43:11	165:31:23	April 23/15:25:24
CSM orbit change	169:28:48	169:17:00	April 23/19:11:01
End EVA 3	171:23:29	171:11:41	April 23/21:05:42
LM ascent	175:43:35	175:31:47	April 24/01:25:48
Docking	177:51:48	177:40:00	April 24/03:34:01
LM jettison	195:12:00	190:00:12	April 24/20:54:13
Lunar orbit plane change (deleted)	—	—	—
P&FS launch	196:13:55	196:02:07	April 24/21:56:08
TEI	200:33:20	200:21:32	April 25/02:15:33

Table 1 (contd)

Event	Ground elapsed time, hr:min:sec	Actual elapsed time, hr:min:sec	Date/Greenwich mean time, hr:min:sec
LM battery depletion	235:57:39	211:11:39	April 25/13:05:40
Fifth midcourse	239:21:02	214:35:02	April 25/16:29:03
P&FS commanded on	241:16:30	216:30:30	April 25/18:24:31
CSM EVA	243:35:00	218:49:00	April 25/20:43:01
Sixth midcourse (deleted)	—	—	—
Seventh midcourse	287:22:00	262:36:00	April 27/16:30:01
Splashdown	290:37:06	265:51:06	April 27/19:45:07

Table 2. DSS 14 tests

Date/GMT, hr:min	Test
April 4/18:00–22:00	Countdown for bistatic test
April 4/22:00–24:00	Bistatic signal flow test
April 5/00:00–05:00	Bistatic final checkout
April 7	CVT/OVT
April 9, 10/06:16–05:25	Data flow test with GDS

Table 3. Apollo 16 tracking

Date/GMT, hr:min	Problems
DSS 11	
April 16/20:44-06:47	PA3 beam voltage not controllable remotely
April 17/19:14-07:11	Defective iso-amp in system 3 ranging
April 18/19:31-07:23	None
April 19/19:18-07:48	None
April 20/20:12-08:43	None
April 21/21:30-08:30	PA3 and PA4 failed during pretrack tests. Caused by low flow through combiner. Flow increased
April 22/22:09-10:11	Pretrack ranging problem. Replaced relay
April 23/23:06-09:53	None
April 25/00:36-10:46	Defective exciter turning potentiometer on system 3
April 26/00:00-10:44	None
April 27/00:18-10:19	None
DSS 14	
April 16/23:09-03:03	APS problems near zenith
April 17/23:11-07:56	None
April 19/18:46-07:48	Distortion of LM signal when using Mod 3 maser. Switched to PDS maser at 00:30Z. 35 min gap in predicts
April 20/20:04-08:58	Distortion of LM signal when using either maser. Tuning of backup maser caused loss of gain. Confusion over too many predict sets (one set for each mission contingency)
April 21/20:58-09:29	None
April 22/21:59-09:56	TDH doppler counter hung up 03:02-09:56Z
April 23/22:57-05:15	None
April 25/05:33-05:50	None (LCRU track)
April 26/06:25-06:46	↓
April 27/06:10-06:54	
April 28/06:24-06:45	
April 29/07:26-07:59	None (LCRU track)
April 30/06:38-08:00	No LCRU signal received

Table 3 (contd)

Date/GMT, hr:min	Problems
DSS 42	
April 17/03:18-11:19	None ↓
April 18/03:45-12:10	
April 19/03:58-12:25	
April 20/04:52-13:09	
April 21/04:39-14:04	
April 22/05:25-14:26	
April 23/05:29-16:03	
April 24/05:51-16:56	
April 25/06:01-17:14	
April 26/05:59-17:23	
April 27/05:51-18:28	
DSS 61	
April 17/10:31-21:04	None ↓
April 18/11:05-00:40	
April 19/11:17-00:17	
April 20/12:28-00:59	
April 21/13:36-00:42	
April 22/13:57-02:07	
April 23/15:00-02:06	
April 24/16:42-03:05	
April 25/16:54-02:34	
April 26/16:35-02:27	

Pioneer Venus Mission Support

A. J. Siegmeth
Mission Support Office

The Deep Space Network (DSN) has advanced capabilities which can be used for spaceflight missions to Venus. This presentation was given to the Pioneer Venus study team on the ranging and S/X-band systems, which can enhance the navigational accuracy of deep space missions.

An introduction to the *Pioneer Venus Mission* was given in Ref. 1. The Ames Research Center (ARC) plans to award two Phase B Study Contracts during July 1972. It is planned to complete this study within nine months.

On June 15, 1972, DSN/JPL representatives gave to the members of the ARC Study Teams a detailed presentation on advanced DSN capabilities, which will be implemented during the next three years. These new capabilities are the DSN Ranging System and S- and X-band dual-frequency system. These capabilities will be used by the approved *Mariner Venus-Mercury 1973*, *Helios*, and *Viking* Missions. The DSN team elaborated on the limitations of the DSN Tracking System used to precisely navigate spacecraft with predetermined target areas of planetary missions. To improve the required accuracies, the advantages of two-station tracking methods were explained using the Differenced Range method. It was emphasized that a spacecraft ranging capability provides faster trajectory

solutions, reveals modeling errors, and makes it possible to use the differenced range versus integrated doppler (DRVID) solutions. This technique can be helpful to determine charged particle effects on tracking accuracies. Simultaneous data obtained from two or three stations and further quasi very long baseline interferometer (QVLBI) techniques can reduce considerably the errors of ephemeris uncertainties, but these techniques need charged particle calibrations using S/X-band capabilities. These capabilities can also lead to better calibration of conventional data, can complete the calibration of differenced data, and can be helpful in the close vicinity of the Sun. The advantages of the differential VLBI techniques using well-known locations of extra-galactic radio sources versus the position of a spacecraft can also enhance the navigational accuracies. References 1-14 describe these techniques in more detail. Information was also given on the spacecraft ground equipment configurations and implementation plans with special emphasis on the ranging and S/X-band capabilities.

References

1. Hamilton, T. W., and Trask, D. W., "DSN Inherent Accuracy Project," in *The Deep Space Network Progress Report*, Technical Report 32-1526, Vol. I, pp. 11-13. Jet Propulsion Laboratory, Pasadena, Calif., Feb. 15, 1971.
2. Winn, F. B., and Leavitt, R. K., "Refractivity Influence on DSS Doppler Data," in *The Deep Space Network Progress Report*, Technical Report 32-1526, Vol. I, pp. 31-41. Jet Propulsion Laboratory, Pasadena, Calif., Feb. 15, 1971.
3. MacDoran, P. F., Callahan, P. S., and Zygielbaum, A. I., "Probing the Solar Plasma With *Mariner* Radio Metric Data, Preliminary Results," in *The Deep Space Network Progress Report*, Technical Report 32-1526, Vol. I, pp. 14-21. Jet Propulsion Laboratory, Pasadena, Calif., Feb. 15, 1971.
4. von Roos, O. H., "Second Order Charged Particle Effects on Electromagnetic Waves in the Interplanetary Medium," in *The Deep Space Network Progress Report*, Technical Report 32-1526, Vol. II, pp. 42-48. Jet Propulsion Laboratory, Pasadena, Calif., Apr. 15, 1971.
5. von Roos, O. H., "Analysis of the DRVID and Dual Frequency Tracking Methods in the Presence of a Time-Varying Interplanetary Plasma," in *The Deep Space Network Progress Report*, Technical Report 32-1526, Vol. III, pp. 71-76. Jet Propulsion Laboratory, Pasadena, Calif., June 15, 1971.
6. Ondrasik, V. J., and Mottinger, N. A., "An Examination of the Effects of Station Longitude Errors on Doppler Plus Range and Doppler Only Orbit Determination Solutions With an Emphasis on a *Viking* Mission Trajectory," in *The Deep Space Network Progress Report*, Technical Report 32-1526, Vol. IV, pp. 71-77. Jet Propulsion Laboratory, Pasadena, Calif., Aug. 15, 1971.
7. Rourke, K. H., and Ondrasik, V. J., "Application of Differenced Tracking Data Types to the Zero Declination and Process Noise Problems," in *The Deep Space Network Progress Report*, Technical Report 32-1526, Vol. IV, pp. 49-60. Jet Propulsion Laboratory, Pasadena, Calif., Aug. 15, 1971.
8. Ondrasik, V. J., and Rourke, K. H., "An Analytical Study of the Advantages Which Differenced Tracking Data May Offer for Ameliorating the Effects of Unknown Spacecraft Accelerations," in *The Deep Space Network Progress Report*, Technical Report 32-1526, Vol. IV, pp. 61-70. Jet Propulsion Laboratory, Pasadena, Calif., Aug. 15, 1971.
9. Fanselow, J. L., et al., "The Goldstone Interferometer for Earth Physics," in *The Deep Space Network Progress Report*, Technical Report 32-1526, Vol. V, pp. 45-57. Jet Propulsion Laboratory, Pasadena, Calif., Oct. 15, 1971.
10. Fliegel, H. F., "A Worldwide Organization to Secure Earth-Related Parameters for Deep Space Missions," in *The Deep Space Network Progress Report*, Technical Report 32-1526, Vol. V, pp. 66-73. Jet Propulsion Laboratory, Pasadena, Calif., Oct. 15, 1971.
11. von Roos, O. H., "Analysis of Dual-Frequency Calibration for Spacecraft VLBI," in *The Deep Space Network Progress Report*, Technical Report 32-1526, Vol. VI, pp. 46-56. Jet Propulsion Laboratory, Pasadena, Calif., Dec. 15, 1971.

References (contd)

12. Rourke, K. H., and Ondrasik, V. J., "Improved Navigation Capability Utilizing Two-Station Tracking Techniques for a Low-Declination Distant Spacecraft," in *The Deep Space Network Progress Report*, Technical Report 32-1526, Vol. VII, pp. 51-60. Jet Propulsion Laboratory, Pasadena, Calif., Feb. 15, 1972.
13. Thomas, J. B., "An Analysis of Long Baseline Radio Interferometry," in *The Deep Space Network Progress Report*, Technical Report 32-1526, Vol. VII, pp. 37-50. Jet Propulsion Laboratory, Pasadena, Calif., Feb. 15, 1972.
14. Thomas, J. B., "An Analysis of Long Baseline Radio Interferometry, Part II," in *The Deep Space Network Progress Report*, Technical Report 32-1526, Vol. VIII, pp. 29-38. Jet Propulsion Laboratory, Pasadena, Calif., Apr. 15, 1972.

Radio Science Support

• K. W. Linnes
Mission Support Office

Since 1967, radio scientists have used the Deep Space Network 26- and 64-m-diameter antenna stations to investigate pulsars, to study the effect of solar corona on radio signals, and to observe radio emissions from X-ray sources. More recently, very long baseline interferometry (VLBI) techniques have been used for high-resolution studies of quasars. During the reporting period, VLBI observations were made of quasars and pulsars. Support was also provided by the 64-m-diameter antenna for the measurement of cosmic background noise, mapping of nearby spiral galaxies, searching for ionized hydrogen in interstellar globular clusters, searching for interstellar molecules, and observing radiation from Jupiter.

I. Introduction

The 26- and 64-m-diameter antenna stations of the DSN have been used for several years to support radio science experiments. NASA, JPL, and university scientists have used key DSN facilities whose particular and unique capabilities were required for the performance of the experiments. In order to formalize the method of selecting experiments and experimenters, a Radio Astronomy Experiment Selection (RAES) Panel was formed in 1969. Notice of availability of these facilities was placed in professional journals to inform the scientific community that they were available for limited use by qualified radio scientists (Ref. 1). No charge is made for use of the standard DSN facilities and equipment; special equipment, however, must be provided by the experimenters. A summary of all experiments conducted through February 1972 is reported in Refs. 2 through 6.

II. Radio Science Operations

The amount of support in this reporting period increased considerably. Completion of the critical phases of the *Mariner 9* activities made available more time on the 64-m antenna at Goldstone (DSS 14). During the March-June period, the experiments conducted under the auspices of the RAES Panel utilized approximately 302 hours of DSS 14 time. This amounts to about 10.5% of the available time. The total for fiscal year 1972 is about 467 hours or 5.3%. Table 1 shows how the support was distributed through the year.

All of the RAES Panel experiments shown in Table 2, except the last four, are a continuation of previous measurements. These four experiments received support for the first time, having been recently approved by the Panel.

The observation of weak radio sources by D. Jauncey and others is a measurement at very low flux levels of the confusion factor due to weak background radio sources; the presence of this background radiation is a limiting factor in number-flux density surveys of radio sources made by radio astronomers. The transcontinental baseline VLBI by T. Clark and others is a feasibility demonstration. The use of three stations simultaneously in California, Massachusetts, and Alaska permits measurement of the closure capability of the technique. Pulsar observation by VLBI techniques is also a feasibility investigation to determine whether this difficult observation can be performed. Data from the observation are being evaluated. The observations by Hills and Klein, searching for ionized hydrogen, are an attempt to detect ionized gas in globular clusters for the purpose of determining the mean mass loss for those stars in a cluster currently evolving to the white dwarf stage. The experiment requires the high angular resolution and extreme sensitivity of the 64-m antenna at Goldstone.

The experiments sponsored by the Office of Space Science (OSS) and Office of Applications (OA) were also supported. The OSS experiments made first use of the new Ku-band (14 GHz) capability to detect interstellar molecules by microwave spectroscopy, and also to observe radio emissions from the outer planets. The OA experiment is a continuation of that described previously using VLBI techniques to make accurate baseline measurements.

III. RAES Panel Activities

The Radio Astronomy Experiment Selection Panel approved several experiments during the reporting period (Table 3).

IV. NASA Radio Science Plan Support

In June, the Laboratory forwarded to the NASA Radio Science Panel inputs to the long-range and annual Radio Science Plan being formulated by the Panel. These inputs are to be used to establish a support plan for fiscal year 1973. As was the case of the inputs supplied in January for the interim FY72 plan, the material included all experiments currently approved by the RAES Panel, description of requirements for all OSS and OA radio science experiments, and, for information, a description of DSN development activities that are related to radio science.

Included in the material on the RAES Panel experiments was the proposal for a *quasar patrol*. The purpose of the proposal is to provide a regularly scheduled set of VLBI observations. Measurements and observations of quasars and galaxies are required to detect the changes and variability in structure and flux output. The activity of such a patrol has been in effect during this reporting period and is characterized by 24-hour periods of observation from the 64-m antenna at Goldstone. The cooperating station is usually the 37-m antenna station at Haystack in Massachusetts and/or the 42-m antenna at the National Radio Astronomy Observatory (NRAO) in Greenbank, West Virginia. The X-band VLBI observations shown in Table 2 by the California Institute of Technology-National Radio Astronomy Observatory (Caltech-NRAO) and Goddard Spaceflight Center-Massachusetts Institute of Technology (GSFC-MIT) groups constituted the patrol for April, May, and June. These observations extend the investigations reported on in the publications cited in Refs. 5 and 6. Reference 7 is a recent publication resulting from this work. The VLBI proposals in Table 3 extend this work to higher frequencies.

References

1. *Bulletin of the American Astronomical Society*, Vol. 2, No. 1, p. 177, 1970.
2. Linnes, K. W., Sato, T., and Spitzmesser, D., "Radio Science Support," in *The Deep Space Network Progress Report*, Technical Report 32-1526, Vol. III, pp. 46-51. Jet Propulsion Laboratory, Pasadena, Calif., June 15, 1971.
3. Linnes, K. W., "Radio Science Support," in *The Deep Space Network Progress Report*, Technical Report 32-1526, Vol. V, pp. 42-44. Jet Propulsion Laboratory, Pasadena, Calif., Oct. 15, 1971.
4. Linnes, K. W., "Radio Science Support," in *The Deep Space Network Progress Report*, Technical Report 32-1526, Vol. VI, pp. 43-45. Jet Propulsion Laboratory, Pasadena, Calif., Dec. 15, 1971.
5. Linnes, K. W., "Radio Science Support," in *The Deep Space Network Progress Report*, Technical Report 32-1526, Vol. VII, pp. 29-31. Jet Propulsion Laboratory, Pasadena, Calif., Feb. 15, 1972.
6. Linnes, K. W., "Radio Science Support," in *The Deep Space Network Progress Report*, Technical Report 32-1526, Vol. VIII, pp. 24-28. Jet Propulsion Laboratory, Pasadena, Calif., Apr. 15, 1972.
7. Shaffer, D. B., et al., "Rapid Change in Visibility Function of the Radio Galaxy 3C120," *Astrophys. J.*, Vol. 173, pp. L147-L150, May 1, 1972.

**Table 1. RAES Panel experiment support at the
64-m antenna station**

Period	Station hours
July–December 1971	88
January 1972	32.5
February	44
March	36.5
April	54.5
May	119.5
June	92
Total	467.0

Table 2. Radio science experiments involving 64-m and 26-m antenna facilities

Experiment	Purpose	Experimenter	DSN facility	Date
RAES PANEL EXPERIMENTS:				
Very long baseline interferometry (medium data bandwidth, S-band)	To determine angular size of radio sources.	J. Gubbay (Univ. of Adelaide)	DSS 14 (64-m antenna) and DSS 41 (26-m antenna)	Jun. 12, 1971
		A. Legg (Space Research Group, WRE)		Jan. 25, 1972
		D. Robertson (Space Research Group (WRE)		Feb. 21, 1972
		A. Moffett (Caltech)		Jun. 19, 1972
Spiral galaxy mapping		B. Seidel (JPL)	DSS 14	
		H. Arp (Hale Observatories)		Oct. 4, 7, 13, 20, 27, 1971 Dec. 8, 1971 Apr. 16, 1972
Quasar structure by X-band VLBI	To monitor time variations and fine structure and apparent position of quasars.	T. Clark (GSFC)	DSS 14 (also MIT Haystack antenna)	Jun. 9, 19 - 1971
		R. Goldstein (JPL)		Sep. 19, 1971
		H. Hinteregger (MIT)		Oct. 2-4, 10, 17, 1971
		C. Knight (MIT)		Jan. 4, 1972
		G. Marandino (Univ. of Maryland)		Feb. 18, 1972
		A. Rogers (MIT Haystack Observatory)		Mar. 10, 1972
		I. Shapiro (MIT)		May 9, 1972
		D. Spitzmesser (JPL)		
X-band VLBI	To study the structure of extra galactic sources with improved resolution.	A. Whitney (MIT)	DSS 14 (also MIT Haystack antenna)	Feb. 1971
		J. Broderick (NRAO)		Nov. 2, 1971
		B. Clark (NRAO)		Feb. 5, 1972
		K. Kellermann (NRAO)		Mar. 4, 1972
		D. Jauncey (Cornell Univ.)		Apr. 24, 1972
		M. Cohen (Caltech)		May 20, 1972
		D. Shaffer (Caltech)		Jun. 6, 1972
Small-scale variations in cosmic background radiation	To search for small-scale spatial variations in the 2.7 K cosmic background radiation of 3.5 cm.	R. Carpenter (Calif. State College of Los Angeles)	DSS 14	Jan. 10, 11, 1972
		S. Gulkis (JPL)		Feb. 11, 12, 22, 1972
		T. Sato (JPL)		Mar. 14, 25, 1972 May 8, 28, 1972
Weak radio source observations	To measure the "confusion distribution" of weak radio sources at 2.3 GHz.	D. L. Jauncey (Cornell Univ.)	DSS 14	Jun. 5, 12, 1972
		M. J. Yerbury (Cornell Univ.)		
		J. J. Condon (Cornell Univ.)		
		D. J. Spitzmesser (JPL)		

Table 2 (contd)

Experiment	Purpose	Experimenter	DSN facility	Date
RAES PANEL EXPERIMENTS (contd):				
Transcontinental baseline VLBI	To measure transcontinental vector baselines by VLBI observation of quasars.	T. A. Clark (GSFC) H. F. Hinteregger (MIT) C. A. Knight (MIT) S. Lippincott (MIT Haystack Observatory) A. E. Rogers (MIT Haystack Observatory) I. I. Shapiro (MIT) A. R. Whitney (MIT)	DSS 14 (also Haystack 37-m antenna and NOAA 26-m antenna in Alaska)	Mar. 18, 1972 Apr. 14, 1972 May 1, 28, 1972 Jun. 26, 1972
Pulsar observations	To measure position and apparent motion of pulsars at 2.3 GHz by VLBI.	T. A. Clark (GSFC) G. S. Downs (JPL) N. C. Erickson (Univ. of Maryland) P. E. Reichley (JPL) N. R. Vandenberg (Univ. of Maryland)	DSS 14 (also NRAO 42-m antenna at Greenbank, West Virginia)	May 4, 1972
Ionized hydrogen observations	To detect free-free emissions from ionized hydrogen in globular clusters.	J. Hills (Univ. of Michigan)	DSS 14	May 22, 29, 1972
OSS EXPERIMENTS:				
Interstellar microwave low-noise spectroscopy	To search for interstellar molecules at 14 GHz.	S. Gulkis (JPL) T. Sato (JPL) B. Zuckerman (Univ. of Maryland) D. Cesarsky (Caltech) J. Greenstein (Caltech)	DSS 14	Apr. 2, 10, 18, 1972 May 2, 6, 14, 17, 1972 June 3, 18, 1972
Planetary radio astronomy	To study radio emissions of Uranus and Jupiter at 14 GHz.	S. Gulkis (JPL) B. Gary (JPL) M. Klein (JPL) M. Jansen (JPL Resident Research Associate) E. Olsen (JPL Resident Research Associate) P. Rosenkranz (JPL Resident Research Associate)	DSS 14	Apr. 29, 30, 1972
OA EXPERIMENT:				
Earth physics VLBI	To demonstrate bandwidth synthesis techniques and to attempt to measure the baseline between DSSs 14 and 12 at Goldstone to 10 cm.	P. MacDoran (JPL) J. Fanselow (JPL) J. Thomas (JPL) J. Williams (JPL)	DSS 14 DSS 12	Apr. 4, 1972

Table 3. Recently approved radio astronomy experiments

Title	Purpose	Experimenters	Facilities required
2-cm VLBI observations	To make detailed measurements on a limited number of radio galaxies and quasars at 15 GHz; to search for weak compact sources in the nucleus of extended radio galaxies and quasars.	B. Clark (NRAO) K. Kellermann (NRAO) M. Cohen (Caltech) D. Shaffer (Caltech)	64-m antenna at Goldstone with Ku-band system (working with 47-m antenna at NRAO, Greenbank, West Virginia)
15.6-GHz VLBI observations	To monitor time variations in the fine structure and apparent positions of quasars at 15.6 GHz.	T. Clark (GSFC) R. Goldstein (JPL) H. Hinteregger (MIT) C. Knight (MIT) G. Marandino (Univ. of Maryland) A. Rogers (MIT Haystack Observatory) I. Shapiro (MIT) D. Spitzmesser (JPL) A. Whitney (MIT)	64-m antenna at Goldstone with Ku-band system (working with 37-m antenna at Haystack Observatory)
Ionized hydrogen detection	To search for microwave emission from ionized hydrogen in globular clusters.	J. Hills (Univ. of Michigan) M. Klein (JPL)	64-m antenna at Goldstone

Preliminary Evaluation of Radio Data Orbit Determination Capabilities for the Saturn Portion of a Jupiter-Saturn-Pluto 1977 Mission

V. J. Ondrasik, C. E. Hildebrand, and G. A. Ransford
Tracking and Orbit Determination Section

Navigation accuracies attainable with radio tracking of an outer-planets spacecraft in the vicinity of Saturn have been investigated. Analysis of the results indicates that navigation accuracy problems associated with low spacecraft declinations and with batch filtering of conventional radio data when unmodeled accelerations are acting on the spacecraft may be avoided by employing range and range-rate data taken simultaneously by two widely separated stations. With the availability of two-station simultaneous data, the uncertainty in Saturn's ephemeris becomes the error source which limits the accuracy of the pre-encounter navigation.

I. Introduction

During the late 1970s and early 1980s, NASA intends to explore the planets Jupiter and Saturn and their environs by means of multiple-planet missions. In designing such missions it is necessary to determine the navigational capabilities commensurate with expected or possible late 1970s technology. The primary portion of any navigation study involves an accuracy analysis to establish the orbit determination capabilities associated with various spacecraft and tracking systems. The results of such a study may then be used to identify the types of tracking systems which will provide data whose inherent quality will not be a limiting error source for outer planet navigation.

A preliminary radio data accuracy analysis for the Saturn portion of a Jupiter-Saturn-Pluto 1977 (JSP77) mission has just been completed and is reported here, with

particular emphasis given to orbit determination capabilities associated with various types of radio data. A somewhat similar study for a Jupiter mission is described by Curkendall and McDanell in Ref. 1. Although the JSP77 mission has been cancelled, the orbit determination precision associated with the Saturn portion of this mission should be very representative of the precision attainable for the Saturn portion of the proposed MJS77 (*Mariner Jupiter-Saturn 1977*) mission.

To obtain preliminary estimates of radio navigation capabilities, covariance analyses were performed for orbit determination solutions based upon the following types of radio data:

- (1) Conventional range and range-rate (doppler).
- (2) Multi-station range-rate and simultaneous range.

- (3) Explicitly differenced range and range-rate.

The main concern of the accuracy analysis was establishing the sensitivities of the solutions to the following quantities:

- (1) Constant station location errors.
- (2) Constant and stochastic spacecraft accelerations.
- (3) Data coverage.
- (4) Length of data arc.
- (5) *A priori* knowledge of the planetary ephemeris.

The orbit determination capabilities are expressed in the usual B-plane coordinates shown in Fig. 1 and described in Ref. 2.

If it is desired that the pre-encounter radio-only solution accuracies be less than 1000 km (1σ), the results of this preliminary accuracy analysis lead to the following conclusions:

- (1) If the spacecraft has a low declination, simultaneous or nearly simultaneous high precision (3-m) range data will be required.
- (2) If the spacecraft is subject to unmodeled accelerations larger than 10^{-14} km/s² during much of the data arc, simultaneous range and range-rate data will be required.

With the availability of simultaneous data to alleviate the degradation of orbit determination precision due to low declinations and unmodeled stochastic accelerations acting on the spacecraft, the planetary ephemeris uncertainty becomes the dominant error source affecting the accuracy of the pre-encounter estimates of the planet-relative spacecraft state.

It has also been concluded that the mass and ephemeris of Saturn should be estimated if optimal navigation accuracies are to be achieved. Thus, improved knowledge of these parameters will be a by-product of the spacecraft orbit determination procedure. The amount of improvement resulting from the use of different types of radio data is discussed in some detail in another article.¹

¹"Determining the Mass and Ephemeris of Saturn by Radio Tracking of a Jupiter-Saturn-Pluto 1977 Spacecraft" by V. J. Ondrasik, et al., in this issue.

²P. A. Penzo, JPL Systems Analysis Section, private communication.

II. Trajectory and Data

The Earth mean equatorial cartesian and B-plane coordinates for the particular JSP77 trajectory that was investigated are given in Tables 1 and 2 and were supplied by P. Penzo.² The temporal behavior of the Earth to spacecraft spherical coordinates is shown in Fig. 2 over the tracking period of encounter (E) - 120 days to $E + 30$ days. The most interesting feature of this figure involves the spacecraft declination which at encounter is almost zero and never rises above 6 deg.

In the integration of the trajectory and variational equations, and the subsequent calculation of data and the associated partial derivatives, the following assumptions were made:

- (1) Only the Sun and Saturn accelerate the spacecraft.
- (2) Saturn and Earth move in ellipses about the Sun.
- (3) The velocity of light equals infinity.

Previous studies have shown that these assumptions will not significantly affect the accuracy analysis results.

In anticipation that data taken simultaneously or nearly simultaneously from two stations will be useful, the simulation tracking pattern shown in Fig. 3 was based upon a "cycle" of data. As shown in this figure, a cycle consists of range and range-rate measurements taken from Deep Space Stations (DSSs 14 (California), 42 (Australia), 61 (Spain), and 14 again. Each pass includes horizon-to-horizon range-rate data taken on the hour, and usually two range points. During the overlap period between stations, the range-rate points will be taken at exactly the same times, and the range point from one station will occur within a few minutes of a range point taken from another station. In practice, the simultaneous range-rate and range information will be obtained by using two-way and three-way doppler data, respectively. If the round-trip light time is less than the overlap time, the information supplied by simultaneous range points may be obtained from nearly simultaneous (~ 15 -min separation) two-way range points. Operationally, precision two-way range points are easier to obtain than three-way range points because problems associated with the synchronization of station clocks are avoided (Ref. 3, pp. 118-119).

III. Data Weights

Although only one range-rate point is taken per hour during a tracking pass, each point is weighted so that it is representative of range-rate points taken once a minute

with a data weight of 1 mm/s. This weight implies that for the outer planet missions both the two- and three-way doppler data will be of the same quality as the best present two-way data.

As shown in Ref. 3, pp. 120–122, the reason for taking precise simultaneous range data is to avoid problems associated with spacecraft at low declinations. Thus, when range data from more than one station are included in the orbit determination solution, these data will be given a weight of 3 m. When the solution contains range data from only one station, they will be given a range weight of 300 m to diminish the errors produced by unmodeled spacecraft accelerations as discussed in Ref. 4. Data weights are data accuracy specifications provided to the orbit determination solution filter, and should be distinguished from expected measurement precision. For example, range data, of a given quality, may be assigned different weights, depending on how well the spacecraft and tracking system can be modeled.

In later sections it will become apparent that the main reason for taking simultaneous range and range-rate data is to diminish orbit determination errors produced by unmodeled spacecraft accelerations. As shown in Ref. 3, pp. 123–124, new data types which are formed by explicitly differencing the simultaneous (or near-simultaneous) range and range-rate data are insensitive to such accelerations. In this study the differenced range and range-rate data are assigned weights of 3 m and 1 mm/s, respectively. Since the differenced data contain very little information about the geocentric range and range-rate, the orbit determination solution must also include some conventional range and range-rate data. However, to insure that these conventional data are used only in the determination of the geocentric range and range-rate components and do not introduce spacecraft acceleration information, they are assigned very loose weights. In this study the conventional range and range-rate data were given weights of 10 km and 100 mm/s, respectively, in the differenced data orbit determination solutions.

IV. Error Sources

In addition to the data noise, two other sources of error are assumed to be present, namely, constant station location errors and unmodeled spacecraft accelerations. It is assumed that the effects of transmission media, polar motion, and other such error sources as well as the actual crust-fixed station location biases can be represented to some degree by considering the effects of constant station

location errors. As shown in Table 3, the assumed errors in the station's cylindrical coordinates, i.e., distance off the spin axis (r_s), longitude (λ), and distance from the equator (z_s), are 1 m, 2 m, and 5 m, respectively. The errors in the position and velocity of the spacecraft which are produced by these constant station location errors were evaluated by using the Double-Precision Orbit Determination Program (DPODP) consider option described in Ref. 5, pp. 109–116. The numbers expressing navigational capabilities given in the following sections could be lowered if the station locations were estimated instead of being considered to be in error by the above amounts. However, experience has shown that only under limited circumstances is it possible to solve for station locations without degrading the solution of the position and velocity of the spacecraft.

The unmodeled spacecraft accelerations are represented with adequate generality as a three-axis, exponentially time-correlated stationary process. As shown in Table 3, the standard deviation of these accelerations is assumed to be 10^{-12} km/s² with a correlation time τ of either 6 days or infinity. The case of $\tau = \infty$, of course, corresponds to a constant acceleration. The analysis technique used to determine the sensitivity of the conventional least-squares batch filter solution for the spacecraft state and planetary mass and ephemeris to the unmodeled spacecraft accelerations is that developed by Curkendall in Ref. 6. If any part of the accelerations were constant or nearly so, it might be possible to estimate these accelerations and thereby diminish the errors they would produce in the solution for the spacecraft's position and velocity. For this reason the list of estimated parameters will often be extended to include three constant spacecraft accelerations.

V. Solution Filter, Estimated Parameters, and A Priori

With only one exception, the orbit determination solutions were obtained with a conventional least-squares batch filter (Ref. 5) estimating the spacecraft state, planetary mass, planetary ephemeris, and constant spacecraft accelerations. The heliocentric *a priori* knowledge of the spacecraft position and velocity was always taken to be 10^7 km and 1 km/s, respectively. The *a priori* knowledge of the constant accelerations was taken as 10^{-12} km/s².

The planetary ephemeris was solved for in terms of Brouwer and Clemence Set III elements described in Ref. 5, pp. 26–29, and Ref. 7. The nominal *a priori* knowledge of the mass and Brouwer and Clemence Set III elements

are given in Table 4 and were recommended by Lieske.³ In order to obtain some idea of how the ephemeris *a priori* influences the orbit determination process, covariance analyses were also performed for solutions with an improved *a priori* knowledge of the planetary ephemeris. The improved *a priori* ephemeris is also shown in Table 4 and is down from the nominal by a factor of three. This nominal ephemeris *a priori* will probably be available if the current level of ephemeris work continues. However, improvement of the nominal *a priori* by a factor of three will require a much larger effort. Figure 4 shows the contribution of the nominal *a priori* ephemeris to the Saturn-centered Earth equatorial B-plane errors. It should be noted that the nominal *a priori* ephemeris uncertainty gives a semi-major axis of the error ellipse of approximately 1200 km.

VI. Error Analyses Sets

In order to obtain some idea of the orbit determination capabilities of the Saturn portion of the JSP77 mission using radio data only, consider covariances were computed for many cases involving different data types, data arc lengths, error sources, *a priori* uncertainties, data coverage, and estimated parameters. These cases are grouped into sets and described in Table 5. Each set is chosen to study one particular feature of the orbit determination procedure.

The orbit determination capabilities are expressed in terms of the semi-major axis (SMAA) and semi-minor axis (SMIA) of the B-plane 1- σ error ellipse, and the standard deviations of the magnitude of the \underline{B} -vector (σ_B) and the linearized time of flight (σ_t). Generally the orbit determination capabilities are given for the data arcs terminating at $E - 11$ days, $E - 5$ days, $E - 2$ days, $E + 4$ days, and $E + 28$ days.

VII. Errors in State Only Solutions Produced by Various Error Sources

To obtain some idea of the size of the spacecraft state errors produced individually by errors in Saturn's mass and ephemeris, station locations, and nongravitational accelerations, a sensitivity matrix was computed for case 1 of Table 5. (See Ref. 8 for a discussion of the sensitivity matrix.) Figure 5 shows the errors in the estimates of $\underline{B} \cdot \underline{R}$, $\underline{B} \cdot \underline{T}$ and linearized time of flight resulting from the

indicated errors associated with various parameters for the solutions made with three-station data arcs starting at $E - 120$ days and terminating at $E - 5$ days and $E - 2$ days. These errors in the B-plane quantities scale directly with the magnitude of the errors from each source.

The sensitivity matrix will change for each different solution. However, the following gross conclusions may be drawn from these results:

- (1) It will be necessary to solve for planetary mass and ephemeris.
- (2) Constant spacecraft accelerations must be estimated if they are expected to be present at a level higher than 10^{-14} km/s².
- (3) Station location errors are not a major concern (primarily since the solution uses simultaneous range).

VIII. Long Arc Solutions Using Single Station, Multi-Station, and Differenced Data

A. Conventional Consider Analysis

To compare the orbit determination capabilities of long data arc (i.e., data starts at $E - 120$ days) solutions using three-station data, single-station data, and explicitly differenced data, error analyses were performed on cases 2, 3, and 4 of Table 5. The one-sigma conventional consider standard deviations, which account for the formal statistics resulting both from data noise only and from constant station location errors, are shown for the pertinent B-plane parameters in Fig. 6 for several different data arc lengths.

The most notable feature of these results is that, irrespective of the data types, for data arcs extending up to $E - 2$ days, the SMAA is not reduced below its value given by the *a priori* ephemeris uncertainty shown in Fig. 4. However, the solutions based upon multi- or single-station tracking do contain some planet-centered information as is evidenced by the improvement in SMIA and σ_B for data arcs terminating at $E - 5$ days or beyond. The differenced data solutions do not show a corresponding reduction in σ_B and SMIA because, as explained in Ref. 3, pp. 123-124, the explicit differencing procedure deletes almost all of the planet-centered acceleration information. When a few days of post-encounter data are included in the solution, the SMAA is reduced below 10 km for solutions based upon all three data types. The post-encounter differenced data solutions take a longer time to improve than do the solutions which employ the conventional data

³J. H. Lieske, JPL Tracking and Orbit Determination Section, private communication.

types because the differenced data obtain planet-relative information only indirectly through changes in the spacecraft-planet-Earth geometry.

Figure 6 also shows that, for data arcs ending at $E - 11$ days or before, the SMAA, σ_B , and SMIA are generally a factor of two larger for the solutions based upon single-station data than for solutions based upon either multi-station or differenced data. This degradation of the solution is a manifestation of the zero-declination problem and is eliminated by the use of simultaneous or nearly simultaneous range data.

Another notable feature is that the time of flight is determined much better from conventional data. Presumably this occurs because much of the time of flight information is supplied by the planet accelerating the spacecraft. A curious result exhibited in Fig. 6 is that the solution based upon multi-station data may degrade from earlier solutions in certain directions if the data arc terminates a few days before encounter. This degradation appears to be a manifestation of a phenomenon that has been observed before; namely, as the information supplied by the planetary-induced accelerations starts to become important, it competes with the information supplied by the spinning Earth, and under certain circumstances the covariance is degraded. This effect has sporadically been the subject of casual investigations, but presently is not well understood.

B. Effects of Unmodeled Accelerations

So far in this section the only factors that have been assumed to degrade the orbit determination solution have been data noise and constant station location errors. An additional error source which is very important is stochastic unmodeled spacecraft accelerations. Such error sources can be particularly damaging because the batch filter is incapable of modeling such a process. The effect of the unmodeled accelerations on the solutions based upon single-station, three-station, and differenced data are shown in Fig. 7 for several data arc lengths. This figure contains only the effects due to unmodeled accelerations with a correlation time of 6 days as described in Table 4.

It is immediately apparent that for solutions based upon three-station data with a 3-m range weight the effects of unmodeled accelerations can be catastrophic. For example, for a multi-station data arc terminating at $E - 4$ days, the stochastic accelerations produce a $30000\text{-km} \times 7000\text{-km} \times 200\text{-second}$ B-plane error ellipsoid. The effects of unmodeled accelerations on the single-station solution are typically an order of magnitude less damaging than

the effects on the multi-station solutions. For a solution based upon a single-station data arc terminating at $E - 4$ days, these accelerations produce a $4000\text{-km} \times 2000\text{-km} \times 40\text{-second}$ B-plane error ellipsoid.

If the solutions are based upon explicitly differenced data, the effects of unmodeled spacecraft accelerations are practically negligible. For example, for a solution based upon a differenced data arc terminating at $E - 4$ days, stochastic accelerations produce only a $100\text{-km} \times 30\text{-km} \times 5\text{-second}$ B-plane error ellipsoid. These errors are two or three orders of magnitude smaller than the ones resulting from conventional data because, as mentioned earlier, the differencing process deletes almost all of the information which is sensitive to the spacecraft accelerations.

With a few days of post-encounter data in the solution, the stochastic acceleration-induced error ellipsoid is reduced to approximately $20\text{ km} \times 20\text{ km} \times 1\text{ second}$ for all three data sets.

IX. Short Arc Solutions

A. Conventional Consider Analysis

The previous section was concerned with orbit determination solutions based upon a "long" arc of data, i.e., the data started at $E - 120$ days. In an attempt to determine if a data arc of this length is necessary, covariance analyses were performed for cases identical to cases 2, 3, and 4 except that data acquisition was initiated at $E - 34$ days, i.e., a "short" arc of data. These short arc cases are described in Table 5. The B-plane errors produced by data noise and station location errors for solutions based upon short arcs of three-station, single-station, and differenced data are shown in Fig. 8.

The most notable feature of this figure is that, for data arcs terminating at $E - 11$ days, the SMAA associated with single-station tracking is approximately five times larger than the SMAA associated with either multi-station or differenced data. This degradation of the single-station data solution is a manifestation of the zero-declination problem, which will be present if simultaneous range data are not used.

Another feature of particular interest is that, for solutions based upon data arcs extending to within five days of encounter, the short arc B-plane error ellipsoids are nearly the same as those associated with the analogous long arc cases.

B. Effects of Unmodeled Accelerations

The parameters describing the B-plane error ellipsoid produced by the unmodeled stochastic accelerations described in Table 3 for three-station, single-station, and differenced data solutions are shown in Fig. 9. As was the case for long arc solutions, the effects of unmodeled accelerations on the single-station and three-station solutions can be disastrous, producing errors of thousands of kilometers. Once more, however, if differenced data are used, the effects of the spacecraft accelerations on the orbit determination solution will be negligible.

X. Ephemeris A Priori Dependence

In previous sections it has been shown that solutions based upon pre-encounter data yield a SMAA for the B-plane error ellipse which is due almost entirely to uncertainties in the planetary ephemeris. To obtain some idea of how much the planet-centered spacecraft state improves with better *a priori* knowledge of the planetary ephemeris, the pertinent error analyses were performed. These cases are described in Table 5.

Figure 10 contains the B-plane error ellipsoid parameters for three-station and differenced data solutions made with the nominal and with $\frac{1}{3}$ nominal or improved ephemeris *a priori* described in Table 3. It is easily seen that improving the *a priori* knowledge of the planetary ephemeris by a factor of three generally produces a reduction in the pre-encounter SMAA by approximately the same factor.

XI. Data Coverage Dependence

To grossly determine the amount of data coverage which will be required, error analyses were performed for a solution which was identical to the long arc three-station data solution (case 2 of Table 5), except half of the data

was deleted. The particular portion of the data which was deleted is indicated by the deletion code in Fig. 3. A comparison of the B-plane parameters associated with the full data coverage and "one-half" data coverage shows differences which are always less than 10%. Thus, it is probably sufficient to use only one-half the data coverage shown.

XII. Summary and Discussion

A study of the results which have been presented in the preceding sections leads to the following tentative conclusions regarding the radio data orbit determination procedure for outer planet missions:

- (1) For solutions made without any data taken after encounter minus a few days, the spacecraft state uncertainty is reduced only slightly from the uncertainty associated with the planetary *a priori* ephemeris.
- (2) If the spacecraft is at a low declination, short arc solutions are substantially improved with the use of simultaneous or near-simultaneous precision range data.
- (3) If the spacecraft is undergoing unmodeled accelerations larger than 10^{-11}km/s^2 , it will probably be necessary to use explicitly differenced simultaneous data.

Thus, with the availability of simultaneous data, the planetary ephemeris uncertainty becomes the dominant error source and the errors associated with zero-declination geometry and/or unmodeled spacecraft accelerations become almost negligible.

As is the case with all accuracy analyses, the results shown in the preceding sections are based upon particular error models and thus are representative of the actual accuracies obtainable only to the degree to which the error model is representative of the true error sources.

References

1. Curkendall, D. W., and McDanell, J. P., "An Investigation of the Effects of the Major Earth-Based Navigation Error Sources for an Outer Planet Mission," paper presented at the AAS 17th Annual Meeting in Seattle, Washington, June 28-30, 1971.
2. Capps, G. S., et al., *The Double Precision Orbit Determination Program: Vol. VI. Matrix Segment*, Jet Propulsion Laboratory EPD 426-6, Apr. 14, 1967 (JPL internal document).
3. Ondrasik, V. J., and Rourke, K. H., "Application of New Radio Tracking Data Types to Critical Spacecraft Navigation Problems," in *JPL Quarterly Technical Review*, Vol. 1, No. 4, pp. 116-132. Jet Propulsion Laboratory, Pasadena, Calif., Jan. 1972.
4. Rourke, K. H., and Ondrasik, V. J., "Improved Navigation Capability Utilizing Two-Station Tracking Techniques for a Low-Declination Distant Spacecraft," in *The Deep Space Network Progress Report*, Technical Report 32-1526, Vol. VII, pp. 51-60. Jet Propulsion Laboratory, Pasadena, Calif., Feb. 15, 1972.
5. Moyer, T. D., *Mathematical Formulation of the Double-Precision Orbit Determination Program (DPODP)*, Technical Report 32-1527. Jet Propulsion Laboratory, Pasadena, Calif., May 15, 1971.
6. Curkendall, D. W., *Problems in Estimation Theory with Applications to Orbit Determination*, Doctoral Dissertation, University of California at Los Angeles, 1971.
7. Brouwer, D., and Clemence, G. M., *Methods of Celestial Mechanics*, pp. 241-242, Academic Press, Inc., New York, 1971.
8. McReynolds, S. R., "The Sensitivity Matrix Method for Orbit Determination Error Analysis, With Application to a Mars Orbiter," in *The Deep Space Network*, Space Programs Summary 37-56, Vol. II, pp. 85-87. Jet Propulsion Laboratory, Pasadena, Calif., Mar. 31, 1969.

Table 1. Saturn, Earth, and spacecraft coordinates at encounter

Coordinate	Object			
	Earth (heliocentric)	Saturn (heliocentric)	Spacecraft (heliocentric)	Spacecraft (planet centered)
X	0.93054×10^8	-0.14201×10^{10}	-0.14203×10^{10}	-0.13472×10^6
Y	0.10558×10^9	-0.66544×10^8	-0.6624×10^8	0.29559×10^6
Z	0.45810×10^8	0.33937×10^8	0.33416×10^8	-0.52131×10^6
\dot{X}	-0.23651×10^2	-0.20706×10^0	-0.17789×10^2	-0.17583×10^2
\dot{Y}	0.17084×10^2	-0.89422×10^1	-0.15492×10^2	-0.65502×10^1
\dot{Z}	0.74133×10^1	-0.36914×10^1	-0.15126×10	0.21789×10^1

Table 2. Equatorial B-plane coordinates

Coordinate	Value
B	0.7686×10^6
$B \cdot R$	0.6479×10^6
$B \cdot T$	0.4135×10^6
C_3	0.2352×10^2
ϕ	57.45 deg

Table 3. Error sources

Error source	Time behavior	Magnitude
Stations:		
(1) Distance off spin axis	Constant	1 m
(2) Longitude	Constant	2 m
(3) Distance off equator	Constant	5 m
Spacecraft accelerations:		
(1) Constant	Constant	10^{-12} km/s ²
(2) Stochastic	Piece-wise constant for 2 days with correlation time of 6 days	Standard deviation of distribution = 10^{-12} km/s ²

Table 4. Nominal and improved planetary mass and ephemeris a priors

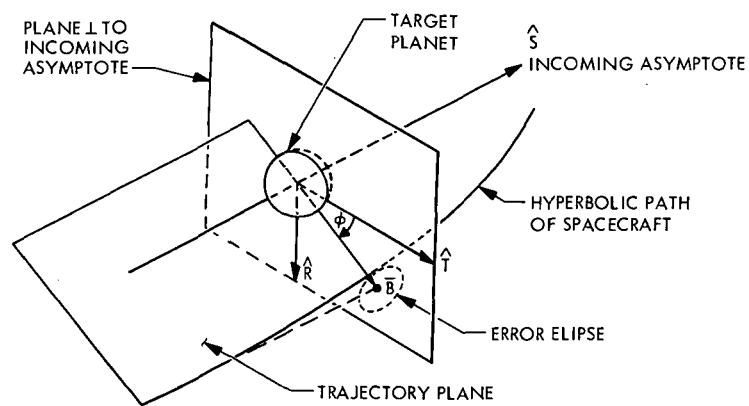
Planet	GM <i>a priori</i> , km ³ /s ²	$10^2 \frac{\sigma_{GM} (a priori)}{GM}$, %	Ephemeris parameter	Ephemeris <i>a priori</i> , rad		σ (ephemeris), 1.5×10^9 km	
				Nominal	Improved	Nominal	Improved
Saturn	0.3×10^5	0.08	DA	0.6×10^{-7}	0.2×10^{-7}	0.9×10^2	0.3×10^2
			DE	0.3×10^{-6}	0.1×10^{-7}	0.45×10^3	0.15×10^3
			DMW	0.6×10^{-6}	0.2×10^{-6}	0.9×10^3	0.3×10^3
			DP	0.3×10^{-6}	0.1×10^{-6}	0.45×10^3	0.15×10^3
			DQ	0.3×10^{-6}	0.1×10^{-6}	0.45×10^3	0.15×10^3
			EDW	0.3×10^{-6}	0.1×10^{-6}	0.45×10^3	0.15×10^3

Table 5. Case numbers and solution sets

Case	Set	Data ^a	Stations	Ephemeris <i>a priori</i> ^b
1	Estimate state only	ρ and $\dot{\rho}$	14, 42, 61	—
2	Long arc solutions	ρ and $\dot{\rho}$	14, 42, 61	Nominal
3		ρ and $\dot{\rho}$	14 only	Nominal
4		Diff	14, 42, 62	Nominal
5	Short arc solutions	ρ and $\dot{\rho}$	14, 42, 61	Nominal
6		ρ and $\dot{\rho}$	14 only	Nominal
7		Diff	14, 42, 61	Nominal
8	Ephemeris-dependence solutions	ρ and $\dot{\rho}$	14, 42, 61	Improved
9		Diff	14, 42, 61	Improved

^a ρ = range; $\dot{\rho}$ = range-rate; diff = explicitly differenced data.

^bSee Table 4.



\hat{S} INCOMING ASYMPTOTE
 \hat{B} MISS PARAMETER ($\hat{B} \perp \hat{S}$)
 \hat{T} AIMING POINT ORIENTATION
 \hat{T} PARALLEL TO EARTH EQUATORIAL PLANE
 \hat{T} AND \perp TO \hat{S}
 $\hat{R} = \hat{S} \times \hat{T}$
 $C_3 = (\text{VELOCITY AT INFINITY})^2$
 $T_f = \text{LINEARIZED TIME OF FLIGHT}$

Fig. 1. B-plane coordinate system

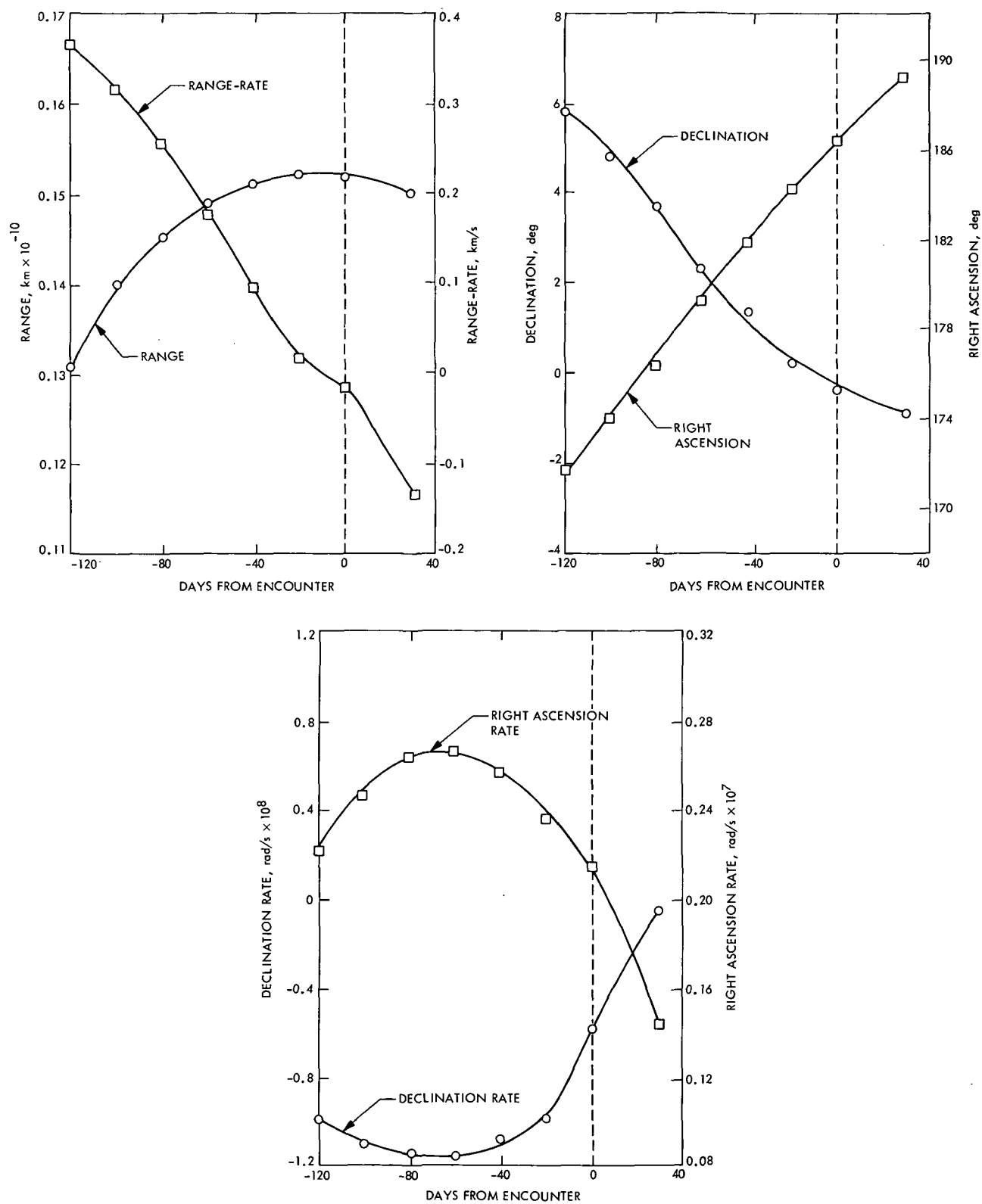


Fig. 2. Earth-spacecraft spherical coordinates

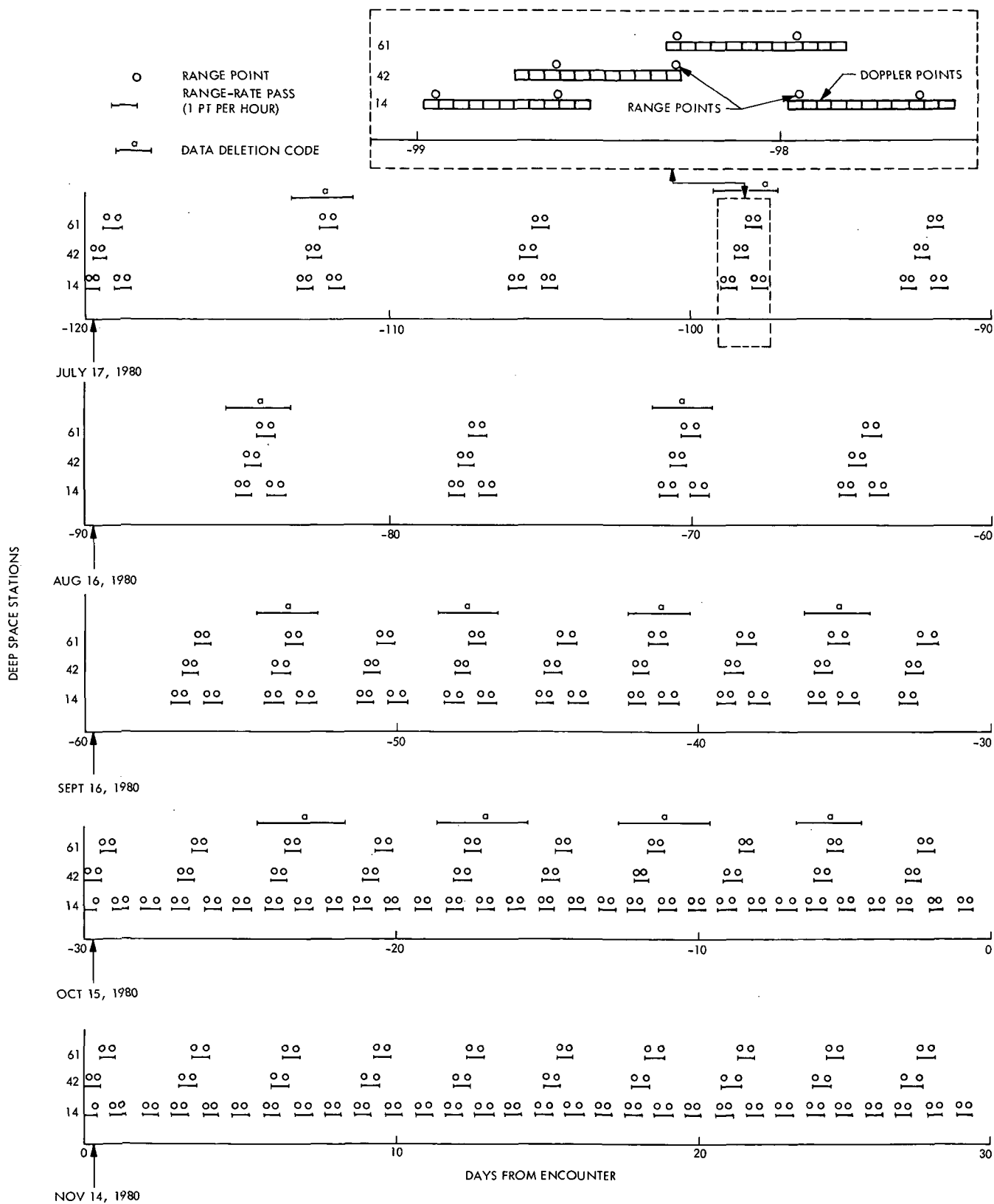


Fig. 3. DSSs 14, 42, and 61 tracking patterns

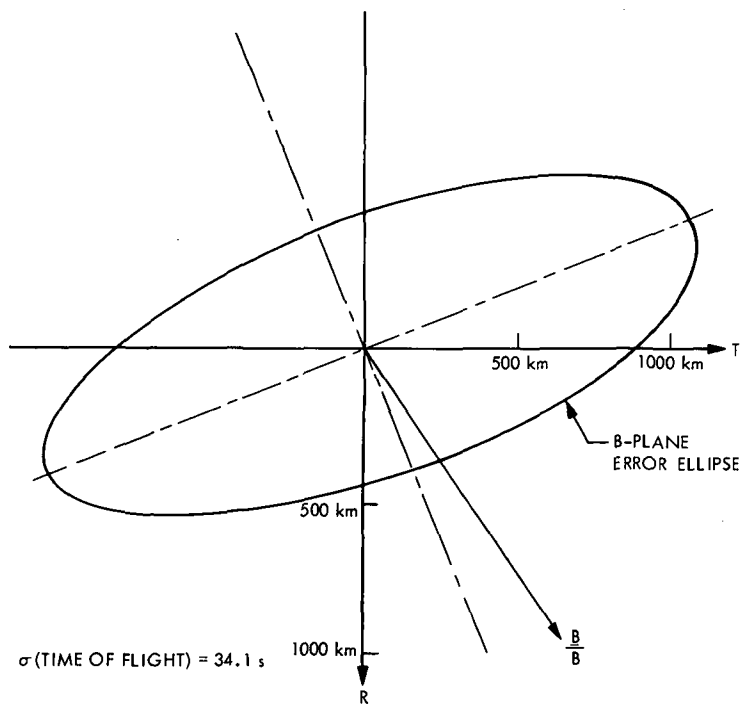


Fig. 4. A priori ephemeris uncertainties mapped into the linearized time of flight and the equatorial B-plane ellipse

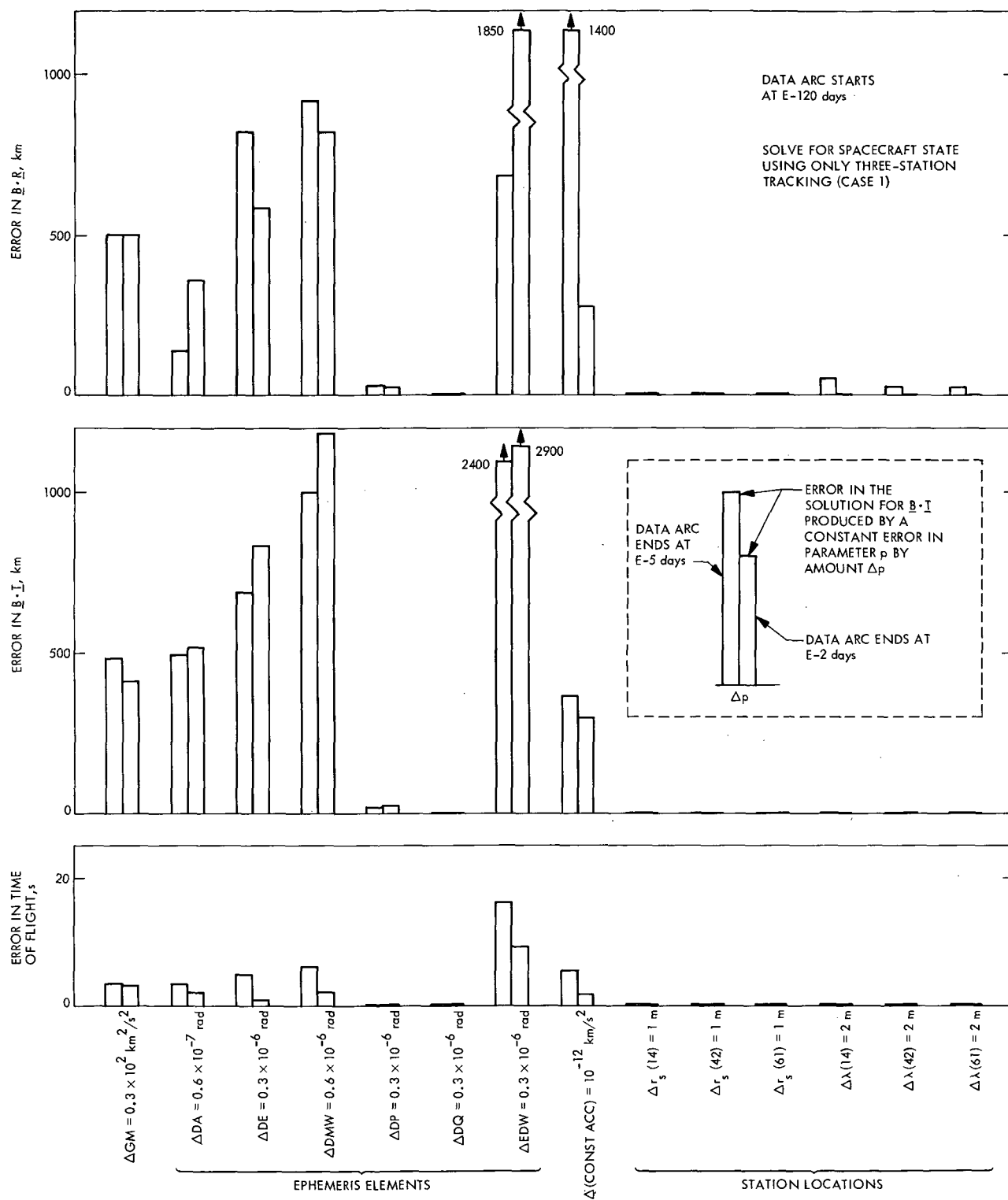


Fig. 5. Errors in B-plane parameters produced by constant error sources for a solution based upon a long arc of three-station data

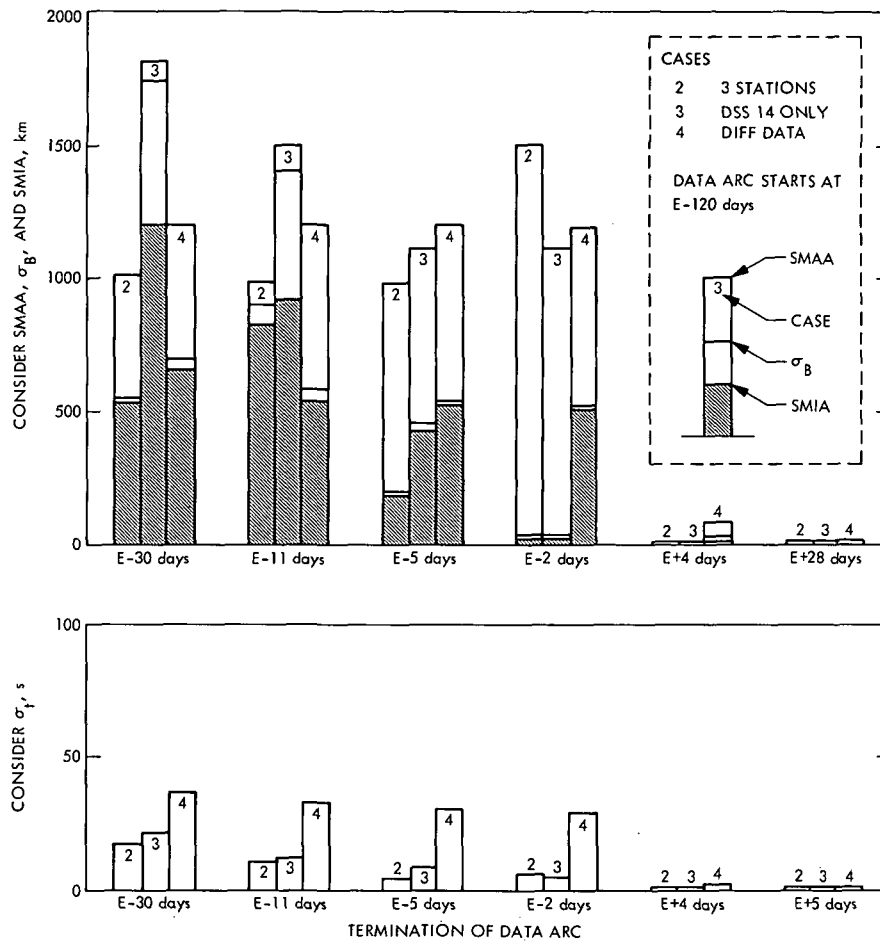


Fig. 6. Effects of data noise and station location errors on long arc solutions

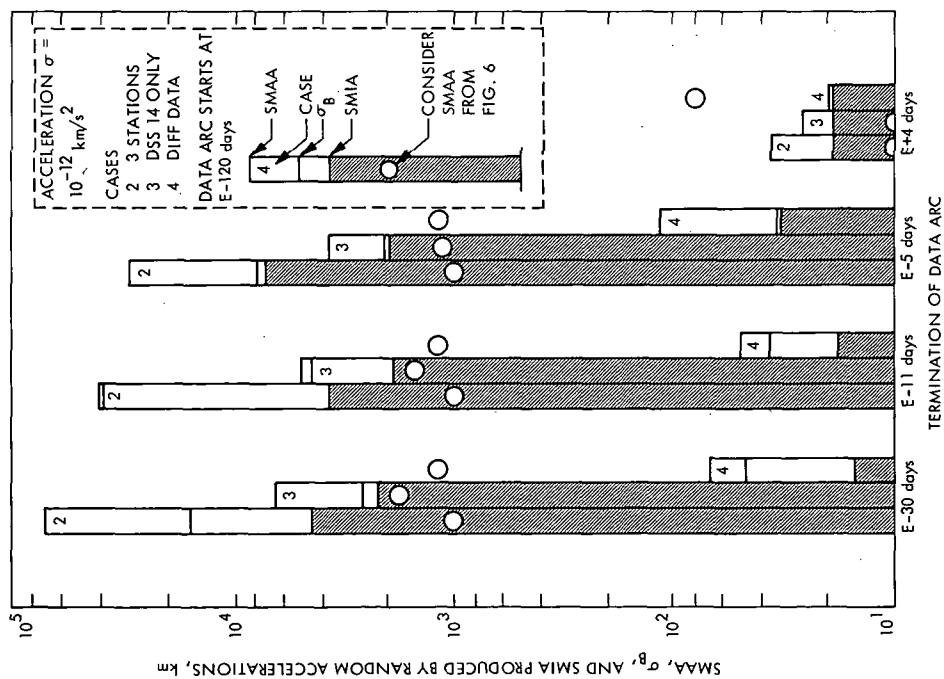


Fig. 7. Effects of unmodeled random accelerations only on long arc solutions using three-station, DSS 14 only, and differenced data

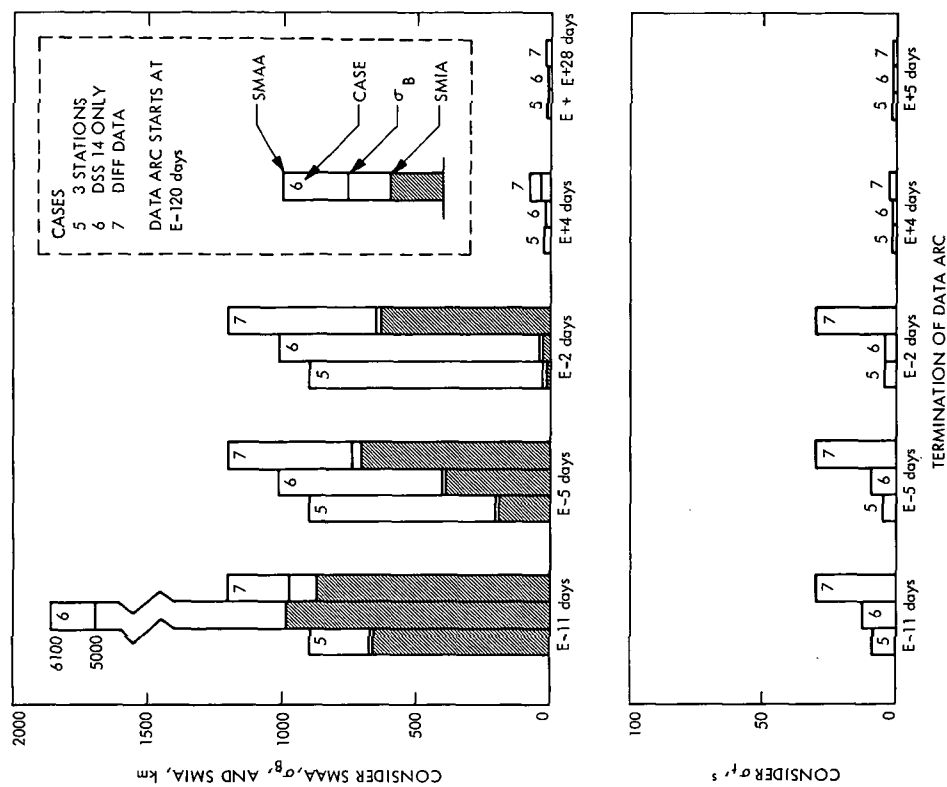


Fig. 8. Effects of data noise and station location errors on short arc solutions

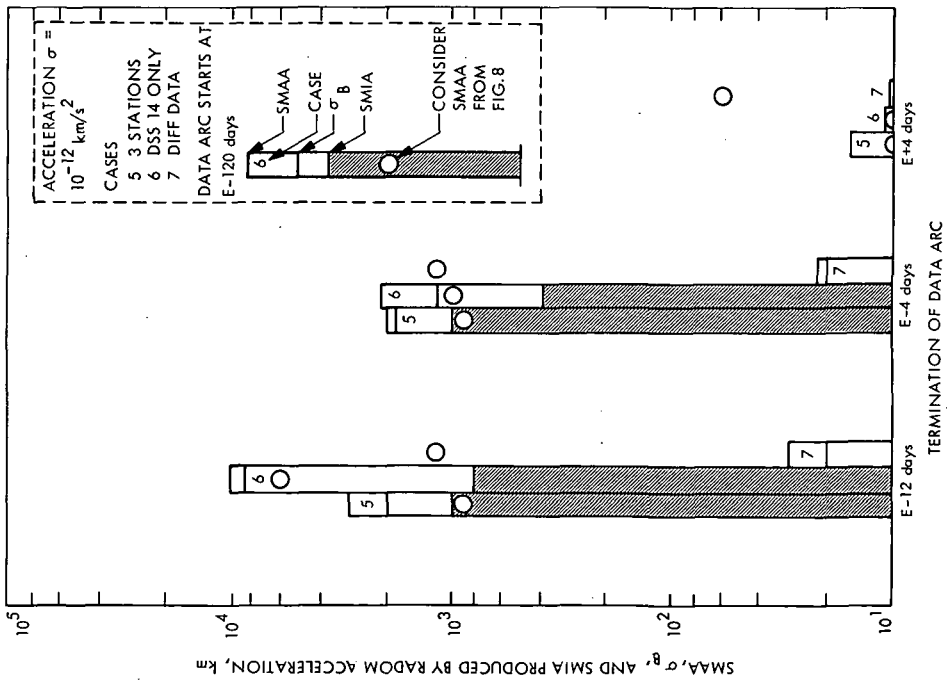


Fig. 9. Effects of unmodeled random accelerations only on short arc solutions using three-station, DSS 14 only, and differenced data

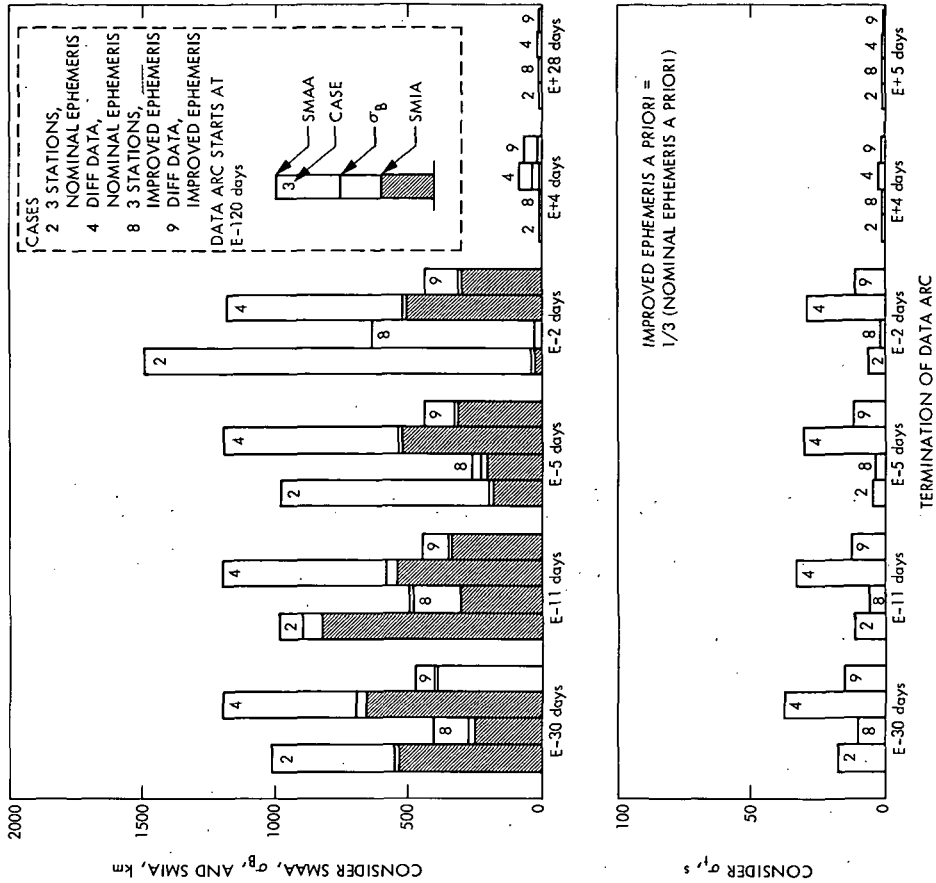


Fig. 10. Effect of planetary ephemeris a priori on long arc solutions

Determining the Mass and Ephemeris of Saturn by Radio Tracking of a Jupiter-Saturn-Pluto 1977 Spacecraft

V. J. Ondrasik, C. E. Hildebrand, and G. A. Ransford
Tracking and Orbit Determination Section

Preliminary estimates of the accuracies with which the mass and ephemeris of Saturn may be determined from radio tracking of an outer planets spacecraft are presented. It is shown that the determination of these parameters should employ radio data taken simultaneously from two stations. Indications are that the uncertainties may be reduced by approximately three orders of magnitude in the mass and by a factor of two in the ephemeris.

I. Introduction

The preliminary orbit determination capabilities associated with various types of radio data for the Saturn portion of a Jupiter-Saturn-Pluto 1977 (JSP77) mission have been established.¹ It was found that obtaining accurate estimates of the planet-centered spacecraft state required estimating the mass and ephemeris of Saturn. Thus, improved knowledge of Saturn's mass and ephemeris will be a byproduct of the spacecraft orbit determination procedure.

The following sections will show the mass and ephemeris accuracy results for solutions made with long and short arcs of three-station, single-station, and differenced data which are corrupted by data noise, constant station location errors, and particular types of unmodeled spacecraft accelerations. If the data are processed properly and

the above error sources are the only ones present, the knowledge of the mass may be improved three orders of magnitude from its *a priori* value and some of the ephemeris elements may be improved by a factor of four. The surprising conclusion resulting from this study is that apparently the most reliable solutions for the planetary ephemeris may be made with explicitly differenced range and range-rate data taken simultaneously from widely separated stations. Thus, implementation of a tracking system which obtains simultaneous data may allow significant improvement in the results of outer planet celestial mechanics experiments.

II. Data, Error Sources, and Solution Sets

The detailed information describing the trajectory, data, data weights, error sources, *a priori*, estimated parameters, and various solution sets is given in Sections II to V of the article referred to in Footnote 1. Briefly, the solution sets which are studied here involve the use of range and range-rate data taken either from three stations

¹See "Preliminary Evaluation of Radio Data Orbit Determination Capabilities for the Saturn Portion of a Jupiter-Saturn-Pluto 1977 Mission," by V. J. Ondrasik, et al., in this issue.

or from a single station, or explicitly differenced range and range-rate data taken simultaneously from widely separated stations. The solution is assumed to be made with a conventional least squares filter which estimates spacecraft state, constant spacecraft accelerations, Saturn's GM, and Saturn's ephemeris in terms of Brouwer and Clemence Set III elements (DA, DE, DMW, DP, DQ, EDW). A discussion of the advantages offered by this set of elements is given in Ref. 1. The data arc starts at either encounter (E) - 120 days (long arc solutions) or E - 34 days (short arc solutions) and generally terminates at E + 4 days or E + 28 days. The batch filter solutions based upon these data are evaluated under the corrupting influence of (1) data noise, (2) 1 m, 2 m, and 5 m errors in the station distance off the spin axis, longitude, and distance from the equator, and (3) unmodeled stochastic spacecraft accelerations of standard deviation 10^{-12} km/s² with a correlation time of six days. The effect of the unmodeled accelerations scales directly with their standard deviations.

III. Accuracy of the Mass Solution

Figure 1 shows the accuracy of the estimate of Saturn's mass (GM) using long arcs of three-station, single-station and differenced data. The effects of random data noise and constant station location errors are accounted for in the conventional consider standard deviations which are shown by open bars; the effects of unmodeled spacecraft accelerations only are shown as solid bars.

The figure shows that improvement of GM from its *a priori* value of 3×10^4 km³/s² (0.1%) may occur very early. If spacecraft accelerations are ignored, it is clear that the three-station and single-station solutions have approximately equal accuracy and both are much superior to the differenced data solutions. The fact that conventional data GM solutions are superior to differenced data solutions is not surprising, because most of the information concerning the planetary mass is supplied through the planetary acceleration and, as discussed in Ref. 2, almost all of this information is deleted by the differencing procedure.

However, it is to be expected that using three-station or single-station data will yield solutions that may be sensitive to unmodeled spacecraft accelerations. This is indeed the case as shown in Fig. 1. The spacecraft accelerations will seriously degrade the solution for GM made with three-station or single-station conventional data. For example, spacecraft accelerations of 10^{-12} km/s² typically degrade the GM solutions based upon three-station and single-station data by two and one orders of magnitude,

respectively, over the accuracies associated with data noise and constant station location errors. Presumably, for the reasons given in Ref. 2, the single-station data solution is less sensitive to the unmodeled accelerations than the three-station data solution because of the difference in the weight given to the range data. When post-encounter data are used, the sensitivity of the GM solution to unmodeled accelerations cannot be reduced below the single-station sensitivity by using differenced data. Thus it appears that the best long arc GM solution would be based upon conventional data with loosely weighted (300 m) range.

Error analyses were also performed using short data arcs. The resulting accuracy estimates were similar to the long arc results and are shown in Fig. 2.

If the spacecraft is subject to unmodeled accelerations less than 10^{-12} km/s² and if the estimate uncertainties are not particularly sensitive to the statistics describing these accelerations, it appears that the GM of Saturn can be estimated with an accuracy of 10^2 km³/s² or 0.0003%.

IV. Ephemeris Accuracies

Figure 3 shows how data noise, constant station location errors, and a particular type of unmodeled acceleration may degrade the solution for the elements of Saturn's ephemeris based upon the long arcs of three-station, single-station, and differenced data. Once again, the effects of data noise and constant station location errors are combined and are shown as the open bars in Fig. 3; the effects of unmodeled accelerations only are shown as solid bars.

This figure also shows that, at most, only four of the Brouwer and Clemence Set III elements can be improved, and if the data are not processed properly some of the elements may be degraded from their *a priori* values.

The surprising feature of Fig. 3 is that the differenced data solution is superior to the conventional three-station or single-station solutions even if there are no unmodeled spacecraft accelerations. The superiority of the differenced data solution is substantially increased if the effects of unmodeled accelerations are taken into account, because the differenced data solution has virtually no sensitivity to spacecraft accelerations while the three-station and single-station solutions do.

The effects of data noise, constant station location errors, and unmodeled spacecraft accelerations on ephemeris solutions based upon short arcs of data are shown in

Fig. 4. Comparison of Figs. 3 and 4 shows that the uncertainties due to the data noise and constant station locations are very similar for the long data arc and short data arc solutions. However, the short data arc solutions based upon three-station or one-station conventional data are much less sensitive to unmodeled accelerations than are the long arc solutions. A brief discussion of why this may occur is given in Ref. 3.

From Figs. 3 and 4 it appears that, if a batch filter is used, and if only the error sources considered above are present, the most reliable estimate of Saturn's ephemeris will be based upon explicitly differenced data. Using the differenced data the uncertainties in the Brouwer and Clemence Set III elements DE, DMW, and DP may be reduced by 50% and those in EDW by a factor of four. This corresponds roughly to reducing the one-sigma uncertainty in Saturn's position at encounter from the *a priori* of 1500 to 850 km.

V. Summary and Discussion

The results of the preceding sections indicate that the solutions for Saturn's GM and ephemeris should be based upon different orbit determination procedures. The best radio data GM solutions are apparently made with conventional data having a loose (300 m) data weight assigned to the range data. If the spacecraft experiences 10^{-12} km/s² accelerations of the type considered in this article it should be possible to determine GM to

0.0003%. The solution seems to be limited by the effects of these accelerations unless their magnitudes are less than 10^{-13} km/s².

The surprising result of this work was that the best ephemeris solutions may be made with explicitly differenced data whether or not the spacecraft is subject to unmodeled accelerations. With the differenced data it should be possible to reduce the uncertainties in the elements DE, DMW, DP, and EDW from their *a priori* values of 0.3×10^{-6} , 0.6×10^{-6} , 0.3×10^{-6} , and 0.3×10^{-6} to 0.2×10^{-6} , 0.4×10^{-6} , 0.2×10^{-6} and 0.07×10^{-6} , respectively.

Although a specific mission to Saturn was considered in this article, the results are probably representative of those for most of the outer planet missions under consideration. Thus, the implementation of a tracking system which provides simultaneous data should significantly increase the precision of the information obtained from outer planet celestial mechanics experiments.

As is the case with all accuracy analysis studies the results shown in the preceding sections are based upon particular error models. Thus, these results are representative of the accuracies actually obtainable only to the extent to which the error model is representative of the true error sources. This study, for example, has not dealt with effects introduced by the gravitational attraction of the spacecraft by either Saturn's rings or by its satellites.

References

1. Moyer, T. D., *Mathematical Formulation of the Double-Precision Orbit Determination Program (DPODP)*, Technical Report 32-1527, pp. 26-29. Jet Propulsion Laboratory, Pasadena, Calif., May 15, 1971.
2. Rourke, K. H., and Ondrasik, V. J., "Improved Navigation Capability Utilizing Two-Station Tracking Techniques for a Low-Declination Distant Spacecraft," in *The Deep Space Network Progress Report*, Technical Report 32-1526, Vol. VII, pp. 51-60. Jet Propulsion Laboratory, Pasadena, Calif., Feb. 15, 1972.
3. Curkendall, D. W., et al., "The Effects of Random Accelerations on Estimation Accuracy With Applications to the Mariner 1969 Relativity Experiment," in *Proceedings of the Conference on Experimental Tests of Gravitation Theory*, California Institute of Technology, Pasadena, Calif., Nov. 1970.

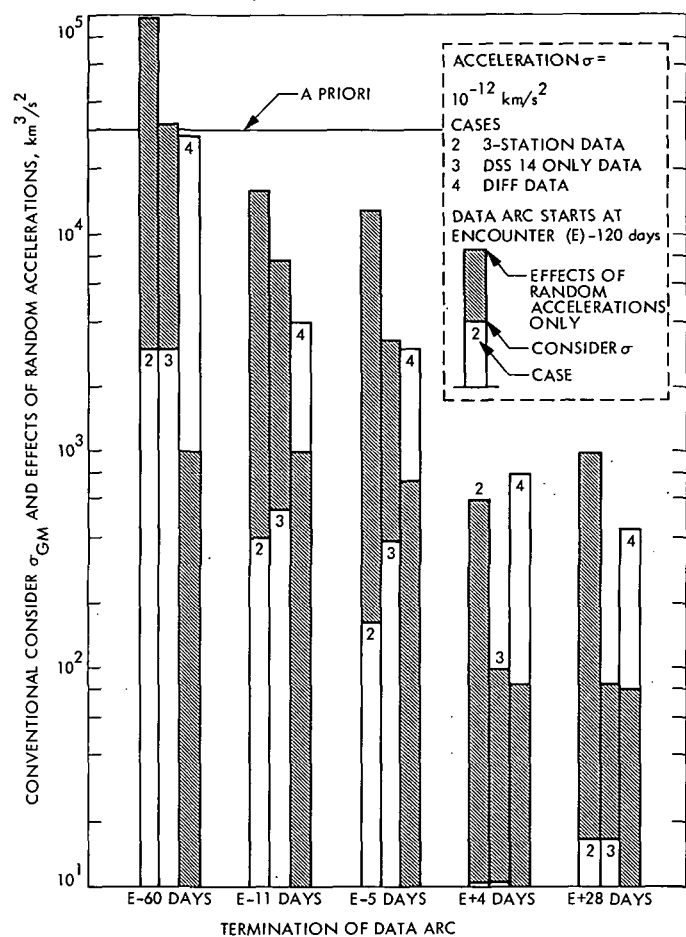


Fig. 1. Effects of data noise, station location errors, and spacecraft accelerations on a GM solution based on a long data arc

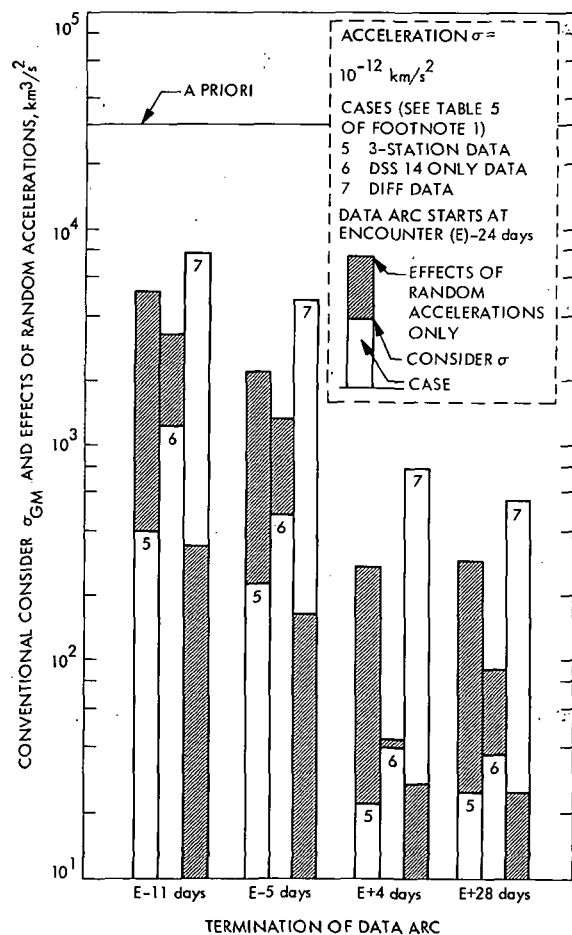


Fig. 2. Effects of data noise, station location errors, and spacecraft accelerations on a GM solution based on a short data arc



DSN Station Clock Synchronization by Maximum Likelihood VLBI

W. J. Hurd

Communications Systems Research Section

The clocks at the DSN ground stations can be accurately synchronized by very long baseline interferometry (VLBI) at lower operational cost than with the existing Moon bounce system. More than an order of magnitude improvement in accuracy can be attained using existing DSN hardware, and ultimate accuracies on the order of 10 nanoseconds are possible. The purpose of the analysis described in this article is to optimize the acquisition and processing of the VLBI data subject to hardware constraints, in order to achieve the best possible time synchronization estimate for a given amount of data, and the most efficient usage of the DSN facilities.

I. Introduction

The clocks at the DSN ground stations can be synchronized by using the station antennas as very long baseline interferometers receiving the random signal from a quasar radio source. Synchronization accuracies more than an order of magnitude better than currently attained by the Moon bounce system are achievable using only existing DSN hardware. A semi-real-time system could be implemented using the TCP 920 computers for data acquisition and the Ground Communications Facility (GCF) to bring the data to a central point for processing. Operational costs should prove to be less than for the existing Moon bounce system.

The fundamental limitations on the time synchronization accuracy achievable by very long baseline interferometry (VLBI) are due primarily to the uncertainties in the station position, the radio point source position, and

the propagation delays in the atmosphere. These limitations are currently on the order of 100 nanoseconds (ns), but are expected to be reduced to less than 10 ns within a few years. Hardware restrictions can, of course, place practical limitations on the accuracies which can be achieved with a given implementation. Use of the XDS 920 computer for data acquisition limits both the sampling rate and the number of samples which can be taken phase coherently, and the GCF data rates restrict the amount of data which can be handled in a reasonable length of time to a few million bits. With these restrictions, synchronization accuracies of 300–500 ns are achievable. This is compatible with the current inherent limitations of about 100 ns.

The pertinent analytical problem considered here is the optimization of the processing of the received signals in order to obtain the best possible estimation of the time of

arrival difference with a given amount of data. The amount of data required for a given accuracy of time sync is thus minimized, which is important for the following reasons:

- (1) The amount of data which must be stored and buffered at the stations and then transmitted to the computation center is reduced. This is important both because of the storage requirements and because of the low data rates of the GCF.
- (2) The number of computations required is proportional to the number of data samples and is thus reduced.
- (3) The observation interval is shortened, which reduces the station time required for data acquisition, and reduces the stability requirements of the local oscillators, which must be phase stable over the observation time. The rubidium frequency standards now in the DSN have adequate stability for the system proposed here, but not for existing systems with much lower sampling rates and less efficient processing.

II. Summary of Results

The primary objective of this work is to optimize the filtering, sampling, and processing of the received radio signals for the estimation of time synchronization. The method of analysis also leads to quasi-optimal estimates of signal strength and fringe rate and phase, conditioned on the sample values, although different sampling strategies might be used if these were the parameters of primary interest. This is accomplished by deriving an approximate maximum likelihood estimator (MLE) for the time of arrival difference and the other parameters under appropriate assumptions as to signal statistics and mechanization limitations. Some of the key results of the analysis and the resulting estimator are:

- (1) The two orthogonal components of the signal from the radio source should both be utilized. This can be accomplished by dual-channel (phase quadrature) processing at both receivers. Dual-channel processing has an inherent 6-dB advantage over single-channel processing, which appears to be the standard means of processing VLBI signals at the present time. The gain is 6 dB per sample, but only 3 dB per bit of data, since there are twice as many bits per sample. The gain arises from utilization of all of the received signal energy and therefore applies to all VLBI processing, not just to time estimation. For time synchronization, an additional

1.2-dB gain can be realized by properly skewing the sampling times in the two channels.

- (2) The MLE results naturally in an optimal method for estimating time synchronization to greater accuracy than the time interval between adjacent samples. This is important because accuracy significantly better than the sampling interval is required. Previous methods for time estimation generally rely on interpolation between the sampling times using the appropriate correlation function.
- (3) The MLE procedure properly accounts for the variation in time difference over the observation time. This is important because the change in the time difference can be greater than the desired synchronization accuracy.

A. Estimator SNR

An approximate MLE is derived under the assumptions that the energy emitted by the radio point source is white and gaussian, that the received signals at the two stations are sampled at the same uniform rate, and that pre-filtering assures that all samples at each ground station are independent of one another. Assuming that the local oscillator phases do not change, the approximate MLE procedure is to square law envelope detect for each possible time difference, using weighting coefficients appropriate for each time difference, and to choose the time difference which maximizes the detector output. If insufficient data can be taken while the phase remains constant, the process is repeated and the detector outputs suitably combined. If the envelope detection is performed using N data samples, and this is repeated L times, then the detector output signal-to-noise ratio (SNR) is of the form

$$R = \frac{L}{2} \frac{r}{1 + \frac{1}{2r}} \quad (1)$$

where

$$r = KK_0\rho^2N \quad (2)$$

In the expression, ρ^2 is the product of the receiver input SNRs and there are NL total sample points at each receiver. The factor K depends on the sampling method and ranges from $1/2$ for real samples (one channel at each receiver) to 0.657 for complex (quadrature phase) samples. The factor K_0 depends on the quantization, and ranges from $(2/\pi)^2$ for hard limiting to 1 for no quantization.

When the number of bits of data which can be taken is the limiting factor, then complex sampling is about

4.2 dB better than real sampling. Also, it appears best to hard limit. If the limiting factor is the sampling rate in bits per second, then hard limiting is certainly optimum, since the estimation error is inversely proportional to the sampling rate. Also, it may be better to use real rather than complex samples if the SNR is sufficiently high, but to use complex samples if the SNR is marginal.

B. Time Estimate Error

An approximate relationship for the mean square error in the time estimate is derived in *Section VIII*. The analysis has been confirmed by simulation. Results indicate that the rms error is slightly less than the time between samples divided by $R^{1/2}$.

C. Example System

A system could currently be implemented in the DSN using one 64-m-diameter antenna and one 26-m-diameter antenna, with noise temperatures of 25 K and 40 K, and using an XDS 920 for data acquisition. The computer limits the sampling rate to 500,000 data bits per second, and the total number of bits which can be acquired while the oscillator phases remain constant to about 300,000. Using hard limiting and complex sampling, the detector output SNR is about $1.2 LS^2$, where S is the radio source intensity in flux units and the computer memory is filled L times. Of the radio stars which are point sources over the baseline from California to Australia, approximately ten are known with intensities of 2 flux units (fu) or greater, and four with intensities of 3 fu or greater. Time sync to significantly better than the 4-microsecond (μs) sampling interval can be achieved with the strongest four sources using only one batch of data, and with many sources using 5-10 batches of data.

III. Problem Formulation and Data Sampling

The radio energy emitted by the radio point source is essentially white and gaussian. However, because we can only observe the energy in the bandwidth of our receivers, we can consider the signal to be a narrow-band gaussian process. The signal plus noise at the outputs of the two receivers can be represented as

$$X(t) = [n(t) + s(t)] \cos(\omega_1 t + \phi_1) + [m(t) + r(t)] \sin(\omega_1 t + \phi_1) \quad (3)$$

and

$$Z(t) = [p(t) + s(t - \delta)] \cos(\omega_2 t + \phi_2) + [q(t) + r(t - \delta)] \sin(\omega_2 t + \phi_2) \quad (4)$$

where

t = time

$\delta = \delta(t)$ = difference in time delay

$\omega_1 - \omega_2$ = difference in doppler shift

ϕ_1, ϕ_2 = random phase angles

$s(t), r(t)$ = noise processes representing signal

$n(t), m(t), p(t), q(t)$ = receiver noise

All of the noise processes are assumed independent and band-limited only by the receivers. The difference frequency $\omega_1 - \omega_2$ and phase $\phi_1 - \phi_2$ are assumed to be constant over the observation time; however, the time delay $\delta(t)$ varies due to the rotation of the Earth. We can assume this to be linear and known, $\delta(t) = \delta_0 + \dot{\delta}t$. The difference frequency and phase are essentially constant only because the change in δ is small compared to the reciprocal of the difference frequency.

Suppose now that we observe $X(t)$ beginning at $t = 0$, and $Z(t)$ beginning at $t = \tau$. This time offset τ is not precisely known, because the clocks at the two stations are not precisely synchronized. We desire to form an estimate $\hat{\tau}$ of τ from the received signals, and to use this estimate to synchronize the clocks.

In order to extract the maximum information from the received signals, both the sine and cosine components of the random processes must be processed. The received signals are thus demodulated to baseband in two channels, using quadrature phase reference signals derived from rubidium frequency standards which we require to be frequency and phase stable over the observation interval. The signals are then filtered and sampled, with the filtering assuring that all samples in each channel are independent of one another. The demodulated and filtered signals, with $*$ denoting convolution, are

$$x(t) = [X(t) \cos(\omega_3 t + \phi_3)] * h_x(t) \quad (5)$$

$$y(t) = [X(t) \sin(\omega_3 t + \phi_3)] * h_y(t) \quad (6)$$

at the X receiver, and

$$z(t) = [Z(t) \cos(\omega_4 t + \phi_4)] * h_z(t) \quad (7)$$

$$w(t) = [Z(t) \sin(\omega_4 t + \phi_4)] * h_w(t) \quad (8)$$

at the Z receiver. We have represented the filtering by convolutions with h_x, h_y, h_z , and h_w , the filter weighting functions.

Since the frequency and phase reference for a narrow-band process can be chosen arbitrarily, we can choose the frequency and phase reference of either X or Z arbitrarily. For convenience, we chose $\omega_1 = \omega_3$ and $\phi_1 = \phi_3$, and we define $\omega = \omega_2 - \omega_4$ and $\phi = \phi_2 - \phi_4$. The difference frequency ω , also called the stopped fringe rate, is determined by the relative doppler between X and Z , as reflected by ω_2 , and by the reference ω_4 . The difference or fringe phase ϕ is random, and uniformly distributed. With this simplification, the observed processes are

$$x(t) = [n(t) + s(t)] * h_x(t) \quad (9)$$

$$y(t) = [m(t) + r(t)] * h_y(t) \quad (10)$$

$$z(t) = \{[p(t) + s(t - \delta)] \cos(\omega t + \phi) + [q(t) + r(t - \delta)] \sin(\omega t + \phi)\} * h_z(t) \quad (11)$$

$$w(t) = \{[q(t) + r(t - \delta)] \cos(\omega t + \phi) - [p(t) + s(t - \delta)] \sin(\omega t + \phi)\} * h_w(t) \quad (12)$$

The four observables are now sampled, all at a uniform and identical rate, with a sampling interval Δ . Independence of the samples in each channel is assured by having the weighting functions be zero outside of the interval $(0, \Delta)$, and by the whiteness of the noise processes. A remaining parameter which can be varied is the relative times of the samples in the sine and cosine channels, so we leave this arbitrary. As references, we assume that the sampling of $x(t)$ begins at $t = 0$, and the sampling of $z(t)$ begins at $t = \tau$, i.e., at the delay we wish to estimate. The samples of y and w occur Δ_1 and Δ_2 after the samples of x and z . Thus, the samples are

$$X_j = x(j\Delta)$$

$$Y_j = y(j\Delta + \Delta_1)$$

$$Z_j = z(j\Delta + \tau)$$

$$W_j = w(j\Delta + \tau + \Delta_2)$$

At this point we make the further assumption that ω is a very low frequency compared to the sampling rate, so that the factors $\cos(\omega t + \phi)$ are constant over Δ and can be brought outside of the convolution integrals. This assumption is reasonable, since ω can be chosen by the experimenter.

We now normalize the observables to unit variance, and define the input SNR to be

$$\rho^2 = \frac{S_x S_z}{(N_x + S_x)(N_z + S_z)} \quad (13)$$

where S_x , S_y , N_x , and N_y are the input signal and noise spectral densities. In practice, ρ will not exceed 10^{-2} . The observable covariances can then be expressed as

$$E\{X_i Z_j\} = A_{ij} = \rho a_{ij} \cos(j\Delta\omega + \phi) \quad (14)$$

$$E\{X_i W_j\} = B_{ij} = -\rho b_{ij} \sin(j\Delta\omega + \phi) \quad (15)$$

$$E\{Y_i Z_j\} = C_{ij} = \rho c_{ij} \sin(j\Delta\omega + \phi) \quad (16)$$

$$E\{Y_i W_j\} = D_{ij} = \rho d_{ij} \cos(j\Delta\omega + \phi) \quad (17)$$

The a_{ij} , b_{ij} , c_{ij} , d_{ij} reflect the dependence on $\tau - \delta(t)$, and are constant for fixed $i - j$ when $\tau - \delta$ is constant. In any case, they vary slowly in $i - j$. Also, the sinusoidal variation in the covariances is slow in j , because $\omega\Delta \ll 1$. Thus, for each $i - j$ there is a range of j for which the covariances are essentially constant.

IV. Derivation of Approximate Maximum Likelihood Estimator

The general procedure of maximum likelihood estimation is to maximize the *a posteriori* probability density function (pdf) of the observables, conditioned on the unknown parameters. The values of the parameters which maximize the pdf for the given set of observables are chosen as the maximum likelihood (ML) estimates. The parameters to be estimated here are ρ , τ , ϕ , and ω . In this section, we derive approximate maximizations of the pdf with respect to ρ and ϕ . The resulting function must then be maximized numerically with respect to τ and ω in order to obtain estimates of all the parameters.

The first step in our problem is to find the joint pdf of the observables X_i , Y_i , Z_i , and W_i , conditioned on the unknown parameters ρ , ϕ , τ , and ω . This pdf depends only on the conditional covariance matrix, since the observables are jointly gaussian and zero mean. Suppose we define a row vector U having as its components all of the observables:

$$U = (X_1, X_2, \dots, X_N, Y_1, Y_2, \dots, Y_N, Z_1, Z_2, \dots, Z_N, W_1, W_2, \dots, W_N) \quad (18)$$

where N is the number of samples of each variable.

Then the covariance matrix of U is

$$\Lambda = \begin{pmatrix} I & 0 & A & B \\ 0 & I & C & D \\ A^t & C^t & I & 0 \\ B^t & D^t & 0 & I \end{pmatrix} \quad (19)$$

where A , B , C , and D are the covariance matrices with elements A_{ij} , B_{ij} , etc., given by Eqs. (14) through (17), and the conditional pdf of the observables is

$$P(U|\rho, \phi, \tau, \omega) = \frac{c}{|\Lambda|^{1/2}} \exp \left\{ -\frac{1}{2} U \Lambda^{-1} U^t \right\} \quad (20)$$

The covariance matrix Λ depends on the parameters ρ , ϕ , τ , and ω , and c is a constant.

The major problem at this point is to invert the covariance matrix. We can do this only in series form, and it is the truncation of this series in the maximization procedure which causes our estimator to be only approximately maximum likelihood.

To proceed we define a matrix P such that

$$\Lambda = I + P \quad (21)$$

The matrix P has at most four nonzero elements in each row and column, because A , B , C , and D have at most two nonzero elements in each row and column. Furthermore, the nonzero elements of P are proportional to ρ and do not exceed ρ in absolute value. Thus we can expand Λ^{-1} in a power series, and bound the terms:

$$\Lambda^{-1} = I - P + P^2 - P^3 + \dots \quad (22)$$

Since the two principal quadrants of P are zero, the principal diagonal elements of P^n are zero for odd n . The other elements are bounded by

$$\begin{aligned} \max_{i,j} |(P^n)_{ij}| &\leq 4\rho \max_{i,j} |(P^{n-1})_{i,j}| \\ &\leq 4^{n-1} \rho^n \end{aligned} \quad (23)$$

where $(P^n)_{ij}$ denotes the ij element of P^n .

Closer bounds can be obtained utilizing properties of the cross covariances for particular cases.

The conditional pdf can now be written as

$$\begin{aligned} P(U|\rho, \phi, \tau, \omega) = \\ c \exp \left\{ -\frac{1}{2} U (I + P)^{-1} U^t - \frac{1}{2} \log \det (I + P) \right\} \end{aligned} \quad (24)$$

Using a well-known matrix identity,

$$\begin{aligned} \log \det (I + P) &\equiv \text{Tr} \log (I + P) \\ &= \text{Tr} \left(P - \frac{P^2}{2} + \frac{P^3}{3} - \frac{P^4}{4} + \dots \right) \end{aligned} \quad (25)$$

The odd power terms can be deleted, since the principal diagonal of P^n is zero for odd n . Thus

$$\log \det (I + P) = -\text{Tr} \left(\frac{P^2}{2} + \frac{P^4}{4} + \dots \right) \quad (26)$$

We now define a likelihood function $L_1(U|\rho, \phi, \tau, \omega)$ as the exponent of the conditional pdf, and maximization of L_1 is equivalent to maximization of the pdf.

$$\begin{aligned} L_1(U|\rho, \phi, \tau, \omega) = &-\frac{1}{2} U (I - P + P^2 - \dots) U^t \\ &+ \frac{1}{2} \text{Tr} \left(\frac{P^2}{2} + \frac{P^4}{4} + \dots \right) \end{aligned} \quad (27)$$

It is not feasible to maximize L_1 analytically with respect to any of the parameters without neglecting terms in P of higher order than P^2 . With this approximation, we can maximize with respect to ρ and ϕ . Since normally τ and ω are the parameters of primary interest, the approximate solutions for ρ and ϕ usually suffice, but greater accuracy can be obtained numerically if required.

To proceed, we define a new matrix Q by

$$Q = \frac{1}{\rho} P = \frac{1}{\rho} \begin{pmatrix} \bigcirc & A & B \\ & C & D \\ A^t & C^t & \bigcirc \\ B^t & D^t & \bigcirc \end{pmatrix} \quad (28)$$

Next we drop the UIU^t term in L_1 , which is independent of the parameters, to obtain

$$L_2(U|\rho, \phi, \tau, \omega) \approx \frac{1}{2} U (\rho Q - \rho^2 Q^2) U^t + \frac{1}{4} \rho^2 \text{Tr} (Q^2) \quad (29)$$

By differentiating with respect to ρ , we see that L_2 is maximized for the conditional estimate of ρ

$$\hat{\rho} = \frac{UQU^t}{2UQ^2U^t - \text{Tr}(Q^2)} \quad (30)$$

The denominator of this expression can be approximated by its mean, which is $\text{Tr}(Q^2)$, so

$$\hat{\rho} \approx \frac{UQU^t}{\text{Tr}(Q^2)} \quad (31)$$

The variance of the denominator of Eq. (30) is also on the order of $\text{Tr}(Q^2)$. Therefore, since $\text{Tr}(Q^2) \approx 4N$, the

approximation is good when N is large, say 10^4 or greater, which will always be true in VLBI problems.

A new likelihood function is now obtained by substituting the value of $\hat{\rho}$ into Eq. (29), and again approximating UQ^2U^t by $\text{Tr}(Q^2)$:

$$L_3(U|\rho, \phi, \tau, \omega) \approx \frac{[UQU^t]^2}{\text{Tr}(Q^2)} \quad (32)$$

Since the elements of Q vary slowly except for the sinusoidal variation, $\text{Tr}(Q^2)$ is essentially independent of Q and ω so long as $N\Delta\omega \gg \pi$. This can be assured by controlling ω by selecting the local oscillator frequencies. Neglecting any slight variation of $\text{Tr}(Q^2)$, L_2 can be maximized over ϕ . To do this, Q is expressed

$$Q = R \cos \phi + S \sin \phi \quad (33)$$

where R and S do not depend on ϕ and are given by

$$R = \begin{pmatrix} \bigcirc & R_0 \\ R_0^t & \bigcirc \end{pmatrix} \quad (34)$$

$$S = \begin{pmatrix} \bigcirc & S_0 \\ S_0^t & \bigcirc \end{pmatrix} \quad (35)$$

where

$$R_0 = \begin{pmatrix} (a_{ij} \cos j\Delta\omega) & -(b_{ij} \sin j\Delta\omega) \\ (c_{ij} \sin j\Delta\omega) & (d_{ij} \cos j\Delta\omega) \end{pmatrix} \quad (36)$$

$$S_0 = \begin{pmatrix} -(a_{ij} \sin j\Delta\omega) & -(b_{ij} \cos j\Delta\omega) \\ (c_{ij} \cos j\Delta\omega) & -(d_{ij} \sin j\Delta\omega) \end{pmatrix} \quad (37)$$

The derivative of the likelihood ratio with respect to ϕ is then

$$\frac{d}{d\phi} L_3 = \frac{2(UQU^t)U(S \cos \phi - R \sin \phi)U^t}{\text{Tr}(Q^2)} \quad (38)$$

and the value of ϕ which maximizes L_3 is

$$\hat{\phi} = \text{Arctan} \frac{USU^t}{URU^t} \quad (39)$$

The new likelihood ratio is the maximum of L_3 ,

$$L(\hat{\rho}, \hat{\phi}, \tau, \omega) = \frac{(URU^t)^2 + (USU^t)^2}{\text{Tr}(Q^2)} \quad (40)$$

This is as far as we can proceed analytically. To find the final approximate ML estimates of all the parameters, L is maximized numerically over τ and ω . When only $\hat{\tau}$ is required, ω is usually known *a priori*, so that the numerical maximization is only over one parameter, τ .

V. Probability Distribution and SNR of the Estimator

The estimation procedure is to compute $L(\hat{\rho}, \hat{\phi}, \omega_j, \tau_i)$ for all possible values of ω_j and τ_i in the regions of uncertainty of ω and τ , and to choose as $\hat{\omega}$ and $\hat{\tau}$ the values of ω_j and τ_i which maximize L . In order that the estimation error be small, it is important that the maximum of L occurs near ω and τ . For example, suppose that ω is known, but the uncertainty in τ is over a range of $M\Delta$, and we compute L for $\tau_i = \tau + i\Delta + \epsilon$, $i = -M/2, -M/2 + 1, \dots, M/2$, where ϵ is small. L is computed for M independent incorrect values of τ_i , and for one value, $\tau + \epsilon$, near the correct value τ . If any of the M values of L for incorrect τ_i exceeds the value for $\tau + \epsilon$, there will be a large error in the estimate. It is important that the probability of this occurring be small, and to estimate this probability we must know the distribution of the estimator.

In the expression for L , Eq. (40), only the components of the random vector U depend on the actual parameters. The matrices R and S and the denominator term $\text{Tr}(Q^2)$ depend only on the filter weighting functions, the sampling times, and the assumed parameter values ω_j and τ_i . The terms URU^t and USU^t are weighted sums of large numbers of random variables. They are therefore approximately gaussian, by the Central Limit Theorem, and, as we show later, their variances are approximately the same. Thus L is approximately the sum of squares of two independent gaussian variables with the same variance, and is therefore approximately Chi-squared distributed with one degree of freedom. Letting v denote $L(\hat{\rho}, \hat{\phi}, \omega_j, \tau_i)$, and $m_r, m_s, \sigma_r^2, \sigma_s^2$ denote the means and variances of URU^t and USU^t , and assuming $\sigma = \sigma_r = \sigma_s$, the density of the estimator conditioned on the actual values ω and τ is approximately

$$p(v|\tau, \omega) \approx \frac{1}{2\Psi} \exp\left\{-\frac{v+a^2}{2\Psi}\right\} I_0\left(\frac{a\sqrt{v}}{\Psi}\right) \quad (41)$$

where

$$\Psi = \frac{\sigma^2}{\text{Tr}(Q^2)} \quad (42)$$

$$a^2 = \frac{m_r^2 + m_s^2}{\text{Tr}(Q^2)} \quad (43)$$

In evaluating the required statistics, we observe that the coefficients a_{ij} , b_{ij} , c_{ij} , and d_{ij} depend on the filter weighting functions and sampling times, as well as on the assumed values of the parameters, ω_j and τ_i . For convenience, we suppress this dependence, and also the dependence on ω_j , since estimation of τ is our primary interest. We explicitly carry the dependence on τ and τ_i , the actual and assumed values of the time difference.

The normalizing factor $\text{Tr}(Q^2)$ is equal to the sum of the squares of the elements of Q . Each weighting coefficient appears twice in Q , so

$$\begin{aligned} \text{Tr}(Q^2) = 2 \sum_{m,n=1}^N [a_{mn}^2(\tau_i) + d_{mn}^2(\tau_i)] \cos^2(n\Delta\omega + \phi) \\ + [b_{mn}^2(\tau_i) + c_{mn}^2(\tau_i)] \sin^2(n\Delta\omega + \phi) \end{aligned} \quad (44)$$

Since the coefficients vary slowly in n for fixed τ_i and fixed $m - n$, the trigonometric terms average out approximately to $1/2$, and

$$\text{Tr}(Q^2) \approx \sum_{m,n=1}^N a_{mn}^2(\tau_i) + b_{mn}^2(\tau_i) + c_{mn}^2(\tau_i) + d_{mn}^2(\tau_i) \quad (45)$$

To evaluate the means and variances, we write the variables in terms of the original observables. First,

$$\begin{aligned} URU^t = 2 \sum_{m,n=1}^N [X_m Z_n a_{mn}(\tau_i) + Y_m W_n d_{mn}(\tau_i)] \cos n\Delta\omega \\ + [-X_m W_n b_{mn}(\tau_i) + Y_m Z_n c_{mn}(\tau_i)] \sin n\Delta\omega \end{aligned} \quad (46)$$

Using the covariances given by Eqs. (14) through (17), the mean of URU^t is

$$\begin{aligned} m_r(\tau_i, \tau) = 2\rho \sum_{m,n=1}^N [a_{mn}(\tau) a_{mn}(\tau_i) + d_{mn}(\tau) d_{mn}(\tau_i)] \\ \times \cos(n\Delta\omega) \cos(n\Delta\omega + \phi) \\ + [b_{mn}(\tau) b_{mn}(\tau_i) + c_{mn}(\tau) c_{mn}(\tau_i)] \\ \times \sin(n\Delta\omega) \sin(n\Delta\omega + \phi) \end{aligned} \quad (47)$$

$$\approx \rho \cos \phi F(\tau_i, \tau) \quad (48)$$

where

$$\begin{aligned} F(\tau_i, \tau) = \sum_{m,n} a_{mn}(\tau) a_{mn}(\tau_i) + b_{mn}(\tau) b_{mn}(\tau_i) \\ + c_{mn}(\tau) c_{mn}(\tau_i) + d_{mn}(\tau) d_{mn}(\tau_i) \end{aligned} \quad (49)$$

A similar result holds for m_s with $\cos \phi$ replaced by $\sin \phi$, and

$$m_r^2 + m_s^2 \approx \rho^2 F^2(\tau_i, \tau) \quad (50)$$

Since

$$\text{Tr}(Q^2) = F(\tau_i, \tau_i) \quad (51)$$

we observe that when the assumed value τ_i is equal to the correct value, τ ,

$$m_r^2 + m_s^2 = \rho^2 \text{Tr}^2(Q^2) \quad (52)$$

and is zero when $\rho = 0$ or when τ_i is so far from τ that $a_{mn}(\tau) a_{mn}(\tau_i) = 0$, etc. The product random variables $X_m Z_n$, $Y_m W_n$, $X_m W_n$ and $Y_m Z_n$ are all independent, and their variances are essentially unity since $\rho^2 < 1$. Thus the variances of weighted sums of these variables are just the sums of the squares of the weighting coefficients, so

$$\begin{aligned} \sigma_r^2 = \sigma_s^2 = \sigma^2 \\ \approx 4 \cdot \frac{1}{2} F(\tau_i, \tau_i) \\ \approx 2 \text{Tr}(Q^2) \end{aligned} \quad (53)$$

The factor of four arises because each term in the summation occurs twice, and the factor of one-half arises from the trigonometric factors.

Finally,

$$\Psi = \frac{\sigma^2}{\text{Tr}(Q^2)} \quad (54)$$

and

$$a^2 = \begin{cases} 0, & \text{for } |\tau_i - \tau| > \Delta \\ \rho^2 \text{Tr}^2(Q^2), & \text{for } \tau_i = \tau \end{cases} \quad (55)$$

A. Estimator SNR

A convenient figure of merit is the signal-to-noise ratio of the estimator function, which we define to be the ratio of the squared difference in the means of L (or v) for $\tau_i = \tau$ and for $|\tau_i - \tau| > \Delta$, to the variance. The mean and variance are

$$E\{L\} = 4 + a^2 \quad (56)$$

and

$$\text{Var}\{L\} = 16 + 8a^2 \quad (57)$$

so the SNR is

$$R = \frac{r^2}{1 + 2r} = \frac{1}{2} \frac{r}{1 + \frac{1}{2r}} \quad (58)$$

where

$$r = \frac{\rho^2}{4} \text{Tr}(Q^2) = \frac{a^2}{4} \quad (59)$$

Clearly the distribution of L depends only on the SNR.

B. SNR Required for Small Estimator Errors

Suppose instead of calculating $L(\tau_i)$ for all possible τ_i and choosing the maximum, $L(\tau_i)$ is calculated for various values until a threshold, say T , is exceeded. Then the error in τ will be small if $L(\tau + \epsilon)$ exceeds T for $|\epsilon| < \Delta$, but no other $L(\tau_i)$ calculated exceeds T . The probability that this occurs can be calculated from the distributions of L for the correct and incorrect values of τ_i . Figure 1 shows the probability that $L(\tau)$ fails to exceed various thresholds, T , as a function of the SNR. For example, if the SNR is 12, a threshold of 32 will be exceeded by $L(\tau)$ with probability about $1 - 10^{-3}$. For $|\tau_i - \tau| > \Delta$ or for $\rho = 0$, the density of L is exponential with mean 4, so the probability that T is exceeded is

$$P(L > T | \rho = 0) = \exp\{-T/4\} \quad (60)$$

For $T = 32$, this probability is 0.33×10^{-3} , and it is fairly likely that T will be exceeded on noise alone if L is calculated for too many incorrect values of τ_i before it is calculated for a τ_i close to τ . Clearly there is a tradeoff between SNR, threshold value, and the initial uncertainty in τ . A SNR of 10 to 20 should prove adequate when the initial uncertainty is not too large.

VI. Effect of Quantization or Limiting of Samples

We have shown that maximization of L results in approximately ML estimation when the original data samples X_j , Y_j , Z_j and W_j are gaussian. This is no longer true if the samples are quantized, but the same estimator function can certainly still be used. The only effect is to decrease the estimator SNR and increase the error by decreasing the correlation coefficients. For hard limiting, the effect is to replace ρ by $(2/\pi)\rho$ throughout, which causes a loss of approximately $(2/\pi)^2$ or 4 dB in R . The reason that ρ is replaced by $(2/\pi)\rho$ is that the means of the cross products of the data samples are so reduced. This can be shown by considering two normal variables,

say x and y , with correlation ρ , and showing that for $\rho < 1$, the expected value of $\text{sgn}(xy)$ is approximately $(2/\pi)\rho$.

VII. Selection of Sampling Times and Filter Weighting Functions

The problem of choosing an optimum set of sampling times and filter weighting functions is considerably more complex than that of deriving the approximate ML estimator as a function of these variables. In particular, what we really wish to optimize is some cost function of the error in the estimate of τ —but we have already admitted failure in this respect by limiting our choice to the MLE. However, given our choice of estimator, the parameter R is clearly a significant figure of merit, as it is closely related to the probability that the estimation error is no worse than one sampling interval.

Because we cannot truly optimize, we will make some reasonable assumptions which are compatible with practical implementation, and show that we can do quite well. In particular, R depends on the actual value of $\tau - \delta$, so we must be concerned with the minimum of R over $\tau - \delta$. We will obtain a minimum which is almost as large as possible.

The estimator SNR increases with the input SNR and $\text{Tr}(Q^2)$, which in turn depends on the number of samples, on $\tau - \delta(t)$, and on the sampling and filtering. Since $\text{Tr}(Q^2)$ is roughly proportional to N , we define K such that

$$K = \frac{\text{Tr}(Q^2)}{4N} = \frac{1}{4N} \sum_m \sum_n a_{mn}^2 + b_{mn}^2 + c_{mn}^2 + d_{mn}^2 \quad (61)$$

The functions a , b , c , and d depend on $\tau - \delta(t)$. However, since they are constant for fixed $m - n$ when $\tau - \delta$ is constant, the minimum over τ of K is clearly smallest when δ is constant. Then, since the coefficients are nonzero only for $|m - n| < N$

$$K(\tau, \delta) \approx \frac{1}{4} \sum_{m-n} a_{mn}^2 + b_{mn}^2 + c_{mn}^2 + d_{mn}^2 \quad (62)$$

We must now consider the effect of the sampling and filtering on a , b , c , and d .

From here on, we restrict ourselves to using identical filters in the four channels:

$$h(t) = h_x(t) = h_y(t) = h_z(t) = h_w(t) \quad (63)$$

The justification for this restriction is that this is the only way that any cross correlation can be as high as ρ^2 , and it

assures that this occurs whenever the signal components in the two receivers are in the same phase relationship to the sampling times.

The functions a , b , c , and d then become identical except for the effect of the sample point skewing, reflected by Δ_1 and Δ_2 . Furthermore, the shape of the function is the same as the correlation function at the output of the filter; i.e.,

$$r(\beta) = \int_{-\infty}^{\infty} h(\alpha) h(\beta - \alpha) d\alpha \quad (64)$$

and, letting $k = m - n$,

$$\left. \begin{aligned} a_{mn}(\tau - \delta) &= r(\tau - \delta - k\Delta) \\ b_{mn}(\tau - \delta) &= r(\tau - \delta + \Delta_2 - k\Delta) \\ c_{mn}(\tau - \delta) &= r(\tau - \delta - \Delta_1 - k\Delta) \\ d_{mn}(\tau - \delta) &= r(\tau - \delta + \Delta_2 - \Delta_1 - k\Delta) \end{aligned} \right\} \quad (65)$$

Because $h(\alpha)$ is nonzero only for $0 \leq \alpha < \Delta$, $r(\tau)$ is nonzero only for $|\tau| < 2\Delta$. This means that a_{mn} , b_{mn} , c_{mn} , and d_{mn} are nonzero for at most two values of $k = m - n$. We now define

$$A(\beta) = \sum_k r^2(\beta - k\Delta) \quad (66)$$

Because of the symmetry of $r(\beta)$, this function depends only on the minimum distance of β from an integer multiple of Δ .

For a given filter, K depends only on $\tau - \delta$, Δ_1 , and Δ_2 as

$$\begin{aligned} K(\tau - \delta, \Delta_1, \Delta_2) &= \frac{1}{4} [A(\tau - \delta) + A(\tau - \delta + \Delta_2) \\ &\quad + A(\tau - \delta - \Delta_1) \\ &\quad + A(\tau - \delta + \Delta_2 - \Delta_1)] \end{aligned} \quad (67)$$

We are interested in maximizing the minimum value of K with respect to $\tau - \delta$ by selection Δ_1 and Δ_2 . If the samples are not skewed, i.e., $\Delta_1 = \Delta_2 = 0$, the minimum of K is the minimum of A , which is the worst we can do. The best we can do is the average of A , and the closest we can come to this average is to pick different nonzero values of Δ_1 and Δ_2 .

Garsia, Rodemich, and Rumsey (Ref. 1) have shown that for all normalized correlation functions $c(t)$ which

are zero outside of the interval $(-1, 1)$,

$$\int_{-1}^1 c^2(t) dt \leq 0.68698 \dots \quad (68)$$

This bound is exactly the upper bound on the average of $A(\beta)$.

We can now show that the moving window filter,

$$\begin{aligned} h(t) &= \frac{1}{\Delta}, & \text{for } 0 \leq t \leq \Delta \\ &= 0, & \text{otherwise} \end{aligned} \quad (69)$$

is almost optimum. For this filter, the average of A is $\frac{2}{3}$ —very close to the upper bound. We achieve a minimum K of $\frac{2}{3}$ by choosing $\Delta_1 = \Delta/2$ and $\Delta_2 = \Delta/4$, and a minimum of $\frac{5}{8}$ for $\Delta_1 = \Delta_2 = \Delta/2$, or $\Delta_1 = \Delta/2$, $\Delta_2 = 0$. The loss relative to the upper bound is only 0.2 dB in the first case, and 0.4 dB in the second case.

We define the best minimum value of K to be K_c :

$$K_c = \frac{21}{32} \approx 0.657 \quad (70)$$

If no skewing is used, the minimum of K is $\frac{1}{2}$; skewing improves the SNR by 1.0 to 1.2 dB.

A. Real Versus Complex Sampling

By real rather than complex sampling, we mean using only the sine or cosine components at the receivers. For example, we use only the X_j and Z_j , rather than X_j , Y_j , Z_j , and W_j . This may be desirable when memory size or access time is the limiting factor in implementation.

Using only the X_j and Z_j is equivalent to letting the weighting functions in the Y and W channels be zero. Then b_{mn} , c_{mn} , and d_{mn} are all zero, and

$$K = \frac{1}{4N} \sum_{m,n} a_{mn}^2 \quad (71)$$

The worst case is again when δ is constant, and now sample time skewing cannot be used to average K over $\tau - \delta$. The minimum value of K over $\tau - \delta$, which we denote by K_r , is

$$K_r = \frac{1}{8} \quad (72)$$

Since R is proportional to K , the loss for real sampling compared to complex sampling is

$$\frac{K_r}{K_c} = \frac{0.125}{0.657} = 0.19 \quad (73)$$

or approximately 7.2 dB.

If the fundamental limitation is memory size, then the loss is 3 dB less than this, or 4.2 dB, since twice as many real as complex samples can be taken.

If the sampling rate is limited by the memory speed rather than by the receiver bandwidth, we must realize that the sampling rate can be twice as high with real sampling rather than complex. Real sampling has a distinct advantage here, because for a fixed estimator SNR, the error in time estimation is inversely proportional to sampling rate. Real sampling might be better in spite of the 4.2-dB loss in SNR, provided that the SNR is high enough so that τ is almost certainly resolved to better than one sampling interval.

B. Final Estimator SNR

Considering the effects of quantization, filtering, and sampling, the minimum SNR which can be guaranteed is

$$R_{\min} = \frac{1}{2} \frac{r}{1 + \frac{1}{2r}} \quad (74)$$

where

$$r = K_0 K_p^2 N \quad (75)$$

The factor K_0 is due to quantization, and varies from $(2/\pi)^2$ for hard limiting to 1 for no quantization. The factor K depends on the sampling method. If real rather than complex sampling is used, then

$$K = K_r = \frac{1}{8} \quad (76)$$

For complex sampling with proper skewing,

$$K = K_c = \frac{21}{32} = 0.657 \quad (77)$$

VIII. Mean Square Error of Time Estimate

In this section we derive an approximation to the mean square error in estimation of τ using a method similar to that used by Helstrom (Ref. 2) for ML estimation of the time of arrival of radar signals. Since the method is valid

only when the estimator SNR is sufficiently high, a simulation of the received signals and the processing is conducted to test the validity of the approximations at fairly low SNRs. The simulation confirms the analysis, with the mean square errors being slightly greater than calculated, as would be expected considering the approximations used.

A. Calculation of Mean Square (MS) Error

The first step is to write L in terms of signal and noise components. We explicitly carry the dependence on τ and on the assumed value τ_i only when deleting this dependence might be confusing. Let

$$URU^t = r(\tau_i, \tau) + m_r(\tau_i) \quad (78)$$

$$USU^t = s(\tau_i, \tau) + m_s(\tau_i) \quad (79)$$

where, as before, m_r and m_s are the means of URU^t and USU^t , and r and s are the noise portions. Any slight dependence of r and s on τ is neglected. Then

$$L(\tau_i, \tau) = \frac{m_r^2 + m_s^2}{\text{Tr}(Q^2)} + \frac{2(rm_r + sm_s)}{\text{Tr}(Q^2)} + \frac{r^2 + s^2}{\text{Tr}(Q^2)} \quad (80)$$

When R is sufficiently high, the quadratic noise terms become insignificant, and L can be approximated by

$$L(\tau_i) \approx L_0(\tau_i, \tau) + M(\tau_i, \tau) \quad (81)$$

where

$$L_0(\tau_i, \tau) = \frac{m_r^2 + m_s^2}{\text{Tr}(Q^2)} = \rho^2 \frac{[F(\tau_i, \tau)]^2}{\text{Tr}(Q^2)} \quad (82)$$

and

$$M(\tau_i, \tau) = \frac{2(rm_r + sm_s)}{\text{Tr}(Q^2)} \quad (83)$$

Since the estimate $\hat{\tau}$ of τ is the value of τ_i which maximizes L , the derivative of L with respect to τ_i is zero at $\tau_i = \hat{\tau}$; i.e.,

$$0 = L'(\tau_i, \tau) \Big|_{\tau_i = \hat{\tau}} \approx L'_0(\tau_i, \tau) + M'(\tau_i, \tau) \Big|_{\tau_i = \hat{\tau}} \quad (84)$$

where primes denote differentiation with respect to τ_i . We now expand the L'_0 term in a Taylor series about $\tau_i = \tau$, and retain only the first order term:

$$L'_0(\tau_i, \tau) + (\hat{\tau} - \tau)L''_0(\tau_i, \tau) + M'(\tau_i, \tau) \Big|_{\tau_i = \tau} \approx 0 \quad (85)$$

Since the signal only term L_0 is maximized at $\tau_i = \tau$, its derivative there is zero, and

$$\tau - \hat{\tau} \approx \frac{M'(\tau_i, \tau) \big|_{\tau_i = \tau}}{L''(\tau_i, \tau) \big|_{\tau_i = \tau}} = \frac{M'(\tau, \tau)}{L''_0(\tau, \tau)} \quad (86)$$

Finally, since L_0 does not depend on noise, the mean square error in the estimate of τ is

$$E\{(\tau - \hat{\tau})^2\} = \frac{E\{[M'(\tau, \tau)]^2\}}{[L''_0(\tau, \tau)]^2} \quad (87)$$

The terms $E\{M'^2\}$ and L''_0 can be evaluated for specific coefficient functions, with these functions being determined from Eqs. (64) and (69). The coefficients for the optimum skewing, $\Delta_1 = \Delta/2$ and $\Delta_2 = \Delta/4$, and normalizing to $\delta = 0$ and $\Delta = 1$, are shown in Fig. 2.

For these parameters

$$L''_0 \bigg|_{\tau_i = \tau} = \frac{\rho^2}{4} \left[\frac{2[F'(\tau, \tau)]^2 - 16N \text{Tr}(Q^2)}{\text{Tr}(Q^2)} \right] \quad (88)$$

and

$$\begin{aligned} E\{[M'(\tau, \tau)]^2\} &= \frac{\rho^2}{4 \text{Tr}(Q^2)} (16N \text{Tr}(Q^2) - 2[F'(\tau, \tau)]^2) \\ &= \frac{\rho^2}{4 \text{Tr}(Q^2)} (42N^2) \end{aligned} \quad (89)$$

Finally, the mean square error is

$$\begin{aligned} \epsilon^2(\tau) &= E\{(\hat{\tau} - \tau)^2\} = \frac{4}{\rho^2} \frac{\text{Tr}(Q^2)}{42N^2} \\ &= \frac{4}{\rho^2 N} \frac{8\tau^2 - 2\tau + \frac{11}{4}}{42} \quad (90) \\ &\quad (\tau \text{ taken modulo } \frac{1}{4}) \end{aligned}$$

Averaging over τ , the mean square (MS) error is

$$\epsilon_{\text{ave}}^2 = \frac{16}{63\rho^2 N} \quad (\text{no limiting}) \quad (91)$$

This MS error is of course increased by a factor of $(\pi/2)^2$ when hard limiting is used, to

$$\epsilon_{\text{ave}}^2 = \frac{4\pi^2}{63\rho^2 N} = \frac{0.626}{\rho^2 N} \quad (\text{hard limiting}) \quad (92)$$

B. Comparison of R and MS Error

It is interesting that for high SNRs, both $R(\tau)$ and $\epsilon^2(\tau)$ vary with τ in direct proportion to $\text{Tr}(Q^2)$. This is not what one would intuitively expect, since one would expect the MS error to be inversely proportional to R . The explanation for this is that for high SNRs, the variation of ϵ^2 with τ depends on the second derivative of the mean of the estimator function, which introduces the particular dependence on $\text{Tr}(Q^2)$. In any case, the effect is very minor, since $\text{Tr}(Q^2)$ varies only plus 3 percent and minus 1.5 percent about its average value.

C. Simulation Results

A simulation was conducted for two different SNRs and two values of τ , with the resulting rms errors compared to the calculated values in Table 1. The rms errors are the average of 160 cases for each set of parameters, using $N = 19840$.

The rms errors obtained in the simulation were typically about ten percent higher than the calculated values. This is because the calculated values are not accurate at the relatively low SNRs used, primarily because typical errors in $\hat{\tau}$ are large enough that truncation of the power series for L_0 causes significant error. There is also an error in the MS error of approximately $1/(4R)$ percent due to neglecting the quadratic noise terms. In Table 1, the observed errors are higher for $\tau = 0.125$ than for $\tau = 0$, whereas the calculated errors are higher for $\tau = 0$. We again feel that the calculated values are in error at the SNRs in the simulation, because of the series approximation. Unfortunately, it was not practical to conduct further simulations at higher SNRs, because of computer time limitations. Higher SNRs require more computer time, as N must be increased rather than ρ , for increasing ρ would render the assumed degradation of $(\pi/2)^2$ due to hard limiting to be in error.

IX. Performance of Proposed System

The system proposed for DSN time synchronization is performance limited by the antenna sizes and receiver noise temperatures and by the restriction of using an XDS 920 computer at each site for data buffering. The 920 computers limit the sampling rate to 500 kbps, and the total number of bits of data to 300,000. The antennas assumed are one of 64 m (210 ft), with a noise temperature of 25 K, and one of 26 m (85 ft), with a noise temperature of 40 K.

A radio star with a flux density of 1 fu causes an increase in system temperature of 0.6 K and 0.1 K for 64 m

and 26 m antennas, respectively. Therefore, letting S be the source intensity, the input SNR is approximately

$$\rho^2 = \frac{0.06 S^2}{40 \times 25} = 6 \times 10^{-5} S^2 \quad (93)$$

and, for complex sampling,

$$\rho^2 N \approx 9 S^2 \quad (94)$$

For a system using complex sampling and hard limiting,

$$\begin{aligned} r &= KK_q \rho^2 N \\ &= (0.657) \left(\frac{2}{\pi} \right)^2 \rho^2 N \\ &= 2.4 S^2 \end{aligned} \quad (95)$$

The minimum output SNR is

$$\begin{aligned} R_{\min} &= \frac{1}{2} \frac{r}{1 + \frac{1}{2r}} \\ &\approx \frac{r}{2} = 1.2 S^2 \end{aligned} \quad (96)$$

If real samples are used, N doubles but K drops to $1/2$, and

$$r \approx 0.91 S^2 \quad (97)$$

$$R \approx 0.45 S^2 \quad (98)$$

A. Post Detection Integration

The final SNR can be improved by filling the memory in the computer at each station several times, writing out onto magnetic tape between fills. Since it would take several seconds to dump the core onto tape, the local oscillator phase may change between batches of data. Nevertheless, the SNR can be increased in direct proportion to the number of batches of data. If L batches of data are used, the final SNR is

$$\frac{L}{2} \frac{r}{1 + \frac{1}{2r}} \quad (99)$$

where r is as before. With ten batches of data and complex sampling, a SNR of 10 could be obtained from a 1-fu source, and an SNR of over 40 from a 2-fu source.

References

1. Garsia, A., Rodemich, E., and Rumsey, H., "On Some Extremal Positive Definite Functions," *J. Mathematics Mechanics*, Vol. 18, No. 9, pp. 805-834, Mar. 1969.
2. Helstrom, C. W., *Statistical Theory of Signal Detection*, Chapter VIII. Pergamon Press, New York, 1960.

Table 1. Simulation results

ρ^2K	τ	$R(\tau)$	RMS estimation error	
			Simulation	Calculated
71.42	0	9.53	0.104	0.0950
71.42	0.125	9.10	0.114	0.0927
71.42	Average	9.25	0.109	0.0935
285.7	0	38.8	0.0512	0.0475
285.7	0.125	37.1	0.0555	0.0464
285.7	Average	37.7	0.0534	0.0418

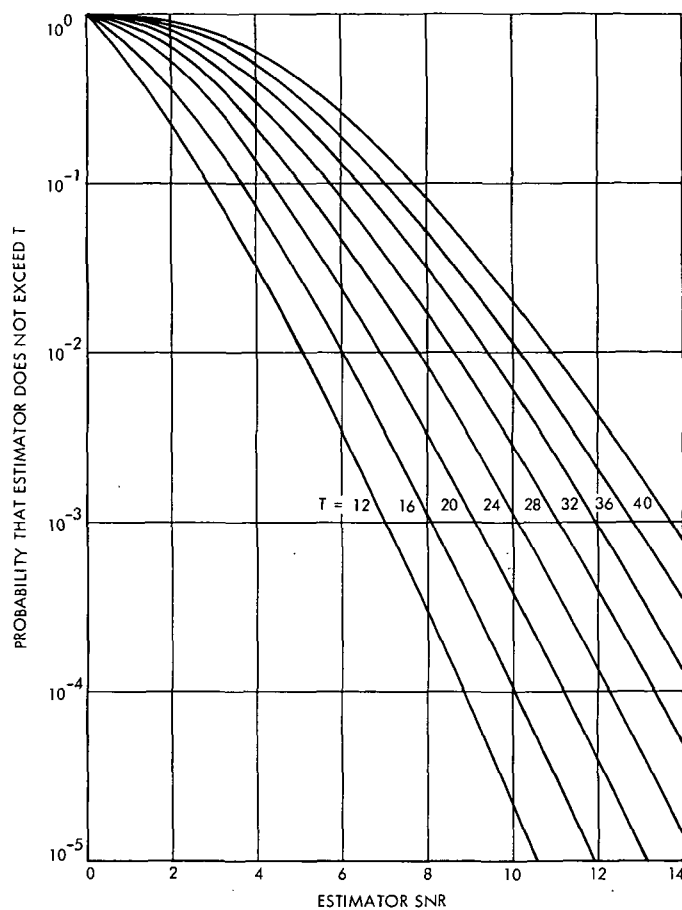


Fig. 1. Probability that estimator does not exceed threshold for correct value of τ_i

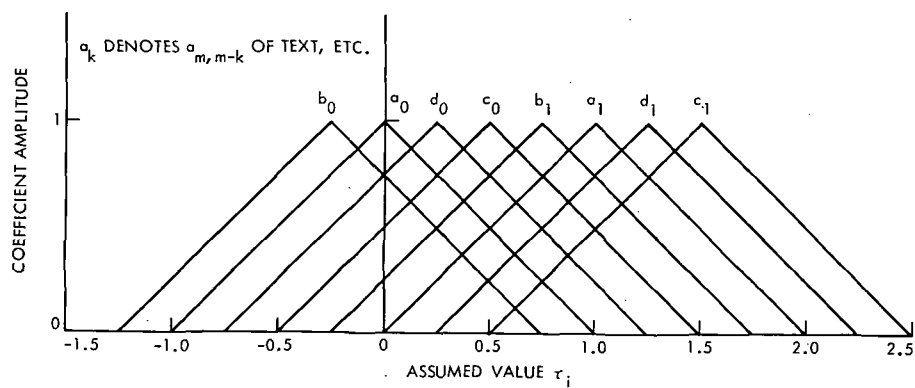


Fig. 2. Weighting coefficients for optimum sampling

Frame Synchronization in Time-Multiplexed PCM Telemetry With Variable Frame Length

U. Timor

Communications Systems Research Section

New methods of parallel and serial synchronization for time-multiplexed phase-coherent telemetry signals are presented. In the parallel case, i.e., when the sync code is transmitted on a separate channel, M synchronization codes are generated by concatenating a common pseudonoise (PN)-like sequence of short length with words from a self-synchronizing code. The frame synchronizer can lock on any of the M codes, which is particularly useful when frames of different lengths have to be transmitted. In the serial case, that is, when each frame starts with an identical sync code, false sync due to replicas of the code randomly generated by the data is completely eliminated by transferring the sync code to the quadrature channel, while the data are transmitted on the in-phase channel.

I. Introduction

In time-multiplexed pulse-code-modulated (PCM) telemetry, binary data signals from several sources are grouped into frames, which have to be identified at the receiver in order to demultiplex the data. Frame synchronization is obtained by inserting in series (e.g., at the beginning of each frame), or in parallel (i.e., on a separate sync channel), a frame sync code (FSC). At the receiver, the frame synchronizer correlates the received signal with its own replica of the FSC, for different bit shifts, until synchronization is acquired. The synchronization is then maintained by verifying the repetition of this code at each frame, provided the frame length is fixed.

In some future cases, such as would occur in the adaptive telemetry era in the late 1970s and beyond, data rates

and the number of data sources are not fixed, and it is advantageous to change the frame length and data format. In this case, at any instant of time, one of M possible frames is transmitted, and the receiver has to detect which frame is being sent while acquiring synchronization. However, standard methods of serial and parallel synchronization are inefficient for this task. In parallel synchronization, the FSC is usually a PN sequence (or a combination of several PN sequences) of total length equal to the frame length, and thus frames of different lengths have different PN sequences associated with them. The frame synchronizer correlates the received FSC with the various synchronization codes to determine which one is being transmitted, resulting in an increased complexity and degraded performance. In serial synchronization, the main problem is that of false sync due to replicas or "almost replicas" of the FSC, generated by the random

data. The probability of false sync can be reduced by verifying the occurrence of the FSC on successive frames, but only if the frame length is known.

We will present new methods for parallel and serial synchronization, which avoid the described problems, and which can be used in multiframe systems. In the parallel synchronization case, a common PN-like sequence of short length (typically, two orders of magnitude smaller than the frame length) is used for all frames, and the FSC is generated by concatenating this sequence with words from a self-synchronizable code. In the serial case, the false sync due to random data is completely eliminated by transmitting the FSC, serially, on the quadrature channel, while the data are sent on the in-phase channel. For both methods, the acquisition time is considerably reduced.

II. Parallel Synchronization

In parallel synchronization, the time-multiplexed data and the FSC are frequency multiplexed, that is, both data and sync are transmitted simultaneously on different subcarriers. Since the power allocated to the sync is always small compared to the data power, the loss due to cross-modulation between the sync and the data is negligible. For example, if the power allocated to the sync channel is 5% of the data power, and 5% of the total power is transmitted as RF reference, the crossmodulation loss, using interplex (Ref. 1), is only 0.25%.

If the frame length N is fixed, the synchronization code can be a PN sequence of length N , which has an in-phase correlation of N and all out-of-phase periodic correlations of -1 . The frame synchronizer correlates the incoming code with its own replica, for various bit shifts, and acquires synchronization using maximum-likelihood or threshold decision rules. If there are M possible frames, each with its own PN sequence, the frame synchronizer has to correlate the incoming code with all PN sequences to find the one which can be synchronized. This slows the acquisition and increases the complexity of the receiver.

In the next section we will describe a two-step multi-frame synchronization method, where at the first step partial synchronization is obtained, no matter which frame is sent, while at the second step a self-synchronized decoder determines the frame and completes the synchronization. The only constraint on the frame lengths is that all of them are divisible by a common integer K , typically 2 orders of magnitude smaller than the frame lengths.

III. Parallel Synchronization for Several Frame Lengths

Let F_1, \dots, F_M be M different frame formats having lengths N_i , respectively, where

$$N_i = m_i K, \quad i = 1, \dots, M \quad (1)$$

and $\min(m_i) \gg 1$.

Typically, K is of the order of 15–25 and $N_i > 1000$, so that condition (1) is not a severe restriction on the N_i 's.

Let $D = \{d_i\}$ be a self-synchronizable binary code dictionary of size M and word lengths $W_i = m_i$, $i = 1, \dots, M$, i.e., $d_i = \{d_{i1}, \dots, d_{im_i}\}$ and $d_{ij} = \pm 1$.

Finally, let C be a binary sequence of length K , to be chosen later. The frame synchronization code S_i for F_i is the concatenation of d_i and C , that is,

$$S_i = d_{i1}C, d_{i2}C, \dots, d_{im_i}C \quad (2)$$

Clearly, S_i is a binary sequence of length $N_i = Km_i$, composed of m_i successive $\pm C$.

The acquisition is performed in two steps:

(1) Step I: C-synchronization

Let C be chosen such that the absolute values of all $2(K-1)$ out-of-phase correlations of C with (C, C) and $(C, -C)$ (Fig. 1) are small compared to K , which is the inphase autocorrelation of C .

PN sequences yield small out-of-phase correlations for the (C, C) case, but not necessarily for the $(C, -C)$ one. Let $r(\ell)$ be the partial correlation of C when shifted ℓ bits to the right (Fig. 2).

The out-of-phase correlations of C with (C, C) and $(C, -C)$ are, respectively,

$$\left. \begin{aligned} R_+(\ell) &= r(\ell) + r(-\ell) \\ R_-(\ell) &= r(\ell) - r(-\ell) \end{aligned} \right\} \quad \ell = 1, \dots, K-1 \quad (3)$$

and their maximum absolute value is

$$R \triangleq \max_{1 \leq \ell \leq K-1} \{ |R_+(\ell)|, |R_-(\ell)| \} \quad (4)$$

Given K , we want to find sequences C which yield the smallest possible R . A necessary condition for a sequence

C to have a small R is that

$$\hat{R} \triangleq \max_{-(K-1) \leq l \leq K-1} |r(l)| \quad (5)$$

is small, so the search can be narrowed to sequences which have small \hat{R} .

Case 1: $\hat{R} = 1$

These are Barker sequences (Ref. 2), which exist for $K = 3, 5, 7, 11$, and 13 . All of them yield $R = 1$.

Case 2: $\hat{R} = 2$

Such sequences have been found for all lengths $K \leq 21$ and $K = 25$ and 28 (Ref. 3) yielding the following R 's:

$$R = 2, \quad \text{for } K = 14 \text{ and } 18$$

$$R = 3, \quad \text{for } K = 15, 17, 19, 21, \text{ and } 25$$

$$R = 4, \quad \text{for } K = 16, 20, \text{ and } 28$$

Case 3: $\hat{R} = 3$

Such sequences are known for all lengths $K \leq 34$ (Ref. 3) and yield the following R 's:

$$R = 4, \quad \text{for } K = 24 \text{ and } 26$$

$$R = 5, \quad \text{for } K = 23, 27, 29, 31, \text{ and } 33$$

$$R = 6, \quad \text{for } K = 22, 30, 32, \text{ and } 34$$

The sequences are listed in the Appendix.

To acquire C -correlation, the frame synchronizer correlates the incoming code S_i with C , for all K possible bit shifts, to find the maximum correlation. The performance can be improved by correlating L C -sequences, for each bit shift, and adding their absolute values.

(2) Step II: Frame Synchronization

Once C -synchronization is obtained, S_i is demodulated by C to yield the binary sequence

$$\cdots d_{im_i}, d_{i1}, \cdots, d_{im_i}, d_{i1}, \cdots, d_{im_i}, d_{i1}, \cdots$$

which is composed of the codeword d_i , repeated for each frame. By decoding this bit stream d_i can be found, yielding frame synchronization as well as frame length

and data format. As mentioned before, D is a self-synchronizable code; for example, a prefix code (all words start with the same prefix). The d_i -bit signal-to-noise ratio (SNR) is K times the S_i -bit SNR, and thus is of the same order of magnitude as the data-bit SNR. Also, the word length (typically 50–100) is comparable to the size (M) of the dictionary. Therefore, the redundancy of the code is very large, and both prefix and suffix can be chosen to correct several bit errors and assure an almost error-free synchronization.

IV. Serial Frame Synchronization on the Quadrature Channel

In serial frame synchronization a portion of each frame (e.g., the first K bits of the frame) consists of a code sequence, repeated at each frame. It is well known (Ref. 2) that a false synchronization can occur, even without noise, due to a replica of the code sequence, generated by the data. We will present a method which eliminates this possibility, by transferring the serial code to the quadrature channel. That is, during the data period all the energy is transmitted on the in-phase channel, while during the sync period of the frame, all the energy is transferred to the quadrature channel.

Let $S(t)$ be a binary time-multiplexed signal, partitioned into frames of duration T , where each frame starts with an identical sync code $\hat{S}_s(t)$, $t \in [0, T_s]$. Thus,

$$S(t) = \begin{cases} S_s(t), & t \in [0, T_s] + nT \\ S_d(t), & \text{elsewhere} \end{cases} \quad (6)$$

where

$$S_s(t) = \hat{S}_s(t) + \hat{S}_s(t - T) + \hat{S}_s(t - 2T) + \cdots \quad (7)$$

is a periodic repetition of $\hat{S}_s(t)$ with period T , and $S_d(t)$ is the data signal.

If $C(t)$ is the indicator function of $[0, T_s] + nT$, then

$$S_s(t) = S(t) C(t)$$

and

$$S_d(t) = S(t) (1 - C(t)) \triangleq S(t) \bar{C}(t)$$

Consider the phase modulated signal

$$y(t) = \sin[\omega t + \theta(t)] \quad (9)$$

where ω is the carrier frequency,

$$\theta(t) = \theta S(t) b(t) \bar{C}(t) + \frac{\pi}{2} (1 + S(t)) C(t) \quad (10)$$

$$= \begin{cases} \theta S_d(t) b(t), & \text{during the data signal} \\ \frac{\pi}{2} (1 + S_s(t)), & \text{during the sync signal} \end{cases}$$

and $b(t)$ is a squarewave subcarrier.

Clearly, the carrier is four-phase modulated, where the phases are $\pm\theta$ during the data period and 0 or π during the sync period.

The received signal is

$$r(t) = \sqrt{2P} y(t) + n(t) \quad (11)$$

where P is the total received power and $n(t)$ is a zero mean white gaussian noise of one-sided spectral density N_0 . From Eqs. (9) to (11),

$$r(t) = n(t) + \begin{cases} S_d(t) b(t) \sin \theta \sqrt{2P} \cos \omega t + \cos \theta \sqrt{2P} \sin \omega t, & \text{during the data signal} \\ -S_s(t) \sqrt{2P} \sin \omega t, & \text{during the sync signal} \end{cases} \quad (12)$$

Thus, the data signal $S_d(t)$ and the sync code $S_s(t)$ are not only disjoint in time, but transmitted on different channel, that is, $S_d(t)$ is received on the in-phase channel ($\cos \omega t$) while $S_s(t)$ is received on the quadrature channel ($\sin \omega t$).

Assuming perfect coherent demodulation, the output of the inphase and quadrature correlations, $r_1(t)$ and $r_2(t)$, respectively, are (Fig. 3):

$$r_1(t) = n_1(t) + \begin{cases} \sqrt{P} \sin \theta S_d(t) b(t), & \text{during data signal} \\ 0, & \text{during sync signal} \end{cases}$$

$$r_2(t) = n_2(t) + \begin{cases} \sqrt{P} \cos \theta, & \text{during data signal} \\ -\sqrt{P} \sin \theta S_s(t), & \text{during sync signal} \end{cases}$$

where n_1 and n_2 are independent noise processes.

The modulation index θ determines the amount of unmodulated carrier, transmitted for phase reference.

Since synchronization is acquired and maintained using $r_2(t)$, no false sync occurs due to the random data. Also, since $\sin^2 \theta \gg \cos^2 \theta$ (only a small fraction of the power is transmitted for carrier reference), the SNR in the quadrature channel is large during the sync period of the frame and small during the data period. Therefore, a coarse search of $S_s(t)$ can be made, using a SNR detector, to speed up the acquisition.

Note that the synchronization code does not have to be at the beginning of the frame, but can be distributed anywhere (not necessarily continuously). In this case, $C(t)$ is the indicator function of the synchronization bits, and the same analysis holds.

A. Carrier Tracking

The incoming signal is correlated with the output of the voltage-controlled oscillator (VCO), $\sqrt{2} \cos(\omega t + \phi)$, where ϕ is the phase error in tracking, to yield

$$r_1(t) = n_1(t) + \begin{cases} -\sqrt{P} \cos \theta \sin \phi + \sqrt{P} \sin \theta \cos \phi S_d(t) b(t), & \text{during data signal} \\ \sqrt{P} \sin \theta S_s(t) \sin \phi, & \text{during sync signal} \end{cases} \quad (13)$$

Since $S_s(t)$ can be chosen to have a negligible low frequency component [otherwise, we can transmit $S_s(t) b(t)$ instead of $S_s(t)$], the output of the loop filter is the error signal

$$e(t) = n_1(t) + \begin{cases} -\sqrt{P} \cos \theta \sin \phi, & \text{during data signal} \\ 0, & \text{during sync signal} \end{cases} \quad (14)$$

Thus, the VCO is not controlled during the relatively short sync period, which is usually less than 5% of the time. However, the duration T_s of the sync is much shorter than the time constant of the loop, and there is little danger of losing lock during the sync period. The effective loop SNR is

$$\frac{P \cos^2 \theta}{N_0 B_L} \left(1 - \frac{T_s}{T}\right) \quad (15)$$

If a Costas loop is used, with bandpass filters for $S_s(t)$ and

$s(t) b(t)$, then tracking is performed during the whole period.

V. Conclusion

New methods of parallel and serial synchronization for time-multiplexed signals have been presented. In the parallel case, synchronization can be obtained for any of M synchronization codes, which is particularly useful when frames of different lengths have to be transmitted. In the serial case, the false sync due to a replica of the code generated by the random data is eliminated.

Appendix

Sequences With Small Partial Correlations

The following is a list of binary sequences of length K , which have small partial correlations R (Eq. 5) and R (Eq. 4). The sequences are described by the following notation:

$$n_1 n_2 n_3 n_4 \dots \equiv \underbrace{1 \dots 1}_n \underbrace{0 \dots 0}_n \underbrace{1 \dots 1}_n \underbrace{0 \dots 0}_n \dots$$

K	Sequence	\hat{R}	R
3	2 1	1	1
5	3 1 1	1	1
7	3 2 1 1	1	1
11	3 3 1 2 1 1	1	1
13	5 2 2 1 1 1 1	1	1
14	5 2 2 2 1 1 1	2	2
15	5 2 2 1 1 1 2 1	2	3
	6 2 2 1 1 1 2	2	3
16	3 1 3 4 1 1 2 1	2	4
	5 2 2 2 1 1 1 2	2	4
17	2 2 5 1 1 1 1 2 1 1	2	3
	4 2 2 1 2 1 1 1 1 2	2	3
18	5 1 1 2 1 1 3 2 2	2	2
19	4 3 3 1 3 1 2 1 1	2	3
20	5 1 3 3 1 1 2 1 1 2	2	4
21	6 1 1 3 1 1 2 3 2 1	2	3
	5 1 1 3 1 1 2 3 2 2	2	3
	3 5 1 3 1 2 1 1 1 2 1	2	3
22	8 3 2 1 2 2 1 1 1 1	3	6
23	1 2 2 2 2 1 1 1 5 4 1 1	3	5
24	8 3 2 1 1 1 1 2 2 1 2	3	4
25	3 2 3 6 1 1 1 1 1 2 1 2 1	2	3
26	8 2 1 1 2 2 1 1 1 1 2 3 1	3	4
27	2 1 2 1 1 2 1 3 1 3 1 3 4 2	3	5
28	2 1 2 1 1 2 1 3 1 3 1 3 4 3	2	4
	3 2 3 6 1 1 1 1 1 2 1 2 1 2 1	2	4
29	2 1 2 1 1 2 1 3 1 3 1 3 4 4	3	5
30	7 1 2 2 1 1 1 1 2 1 1 3 4 2 1	3	6
31	3 2 2 3 6 1 1 1 1 1 1 2 1 2 1 3	3	5
32	6 1 3 2 1 3 3 1 1 2 1 2 1 1 3 1	3	6
33	6 3 1 2 3 2 1 1 3 2 1 1 2 2 1 1 1	3	5
	6 3 1 2 2 2 1 1 1 3 2 4 1 1 1 2	3	5
	6 3 1 2 1 1 1 2 1 2 2 3 1 1 1 3 1 1	3	5
34	7 4 2 1 1 2 1 1 2 2 2 2 1 1 1 1 1 1 1	3	6

References

1. Butman, S., and Timor, U., "Interplex—An Efficient Multi-Channel PSK/PM Telemetry System," *Proc. of ICC*, June 1971.
2. Stiffler, J. J., *Theory of Synchronous Communication*. Prentice Hall, Inc., New Jersey, 1971.
3. Turyn, R., "Sequence With Small Correlation," in *Error Correcting Codes*. Edited by Mann. John Wiley & Sons, Inc., New York, 1968.

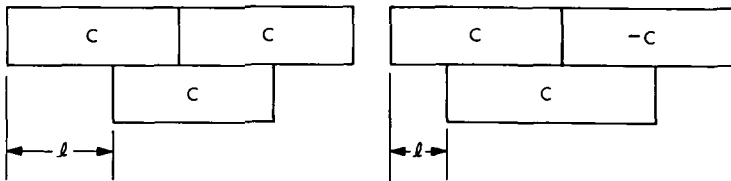


Fig. 1. l -shift correlation of C with (C, C) and $(C, -C)$

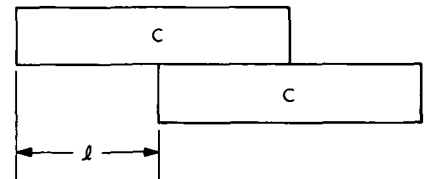


Fig. 2. l -shift partial correlation of C

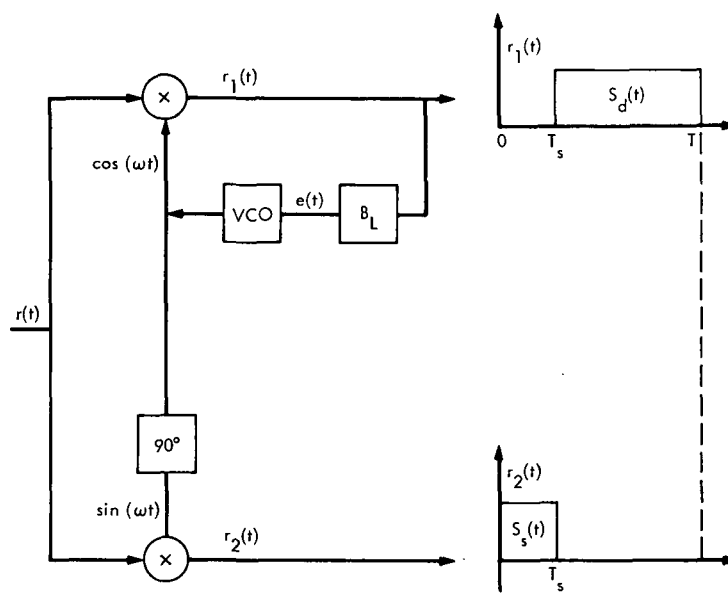


Fig. 3. Receiver for quadrature serial synchronizer

L-Band Frequency Multipliers: Phase Noise, Stability, and Group Delay

J. MacConnell and R. Meyer
Communications Systems Research Section

In this article, three 100- to 1400-MHz frequency multipliers are evaluated for use in the hydrogen maser receiver-synthesizer, with the conclusion that significant advancements have been made in the design of step recovery diode multipliers. In addition, while it appears that the group delay performance in multipliers can be quite good, there are substantial problems that prevent resolving group delays of <1 nsec in frequency multipliers.

I. Introduction

Three different types of $\times 14$ frequency multipliers were tested. First, a discrete-component frequency multiplier was built using Schottky barrier diodes as the only non-linear elements in an attempt to achieve the lowest possible phase noise. Next, Zeta Laboratories, which claims to have made important advancements in multiplier design, supplied two $\times 14$ multipliers to JPL for evaluation and testing. Finally, a unit which typifies conventional step-recovery-diode multiplier design was obtained from Frequency Sources, Inc. as a second source in procurement specifications.

II. Construction and Design of the Multipliers

The JPL $\times 14$ multiplier¹ uses commercial modular components assembled on an aluminum plate and inter-

connected with semi-rigid coax. The only adjustments required are the insertion of attenuators in the lines to set the power levels.

The Zeta multiplier is unusual in that it employs a sampling phase-locked loop to reference a 1400-MHz strip-line voltage-controlled oscillator (VCO) to the input. This technique has the advantage of holding the output power level constant, independent of level or frequency, but it requires a VCO with good phase noise characteristics. The unit is quite complex, utilizing a strip line and two printed circuit boards incorporating a total of ten transistors and two integrated circuits. However, there are only two RF adjustments plus a trimpot, which adjusts a digital searching circuit that sweeps the VCO to acquire lock. An isolator is required at the output to prevent pulling of the VCO and erratic phase lock.

The Frequency Sources $\times 14$ multiplier typifies the present design of step-recovery-diode multipliers by

¹Described in detail in Ref. 1.

incorporating a high-powered two-transistor amplifier with many tuning adjustments in addition to a three-stub tuner on the output. Although the circuit design is relatively simple, the numerous tuning adjustments result in a complex alignment procedure and a rather narrow bandwidth.

III. General Performance

Table 1 gives a direct comparison of these three very different multipliers over a wide variety of parameters. The cost of the JPL $\times 14$ multiplier (basic parts, no packaging) is approximately four times that of the other units. The JPL $\times 14$ multiplier's output level and bandwidth are the most sensitive to the input level due to the numerous doublers and filters; however, the absence of high- Q circuits provides a much wider bandwidth compared to that of the other multipliers. The output level of the Frequency Sources multiplier remains relatively constant over a wide range of input power, which probably indicates a good matching network that keeps the step recovery diode well saturated. However, the high- Q circuits tend to narrow the bandwidth and allow the center frequency to shift nearly 3 MHz over a 0–50°C temperature range. The Zeta multiplier's output is perfectly flat since the VCO requires only an input signal greater than –3 dBmW in order to acquire lock. Although 13 MHz is the bandwidth in which the Zeta multiplier will reliably acquire lock, the actual information capacity of the multiplier is very low since the phase modulation capability is limited by a loop bandwidth of only 2.6 kHz.

IV. Stability

Instability is caused when a phase drift rate (equivalent to a frequency offset) is generated by a change in temperature. To compare the multipliers, a 5°C step change in temperature was arbitrarily assigned as a worst-case situation, and the maximum rates of change in phase were subsequently recorded. Since the stability depends only on the rate of change in the phase, and not the absolute change, the thermal isolation of the module affects greatly the degree of stability actually attained. However, un-isolated measurements are meaningful in that it has been determined that, when a device is mounted inside a module and then placed in a rack as part of a system, a factor-of-10 improvement over the free air stability can be expected. However, to obtain improvement factors of 100 or 1000, special insulation or ovens are definitely required. The three multipliers are judged about equal in stability when operating as part of a packaged system. The JPL $\times 14$ multiplier exhibited a poorer

stability because its tubular filters were exposed to the oven's air blast without benefit of any thermal shielding. It should also be emphasized that, since the measured free air stability depends largely on the magnitude of the temperature change selected for the test (i.e., the temperature coefficient of phase is not constant), the temperature step should be the same as the actual variation expected in the system environment.

V. Phase Noise

The power spectral density of phase noise for the Zeta multiplier is equal to the noise of the JPL $\times 14$ and is 12 db lower than that of the Frequency Sources multiplier. Apparently, Zeta actually has made advances in the design of step-recovery-diode multipliers. From the research performed so far, the improvement in phase noise is the most likely due to a reduction in the overall positive feedback present in the multiplier circuit. The fact that the step recovery diode is a one-port device exhibiting a negative resistance characteristic has always placed severe constraints on the circuit design, in which the objective is to eliminate parametric instabilities while simultaneously maximizing efficiency and bandwidth. In the Zeta multiplier, the step recovery diode only pulses the sampling gate and therefore eliminates the customary filtering and idling circuits required.

VI. Group Delay

Group delay is defined as the time required for information to pass through a system. Alternatively, group delay can be viewed as $d\phi/d\omega$, where ϕ , in rad, is the phase shift through the system, and ω is the input frequency in rad/sec. These two interpretations of group delay suggest two methods of measurement.

For simplicity, first consider the case of a system where the input and output frequencies are the same. Figure 1a depicts an arrangement that measures $\Delta\phi/\Delta\omega$ by shifting the frequency an amount $\Delta\omega$ and then recording the resultant change of phase. The process is then repeated over the desired range of frequencies.

Figure 1b is a second method for determining group delay that essentially measures the time required for modulation to pass through the system. Here, the signal source is amplitude-modulated by a modulating frequency and then detected after passing through the sys-

tem under test. By comparing the phase of the modulated and detected signals, the group delay is simply:

$$t_d = \frac{\phi}{360f_m}$$

where

t_d = group delay, sec

ϕ = phase shift, deg

f_m = modulating frequency, Hz

Obviously, to avoid ambiguities in the above equation, the group delay must be less than the period of the modulating frequency. In addition, the delays of the modulator and detector must be subtracted from the measured delay to obtain the absolute delay of the device under test. In a system, since it is usually sufficient to know only the *change*² in group delay as a function of various parameters, it is not necessary to calibrate the absolute delays of the modulator and detector. Although the resolution of this system improves as the modulating frequency increases, it is important that the frequency of modulation remain small with respect to the bandwidth of the device under test to insure that the carrier and both sidebands see approximately the same transfer function.

Measuring the group delay of frequency multipliers or dividers with the techniques of Fig. 1 will not succeed, because the input and output frequencies are no longer the same. The system of Fig. 2a resolves this difficulty by creating a reference channel with a second device. Group delay is measured as in Fig. 1b, except that phase modulation must be used since amplitude modulation will not pass undistorted through the usual type of multi-

plier or divider. Often, the group delay of the modulator is a function of the source frequency; so, to prevent error, the modulation frequency is detected prior to entering the device under test by means of a second phase detector (Fig. 2b). The phase detector consists of a double-balanced mixer with the input signals supplied in quadrature by a variable phase shifter. Since the phase detector is a symmetric device reading the phase difference between two channels, its effect on the group delay is negligible, provided the S-curve is linear. Any non-linearity present in which the phase detection slope becomes a function of the operating point can easily be observed by varying the phase shifters and noting any change in the phase meter reading.

The group delay of the JPL $\times 14$ multiplier was measured with the system of Fig. 3, using a modulation frequency of 2.777 MHz. This frequency is well within the bandwidth of the multiplier and allows a conversion of 1 nsec/deg of phase. Since the modulation index must be kept low in order that there be only one pair of sidebands after $\times 14$ multiplication, the detected signal at the reference point A is too small for the vector voltmeter to lock onto it. Therefore, the reference for the vector voltmeter must be taken directly from the 2.777-MHz source and then the results corrected for the group delay characteristic of the phase modulator. This is accomplished by recording the group delay response in the "calibrate" position of Fig. 3 and then subtracting it from the final results.

The resolution of this test system is about 0.1 nsec; however, after many runs to verify repeatability, it was determined that there is an overall uncertainty of about ± 0.5 nsec in the data. This is attributed to the fact that certain delays in the system, especially in the phase modulator, are very sensitive to signal level. Figure 4 shows the variation in group delay for only the discrete $\times 14$ multiplier, since the bandwidths of the other multipliers were too narrow to use a high enough modulation frequency for adequate resolution.

²Group delay distortion arises when the spectral components of a complex waveform are delayed unequally during transmission, because the group delay of a device is a function of frequency. Thus, in most systems it is the variation of the group delay with frequency, temperature, or power supply voltage that results in distortion or timing errors.

Reference

1. Lutes, G., MacConnell, J., and Meyer, R., "Hydrogen Maser: Low Phase Noise, L-Band Frequency Multiplier," in *The Deep Space Network Progress Report for November and December 1971*, Technical Report 32-1526, Vol. VII, pp. 81-83, Jet Propulsion Laboratory, Pasadena, Calif., Feb. 15, 1972.

Table 1. Comparison of frequency multipliers

Parameter	JPL $\times 14$	Zeta	Frequency sources	Unit
Output power @ 13-dBmW input	17.0	17.2	17.4	dBmW
1-dB output bandwidth @ 13-dBmW input	28	13 ^a	3.7	MHz
Spurious level	>60	>60	>60	dB down
Power spectral density of phase noise ^b @ 10 Hz	-110 dB	-110 dB	-98 dB	rad ² /Hz
Phase noise ^c @ 10 Hz	180	180	730	$\mu\text{deg rms/Hz}^{1/2}$
Phase drift	4.1	3.7	3.7	deg/ $^{\circ}\text{C}$
Phase drift rate for a 5 $^{\circ}\text{C}$ step change in temperature	90	27	18	mdeg/sec
Stability for a 5 $^{\circ}\text{C}$ step change in temperature	18	5.4	3.6	parts/ 10^{14}
Change in output power over 0-50 $^{\circ}\text{C}$	4	1	1.5	dB
Change in output power for a 6-dB change in input level	4	0	0.8	dB
Change in output power for a 20% change in power supply voltage	1	1	0.5	dB
Change in bandwidth over 0-50 $^{\circ}\text{C}$	4	—	2	MHz
Change in bandwidth for a 6-dB change in input level	20	0	0.2 ^d	MHz
Change in group delay for a 10 $^{\circ}\text{C}$ change in temperature	1	—	—	nsec
Bandwidth for a 1-nsec variation in group delay	11.2	—	—	MHz
Number of RF tuning adjustments	0	2	16	—
Number of transistors and integrated circuits	14 ^e	12	2	—
DC power required	24 V @ 320 mA 15 V @ 75 mA 12 V @ 55 mA	28 V @ 200 mA	28 V @ 200 mA	—
Size	41 \times 33 \times 5 (16 \times 13 \times 2)	10 \times 10 \times 5 (4 \times 4 \times 2)	15 \times 6 \times 4 (6 \times 2.5 \times 1.5)	cm (in.)

^aMultiplier utilizes a phase-locked loop that will reliably acquire lock within a 13-MHz bandwidth.

^bSystem noise: -145 dB rad²/Hz.

^cSystem noise: 3.2 $\mu\text{deg rms/Hz}^{1/2}$.

^dCenter frequency of the bandwidth shifts about ± 1.3 MHz for a $\mp 25^{\circ}\text{C}$ change in temperature.

^eNumber of modular components.

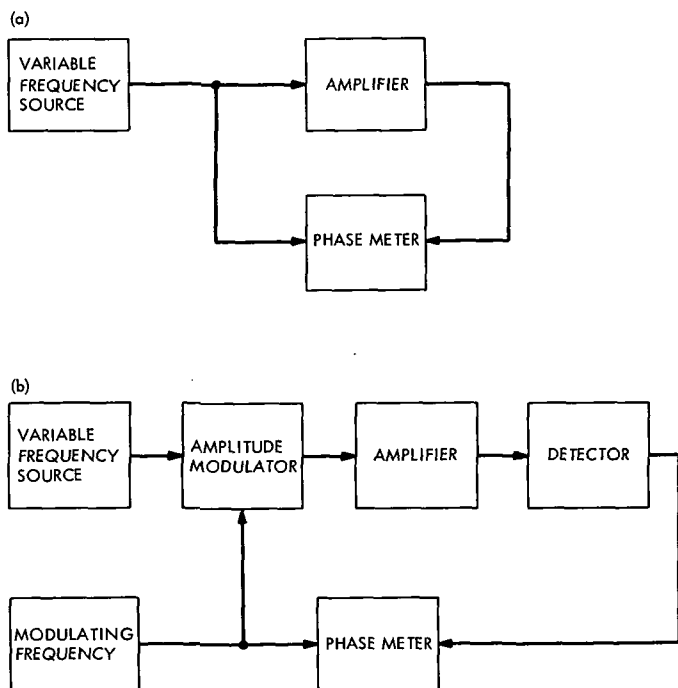


Fig. 1. Group delay measurement of amplifiers

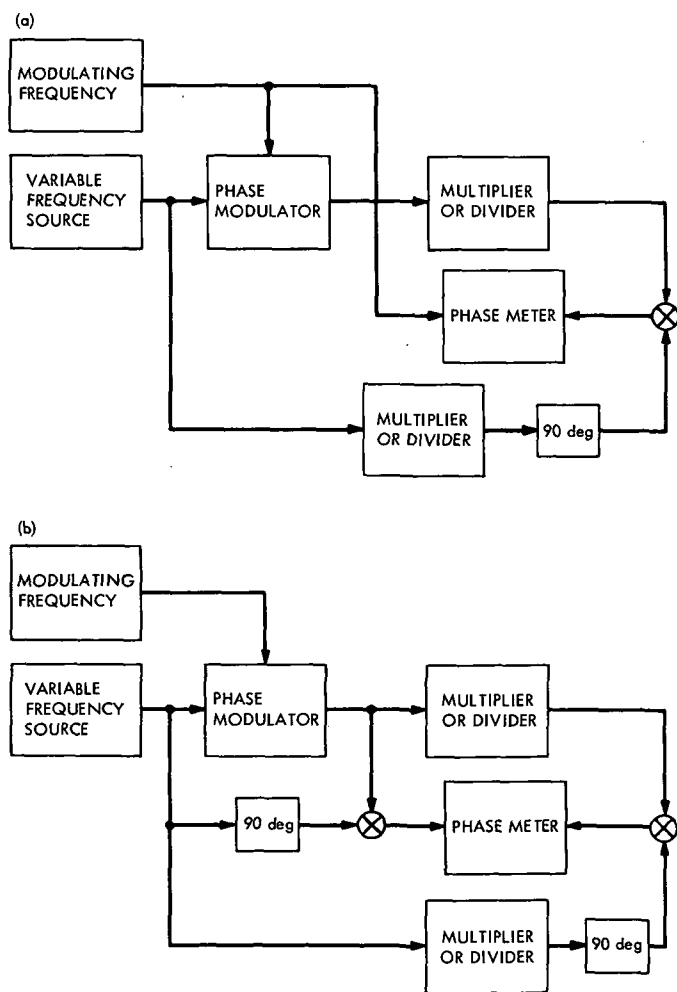


Fig. 2. Group delay measurement of multipliers and dividers

A Minimization Algorithm for a Class of Functions

L. R. Welch¹

Communications Systems Research Section

Let N be a positive integer and A_0, \dots, A_N be non-negative numbers with at least one positive. Define

$$G(x) = \frac{N}{x} + \sum_{k=0}^N A_k x^k$$

The problem is to compute $z > 0$ with

$$G(z) = \min_{x > 0} G(x)$$

This article gives a simple algorithm requiring $\lceil (3/2)(\ln N / \ln 2) \rceil + 8$ evaluations of a polynomial of degree $N + 1$ and 6 evaluations of its derivative. This algorithm is required to optimize the DSN resource allocation process.

I. Introduction

Let N be a positive integer and A_0, \dots, A_N be non-negative numbers with at least one positive. Define

$$G(x) = \frac{N}{x} + \sum_{k=0}^N A_k x^k$$

The problem is to compute $z > 0$ with

$$G(z) = \min_{x > 0} G(x)$$

This article gives a simple algorithm requiring $\lceil (3/2)$

$\times (\ln N / \ln 2) \rceil + 8$ evaluations of a polynomial of degree $N + 1$ and 6 evaluations of its derivative. This algorithm is required to optimize the DSN resource allocation process.

II. Analysis

The derivative of G is

$$\begin{aligned} G'(x) &= \frac{-N}{x^2} + \sum_{k=1}^N A_k k x^{k-1} \\ &= \frac{-N + \sum_{k=1}^N A_k k x^{k+1}}{x^2} \end{aligned}$$

¹Consultant from USC Electrical Engineering Department.

Let $B_0 = -N$, $B_1 = 0$, $B_k = (k-1)A_{k-1}$ for $k \geq 2$, and

$$f(x) = \sum_{k=0}^{N+1} B_k x^k$$

Then $f(z) = 0$ and the problem becomes one of finding the roots of $f(x) = 0$, $x > 0$.

III. The Algorithm

Step I: Define

$$\sup = \exp \left(\min_{\substack{2 \leq k \leq N+1 \\ B_k \neq 0}} \left[\frac{1}{k} \ln \frac{N}{B_k} \right] \right)$$

$$\text{GLB} = \exp \left(\min_{\substack{2 \leq k \leq N+1 \\ B_k \neq 0}} \left[\frac{1}{k} \ln \frac{1}{B_k} \right] \right)$$

$$L = \left\lceil \frac{3}{2} \left(\frac{\ln N}{\ln 2} \right) \right\rceil + 2$$

Step II:

$$\text{Let } x = \frac{\sup + \text{GLB}}{2}.$$

If $f(x) \geq 0$, set $\sup = x$.

If $f(x) < 0$, set $\text{GLB} = x$.

Do this calculation L times.

Set $x = \sup$.

Step III (Newton's method):

$$\text{Replace } x \text{ by } x - \frac{f(x)}{f'(x)}.$$

Do this calculation six times.

Set $z = x$.

IV. Results

The relative error in z is less than 10^{-40} if the arithmetic is executed with infinite precision, and the relative error in $G(z)$ will be smaller. If the arithmetic is executed with s decimal digits of accuracy, the relative error will be on the order of $N^2 10^{-s}$, $s < 40$.

V. Validity of the Algorithm

Since $f(0) = -N$ and $f'(x), f''(x)$ are positive for $x > 0$, there is a unique root on the positive axis. The solution

can be bounded as follows: Define

$$\begin{aligned} \sup &= \exp \left(\min_{\substack{2 \leq k \leq n \\ B_k \neq 0}} \left[\frac{1}{k} \ln \frac{N}{B_k} \right] \right) \\ &= \left(\frac{N}{B_{k_0}} \right)^{1/k_0} \end{aligned}$$

$$\begin{aligned} \text{GLB} &= \exp \left(\min_{\substack{2 \leq k \leq n \\ B_k \neq 0}} \left[\frac{1}{k} \ln \frac{1}{B_k} \right] \right) \\ &= \left(\frac{1}{B_{k_1}} \right)^{1/k_1} \end{aligned}$$

Then the following statements are true:

$$(A) \text{GLB} \leq z \leq \sup$$

Proof: If $0 \leq z < \text{GLB}$, then

$$f(z) = -N + \sum_{k=2}^{N+1} B_k z^k < -N + \sum_{k=2}^{N+1} B_k \cdot \frac{1}{B_k} \leq 0$$

Thus, $f(z) < 0$, a contradiction. If $z > \sup$, then

$$f(z) = -N + \sum_{k=2}^{N+1} B_k z^k > -N + B_{k_0} \cdot \frac{N}{B_{k_0}} = 0$$

Thus, $f(z) > 0$, a contradiction.

$$(B) \frac{\sup - \text{GLB}}{z} < N^{1/2}$$

Proof:

$$\sup = \left(\frac{N}{B_{k_0}} \right)^{1/k_0} \leq \left(\frac{N}{B_{k_1}} \right)^{1/k_1} = (N)^{1/k_1} \text{GLB}$$

Now

$$\frac{\sup - \text{GLB}}{z} < \frac{\sup}{\text{GLB}} \leq N^{1/k_1} \leq N^{1/2}$$

(C) After step II of the algorithm,

$$\frac{\sup - \text{GLB}}{z} < \frac{1}{2N}$$

Proof: Each step of the algorithm divides $(\sup - \text{GLB})$ by two. Therefore,

$$\frac{\sup - \text{GLB}}{z} < N^{1/2} 2^{-L} < N^{1/2} 2^{-(3/2)(\ln N / \ln 2) + 1} = \frac{1}{2N}$$

(D) Since $f'(x)$ and $f''(x)$ are positive for $x > 0$, if x_0, x_1, \dots are computed using Newton's method beginning with $x_0 > z$, the x 's form a monotone sequence decreasing to z .

$$(E) \quad |x_t - z| < \frac{2z}{N} \left(\frac{1}{2}\right)^{2t}$$

Proof:

$$x_{t+1} - z = x_t - z - \frac{f(x_t)}{f'(x_t)} = \frac{(x_t - z)f'(x_t) - f(x_t)}{f'(x_t)}$$

Using Taylor's theorem with the remainder for the numerator,

$$\begin{aligned} |x_{t+1} - z| &= \frac{\frac{(x_t - z)^2}{2} [f''(\epsilon) + (\epsilon - z)f^{(3)}(\epsilon)]}{f'(x_t)} \\ &< \frac{(x_t - z)^2}{2} \frac{[f''(x_t) + (x_t - z)f^{(3)}(x_t)]}{f'(x_t)} \end{aligned}$$

However, for polynomials of degree N or less with all positive coefficients, $zh'(z) \leq Nh(z)$. This gives

$$(x_{t+1} - z) < \frac{(x_t - z)^2}{2} \frac{N}{z} \left(1 + \frac{N}{z}(x_t - z)\right)$$

Use of $(x_0 - z) < (z/N) \cdot \frac{1}{2}$ and the above inequality produces the statement (E).

Tracking and Ground Based Navigation: Performance of Hydrogen Maser Cavity Tuning Servo

S. Petty and C. Finnie
Communications Elements Research Section

An experimental automatic cavity tuner has been demonstrated with the atomic hydrogen maser frequency standards developed by the Jet Propulsion Laboratory. The ability of this tuner to prevent RF cavity frequency drift in the maser is shown, and the methods used to modulate hydrogen transition line width in the maser during tuner operation are compared.

I. Introduction

The long-term frequency stability of a hydrogen maser atomic frequency standard is primarily determined by the stability of the microwave cavity resonant frequency. Temperature controller drift, mechanical vibration, power outages during maintenance periods, etc., cause cavity frequency displacements which will pull the maser output frequency if not periodically corrected. The maser output frequency is pulled by the cavity resonant frequency by the ratio of hydrogen transition line width to microwave cavity bandwidth.

An experimental autotuner (automatic cavity tuner) has been developed at JPL which removes long-term RF cavity drift. This unit increments hydrogen transition line width and servos the cavity frequency such that this increment in line width does not measurably change

maser output frequency. A more detailed description of the autotuner can be found in Refs. 1 and 2.

A reference frequency standard is required to enable the autotuner to make difference measurements of maser output frequency at the two different hydrogen transition line widths. Since only a relative frequency difference measurement is needed, absolute frequency calibration of this reference standard is not important.

II. Performance

The performance of the experimental autotuner has been demonstrated at Goldstone with the two JPL hydrogen masers. The response of the autotuner to a specific cavity frequency offset has been measured, and the data are summarized in Fig. 1. The vertical axis represents fractional maser offset frequency (caused by pulling from

an offset cavity frequency), and the horizontal axis represents elapsed running time of the autotuner. For each type of reference standard, the maser cavity was purposely retuned away from the hydrogen transition frequency so as to pull the maser output frequency 2.7 parts in 10^{12} . Then the autotuner was turned on and allowed to servo the cavity frequency and reduce maser offset frequency to some limiting value as determined by the frequency stability characteristics of the reference oscillator. The ultimate tuning accuracy achieved by the autotuner and the elapsed time required to reach this accuracy are labeled in the figure for both types of reference standards. Using a second hydrogen maser as a reference, the autotuner maintained maser offset frequency to less than 1 part in 10^{14} after $2\frac{1}{2}$ hours. A rubidium frequency standard, when compared with a hydrogen maser, has approximately two orders of magnitude less frequency stability for measurement times of 100 seconds; therefore, autotuner integration times must be longer when this type of standard is used as a reference oscillator. When using a Hewlett-Packard Model 5065A Rb standard, the autotuner required 15 hours to reduce and hold maser offset frequency to within 7.5 parts in 10^{14} .

It should be noted that the data in Fig. 1 do not represent an attempt to achieve an optimum tradeoff between response time and ultimate tuning accuracy. Therefore, it is expected that a selection of different autotuner servo parameters will result in improved tuning accuracy in

the case of the rubidium reference standard, at the expense of slower response times.

III. Transition Line Width Modulation

There are three methods used to periodically vary hydrogen transition line width in the JPL hydrogen masers during autotuner operation. These are:

- (1) Vary the RF power to the hydrogen dissociator.
- (2) Vary the flow rate of hydrogen gas into the maser system.
- (3) Modulate the cross-sectional area of the atomic hydrogen beam in the maser with the use of a mechanical shutter.

During the autotuner performance tests at Goldstone, it was found that both methods (1) and (2) generated thermal transients in the maser which adversely affected cavity resonant frequency stability. The end result was that when the autotuner was turned off, the maser frequency would commence to drift many parts in 10^{14} from the previous "tuned" value. As a solution to this problem, a mechanical hydrogen beam chopper has been designed and fabricated which is not expected to disturb magnetic or thermal conditions in the maser sufficiently to affect maser frequency stability. This unit will be described in a future article.

References

1. Finnie, C., "Frequency Generation and Control: Atomic Hydrogen Frequency Standard," in *The Deep Space Network Progress Report*, Technical Report 32-1526, Vol. I, pp. 73-75. Jet Propulsion Laboratory, Pasadena, Calif., Feb. 15, 1971.
2. Finnie, C., "Design of Hydrogen Maser Cavity Tuning Servo," in *The Deep Space Network Progress Report*, Technical Report 32-1526, Vol. II, pp. 86-88. Jet Propulsion Laboratory, Pasadena, Calif., Apr. 15, 1971.

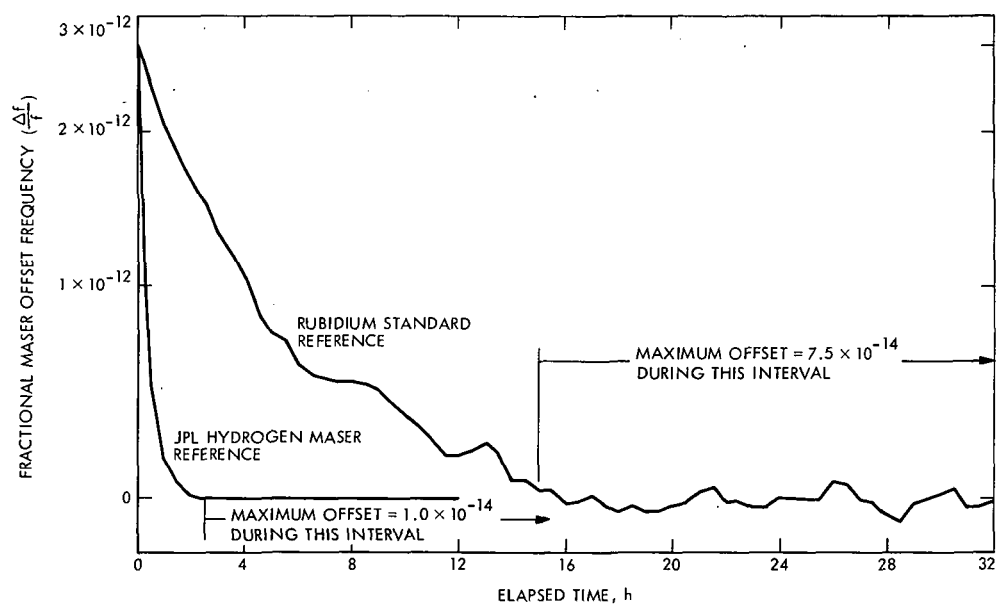


Fig. 1. Response time and tuning accuracy of automatic cavity tuner

Tracking and Ground Based Navigation: A Description of the Weather Project

M. S. Reid

Communications Elements Research Section

The Weather Project forms part of an overall Radio Systems Development Project which seeks to optimize the spacecraft-to-ground communications link. In order to meet the future requirements of the planetary exploration program, a study of, inter alia, weather-dependent characteristics of X- and K-band propagation through the atmosphere is imperative. The objective of the Weather Project is, therefore, the statistical prediction of the performance of the DSN at X-band, and in the future at K-band.

This article discusses the general approach of the Weather Project, the measurements, the calibrations, the equipment, and the methods. Problems encountered are also discussed as well as the proposed future work.

I. Introduction

The Weather Project forms part of an overall Radio Systems Development Project which seeks to optimize the spacecraft-to-ground communications link. In order to meet the future requirements of the planetary exploration program a study of, *inter alia*, weather-dependent characteristics of X- and K-band propagation through the atmosphere is imperative. Statistical correlations of weather and communications capability at X- and K-bands are needed to provide practical predictions of link performance for these missions. The objective of the Weather Project is, therefore, the statistical prediction of the performance of the DSN at X-band, and in the future at K-band.

This article discusses the general approach of the Weather Project, the measurements, the calibrations, the equipment, and the methods. Problems encountered are also discussed as well as the proposed future work. A preliminary analysis of the results for calendar year 1971 will be presented in a subsequent article.

II. Previous Data

Prior to the start of the Weather Project, no K-band system was available in the DSN, and the only suitable X-band data for the DSN was the information contained in the Deep Space Network/Flight Project Interface Design Handbook (Ref. 1). These data were derived primarily from a contractor report submitted to JPL (Ref. 2)

which calculated signal attenuation due to cloud cover from meteorological measurements. The meteorological data for Goldstone were taken from soundings at Daggett, California and from Edwards Air Force Base. Figure 1, which is taken from Ref. 1, shows the form of these data. The figure shows calculated relative increase in system temperature due to cloud cover at DSS 14 as a function of elevation angle for one percent probability conditions. The Weather Project thus requires experimental data, both microwave and meteorological, taken at the 64-m-diameter antenna sites.

III. General Plan

The general plan of the project is discussed in this section. The Earth's atmosphere, particularly changing weather conditions, has many effects on a microwave signal travelling through it. In the microwave bands of interest to space communications, these effects are primarily atmospheric noise which degrades the ground system sensitivity and attenuates the received or transmitted signal. In the bands of interest these effects are due primarily to water vapor, clouds, and liquid water or ice. Wind can also degrade system performance in at least two ways. This will be considered separately and is not treated in this article.

Microwave system temperature measurements at S-, X-, and K-bands are being made and recorded at DSS 14. Ground level meteorological measurements are also recorded at DSS 14. Studies will be performed to correlate the microwave and meteorological data. Meteorological parameters important in establishing X-band performance will be identified. The experimental data will yield short-term X-band performance (noise temperature and attenuation) statistics, which will assist in the development of the elements of a transfer function or functions H , which will transform meteorological data into X-band performance data. The transfer function will be tested against measured microwave and meteorological data. The probability distributions of the transfer function will then be derived.

Experimental K-band data are recorded at DSS 14 to give further insight into the X-band problem as well as to provide K-band performance specifications in the future. S-band data are recorded at DSS 14 not only for further insight into X-band problems, but also to help with the problem of deriving X-band performance statistics for the overseas 64-m antenna sites at an early date.

DSS 43 and DSS 63 will soon be operational, and it will be possible to record S-band data at these sites. No X-band systems will be available at DSS 43 or DSS 63 until about January 1975. This will not allow sufficient X-band data to be recorded at these stations before their preliminary X-band performance statistics are required. Hence, it is proposed to record S-band data at DSS 14, 43, and 63 as well as meteorological data at all these stations. Studies are underway to investigate the feasibility of predicting overseas X-band performance statistics from recorded S-band and meteorological data. These studies will be reported later.

IV. Equipment, Measurements, and Methods

Experimental data are being taken only at DSS 14 at this time. The following measurements are being made and recorded in analog form: (1) microwave: system operating noise temperature T_{op} , and antenna elevation angle θ , as functions of time; and (2) meteorological: ground air temperature and humidity, barometric pressure, wind speed and direction, and rainfall.

The X-band system in the multifrequency X- and K-band (MXK) cone is used as a total power radiometer, and the output is recorded as a function of time on a strip chart recorder, along with antenna elevation angle. This system operates 24 hours per day or as close to this as is possible in practice. In order to calibrate the system and to remove the effects of the slow gain drifts that are experienced, an automatic waveguide switch controller was set up to switch the system between the antenna and the ambient load in the time ratio 55 minutes to 5 minutes. Furthermore, a short calibration is performed manually approximately once per day. This procedure sets the detector and recorder scales, and adjusts the zero positions and calibrates T_{op} .

The advantages of using the X-band system in the MXK cone for the Weather Project are several. An existing system is being used, and experience is being gained in its operation by JPL and Goldstone personnel. Weather data are recorded not only when the antenna is at zenith but also when the station is tracking spacecraft at S-band. This yields atmospheric data at elevation angles typical of tracking operations, and it is also cost effective.

The preliminary data analysis consists of determining for what period of time T_{op} increases over that value to be expected in clear, dry weather, at the given antenna elevation angle of each data point, and by how

much. The results, presented in statistical and graphical form, report increases in T_{op} due only to atmospheric effects, as far as this is possible, and as a function of elevation angle and time of year. Further data analysis will correlate meteorological data with the microwave data as well as deriving atmospheric attenuation as functions of elevation angle and time of year. These experimental data will be compared with the theoretical predictions of Refs. 1 and 2.

S-band and K-band radio metric data have recently been added to the recording system for the reasons discussed above. Various problems have militated against these data being recorded on a 24-hour per day basis. For example, when the station is tracking a spacecraft two-way through the polarization diversity S-band (PDS) cone, it is not possible to connect the S-band Megawatt Transmit (SMT) maser to the SMT horn, as this is a forbidden waveguide switch position to protect the SMT maser from the S-band transmitter. S- and K-band microwave data are therefore recorded on a best effort basis.

In order to improve both the dynamic range and the resolution of the measurement of T_{op} , a digital data acquisition and recording system has been investigated. A preliminary version (see Fig. 2) has been implemented and operated in parallel with the analog recordings. Data are recorded once per minute and the system has a capability of 10 simultaneous channels and 12 status indicator channels. The recording is on magnetic tape with a paper tape printout for real-time monitoring. The analog recordings are considered as a back-up to the digital recordings when operated in parallel with them. X- and K-band radio metric data have been implemented in the digital system as well as antenna elevation angle, day number and time, ground air temperature, and humidity. Consideration is being given to the digital recording of the other measured parameters as well as improvements to the digital system.

V. Calibrations and Problems

Any receiver gain change is indistinguishable in the radiometer output from a change in atmospheric noise temperature. As the maser gain drifts in a period of several hours, it is necessary to make gain calibrations continually. For this purpose an automatic waveguide switch controller was set up, as stated above, to switch the radiometer between the feedhorn and a waveguide ambient load. Another switch position was a zero reference calibration point. These calibrations consumed only five minutes in every hour.

The reliability of the timing and control circuits of this automatic switch proved to be a problem, and calibration capability was lost when the physical temperature of the ambient load was not recorded. Furthermore the analog recording system was required to record a dynamic range of at least 30 K to 300 K. This severely restricted measurement resolution and prompted an investigation into other measurement methods. The possibility of using a noise-adding radiometer (NAR) (Ref. 3) developed at JPL for recording the weather data is now underway. This will stabilize the radiometer gain, increase dynamic range, and it is expected that the use of the NAR will also improve the accuracy of the weather data as well as facilitate data reduction. Consideration is now being given to improving the data system to avoid the effects of drifts in the digital recording equipment.

One of the prime calibration problems is the determination of a "normal" system temperature profile. The normal or baseline system temperature is that elevation profile which obtains in clear, dry weather and against which atmospheric degradation is measured. The normal profile, however, is a function of both frequency and position of the subreflector. The prime X-band frequency is 8415 MHz, which is the frequency for the *Mariner* Venus-Mercury S/X experiment. A considerable portion of X-band radio science, however, is carried out at 7850 MHz, where the normal profile is different from that at 8415 MHz. Figure 3 shows "fair weather" elevation profiles for S-, X-, and K-bands, with the subreflector correctly positioned in each case. Figure 4 shows X-band "fair weather" profiles for 7850 MHz and 8415 MHz with the subreflector focused on the SMT cone. The 8415-MHz profile with the subreflector positioned on the PDS cone is not identical to the 8415-MHz/SMT profile shown in the figure. Figure 5 is a symbolic representation of a possible explanation for the effect of the misaligned feed system profile. The solid ray paths are drawn for the subreflector positioned on the right-hand cone, and the dotted ray paths obtain for the left-hand cone. This shows the left-hand cone receiving some ground radiation. The antenna moves in elevation in the direction of the arrow only, and therefore at low elevation angles the misaligned feed system is expected to have a slightly lower system temperature because some spillover ground reflections will not be received.

The normal profile is also a function of rotation in azimuth, but this is a smaller effect and will be taken into account in a more detailed analysis of the data. The calibration of the misaligned antenna beam will be carried out by radio astronomical methods; preliminary

measurements on the Moon have been made, but further measurements using radio sources are required.

Another problem which complicates the calibration and measurement of data is interference. Interference is experienced in several forms. The first is a CW signal from certain X-band microwave communications links inside the maser passband. This problem has been temporarily solved by suitable filtering. The other forms of interference are noise bursts, which are presently under investigation, and the interference from the fourth harmonic of the S-band transmitter. Figure 6 shows *Mariner Venus-Mercury* 1973 S/X frequencies. The S-band transmit frequency is 2113.3 MHz, and the ranging sidebands are shown in the figure in relation to the S-band receive frequency 182 MHz away. The fourth harmonic of the S-band transmitter is shown 38 MHz higher than the center of the X-band passband, and the fourth harmonic of the S-band ranging modulation is shown approaching this passband. In certain circumstances interference from the fourth harmonic of some ranging modulation has contaminated the X-band weather data. This problem is also presently under investigation.

VI. Future Work

Previous studies (Ref. 2) have shown that cloud cover has a significant effect on X-band systems. The parameters of importance for microwave transmission and noise generation are the concentration and size distribution of the scattering particles, their ice versus water characteristics, and the temperature and depth of the layers containing the particles. Observations of these cloud parameters are not made on a routine basis. Cloud cover is generally reported at few locations in the Mojave area and then in such broad categories as to be of questionable value.

In order to gain meaningful microwave correlations with cloud cover in the antenna beam, it is proposed to

install a camera on the boresight axis of the 64-m antenna. Color photographs will be taken on a routine basis with automatic turn-on, shut-down, aperture adjustment, and synchronization with day and time. A meteorological analysis of these data will provide more meaningful correlations with the microwave data. An infrared radiometer will be investigated for cloud data at night.

The variable component of atmospheric thermal emission near 22 GHz is dominated by emission from water vapor, which has a resonant line at 22.235 GHz, and by emission from condensed water which exists in clouds and precipitation (Ref. 4). It is theoretically possible to measure total integrated water vapor in the antenna beam and to separate the effects of condensed water (Refs. 5 and 6). Two radiometers have been used for this measurement, one at or close to the water line and the other well off the line center. The frequency of the second radiometer may be either higher or lower than the line center.

As there are several reasons for measuring liquid water and water vapor in the atmosphere, radiometers for this purpose will be investigated. These measurements would add valuable information to the meteorological aspects of the project, particularly as measurements could be made in the line of the antenna beam. Furthermore, the vapor measurements could yield an on-line correction for phase, which would be important at critical times for certain spacecraft experiments as well as for the radio science experiments planned by JPL. The differential signal phase change between S- and X-band, through the Earth's atmosphere, due to water vapor, is important for the S/X experiments and is presently being studied. Finally, the greatest uncertainty in spacecraft tracking after the introduction of Differenced Range Versus Integrated Doppler (DRVID) and X-band will be the troposphere. A worthwhile project would be to correlate doppler and range residuals with total integrated water vapor and liquid water in the antenna beam.

References

1. *DSN Standard Practice, Deep Space Network/Flight Project Interface Design Handbook*, 810-5, Revision C, April 1972, pp. 2-119 (JPL internal document).
2. Smith, T. B., and Chien, C. W., *Cloud Cover Effects on Signal Attenuation at DSN Sites*, Report No. MRI 70 FR-922. Meteorology Research Inc., Calif., Apr. 1970.
3. Batelaan, P. D., Goldstein, R. M., and Stelzried, C. T., "A Noise-Adding Radiometer for Use in the DSN," in *The Deep Space Network*, Space Programs Summary 37-65, Vol. II, pp. 66-69. Jet Propulsion Laboratory, Pasadena, Calif., Sept. 30, 1970.
4. Van Vleck, J. H., *Atmospheric Effects on Radio Wave Phase and Correction of Vapor-Caused Phase Fluctuations by Radiometric Measurements of Water Vapor Emission*, VLA Scientific Memorandum No. 8. National Radio Astronomy Observatory, Greenbank, W. Va., Sept. 1967.
5. Staelin, D. H., "Measurements and Interpretation of the Microwave Spectrum of the Terrestrial Atmosphere near 1-Centimeter Wavelength," *J. Geophys. Res.*, Vol. 71, No. 12, pp. 2875-2881, June 1966.
6. Gaut, N. E., *Studies of Atmospheric Water Vapor by Means of Passive Microwave Techniques*, Technical Report No. 467. Research Laboratory of Electronics, M.I.T., Dec. 1968.

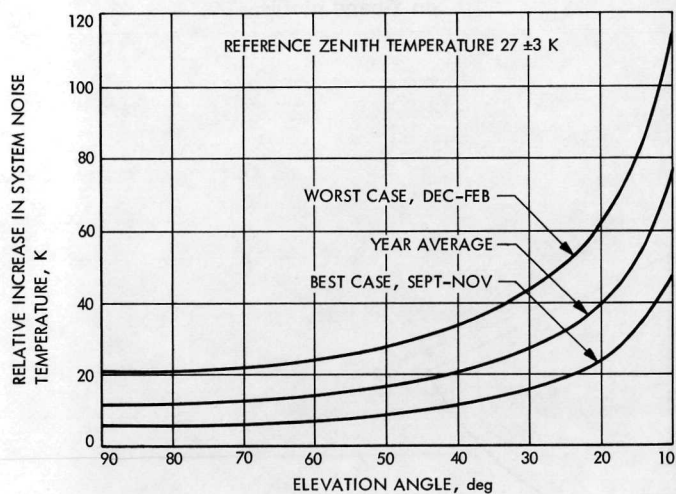


Fig. 1. Increase in system noise temperature at X-band due to cloud cover at DSS 14 for calculated one percent probability conditions

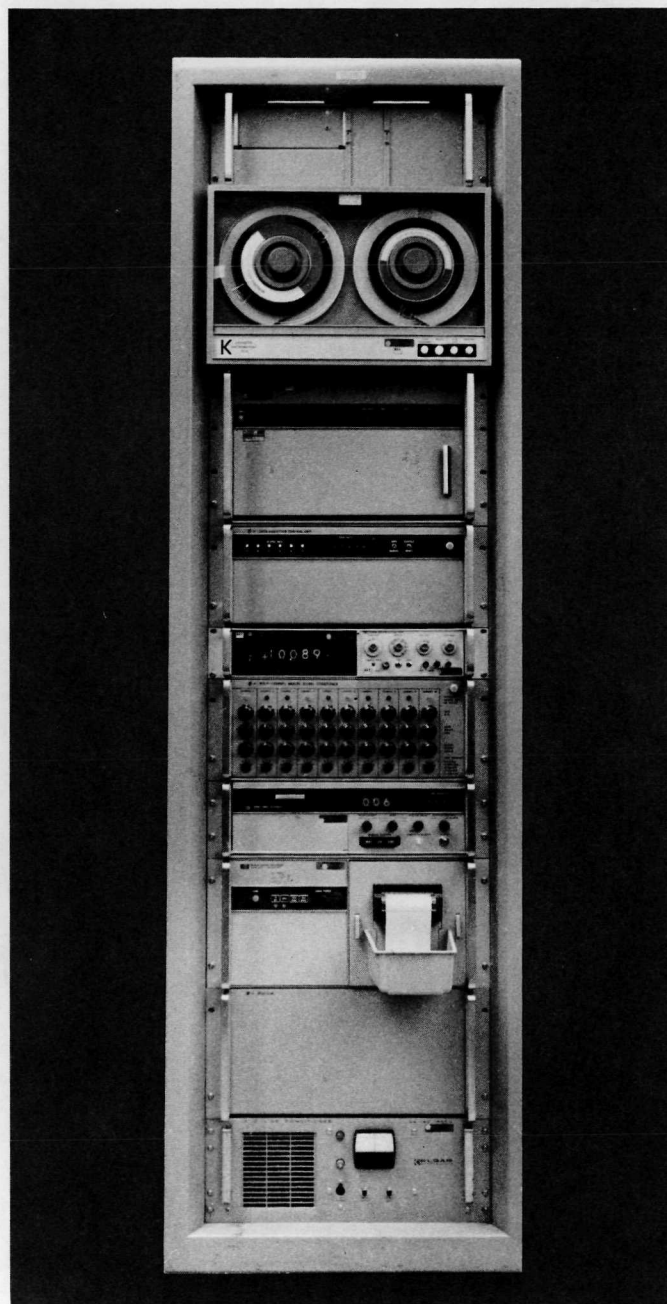


Fig. 2. Preliminary version of data acquisition and recording system

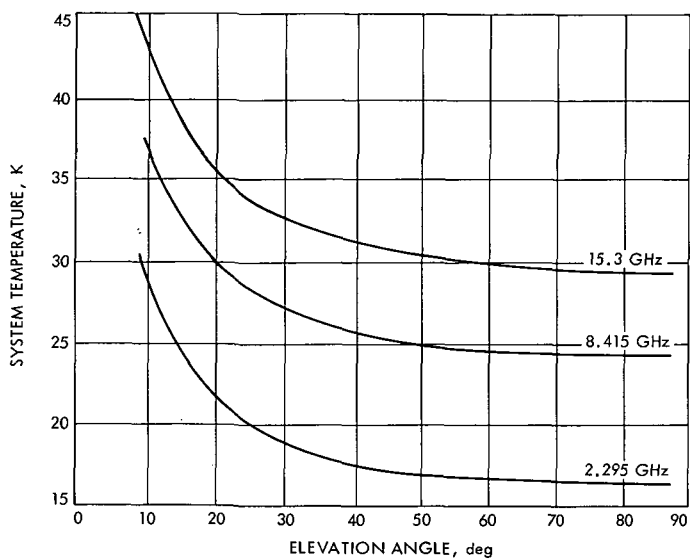


Fig. 3. DSS 14 elevation profiles at S-, X-, and K-bands

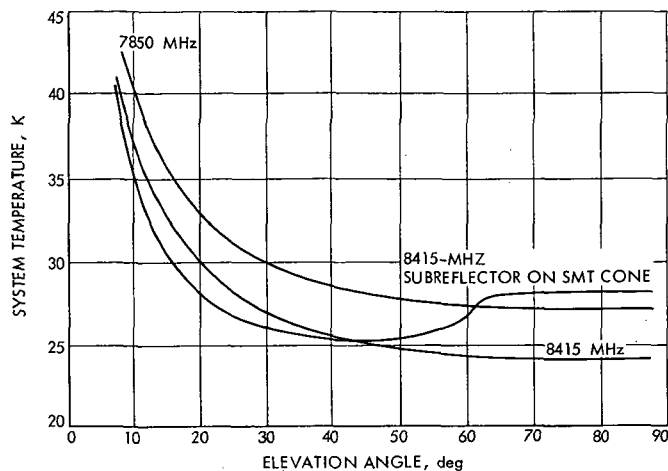


Fig. 4. The effect of frequency and subreflector position on X-band profiles

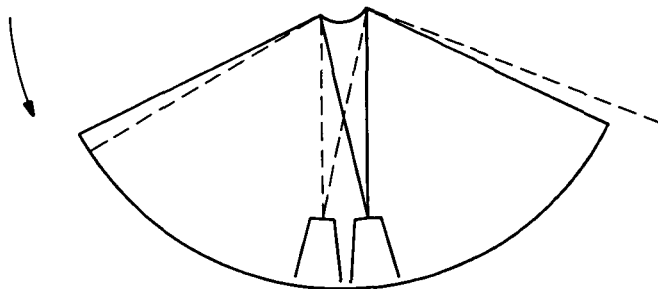


Fig. 5. The effect of misaligned feed system

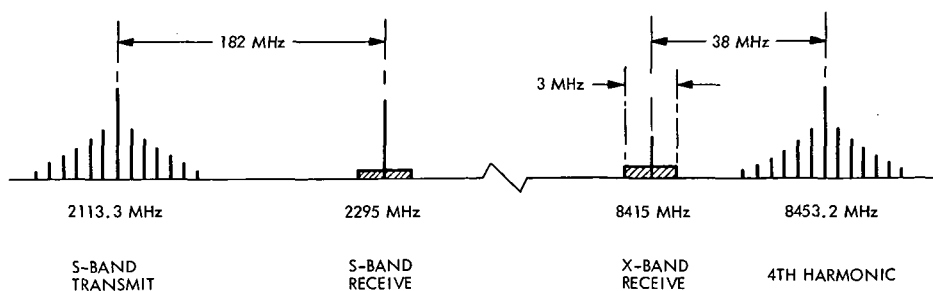


Fig. 6. Mariner Venus-Mercury 1973 S/X frequencies

Improved RF Calibration Techniques: System Operating Noise Temperature Calibrations

M. S. Reid

Communications Elements Research Section

System operating noise temperatures and other calibration data of the S-band radar operational (SRO) cone at DSS 13 and the tricone system at DSS 14 are reported for the period February 1 through May 31, 1972. During this reporting period the tricone system consisted of the polarization diversity S-band (PDS) cone, the S-band megawatt transmit (SMT) cone and the multifrequency X- and K-band (MXK) cone. S-band calibration data for various configuration modes of the PDS and SMT cones are reported as well as X-band calibration data for the MXK cone.

The system operating noise temperature performance of the low noise research cones at the Goldstone Deep Space Communications Complex is reported for the period February 1 through May 31, 1972. The operating noise temperature calibrations were performed with the ambient termination technique¹ (Ref. 1). System temperature calibrations were made on the following cones:

- (1) S-band radar operational (SRO) cone at DSS 13.
- (2) Polarization diversity S-band (PDS) cone at DSS 14.
- (3) S-band megawatt transmit (SMT) cone at DSS 14.
- (4) Multifrequency X- and K-band (MXK) cone at DSS 14.

¹Most of the measurements were taken by DSS 13 (Venus) and DSS 14 (Mars) personnel.

The averaged operating noise temperature calibrations for the SRO cone at DSS 13, and other calibration data, are summarized in Table 1. The maser in operation in the SRO cone throughout this reporting period was serial number 96S5. Measurements made with this maser connected to the gain standard horn at 2278.5 MHz are also shown in Table 1.

Averaged operating noise temperature calibrations, and other calibration data, are presented in Tables 2 and 3 for the tricone system on the 64-m-diameter antenna at DSS 14. Table 2 presents data for the MXK cone at K-band (15.3 GHz) and the SMT cone, both low noise path, with the maser in the SMT cone (serial number 96S4), and diplexed with the maser in the 3A section (serial number 80S1). All the SMT cone data are for 2295 MHz.

PDS cone data are shown in Table 3, where all measurements were taken at 2296 MHz. Maser 80S1 is located in the 3A section and maser 96S3 is in the PDS cone.

All calibration data were reduced with JPL computer program number 5841000, CTS20B. Measurement errors of each data point average are recorded under the appropriate number in the tables. The indicated errors are the standard deviation of the individual measurements and of the means, respectively. They do not include instrumentation systematic errors. The averages were computed using only data with:

- (1) Antenna at zenith.
- (2) Clear weather.
- (3) No RF spur in the receiver passband.
- (4) Standard deviation of computed operating noise temperature due to measurement dispersion less than 0.15 K.

In Tables 2 and 3 the subreflector was correctly positioned on the horn of the system under test for all the calibration data. Table 3 shows two columns of low noise path data for the PDS cone maser. The low noise path system temperature at zenith for the PDS system was running somewhat higher than expected. An investigation was carried out and the problem, which was found to be ruby heating, was cleared by changing the klystron pump conditions. Measurements made after the pump conditions were changed are shown in the second column of low noise path data, where the averaged system operating noise temperature is 18.5 K, as expected.

The PDS cone has been optimized for diplexed operation and therefore has a lower diplexed system temperature than the SMT cone. This is illustrated in Tables 2

and 3 where the PDS and SMT diplexed system temperatures are reported as 23.5 K and 25.7 K, respectively. The SMT cone, however, has been optimized for receive-only operation, and this may also be seen from Tables 2 and 3.

Figure 1 is a plot of system operating noise temperature of the SRO cone at DSS 13 as a function of time in day numbers. The frequency was 2278.5 MHz and the maser was 96S5. Figure 2 is a similar plot of system temperatures with the maser connected to the gain standard horn. SRO cone system temperatures (with maser 96S5) at 2388 MHz are shown in Fig. 3. In these figures data that satisfy the four conditions stated above are plotted as solid circles, while data that fail one or more conditions are plotted as open circles.

Figure 4 is a plot of SMT cone system temperatures as a function of time in day numbers. Both the low noise path with maser 96S4 and the diplexed path with maser 80S1 (3A section) are shown in the figure. Figure 5 is a similar plot for the PDS cone. Low noise and diplexed paths are shown, both using maser 96S3, as well as the date when the klystron pump conditions were changed. The PDS cone system temperature data from the previous reporting period, October 1, 1971 through January 31, 1972 (Ref. 2) have been included in this figure for reference.

In both Figs. 4 and 5 the averaged precision measurements reduced by computer program CTS20B have been augmented by single Y-factor numbers. Although these latter data were taken using the ambient termination method, most of them were not reduced by computer program CTS20B. These data were taken with the antenna at zenith, the subreflector correctly positioned in each case, but with no regard for weather conditions.

References

1. Stelzried, C. T., "Operating Noise-Temperature Calibrations of Low-Noise Receiving System," *Microwave J.*, Vol. 14, No. 6, pp. 41-48, June 1971.
2. Reid, M. S., "Improved RF Calibration Techniques: System Operating Noise Temperature Calibrations," in *The Deep Space Network Progress Report*, Technical Report 32-1526, Vol. VIII, pp. 61-67. Jet Propulsion Laboratory, Pasadena, Calif., Apr. 15, 1972.

Table 1. System operating noise temperature calibrations of the SRO Cone (Maser 96S5) and the gain standard horn (Maser 96S5) on the 26-m antenna at DSS 13

Frequency, MHz	2278.5		2295	2388
	Gain Standard Horn	SRO Cone		
Maser gain, dB	41.6 $\pm 4.10/0.88$ 22 measurements	42.1 $\pm 4.03/0.48$ 70 measurements	43.5 $\pm 0.40/0.20$ 6 measurements	32.4 $\pm 5.9/1.4$ 12 measurements
Follow-up receiver contribution, K	0.07 $\pm 0.07/0.02$ 22 measurements	0.07 $\pm 0.06/0.008$ 63 measurements	0.27 $\pm 0.04/0.02$ 5 measurements	0.13 $\pm 0.04/0.01$ 18 measurements
System operating noise temperature, K	29.2 $\pm 0.53/0.12$ 22 measurements	16.1 $\pm 0.56/0.07$ 63 measurements	15.6 $\pm 0.44/0.20$ 5 measurements	17.1 $\pm 1.0/0.23$ 18 measurements

Table 2. System operating noise temperature calibrations of the SMT and MXK cones on the 64-m antenna at DSS 14

Cone	SMT		MXK
Frequency, MHz	2295		15300
Maser serial number	96S4	80S1 3A Section	148K1
Configuration	Low noise path	Diplexed	Subreflector on K-band horn
Maser gain, dB	—	—	—
Follow-up receiver contribution, K	—	—	0.13 $\pm 0.06/0.05$ 2 measurements
System operating noise temperature, K	15.7 $\pm 0.11/0.05$ 55 measurements	25.7 $\pm 0.21/0.08$ 28 measurements	26.7 $\pm 0.07/0.05$ 2 measurements

Table 3. System operating noise temperature calibrations of the PDS cone on the 64-m antenna at DSS 14

Maser serial number	80S1 (3A Section)		96S3		
Configuration	Low noise path	Diplexed	Low noise path before pump conditions changed	Low noise path after pump conditions changed	Diplexed
Maser gain, dB	40.2 $\pm 0.21/0.12$ 2 measurements	40.4 1 measurement	49.4 $\pm 1.08/0.71$ 36 measurements	49.6 $\pm 2.3/1.0$ 5 measurements	50.4 1 measurement
Follow-up receiver contribution, K	0.06 $\pm 0.01/0.007$ 2 measurements	0.04 1 measurement	0.05 $\pm 0.03/0.005$ 36 measurements	0.09 $\pm 0.05/0.02$ 5 measurements	0.05 1 measurement
System operating noise temperature, K	24.9 $\pm 0.72/0.42$ 2 measurements	29.2 ± 0.31 1 measurement	19.8 $\pm 0.26/0.04$ 36 measurements	18.5 $\pm 0.24/0.10$ 5 measurements	23.5 ± 0.25 1 measurement

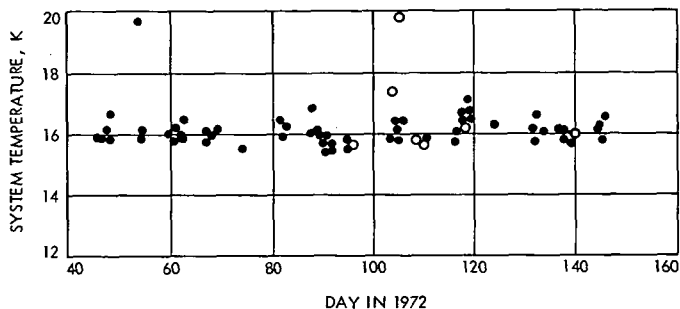


Fig. 1. System operating noise temperatures of the SRO cone at 2278.5 MHz plotted as a function of time in day numbers

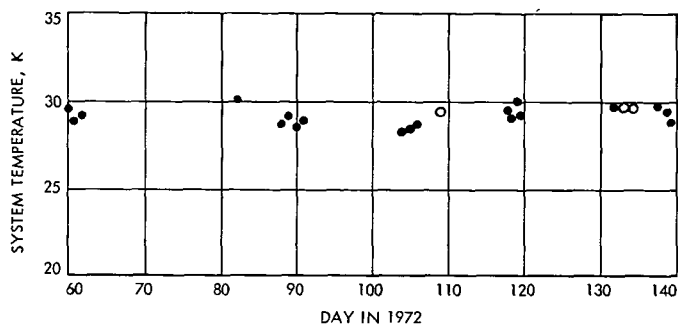


Fig. 2. System operating noise temperatures with the gain standard horn at 2278.5 MHz plotted as a function of time in day numbers

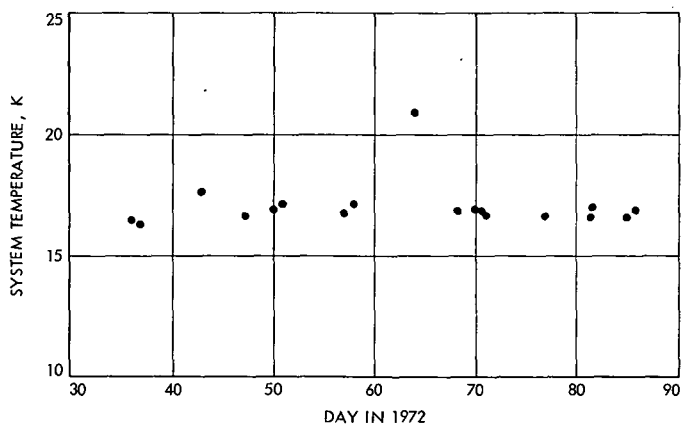


Fig. 3. System operating noise temperatures of the SRO cone at 2388 MHz plotted as a function of time in day numbers

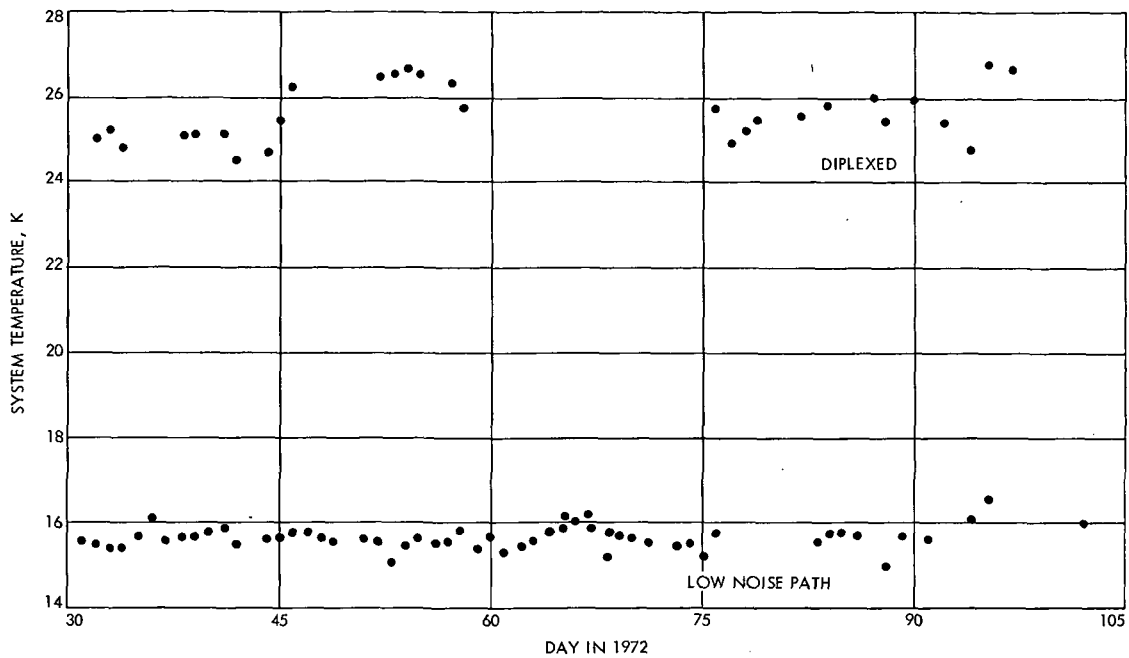


Fig. 4. System operating noise temperatures of the SMT cone, low noise path and diplexed, plotted as a function of time in day numbers

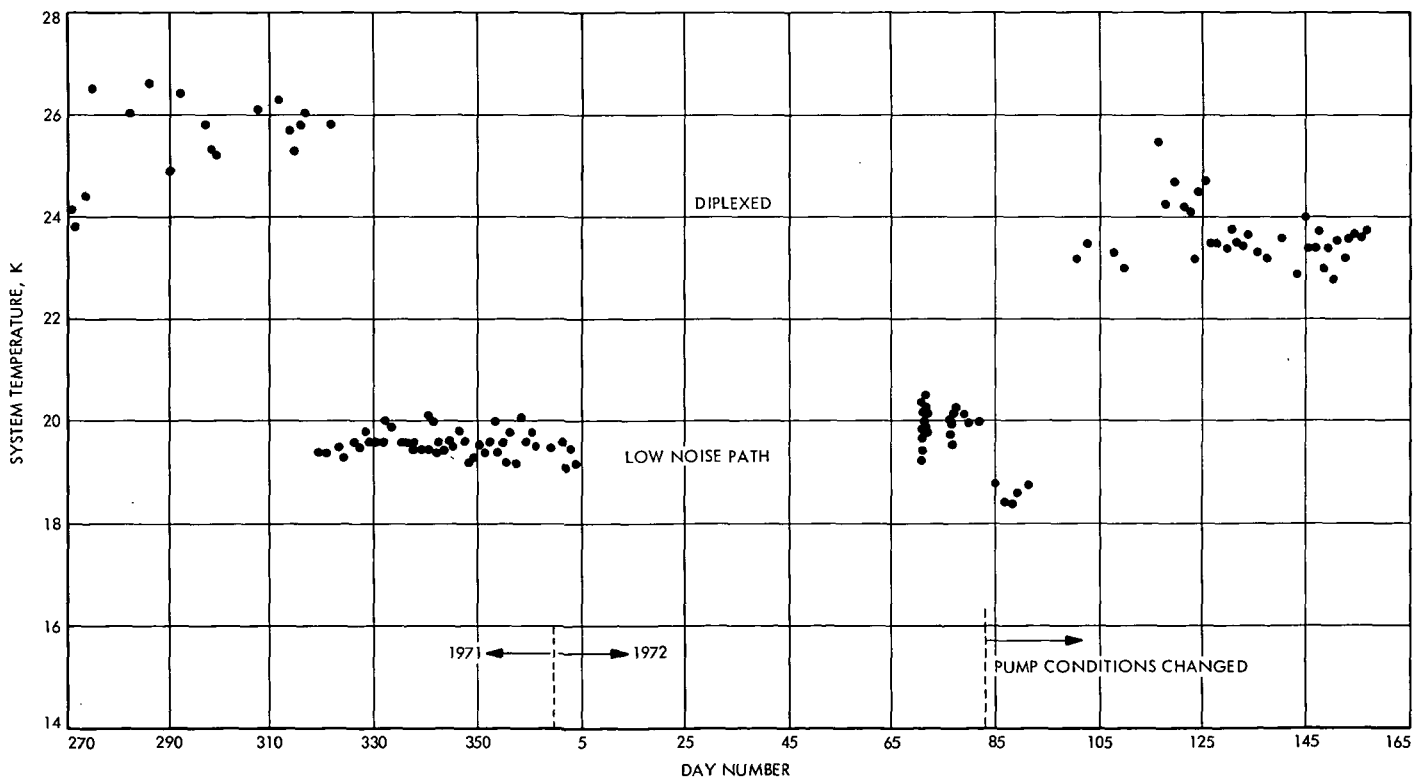


Fig. 5. System operating noise temperatures of the PDS cone, low noise path and diplexed, plotted as a function of time in day numbers

Antenna Study: Performance Enhancement

P. D. Potter

Communications Elements Research Section

A study of possible DSS 14 64-m-diameter antenna gain improvement by utilizing existing dual-reflector shaping techniques has been previously published. That study was restricted to the case of the axially symmetric (unicone) initial 64-m-diameter antenna configuration. After installation of the asymmetrical tricone system, studies of shaping techniques were discontinued pending operational experience with the tricone system at S- and X-bands, and development of new analytical tools for design and analysis of asymmetrical-shaped reflector systems. Recently, the required analytical tools have been developed and are described in this article.

I. Introduction

A study of possible DSS 14 64-m-diameter antenna gain improvement by utilizing existing dual-reflector shaping techniques has been previously published (Ref. 1). That study was restricted to the case of the axially symmetric (unicone) initial 64-m antenna configuration. After installation of the asymmetrical tricone system, studies of shaping techniques were discontinued pending operational experience with the tricone system at S- and X-bands, and development of new analytical tools for design and analysis of asymmetrical-shaped reflector systems. Recently, the required analytical tools have been developed and are described in this article.

Two techniques for obtaining enhanced performance of the DSS 14 64-m antenna have been investigated. Both provide frequency-independent improvement, and both are compatible with the tricone system. The first technique involves use of a shaped, asymmetric, nonhyper-

boloidal subreflector surface in conjunction with a readjustment of the main reflector panels to provide nearly uniform illumination of the antenna aperture and, hence, higher gain. As a part of such a system, the use of a 2-m surface extension (outriggers) has been investigated. The second technique involves covering the quadripod legs with metal plates to direct the scattered energy into the cold sky rather than the hot Earth. The noise temperature improvement afforded by this modification has been analyzed.

The two techniques mentioned above provide a gain improvement of approximately 0.8 to 1.4 dB (with and without outriggers, respectively) and a noise temperature improvement of 2 K, resulting in a figure of merit improvement of approximately 1.4 to 2.2 dB without outriggers and 2.0 to 3.4 dB with outriggers, depending on whether the configuration is optimized for listen-only, 2-way ranging or 2-way radar. This improvement is essentially independent of frequency and elevation angle.

II. Analytical Technique for Design of Asymmetrical-Shaped Dual-Reflector Antenna Systems

The method used for analyzing the shaped reflector modification is as follows: First, a shaped-reflector system is derived assuming a particular feedhorn and an axially symmetric geometry. The resulting main reflector surface is then used together with the tricone geometry to derive a nonsymmetric subreflector surface which preserves constant path length from the feedhorn to all points in the antenna aperture plane. The result is thus a frequency-independent design. Scattering patterns of this nonsymmetric feedhorn/subreflector combination are calculated, and the results are integrated to obtain aperture efficiency and spillover.

The basic approach for synthesizing the subreflector surface and its validity is based on a series of premises:

- (1) In order to be compatible with the tricone configuration, the main reflector should be a figure of revolution.
- (2) The nearly uniform aperture illumination which is achieved in a symmetrical, shaped system is a result of the ray distribution between the main reflector and the subreflector for a given subreflector illumination.
- (3) The subreflector amplitude illumination for the off-axis tricone system is very nearly the same as for the symmetrical system.
- (4) From (2) and (3), if the symmetrical, shaped main reflector design is utilized and a nonsymmetrical subreflector surface can be found which satisfies Snell's Law at each point of its surface, an exact frequency-independent phase solution will have been found and nearly uniform aperture illumination will result.
- (5) There exists a continuous family of subreflector surfaces which satisfy Snell's Law at each point (this is assured by the principle of normal congruence) (Ref. 2, p. 125), and from the Law of Optical Path (Ref. 2, p. 125), all of these surfaces will result in a constant path length between the off-axis feed and the main reflector aperture plane. For each of these surfaces, however, the constant path length will be different.
- (6) If a subreflector surface is computed, which results in constant path length from the feedhorn to the aperture plane, Snell's Law will be automatically satisfied for each point on the subreflector surface

and the problem is solved. This premise is not immediately obvious, but may be demonstrated as follows [it is also implied, but not explicitly stated, by Silver (Ref. 2, pp. 127-128)].

Consider Fig. 1, with the main reflector surface S_1 given by the symmetrical shaping technique. The feedhorn is located at the point A . The plane of the figure contains the point A and ray 1, the latter's geometry being uniquely determined by the given surface S_1 . S_2 is a hypothetical subreflector surface which obeys Snell's Law everywhere and passes through the point P . Consider another ray, ray 2, which intersects S_2 at the point P' . From the Law of Optical Path, the total length $AP'OQ$ equals the length $AP'O'Q'$. Still considering ray 2, consider some other intersection, point P'' . It is clear from the geometry that any selection of P'' other than at P' will result in a different total path length. Thus, with the geometry of the main to subreflector rays given, a constraint of constant total path length is sufficient to ensure that the resulting subreflector surface obeys Snell's Law.

The first step is to calculate the phase and amplitude of the scattered subreflector patterns for the asymmetrical system and demonstrate that these are substantially the same as for the shaped symmetrical system. Consider the coordinate systems shown in Fig. 2. The feed is centered at the point O , with the Z -axis its longitudinal axis, which is taken to be in the plane determined by the main reflector (Z'') axis and the point O . By a straightforward coordinate transformation,

$$X'' = \rho (\cos \phi_R \sin \theta \cos \phi - \sin \phi_R \cos \theta) + R_D \equiv A_4 \rho + R_D \quad (1)$$

$$Y'' = \rho \sin \theta \sin \phi = A_5 \rho \quad (2)$$

$$Z'' = \rho (\sin \phi_R \sin \theta \cos \phi + \cos \phi_R \cos \theta) \equiv A_6 \rho \quad (3)$$

where ρ , θ , ϕ are the polar coordinates of a point on the subreflector in the feed (X, Y, Z) coordinate system.

The next step is to determine the ρ values as a function of θ and ϕ such that intersections occur with rays from the main reflector as given by the symmetrical shaping program. Consider Fig. 3. The point O' is the origin of the X'', Y'', Z'' coordinate system. From geometry,

$$\tan \beta = \frac{H}{G} = \frac{X_p - [(X'')^2 + (Y'')^2]^{1/2}}{Y_p - A + Z''} \quad (4)$$

or

$$(X'')^2 + (Y'')^2 + A_1 (Z'')^2 + A_2 Z'' + A_3 = 0 \quad (5)$$

where

$$A_1 \equiv -\tan^2 \beta \quad (6)$$

$$A_2 \equiv 2 \tan \beta [X_p - \tan \beta (Y_p - A)] \quad (7)$$

$$A_3 \equiv -[X_p^2 - 2X_p \tan \beta (Y_p - A) + \tan^2 \beta (Y_p - A)^2] \quad (8)$$

Combining Eqs. (5) through (8) with Eqs. (1) through (3),

$$A_7 \rho^2 + A_8 \rho + A_9 = 0 \quad (9)$$

where

$$A_7 = A_4^2 + A_5^2 + A_1 A_6^2 \quad (10)$$

$$A_8 = 2A_4 R_D + A_2 A_6 \quad (11)$$

$$A_9 = A_3 + R_D^2 \quad (12)$$

Thus, for each θ, ϕ direction, Eq. (9) may be solved to provide a table of ρ values corresponding to each point on the shaped main reflector surface. The next step is to determine, from this table, the correct $\rho(\theta, \phi)$ which satisfies the constant path length constraint. From Fig. 3,

$$\ell_1 = \rho \quad (13)$$

$$\ell_2 = G/\cos \beta = \frac{(Y_p - A)}{\cos \beta} + \frac{A_6 \rho}{\cos \beta} \quad (14)$$

$$\ell_3 = Y_p \quad (15)$$

The total path length C_T is given by

$$C_T = \ell_1 + \ell_2 + \ell_3 = A_{10} + \left(1 + \frac{A_6}{\cos \beta}\right) \rho \quad (16)$$

where

$$A_{10} = [Y_p + (Y_p - A)/\cos \beta] \quad (17)$$

A set of C_T values, $C_T(N)$, is thus computed corresponding to each point on the main reflector surface. By search of this table, a pair of values is found which bracket the correct given value C_0 . The correct ρ value is then found by interpolation between the corresponding pair of ρ values.

A computer program has been written and utilized to generate the subreflector coordinates and calculate the resulting scattered fields. Numerical results, which show excellent performance, will be given in a future reporting.

III. Noise Temperature Reduction by Quadripod Coverings

A number of tests have been performed in which the system noise temperature of a given feedcone has been measured both on the ground and when antenna-mounted. Although there is considerable scatter in the available data, the antenna-mounted temperatures are consistently higher by 2–4 K. This temperature increase arises primarily from four sources: (1) direct spillover of subreflector scattered energy past the paraboloid edge, (2) scattering of the subreflector scattered energy to the ground by the quadripod, (3) scattering of the feedhorn spillover by the quadripod to the ground, and (4) scattering of the antenna aperture radiation by the quadripod to the ground.

An attempt has been made to derive the observed antenna temperature increase by calculation. To perform this calculation, the antenna was taken to be pointed at zenith and the quadripod was assumed to scatter energy isotropically. A double integration of the scattered energy was performed; the first integration involved the amount of energy intercepted by the quadripod leg as a function of the position along the leg, and the second involved the solid angle subtended by the ground as a function of the position along the leg. Weighting by the amplitude illumination function was included. The results are in general agreement with the observed data and are given in Table I.

In general, the components in Table 1 are difficult to experimentally verify. An attempt was made, however, to experimentally verify component number 5, the direct rear spillover. Since the edge of the antenna occurs at an angular position in the illumination function for which rapid cutoff occurs, this component should be a function of the subreflector axial position. The variation with axial position was calculated from subreflector scattered pattern data to be 0.0048 K per cm of subreflector travel. Data were taken¹ and showed a value of 0.0036 K per cm of travel. While this agreement is not perfect, it shows that the value for component 5 is not grossly in error.

Item 4 in the above table arises from the fact that some of the quadripod scattering is in low elevation angle directions. The value for this effect was obtained by integrating the sky temperature over all directions and subtracting out the zenith value.

It is proposed that items 2, 3, and 4 above may be virtually eliminated by covering the quadripod legs with metal sheets. Since the quadripod has been observed to

¹By Dr. C. T. Stelzried, JPL Communications Elements Research Section.

behave as though it is essentially 100% opaque (by comparison of measured and calculated secondary patterns), such a modification should not significantly affect the antenna gain. The purpose of the leg coverings is to direct the quadripod scattering into the paraboloid and then into the cold sky. To evaluate this concept, a computer program was written to calculate the scattered energy ray directions. Because the quadripod is trapezoidal in cross section, there are four different ray paths to consider: (1) the ray from the antenna focus to the inner side of the quad leg to the paraboloid and out, (2) the ray from the antenna focus to the side of the quad leg to the paraboloid and out, (3) the ray from the aperture to the inner side of the quad leg and out, and (4) the ray from the aperture to the side of the quad leg and out. The calculations showed these ray directions to vary only slightly with position on the quad leg. The resulting ray directions are given in Table 2.

Thus, for evaluation angles above 10 deg, component 2 (Table 1) is eliminated. Component 3 is eliminated for

elevation angles above 55 deg. Component 4 is eliminated and component 1 is reduced to 0.1 deg by use of the low subreflector edge illumination desired in the shaping procedure. Component 5 is a function of elevation angle below an elevation angle of 62 deg. Taking all of the components into account, Fig. 4 shows the differential antenna temperature as a function of elevation angle for the improved system. Also shown is the observed effect for the tricone/SCU configuration. This curve was obtained by subtracting the atmospheric noise contribution from the observed system temperature as a function of elevation angle. A constant noise component was then subtracted out to fit the differential antenna temperature to 3.0 K at zenith.

A final curve in Fig. 4 is the ratio of the existing to improved system noise temperatures versus elevation angle, expressed in dB improvement. It can be seen that the proposed technique of covering the quadripod legs offers an improvement of 0.5–0.6 dB as a function of elevation angle.

References

1. Ludwig, A. C., "Antennas for Space Communications: Shaped Reflector Cassegrainian Antennas," in *Supporting Research and Advanced Development*, Space Programs Summary 37-35, Vol. IV, pp. 266–268. Jet Propulsion Laboratory, Pasadena, Calif., Oct. 31, 1965.
2. Silver, S., *Microwave Antenna Theory and Design*. McGraw-Hill Book Co., Inc., New York, 1949.

Table 1. Calculated differential antenna temperature components

Component	Zenith noise contribution, K
1. Quadripod scattering of horn spillover	0.7
2. Quadripod scattering of subreflector illumination	0.8
3. Quadripod scattering of aperture radiation	0.7
4. Quadripod scattering to the atmosphere	0.1
5. Direct rear spillover	0.7
Total	3.0

Table 2. Quadripod ray directions to antenna axis

Ray	Direction, deg
1	10.2
2	0.1
3	54.8
4	4.9

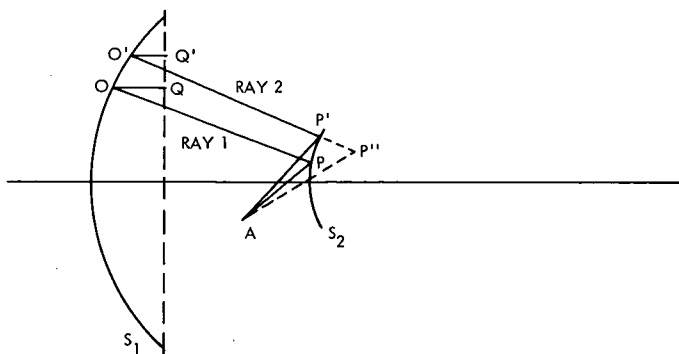


Fig. 1. Path length geometry

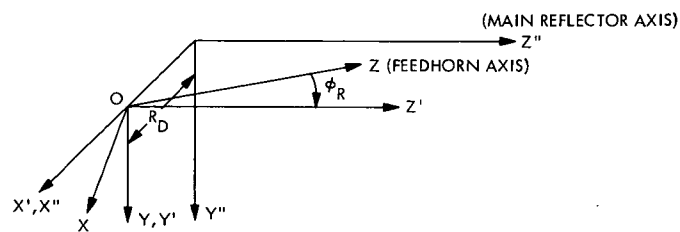


Fig. 2. Coordinate systems

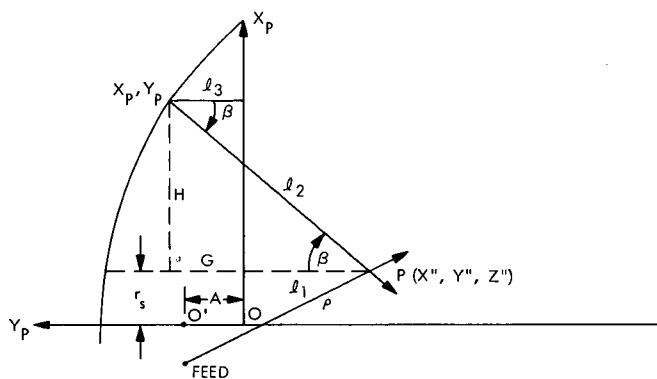


Fig. 3. Ray intersection geometry

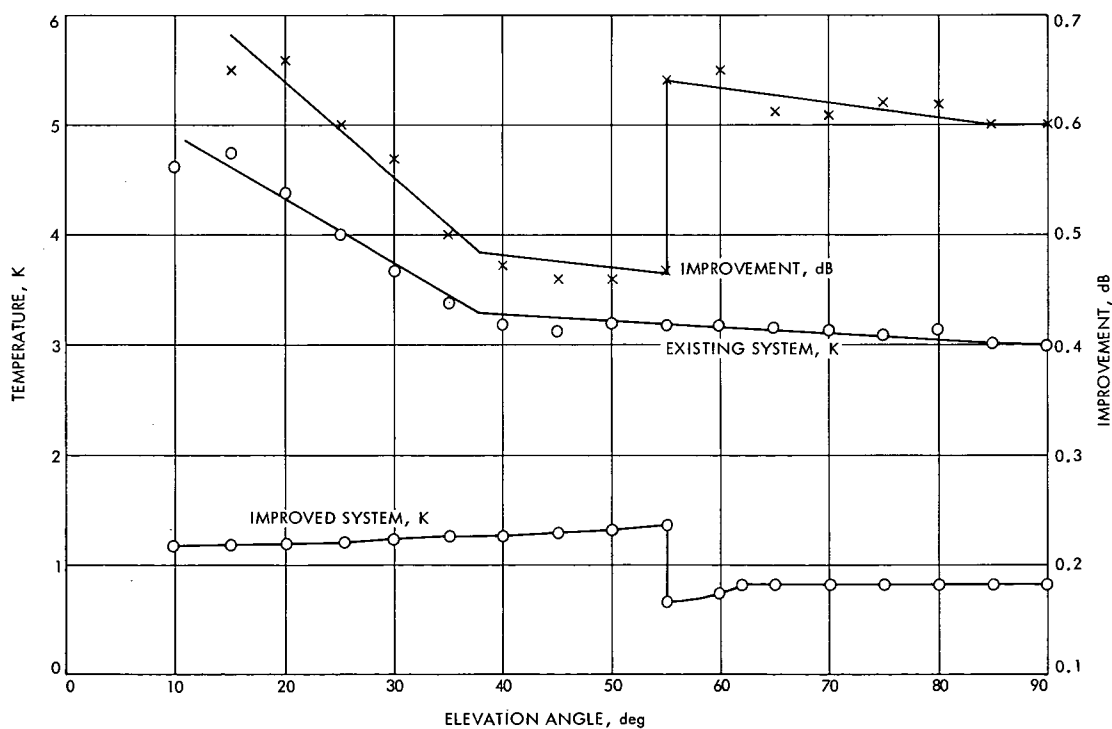


Fig. 4. Quadripod and spillover noise effect

Network Engineering and Implementation: S- and X-Band Feed System

P. D. Potter

Communications Elements Research Section

In support of the Mariner 1973 X-band experiment, it is necessary to implement a dual-frequency microwave feed system for the DSS 14 64-meter-diameter antenna. To fulfill this requirement, a particularly attractive approach, the reflex feed system, is being implemented. The reflex feed configuration and its calculated aperture efficiency performance were described in a previous reporting. Additionally, calculated radio frequency (RF) power dissipation data for the reflex feed were reported. In this article, two questions are analyzed: (1) the S-band effects of possible buckling of the dichroic flat plate caused by RF and solar heating, and (2) the effect of subreflector backscatter on the S-band focus characteristics of the antenna.

I. Effect of Flat-Plate Distortion

As described in the previous reporting (Ref. 1), when the antenna is transmitting at the 400-kilowatt level, approximately 50 watts are dissipated in the relatively thin dichroic flat plate, indicating a possible problem with physical distortion relative to the desired flat surface. An analysis has been performed to determine the effect of buckling on forward spillover and antenna gain. The configuration analyzed is shown in Fig. 1.

The essentially rigorous analysis technique utilized for computing scattered patterns and the results for no data distortion were previously reported (Ref. 1). Four additional cases have been computed: $h = -2.54$ cm, $h = -1.27$ cm, $h = +1.27$ cm, and $h = +2.54$ cm (see Fig. 1). Flat-plate scattered patterns for $m = 1$ ellipsoid illumination and for $h = -1.27$ cm, $h = 0$, and $h =$

$+1.27$ cm are shown in Figs. 2, 3, and 4, respectively. By use of the efficiency program the gain loss as a function of buckling height h was computed; the result is shown in Fig. 5 together with the forward spillover as a function of buckling height. The effect of the forward spillover on gain is included in the gain loss curve of Fig. 5. A future reporting will discuss techniques which will be utilized to control flatness of the dichroic plate.

II. Effect of Subreflector Backscatter on the S-Band Focus Characteristic

The antenna gain, as a function of the axial location of the feed system phase center, may be readily computed. For displacements relative to the paraboloid focus, which are small relative to the antenna physical dimensions, the gain loss is symmetrical with respect to the position which

yields maximum gain. Moreover, for defocusing losses less than approximately 1 dB, the loss is almost exactly quadratic in focus position. Thus,

$$G_{DB}(x) \simeq G_{0DB} - A_2(x - x_0)^2, \text{ dB} \quad (1)$$

where

$G_{DB}(x)$ = antenna gain, dB

G_{0DB} = antenna gain at maximum, dB

A_2 = a constant

x = focus position

x_0 = focus position for maximum gain

When the gain of a cassegrainian antenna, such as the 64-meter-diameter antenna at DSS 14, is measured as a function of focus position of the subreflector, a curve is obtained which is not quadratic as predicted by simple analysis. As a pertinent example, a 64-meter S-band focus curve measured and reported by Levy, et al. (Ref. 2), is shown in Fig. 6. It can be seen in Fig. 6 that a rapidly varying gain loss component is superimposed on the expected variation given by Eq. (1). The effect is qualitatively predicted as follows: A part of the energy scattered by the subreflector is directed toward the feedhorn. Of the energy intercepted by the S-band feedhorn, approximately one-half is captured and appears at the horn output. The remainder is scattered by the feedhorn back toward the subreflector. The phase of this scattered energy relative to the original horn radiation varies cyclically with the horn-to-subreflector spacing (i.e., the focus position) with a period of 1 cycle for every half wavelength of focus movement.

The voltage magnitude of the reflected energy at the feedhorn output is (Ref. 3)

$$|\Gamma| = \frac{G_0}{8\pi M} \cdot \frac{\lambda}{c} \quad (2)$$

where

$|\Gamma|$ = voltage reflection coefficient

G_0 = horn power gain

M = cassegrain magnification factor

$2c$ = cassegrain foci separation

λ = wavelength

For the 64-meter antenna at S-band, $|\Gamma| = 0.0247$, or -32 dB, a value which agrees with experimental tests.

If the horn scattering pattern were the same as the horn radiation pattern, Eq. (2) would predict a cyclical gain variation of 0.4 dB peak-to-peak as a function of focus position, a serious effect. An attempt was made, by hand calculation, to determine the cyclical component in the *Surveyor* focus curve of Fig. 6.

The function which was selected for fitting to the *Surveyor* data was

$$G'DB(x) \equiv [A_0 + A_1x + A_2x^2] + [S_0 + S_1x] \cos\left(\frac{4\pi x}{\lambda} - c\right) \quad (3)$$

where A_0 , A_1 , A_2 , S_0 , S_1 , and c were taken as unknown coefficients. As a fitting criterion, the coefficients were iteratively perturbed to minimize the rms error between Eq. (3) and the nine data points. The resulting coefficient values were

$$A_0 = -0.01572679 \text{ dB}$$

$$A_1 = -0.02980314 \text{ dB/cm}$$

$$A_2 = -0.02403280 \text{ dB/cm}^2$$

$$S_0 = 0.0527394 \text{ dB}$$

$$S_1 = -0.00395247 \text{ dB/cm}$$

$$c = 1.2879880 \text{ radians}$$

The resulting fit is shown in Fig. 7 and the two focus components in Fig. 8. As a partial check, the coefficient A_2 had been previously determined,¹ for uniform paraboloid illumination, with the Radiation Program as -0.02244 dB/cm². A recent computation for the 64-meter tricone system, including the phase and amplitude illumination functions, yielded a value of -0.02126 dB/cm².

As shown in Fig. 8, the reflection effect displaced the point of maximum gain by 0.6 cm. For the reflex feed, if the antenna were focused for S-band, a serious X-band gain loss could result. Thus, it would be desirable to be able to accurately determine the amplitude and phase of the cyclical component from focusing data and to have a means of adjusting the phase angle c to bring this component's maximum into alignment with the X-band focus maximum and essential alignment with the unperturbed S-band maximum. To achieve this objective, provision is being made for adjustment of the ellipsoid tilt and the dichroic flat-plate position and tilt to change the S-band

¹M. S. Katow, JPL DSIF Engineering Section, private communication.

path length to the subreflector without focusing the subreflector.

It is presently planned to develop a curve-fitting computer program which will rapidly determine the amplitude and phase of the cyclical component from measured focus

data and, from this information, determine the proper direction and magnitude of the reflex feed adjustments. Additionally, studies will be made of the best way to take the focus data (e.g., number of points and spacing) to minimize the station time and the error in the phase and amplitude determination.

References

1. Potter, P. D., "S- and X-Band RF Feed System," in *The Deep Space Network Progress Report*, Technical Report 32-1526, Vol. IX, pp. 141-146. Jet Propulsion Laboratory, Pasadena, Calif., June 15, 1972.
2. Levy, G. S., et al., "Lunar Range Radiation Patterns of a 210-Foot Antenna at S-Band," *IEEE Transactions on Antennas and Propagation*, Vol. AP-15, No. 2, pp. 311-313, Mar. 1967. Also available as Technical Report 32-1079, Jet Propulsion Laboratory, Pasadena, Calif.
3. Rusch, W. V. T., and Potter, P. D., *Analysis of Reflector Antennas*, p. 106. Academic Press, Inc., New York, 1970.

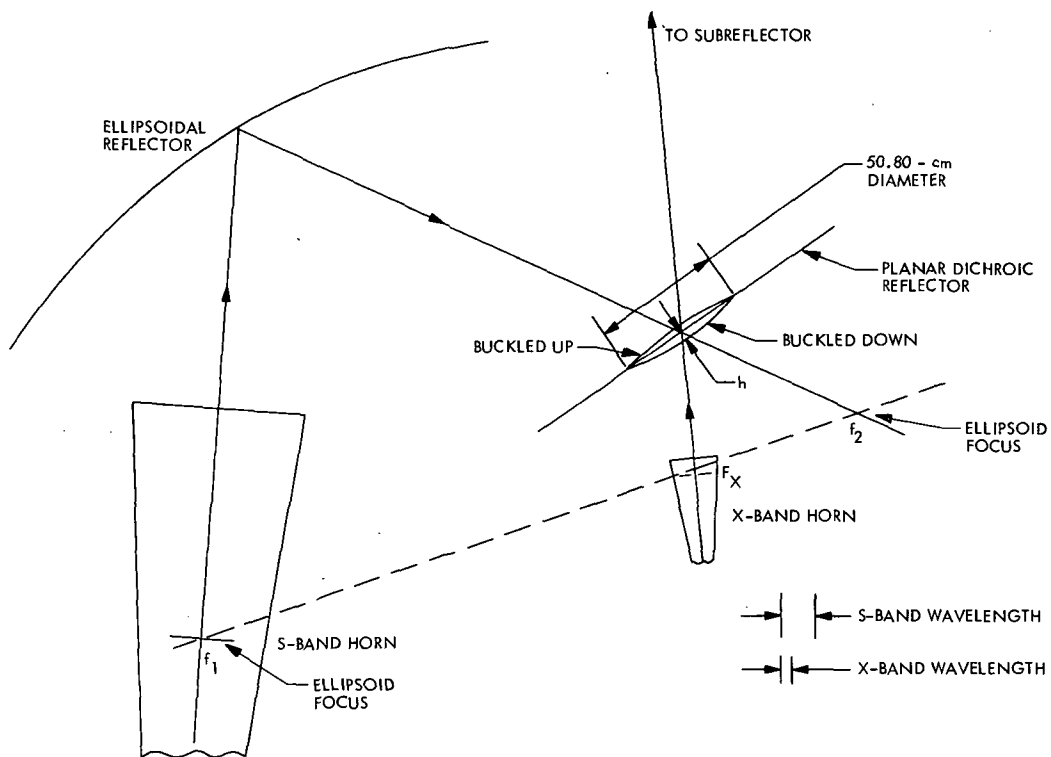


Fig. 1. Geometry of distorted flat plate

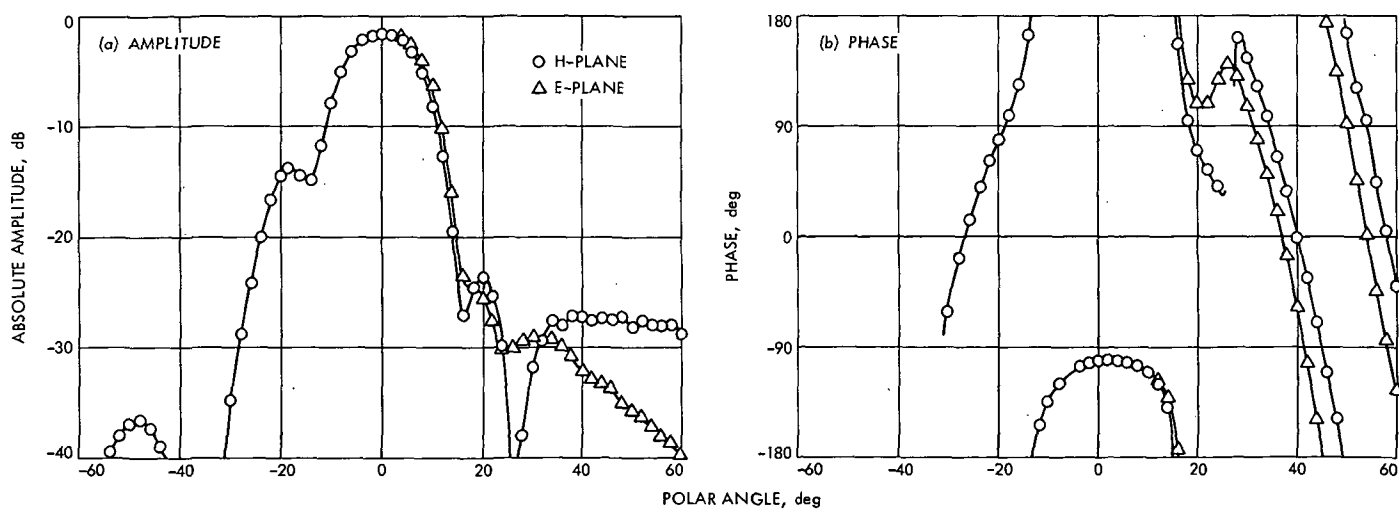


Fig. 2. Flat-plate scattered pattern, $h = -1.27$ cm

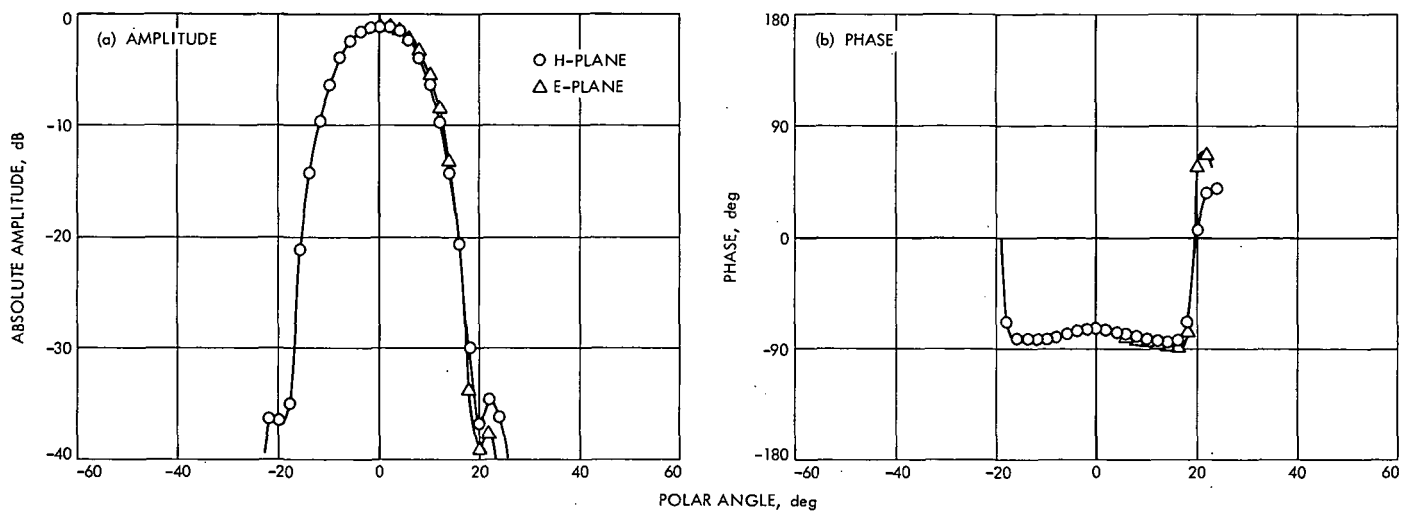


Fig. 3. Flat-plate scattered pattern, $h = 0$ cm

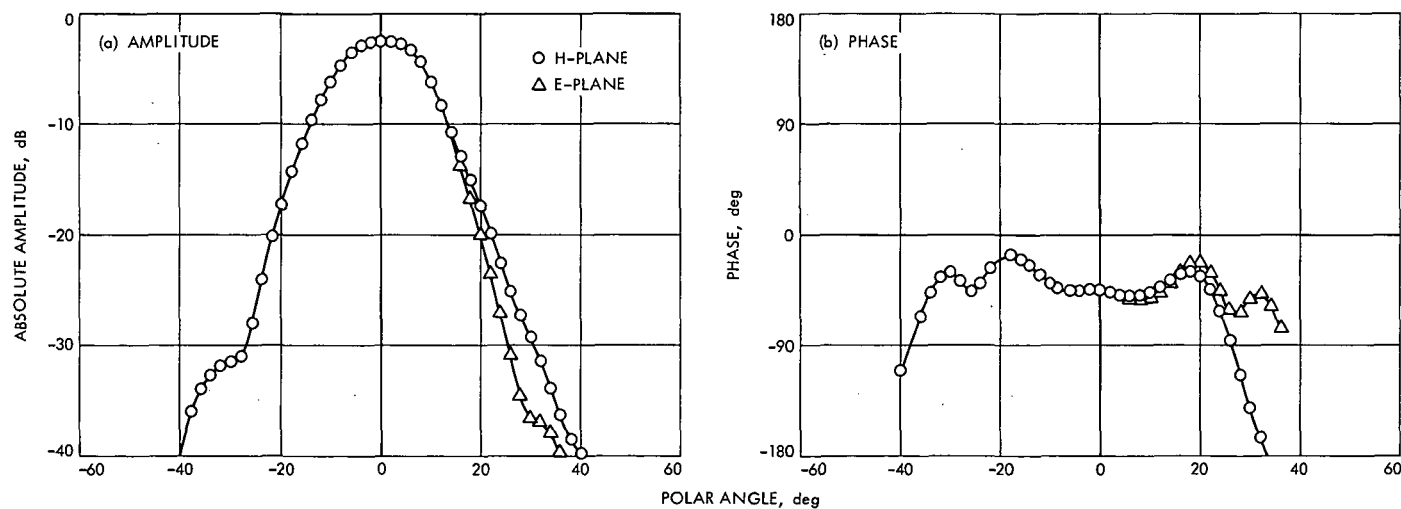


Fig. 4. Flat-plate scattered pattern, $h = +1.27$ cm

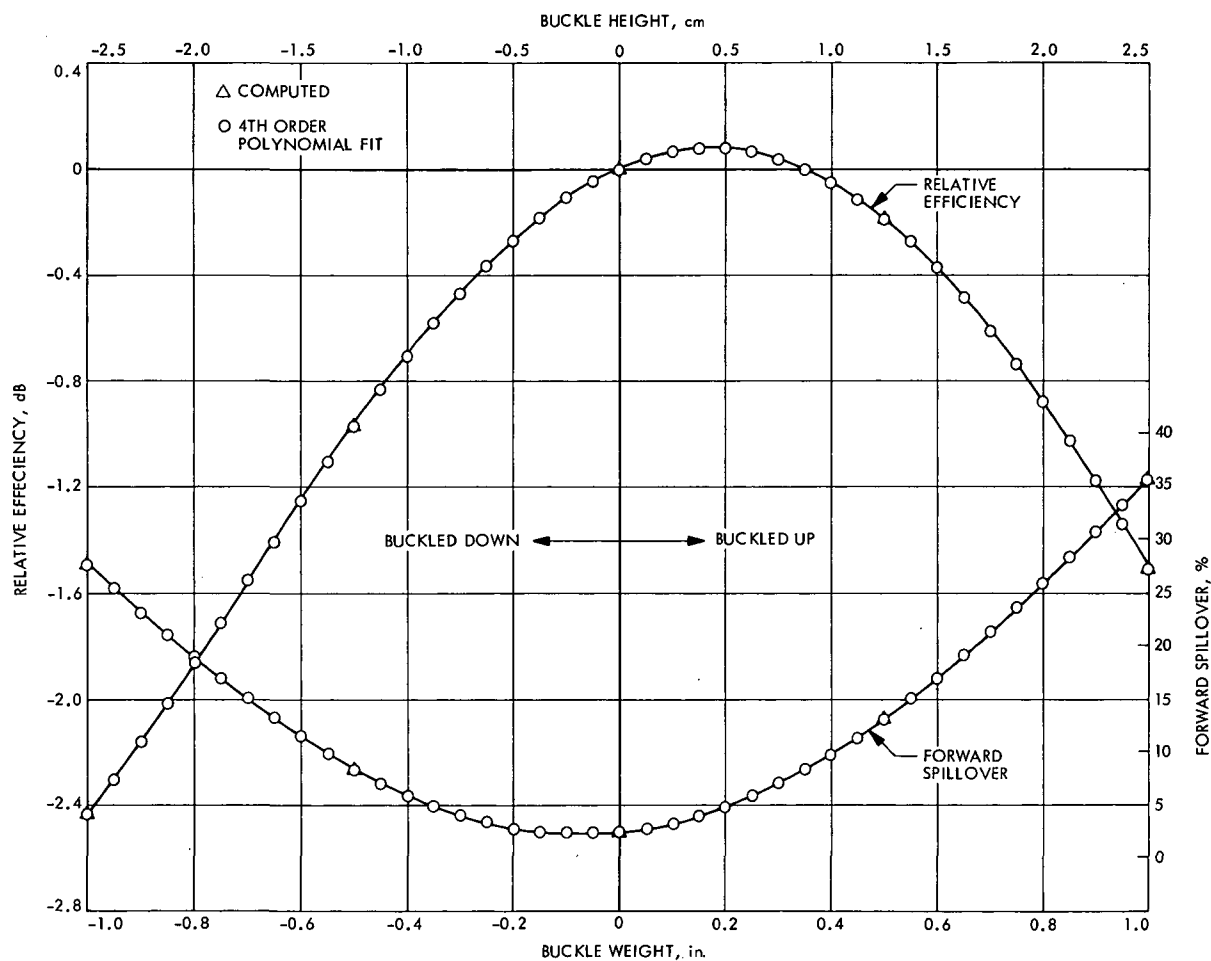


Fig. 5. Forward spillover and relative antenna efficiency vs dichroic plate buckling height

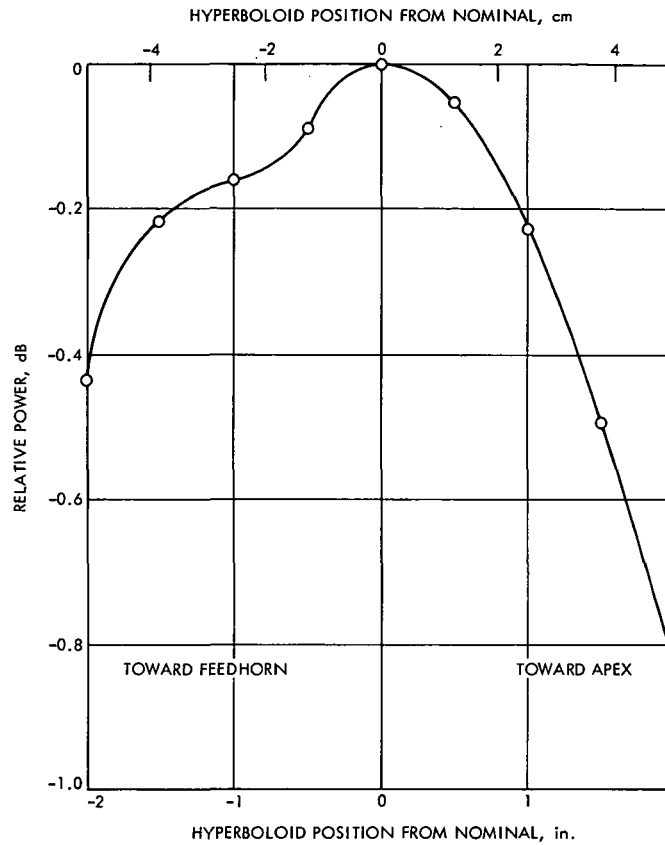


Fig. 6. 64-meter antenna Surveyor focus curve

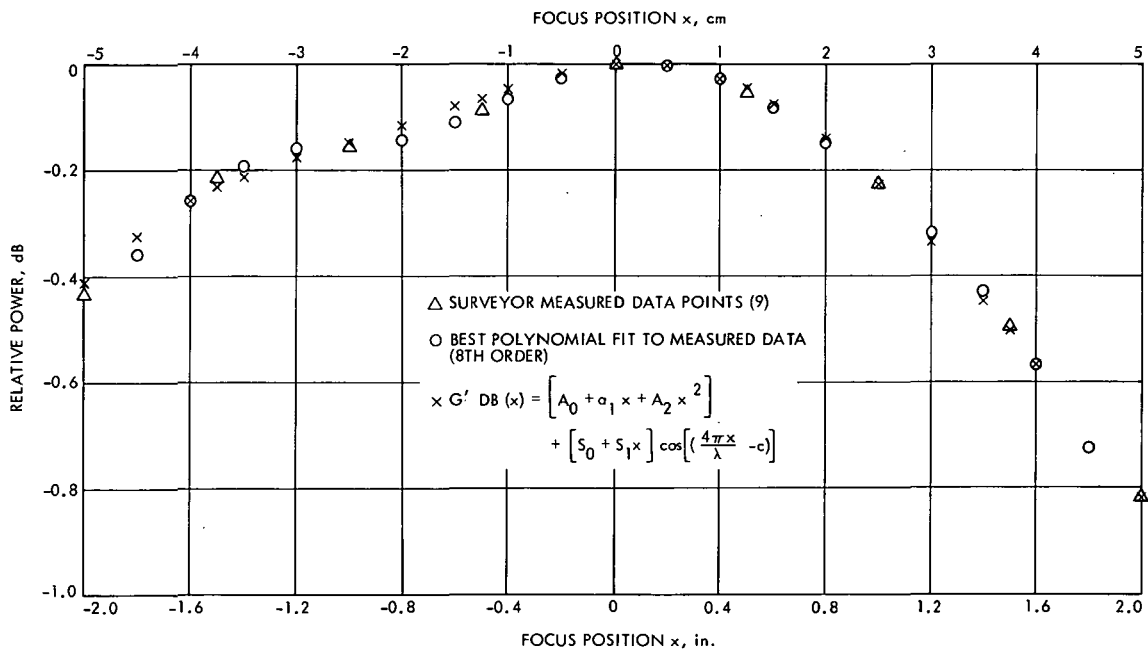


Fig. 7. Surveyor focus data fit

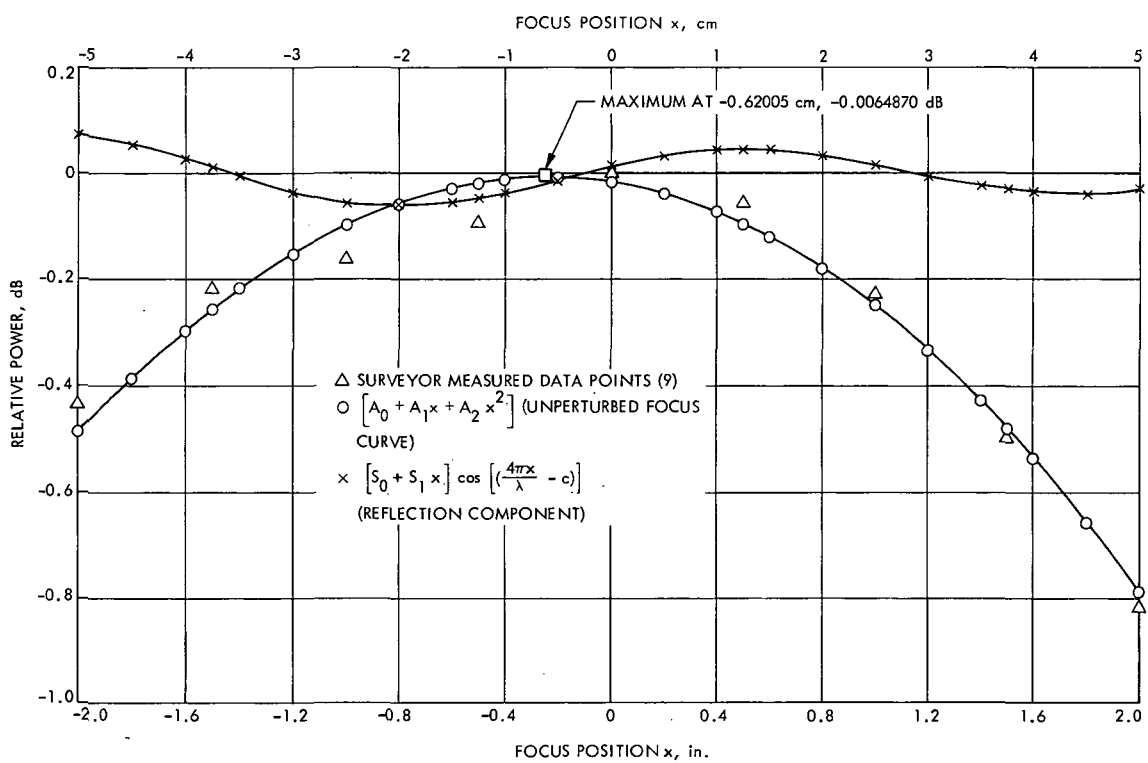


Fig. 8. Surveyor focus data components

Error Analysis of Precision Calibrations of Perforated Plate Mesh Materials on a Tuned Reflectometer System

T. Y. Otoshi

Communications Elements Research Section

This article presents an error analysis of a waveguide technique for precision reflectivity loss measurements of perforated plate mesh materials useful for antenna surfaces, dichroic plates, or RF shields. It is shown that by use of a prescribed experimental procedure, the maximum reflectivity loss measurement error due to imperfect system tuning can typically be kept to less than ± 0.002 dB.

I. Introduction

Perforated plates are useful for such applications as antenna surfaces, dichroic plates, and RF shielding. When the aperture size is small compared to wavelength, it is possible to measure many of the perforated plate RF properties in rectangular waveguides. The waveguide method enables such properties as reflection and transmission coefficients to be measured to a high degree of precision and accuracy.

In a previous article (Ref. 1), it was shown that a waveguide technique can be used to make precision reflectivity loss measurements of perforated plate mesh materials used on antenna surfaces. Overall accuracies of the order of ± 0.005 dB were achieved by use of a prescribed measurement procedure, a dual-channel tuned reflectometer system, and a high-precision insertion loss test set. This article presents the error analysis equation applicable to the measurement technique.

II. Measurement Technique

Figure 1 is a block diagram of the tuned-reflectometer system employed for precision reflectivity loss measurements. The system operates on the dual-channel principle and utilizes a high-precision insertion loss test set (Refs. 2 and 3). Comparisons of the reflected power from the mesh sample and that from a reference short-circuit are made on the insertion loss test set.

A major error in mesh reflectivity loss measurements can be caused by the residual internal reflection coefficient Γ_{2i} as seen looking back into the reflectometer system at the measurement plane. This reflection coefficient can be made small by sliding a short-circuit and adjusting tuner B so that the reflectometer output variations become negligibly small (Ref. 4). In general, it is difficult to reduce the peak-to-peak output variation to less than 0.02 dB. However, it is shown in the following error

analysis that although the peak-to-peak output variation of 0.02 dB can result in a maximum error of ± 0.01 dB, the error on mesh reflectivity loss measurements can generally be reduced to less than ± 0.002 dB if a flat-plate short is used to establish the measurement reference plane and if the mesh sample is then placed at the same reference plane. If a sample holder is used, one can insert a flat-plate short into the sample holder and use the sample holder-short combination to establish the measurement reference plane.

III. Error Analysis

If a dual-channel reflectometer system of the type shown in Fig. 1 is linear and has sufficient isolation between test and reference channel couplers, the error analysis simplifies to that for a single-channel reflectometer system such as the one shown in Fig. 2. When a reference offset short and an unknown load are respectively connected to port 2, the equations for the output voltage waves at port 3 are (Ref. 5)

$$b_{3S} = \frac{B\Gamma_S \left(1 + \frac{1}{K\Gamma_S}\right)}{1 - \Gamma_{2i}\Gamma_S} \quad (1)$$

$$b_{3U} = \frac{B\Gamma_U \left(1 + \frac{1}{K\Gamma_U}\right)}{1 - \Gamma_{2i}\Gamma_U} \quad (2)$$

where

Γ_S, Γ_U = voltage reflection coefficients of the reference offset short and load being calibrated, respectively

B = system constant

K = complex quantity whose magnitude is approximately equal to the directivity ratio ($\gg 1$) of the test channel coupler

Γ_{2i} = internal reflection coefficient of the reflectometer system as seen looking into port 2

Measured reflectivity loss relative to the reference short is defined as

$$R'_{dB} = -20 \log_{10} \left| \frac{b_{3U}}{b_{3S}} \right| \quad (3)$$

while the true relative reflectivity loss is

$$R_{dB} = -20 \log_{10} \left| \frac{\Gamma_U}{\Gamma_S} \right| \quad (4)$$

Then, from subtraction of Eq. (4) from Eq. (3) and substitutions of Eqs. (1) and (2), the error equation can be derived as

$$\epsilon_{dB} = 20 \log_{10} \left| \left(\frac{1 + \frac{1}{K\Gamma_S}}{1 + \frac{1}{K\Gamma_U}} \right) \left(\frac{1 - \Gamma_{2i}\Gamma_U}{1 - \Gamma_{2i}\Gamma_S} \right) \right| \quad (5)$$

For mesh calibrations it is valid to assume that

$$|\Gamma_U|, |\Gamma_S| \approx 1$$

and

$$|\Gamma_{2i}|, \frac{1}{|K|} \ll 1$$

Hence, Eq. (5) simplifies to

$$\epsilon_{dB} \approx 20 \log_{10} \left| 1 + (\Gamma_U - \Gamma_S) \left(\frac{1}{K} - \Gamma_{2i} \right) \right| \quad (6)$$

It follows that

$$|\epsilon_{dB}|_{MAX} \leq 20 \log_{10} \left[1 + |\Gamma_U - \Gamma_S| \left(\frac{1}{|K|} + |\Gamma_{2i}| \right) \right] \quad (7)$$

and for $|\Gamma_U - \Gamma_S| \ll 1$,

$$|\epsilon_{dB}|_{MAX} \leq 8.686 |\Gamma_U - \Gamma_S| \left(\frac{1}{|K|} + |\Gamma_{2i}| \right) \quad (8)$$

In the preparation of test samples it is important that the metallic reflecting surface of the mesh be located at the same distance l from the input flange as the end plate is for the reference offset short (see Fig. 2). Furthermore, the waveguides for the mesh sample holder and reference short should be made from the same material and have the same mechanical dimensions. If these conditions are fulfilled, we may write

$$\Gamma_S \simeq - \left(1 - \frac{2R_S}{\eta_0} \right) e^{-2\gamma l} \quad (9)$$

$$\Gamma_U = S_{11} e^{-2\gamma l} \quad (10)$$

where

R_S = surface resistivity of the end plate, ohms/square

$\eta_0 = 120\pi$, ohms

S_{11} = reflection coefficient of the mesh defined at its metallic reflecting surface

$$\gamma = \alpha + j\beta$$

and α is the attenuation constant (nepers/m), and β is the phase constant (radians/m).

For typically good reference shorts made from high quality copper, the reflection coefficient magnitudes will be very close to unity (Ref. 6). Hence, we may assume $\Gamma_s \simeq -e^{-2\gamma l}$. Substitution into Eq. (8) results in

$$\begin{aligned} |\epsilon_{dB}|_{MAX} &\leq 8.686 e^{-2\alpha l} |1 + S_{11}| \left(\frac{1}{|K|} + |\Gamma_{2i}| \right) \\ &\leq 8.686 |1 + S_{11}| \left(\frac{1}{|K|} + |\Gamma_{2i}| \right) \end{aligned} \quad (11)$$

For convenience of error study, it is desirable to express the error equation in terms of quantities that are usually measured in the calibration procedure. It was shown by Anson (Ref. 4) that when the reflectometer is tuned for small $|\Gamma_{2i}|$, then

$$|\Gamma_{2i}| \approx \frac{M_{dB}}{2(8.686)} \quad (12)$$

where M_{dB} is the peak-to-peak dB output variation of the signal at port 3 when a movable short is connected to port 2 and then slid. After expressing the directivity ratio $|K|$ in dB and substituting Eq. (12) into Eq. (11), the error equation becomes

$$\begin{aligned} |\epsilon_{dB}|_{MAX} &\leq \underbrace{8.686 |1 + S_{11}| 10^{-K_{dB}/20}}_{\text{Directivity error term}} + \underbrace{\frac{M_{dB}}{2} |1 + S_{11}|}_{\Gamma_{2i} \text{ Error term}} \\ &\quad (13) \end{aligned}$$

In the above it can be seen that the directivity error term is generally small because K_{dB} is typically 70 dB or greater. In addition, since most good meshes behave almost like a short-circuit load (i.e., $S_{11} \simeq -1$), it can also be seen that the error due to either term will be small.

Typical good meshes will have reflectivity loss less than 0.2 dB and phase angles within 10 deg of that for a short-circuit. These properties can be described mathematically as

$$0.977 \leq |S_{11}| \leq 1.0$$

$$170^\circ \leq \psi_{11} \leq 180^\circ$$

For mesh materials having these properties, Fig. 3 shows the maximum error curves based on Eq. (13) and typical values of K_{dB} and M_{dB} . For example, when a reflectometer system is tuned for 70 dB directivity and 0.02 dB peak-to-peak output variation when a sliding short is slid, the maximum error on reflectivity loss measurement is ± 0.0022 dB. These are typical system tuning values that are easy to obtain in practice. For more accuracy the reflectometer system can be tuned to give smaller residual errors.

IV. Conclusions

An error analysis has been presented to show that by use of a prescribed measurement procedure, reflectivity loss measurement errors due to imperfect system tuning can be reduced to about ± 0.002 dB. To achieve the improved accuracy using this procedure, it is also required that (1) the mesh sample reflectivity loss be less than 0.2 dB, (2) the mesh reflection coefficient phase angle be within 10 deg of the phase angle of the reference flat-plate short, and (3) the directivity of the test channel coupler be tuned to at least 70 dB.

References

1. Otoshi, T. Y., and Lyon, R. B., "Improved RF Calibration Techniques: A Study of the RF Properties of the 120-ft-diam Antenna Mesh Material," in *The Deep Space Network*, Space Programs Summary 37-66, Vol. II, pp. 52-57. Jet Propulsion Laboratory, Pasadena, Calif., Nov. 30, 1970.
2. Finnie, C. J., Schuster, D., and Otoshi, T. Y., *AC Ratio Transformer Technique for Precision Insertion Loss Measurements*, Technical Report 32-690. Jet Propulsion Laboratory, Pasadena, Calif., Nov. 30, 1964.
3. Otoshi, T. Y., Stelzried, C. T., Yates, B. C., and Beatty, R. W., "Comparisons of Waveguide Losses Calibrated by the DC Potentiometer, AC Ratio Transformer, and Reflectometer Techniques," *IEEE Trans. on Microwave Theory and Techniques*, Vol. MTT-18, No. 7, pp. 406-409, July 1970.
4. Anson, W. J., "A Guide to the Use of the Modified Reflectometer Technique of VSWR Measurement," *J. Res. NBS*, Sec. C, Vol. 65C, No. 4, pp. 217-223, October-December 1961.
5. Kerns, D. M., and Beatty, R. W., *Basic Theory of Waveguide Junctions and Introductory Microwave Network Analysis*, pp. 111-114. Pergamon Press, New York, 1967.
6. Beatty, R. W., and Yates, B. C., "A Graph of Return Loss Versus Frequency for Quarter-Wavelength Short-Circuited Waveguide Impedance Standards," *IEEE Transactions on Microwave Theory and Techniques*, Vol. MTT-17, No. 5, pp. 282-284, May 1969.

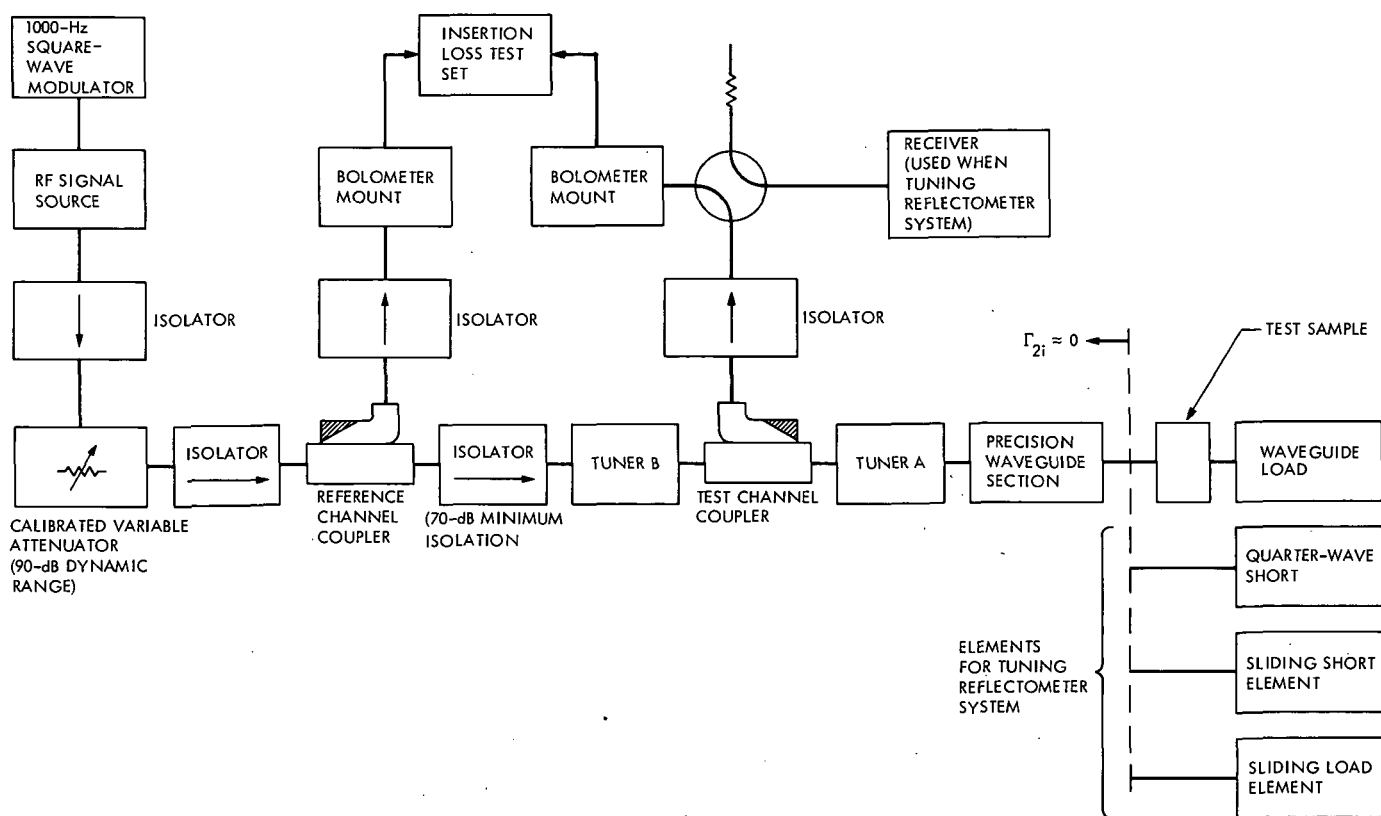


Fig. 1. Block diagram of waveguide system for mesh reflectivity measurements

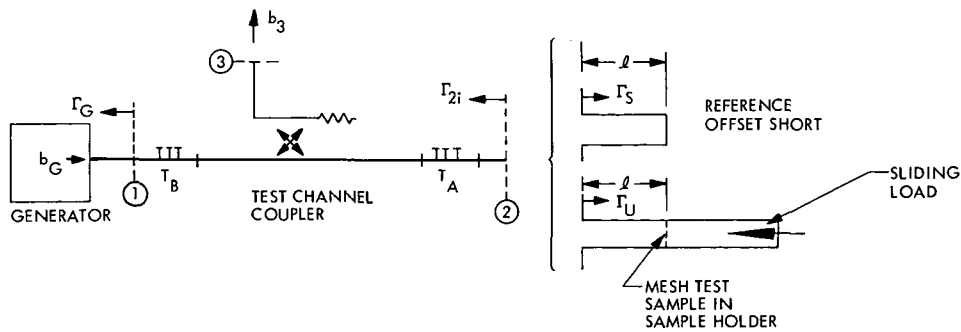


Fig. 2. Simplified block diagram of reflectometer system for error analysis

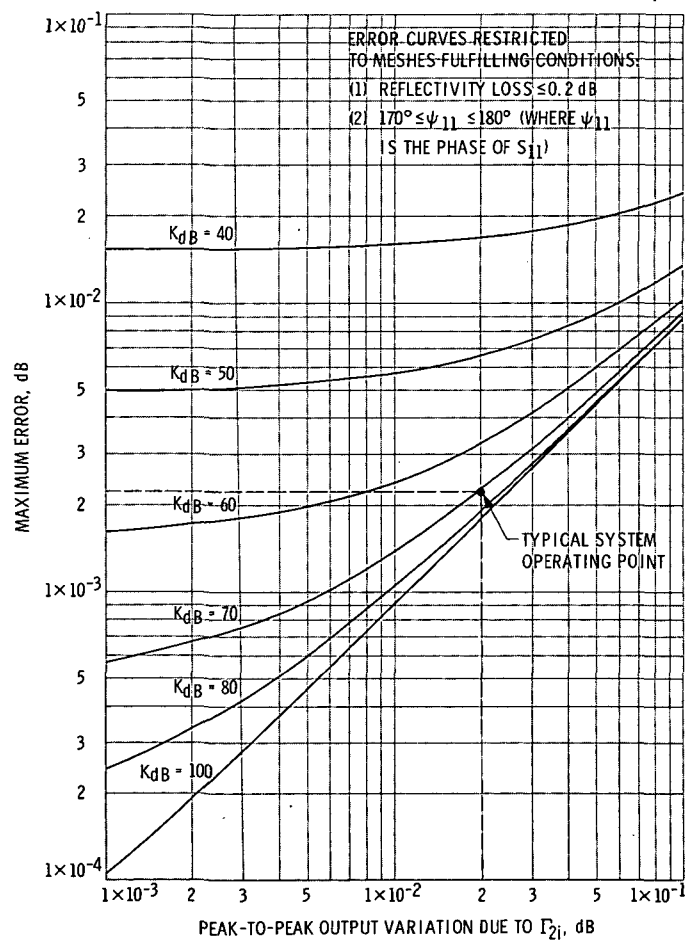


Fig. 3. Maximum error due to residual tuning errors on measurement of reflectivity losses of meshes or short-circuits

DSN Research and Technology Support

E. B. Jackson
R. F. Systems Development Section

The activities of the Development Support Group, including the Microwave Test Facility, during the two-month period ending June 15, 1972, are summarized. Activities include operational clock synchronization, precision antenna gain measurements, weak source observations, pulsar observations, demonstration of SCOUR computer program for automatic antenna tracking, planetary radar experiments, dual-carrier measurements, and shipment of the tricone support structure. Activities at the Microwave Test Facility include DSN klystron testing and general machine shop and other support for the Venus Station. Significant maintenance activities include replacement of an azimuth drive gear reducer and rework of the elevation ball screw nuts on the 26-m-diameter antenna.

During the two months ending June 15, 1972, the Development Support Group was engaged in the following activities.

I. DSS 13 Activities

A. In Support of Section 331

1. **Pulsars.** The Venus Deep Space Station (DSS 13) continues to devote approximately twenty-four hours per week (a total of 205 hours during this period) to the observation of pulsars. Information obtained includes pulse-to-pulse spacing, pulse time of arrival, and pulse shape. Pulsars regularly observed (about 22 of the 50 known pulsars) were tabulated in Ref. 1.

2. **Planetary radar.** As part of the support for the MVM 73 missions, ranging of the planet Venus has been

routinely accomplished using a range resolution of 1500 meters round trip, without interpolation. Range data have been collected on five separate occasions, transmitting and receiving at DSS 14, with modulation generation, control, and data processing taking place at the Venus station. Additionally, three Venus mapping experiments, identified as "active interferometer," have been successfully accomplished. In this latter experiment, both DSS 14 and DSS 13 use a very stable frequency standard (hydrogen maser) and transmissions are made from DSS 14 with reception being simultaneously accomplished at DSS 13 and DSS 14. As before, modulation generation, control, and data processing take place at DSS 13.

Additionally, the Jupiter Moon Callisto is to be a radar target, but the first scheduled attempt was unsuccessful due to inability to get the DSS 14 400-kW R&D transmitter and the DSS 13 SDS 930 computer working.

B. In Support of Section 332

1. *Tricone support structure (TCSS).* The TCSS destined for DSS 63, which has already been completely tested, was dismantled and shipped to Philco-Ford for packaging for overseas shipment. Philco-Ford has completed this packaging, and the TCSS is on its way to DSS 63.

2. *26-m antenna azimuth drive maintenance.* Another of the azimuth drive gearboxes (see Ref. 2) showed signs of incipient failure and was replaced by a previously rebuilt unit. Although still operating on only two gearboxes and hydraulic motors, the two units now in service on the 26-m antenna have been rebuilt, and the other two units are being rebuilt by the manufacturer, Falk Gear Corp.

The oil seal on one of the two elevation drive screws began leaking and required replacement. This opportunity was also utilized to rebuild the oil pumps (within the ball nuts) to assure good lubrication.

C. In Support of Section 333

1. *Precision antenna gain measurement.* Using the Apollo Lunar Surface Experiments Package (ALSEP) and the radio stars Cassiopeia A, Cygnus A, and Virgo A as calibration sources, support of this program continued. Section 333 personnel, assisted by station personnel, collected data with which absolute antenna gain and absolute flux density can be determined. During this period, 102 hours were devoted to ALSEP and 100.5 hours to the radio stars.

2. *Weak source observations.* Using almost completely automated data-taking techniques, measurements continue to be made on a number of radio stars. Thus far in 1972, data have been taken on 25 radio stars, with a wide range of declinations. From this set of 25 stars, it is hoped that a suitable set of calibration sources can be selected for use with both the 26- and 64-m subnets. This set of calibrators will have their absolute flux density determined at DSS 13 and the measurements then transferred to the rest of the network.

3. *Automatic antenna tracking.* In conjunction with a lecture covering the theoretical basis for the technique, the automatic antenna tracking capabilities of the Scan and Correct Using Receiver (SCOUR) computer program were demonstrated using ALSEP 12 and several radio stars as sources. This program, utilizing an SDS 930 computer, gives the 26-m antenna (which is not equipped with a monopulse cone or a tracking receiver) the ability

to automatically correct its "pointing" as a function of received signal strength. With minor modifications this program can be implemented at DSS 14 and provide similar capabilities for the 64-m antenna which also is not equipped with a monopulse feed or tracking receiver.

D. In Support of Section 335

1. *Dual-carrier measurements.* In further support of the Viking Project, measurements were made at DSS 13 to ascertain the best choice of channel frequencies to minimize intermodulation product interference when operating in the dual-carrier mode. Although channel frequency recommendations have been made, a thorough investigation into sources of, and techniques for eliminating, noise bursts and intermodulation products is underway. It is anticipated that the bulk of this program will be carried out at the Venus station after equipping the 26-m antenna with a diplexer, harmonic filter, and bandpass filter to simulate a 64-m antenna with a 400-kW transmitter.

E. In Support of Section 337

1. *Clock synchronization transmissions.* Routine transmissions, as scheduled by DSN scheduling, continue to those stations which have operational receivers. During this period, transmissions were made as tabulated in Table 1.

2. *DSN 400-kW transmitter support (DSS 14).* Due to the importance of the DSN 400-kW transmitter at DSS 14 to the Mariner 9 Project, an intense effort is being made to keep it operational for each committed track. This effort also includes a comprehensive training program for DSS 14 and Technical Staff personnel at Goldstone. DSS 13 aided this program by providing personnel to work shift with the DSS 14 personnel during the Mariner 9 passes for which the transmitter was committed. In addition, certain sections of the training course were taught by DSS 13 personnel while other instruction utilized DSS 13 equipment as schedule conflicts prevented the DSS 14 transmitter from being made available for training activities as much as would have been desirable.

II. Microwave Test Facility (MTF) Activities

A. In Support of Section 333

1. *Antenna panel noise burst generation.* The noise burst testing, using the antenna sections irradiated by the 20-kW transmitter, has temporarily ceased at MTF. The generation of noise by the antenna panels was discovered to be more complex than the simple mechanism of small arcs taking place between the untaped joints on the an-

tenna surface. Deeper portions of the antenna surface, when exposed to RF, also generate noise. The information collected during these experiments, coupled with the discovery that the taping on the subreflector at DSS 14 has numerous cracks in it, has contributed to a decision to launch an extensive investigation of the problem, probably at DSS 13.

B. In Support of Section 335

1. Pocket RF monitor. In view of the high power densities which are and will be present upon DSN antennas, coupled with the necessity for continuing normal operations in a safe manner, a reliable automatic RF field intensity alarm is desirable. Such a device, worn by personnel

likely to be exposed to possibly hazardous fields, would generate an aural alarm if the impinging radiation exceeded the set point, usually 1 milliwatt per square centimeter. A battery-operated low power drain breadboard model has been completed and after life testing will be repackaged into a pocket size unit for "wearability" tests.

C. In Support of Section 337

1. Klystron testing. In continuing support of the DSN transmitters, five model 4KM50SI klystrons were tested and operational parameter values measured. Data sheets were enclosed with the tubes so that DSN stations placing these tubes into service will have proven baseline values with which to work.

References

1. Jackson, E. B., "DSN Research and Technology Support," in *The Deep Space Network Progress Report*, Technical Report 32-1526, Vol. VIII, pp. 68-73. Jet Propulsion Laboratory, Pasadena, Calif., Apr. 15, 1972.
2. Jackson, E. B., and Kolbly, R. B., "DSN Research and Technology Support," in *The Deep Space Network Progress Report*, Technical Report 32-1526, Vol. IX, pp. 147-151. Jet Propulsion Laboratory, Pasadena, Calif., June 15, 1972.

Table 1. Clock synchronization activity from DSS 13

Station	Number of transmissions
DSS 14	21
DSS 41	35
DSS 42	28
DSS 51	14
DSS 62	30
USNO	22

DSN/MSFN Antenna-Pointing and Tracking Implementation

J. H. McInnis, Jr.
DSIF Digital Systems Development Section

The antenna-pointing and tracking-data processing functions at the three DSN/MSFN joint-usage ("wing") tracking stations have been altered to implement a commonality between the two networks. The changes affect both hardware and software and produce station configurations that differ from those of other DSN stations.

I. Introduction

In the latter half of calendar year 1970, a program of reconfiguration of the three DSN/MSFN joint-usage tracking stations was initiated. The goal of the DSN/MSFN integration program was the functional integration of the several equipment subsystems employed by the Deep Space Network and the Manned Space Flight Network (MSFN) at DSSs 11, 42, and 61. Part of the equipment involved was formerly included in the DSN's station hardware complement, and the remainder was formerly unique to the MSFN. As a result of the implementation of this integration program, there is now one set of joint-usage equipment which serves the needs of both networks.

II. Original Configuration, Antenna-Pointing and Tracking-Data Processing

As the joint-usage stations were originally configured, the DSN and MSFN each had a complete and separate complement of equipment to effect antenna pointing and the processing of metric data. The DSN equipment was that of a standard 26-meter station. The MSFN control

facility employed a UNIVAC-1218 computer coupled to an Antenna Position Programmer (APP) to control the antenna servo system. A Tracking Data Processor (TDP) processed MSFN metric data through-put and delivered both teletype and (MSFN-formatted) high-speed data communications outputs to the MSFN.

III. Effects of Integration on Antenna-Pointing and Tracking-Data Processing

It was determined at the start of the DSN/MSFN Integration Program that the UNIVAC-1218 computers were needed by MSFN for other applications and, conversely, that the DSN could make advantageous use of the High-Speed Data Line (HSDL) metric data reporting capability afforded by the TDP. It was decided at that time, therefore, that the various equipment should be merged by removing the UNIVAC-1218 computers and substituting the XDS-910 computers which formed a part of the DSN's Antenna Pointing Subsystem (APS) and by deleting the DSN's Tracking Data Handling Subsystem (TDH) and using the TDP as the source of DSN radio metric data for the affected stations (see Ref. 1).

The original concept would have made use of a common hardware configuration and a single computer program (for the XDS-910) capable of separate operating modes for the DSN and MSFN. During software development, however, it rapidly became apparent that the limited memory capacity of the XDS-910 (8192 words, decimal) precluded such commonality. In consequence, the final integration provided a common hardware set (not all of which is used in both operating modes) and separate operational computer programs for the DSN and MSFN operating modes (see Refs. 2, 3, and 4).

IV. Integrated Configuration—MSFN Mode

The MSFN mode of operation of the integrated station equipment employs the hardware configuration of Fig. 1 and provides the functional and operational features described in the following paragraphs.

As indicated in Fig. 1, metric data processing is entirely in the province of the TDP. Inputs from the various data sources (antenna, receiver, etc.) are automatically combined and formatted to MSFN specifications and are transferred directly from the TDP to the MSFN communications system. In this operating mode, there is no functional tie between the TDP and the APS.

Antenna pointing is accomplished by the APP under the control (either direct or indirect) of the APS XDS-910 computer. Antenna-pointing predict sets are received at the station via standard teletype. The teletype (i.e., Baudot-code) predict messages may be in either MSFN 29-point format or Inter Net Predict (INP) format. In either predict-format case, the predict teletype message tape is read directly into the XDS-910 computer via its optical tape reader. A maximum of two predict sets may be held in the computer at one time.

Once a predict set has been input, the processing proceeds at the option of the operator. Normally, the computer will be instructed to generate and verify an interpolated, time-sequenced drive tape (punched paper tape) for the APP. The use of this drive tape is considered to be a "back-up" mode of operation for the APP and the generation of the drive tape is a requirement when time permits. Approximately 2.25 minutes per hour of pass duration are required for punching and, in addition, approximately two minutes per hour of the pass for tape verification. APP drive tapes normally are computed for 10-second interpolation points, and the time figures quoted are for this interval. After the APP back-up drive tape has been produced and verified, the only APS opera-

tion remaining is real-time computer control of the antenna.

Real-time computer control of the antenna (via the APP) requires an instruction from the operator to the computer with an identity code for the appropriate predict set, the "start time" for antenna movement, and (if desired) a time offset to adjust the predict time values in the event that they do not properly coincide with real time. This latter feature is convenient for test purposes and also for the case where a standard sidereal predict is to be used instead of a current predict set.

APP drive tape punching and verification are considered functionally separate from real-time control and may or may not be employed on any specific occasion. Simultaneous real-time control and punching and/or verification is not possible due to timing limitations within the XDS-910 computer.

V. Integrated Configuration—DSN Mode

The DSN's operating mode at the joint-usage stations requires the equipment configuration shown in Fig. 2. The functional and operational features of this mode of operations, at once both similar to and divergent from those of the MSFN mode, are discussed below.

Metric data, formatted by the TDP to MSFN communications system HSDL specifications, must be reformatted for DSN use to permit transmission over GCF NASCOM HSD circuits. This reformatting is effected in the APS XDS-910 computer. Input of these data to the XDS-910 is via Simulation Conversion Assembly (SCA) HSD Receive Channel No. 2 which has been modified to permit acceptance of such nonstandard inputs.

The metric data reformatting requirements consist primarily of a "bunching" process whereby five of the relatively short TDP HSD "blocks" are assembled into one standard NASCOM HSD message block. In addition, the APS computer performs a statistical sampling function to reduce the data rate to that required by the SFOF. Sample rates can be selected in real time in the range between one sample per second and one sample per minute. Also, certain unnecessary fields of the original TDP data block are suppressed and various items of initialization and real-time, manual-input data (from the Receiver Data Entry Panel) are merged into each sample. The reformatted tracking data are transmitted to the SFOF via HSDL and are also recorded on a digital magnetic tape recorder to provide an Original Data Record

(ODR) so that any data lost in transmission may be recovered to complete the SFOF's Master Data Record (MDR).

DSN-mode antenna pointing is similar to that described under the MSFN mode above, except that the teletype predict messages may be in either JPL/DSN standard format or INP format. In addition, the DSN mode permits transmission of antenna-pointing predict data via direct HSDL connection to the APS computer. Once predict data are input, either by teletype tape or HSDL, processing proceeds as previously described.

Status information covering various significant functions and interfaces is passed to the Digital Instrumentation Subsystem (DIS) at regular intervals for reporting to the SFOF Monitor function.

VI. Summary and Conclusions

The operational equipment concerned with antenna pointing and the processing of tracking data has been integrated at the joint-usage stations. The two operating modes of the integrated stations, although related and overlapping in some degree, are structurally different. The MSFN mode is the simpler of the two from a functional point of view. The DSN mode places a considerably heavier load on the APS computer, both as to core loading and processing time.

To a considerable extent the various items of hardware are not ideally suited to the operational and functional interaction that is required and this is reflected (although not explicitly set forth herein) in some of the functional limitations that will appear obvious to those familiar with either or both of the two systems which previously operated independently.

References

1. *Modification Procedure, DSN/MSFN Integration (APS/APP/TDP/SCA/GCF)*, Procedure No. AP506074A, Oct. 18, 1971 (JPL internal document).
2. *DSN/MSFN Integration, Antenna Pointing Subsystem Software Requirements Document*, IOM 3384-71-218, Nov. 19, 1971 (JPL internal document).
3. *Operation Procedure, APS Operational Program (DSN Mode)*, Procedure No. OP506142A, Mar. 1, 1972 (JPL internal document).
4. *Operating Instructions, APS Operational Program (MSFN Mode)*, IOM 3384-72-016A, Mar. 13, 1972 (JPL internal document).

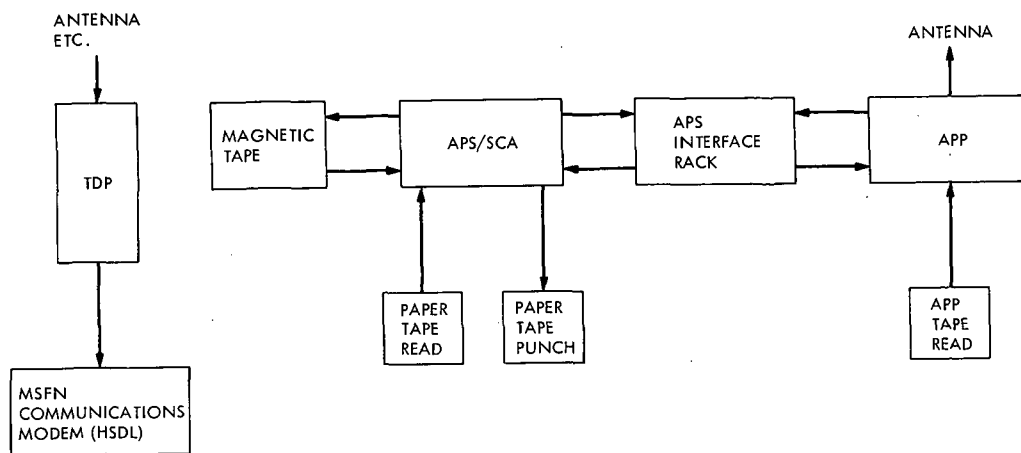


Fig. 1. DSN/MSFN integration (APS/APP/TDP/SCA/GCF), MSFN operating mode

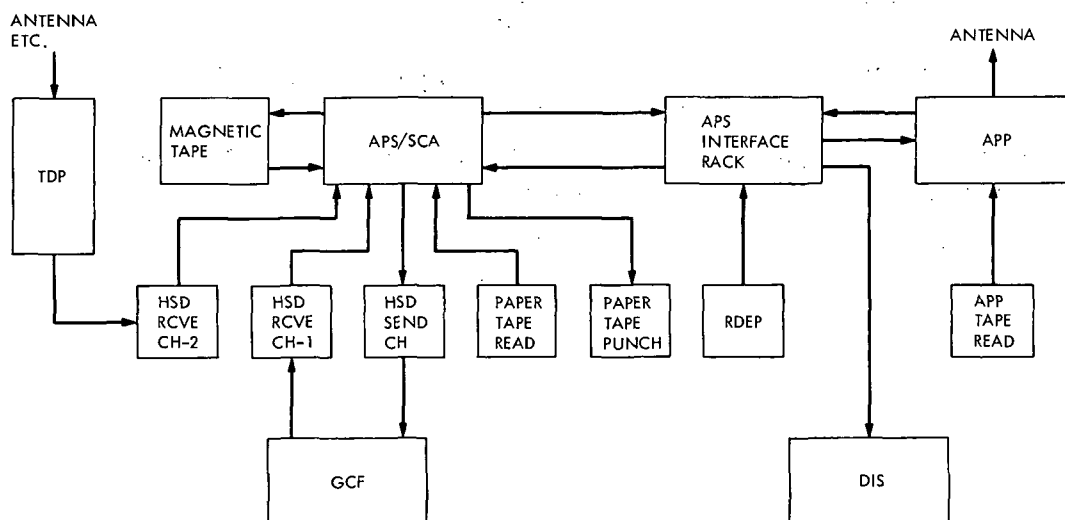


Fig. 2. DSN/MSFN integration (APS/APP/TDP/SCA/GCF), DSN operating mode

The Use of an Interplex Modulation Technique for the Mariner Venus-Mercury 1973 Mission

M. M. Whang

DSIF Digital Systems Development Section

The use of interplex modulation for the Mariner Venus-Mercury 1973 mission necessitates modification of the station ground equipment to effect compatibility. The Simulation Conversion Assembly (SCA) is to be modified to provide a source for generation of simulated telemetry data, using interplex, for system testing, training and software development. Implementation of the SCA hardware modifications, together with a discussion of the simulation test modes, is presented.

I. Introduction

The use of an interplex modulation technique for the Mariner Venus-Mercury 1973 (MVM 73) mission, rather than the conventional two-channel telemetry system, necessitates modifications in the station ground equipment to effect compatibility. As such, the Simulation Conversion Assembly (SCA) is to be modified to provide an interplex capability for system and subsystem testing, training of station personnel, and software development for the DSIF.

The interplex-modulated signal is generated in the Simulation Conversion Assembly and typically is routed to the Subcarrier Demodulator Assembly which, in turn, processes and demodulates the signal. The signal is subsequently routed through the Symbol Synchronizer Assembly (SSA), Block Decoder Assembly/Data Decoder

Assembly (BDA/DDA), and the Telemetry and Command Processor (TCP). The block diagram in Fig. 1 illustrates the configuration for processing simulated telemetry data in the DSIF.

II. SCA Implementation

The existing SCA hardware does not now have the interplexing feature. As such, additional hardware will be required. Further, supporting software must also be developed for MVM 73 system testing, training, and DSIF software development.

An overall SCA interplex block diagram is shown in Fig. 2. A modulo two adder is used to modulate two previously modulated subcarriers. A typical timing diagram is shown in Fig. 3. The timing is drawn on a non-coherent basis. However, the two subcarriers are coherent

for MVM 73. An EXCLUSIVE OR gate (\oplus) is added in the Video Conditioner of the SCA to provide this function. The high-rate data channel remains as is ($D1 \oplus SC1$); while the low-rate data channel (engineering) is modulated again with the high-rate channel subcarrier. Thus, the expression is

$$(D1 \oplus SC1) \oplus (D2 \oplus SC2)$$

The two modulated signals are fed into two separate attenuators for a proper signal mix ratio. Thus, the attenuator will set a modulation index. Typically, a science channel is set to 70 deg ($\theta_1 = 65$ deg for MM 69) and an engineering channel to 30 deg. The attenuators can be programmed to 100 dB (resolution 0.2 dB) manually or by a computer, thus providing various modulation indices.

After setting the modulation index, the two attenuated signals are mixed together by a summing operational amplifier (mixer). The signal from the mixer now contains a simulated spacecraft signal, which is fed into the test transmitter for carrier modulation.

III. Simulation Support for MVM 73

DSIF Simulation Support for MVM 73 is scheduled to commence in April 1973. The simulation function has two basic modes of operation, a local (DSIF) mode and a long loop mode. In the local mode, the SCA provides signals

for several subsystems. These various signals will provide capabilities for subsystem checkout, subsystem software development, and the DSIF integration effort.

The long loop simulation involves SFOF and DSIF via High-Speed Data (HSD) Line. The dynamically changing spacecraft data are generated in the Simulation Center by the 6050 computer. This signal is sent to the DSIF (sometimes simultaneously to two stations) by the Ground Communications Facility (GCF). The SCA will receive the simulated data via HSD and supply the signal to the DSIF. The simulated data will be routed to the TEST TRANSMITTER, RECEIVER, SDA, SSA, BDA/DDA and the TCP. The TCP will format an HSD data block and return it to the SFOF. The SFOF will examine the returned data for verification. Unfortunately, the 117.6-kbps telemetry (uncoded video) for MVM 73 cannot utilize the long loop simulation due to hardware limitations on communication facilities and some DSIF subsystems. However, 2.45-kbps (block coded 32,6) telemetry is able to use both modes.

The SCA provides four independent telemetry channels. Each channel has basically the same hardware with respect to the interplex implementation. This feature will provide flexibility for readily interchanging science and engineering channels. Also, the SCA delivers a high-level signal (bit error rate, word error rate, convolution error rate) for verification of correct decoding in addition to a low-level analog signal.

Reference

1. Butman, S., and Timor, U., "Coding and Synchronization: Interplex—An Efficient Two-Channel Telemetry System for Space Exploration," in *Supporting Research and Advanced Development*, Space Programs Summary 37-62, Vol. III, pp. 57-60. Jet Propulsion Laboratory, Pasadena, Calif., Apr. 30, 1970.

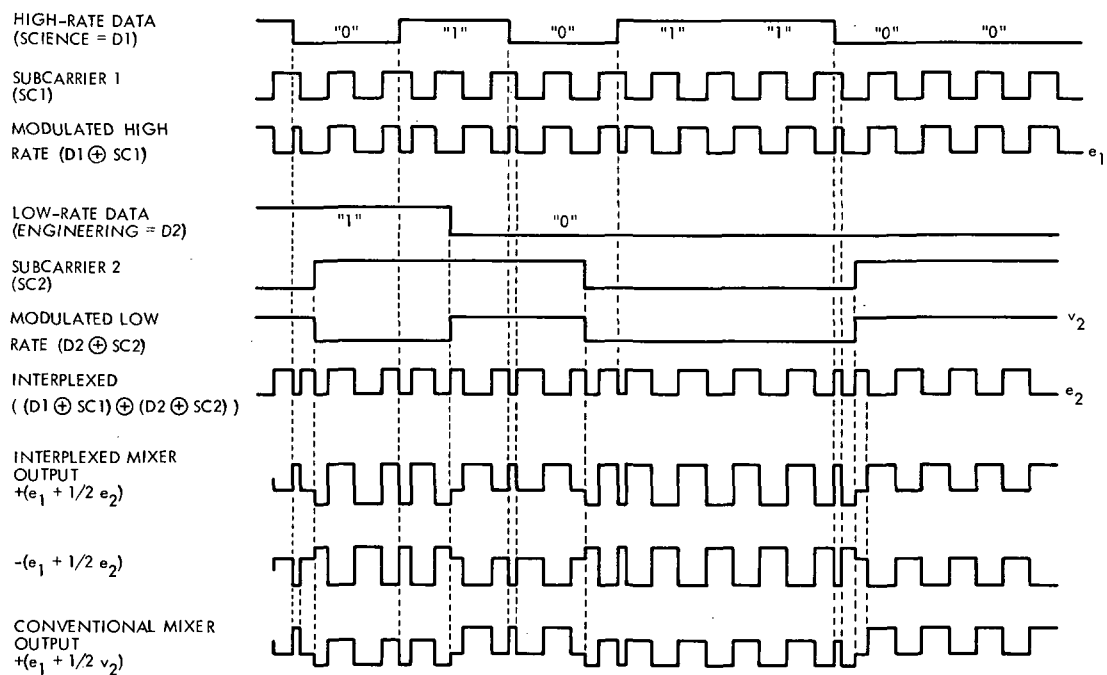


Fig. 3. Simulated non-coherent interplexed data

Post-Detection Subcarrier Recording Subsystem

L. I. DeGennaro and G. B. Hamilton
DSIF Digital Systems Development Section

The Post-Detection Subcarrier Recording Subsystem for the 64-meter stations will be revised from the present configuration at DSS 14. The reasons for the change are to provide for future computer control of the pre/post-calibration process at the new 64-meter stations and to reduce the number of cabinets required to perform the essential functions of the Analog Instrumentation/Recording (AIS/REC) Subsystems. Changes from the present configuration are described, including patching functions, test equipment, and semi-automatic and automatic computer control.

I. Introduction

The Post-Detection Subcarrier Recording Subsystem is being implemented for the 64-meter stations and extends the analog recording capability previously provided by the Analog Instrumentation Subsystem and the Recording Subsystem. The new configuration provides for future computer control for pre-track calibration of the recording equipment. It also provides a semi-automatic calibration mode and an improved coaxial patch panel for signal routing. The revised configuration will also substantially reduce the number of cabinets required to contain the equipment.

A block diagram of the Post-Detection Subcarrier Recording Equipment (PPR) is shown in Fig. 1. A discussion of the modes of operation was contained in Ref. 1. The PPR for the 64-meter stations is being modified in this effort. The primary changes are concerned with the block labeled PPR Signal Conditioning and Testing.

The present AIS and REC Subsystems at the DSIF 64-meter site are being combined and the resultant eight cabinets are being reduced to four. Two of these cabinets contain FRI400 tape recorders and two contain PPR patching, signal conditioning, and test equipment. In addition, these cabinets contain interface and control circuitry enabling semi-automatic and automatic computer control of signal path, setup of test equipment, and calibration and checkout of signal conditioning equipment.

It is planned to delete the previously available wide-band FM capability from the PPR, substituting instead the use of VCOs and mixers combined with direct recording techniques which were successfully used in *Mariner* Mars 1971. The advantages of this are increased flexibility, wider deviation (greater accuracy) and compatibility with the playback facility at CTA 21. In short, the function of the PPR is to record incoming signals, through patching either directly to the tape recorder or through pre-conditioning equipment such as VCOs and mixers. Upon

demand, pre-recorded signals can be supplied to the Subcarrier Demodulator Assembly (SDA) or Symbol Synchronizer Assembly (SSA) through the PPR's discriminators (refer to Fig. 1).

II. New Features of the PPR

In the automatic computer-controlled mode, when implemented, the PPR will be checked and calibrated by a test program loaded into the subsystem computer. The program provides commands, which are stored in the Digital Electronics Subassembly (DES) of the PPR, to configure the subsystem and measure its performance. The PPR test equipment includes a programmable voltage source, a programmable digital voltmeter, a programmable frequency synthesizer, a frequency counter, and a programmable discriminator. The subsystem is configured by a programmable switching relay matrix. The DES transmits the data from the test equipment back to the computer for evaluation. Anomalies, determined by the results of the test program, are printed out on the subsystem input/output typewriter for operator evaluation.

Normally closed contacts of the switching matrix are inserted in the signal path to the tape recorder at various places such as VCO input and output, mixer amplifier input and output, and tape recorder input and output. Switch contacts are also placed in the input/output of the test equipment. Through suitable selection of the switches, test equipment may be applied either to signal conditioning equipment, recording equipment or other test equipment for calibration checkout. The switching matrix is programmed by the computer in the automatic mode.

In the semi-automatic mode the Calibration Test Programming Panel (CTPP) and the Matrix Calibration Panel (MCP) of the PPR are used to operate the PPR. This mode is used when the subsystem computer is not available. The control of the programmable test equipment is performed through the CTPP, and the matrix is configured through the MCP. The operator reads the test equipment front panel displays, in this mode, to determine subsystem anomalies.

A new system of coaxial patch panels will be used in this PPR. The panels utilize a normal-through configuration where the normal (record) mode of operation is pre-patched by means of permanent cables at the rear of the panels. Should it be desired to re-route these under unusual circumstances, a patch cord is inserted breaking the normal path and establishing a new path. Thus, under normal circumstances, no patch cord is visible on any of the panels. In reproduce mode (nonreal-time playback) patch cords are required because of the large number of combinations of paths possible. The normal routing of the signals is interruptible by the programmable switching matrix.

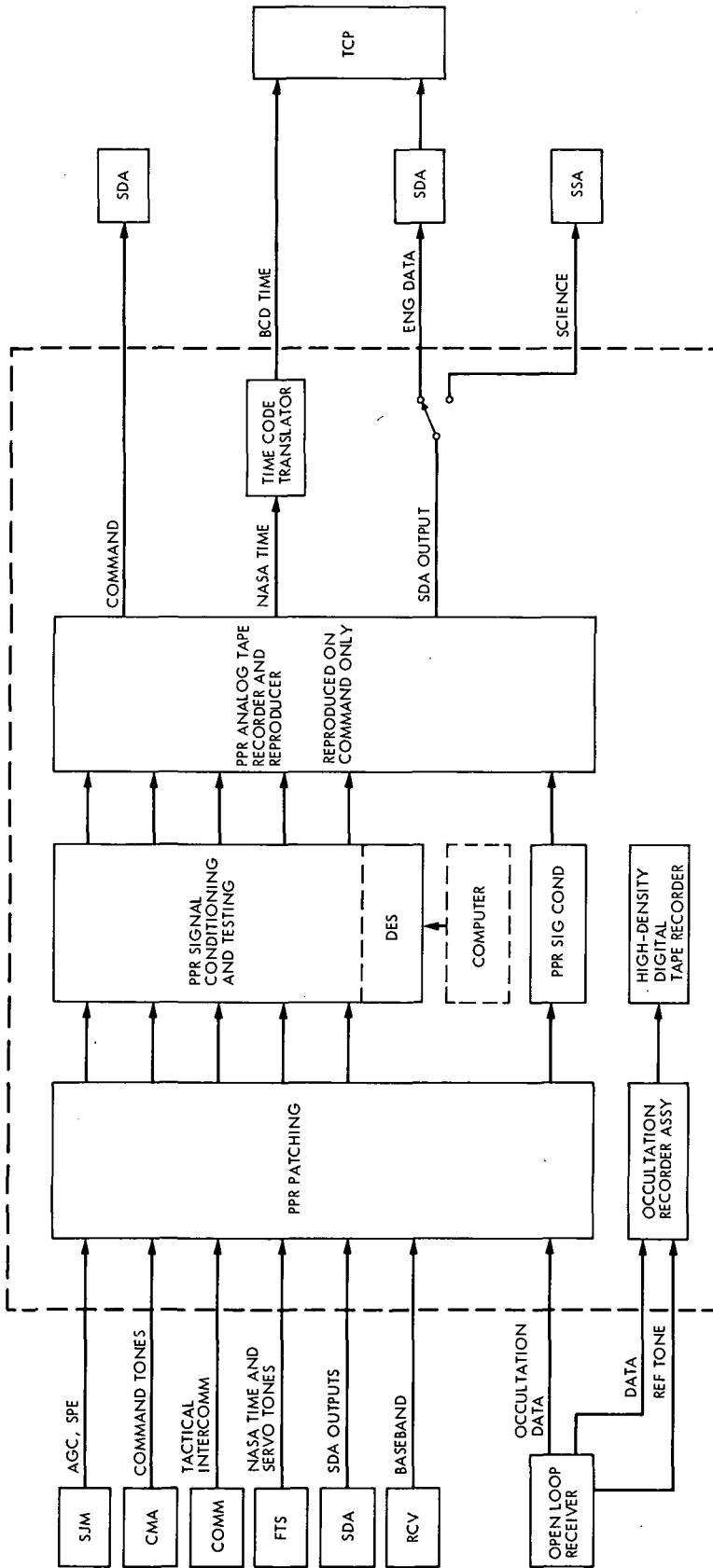
III. Procurement Status

The conceptual design for the new PPR Subsystem has been completed. Vendor proposals for design and fabrication of three Post-Detection Recording Subsystems for the 64-meter sites has been received, reviewed, and evaluated. Award and negotiations of the contract will take place during the latter part of June 1972. The delivery schedule for the three subsystems is mid-December 1972, mid-January 1973, and mid-February 1973.

Reference

1. Hamilton, G., "Post-Detection Subcarrier Recording Equipment Implementation for Analog Recording Playback," in *The Deep Space Network Progress Report*, Technical Report 32-1526, Vol. VII, pp. 182-184. Jet Propulsion Laboratory, Pasadena, Calif., Feb. 15, 1972.

PPR DSS SITE



PPR CTA 21

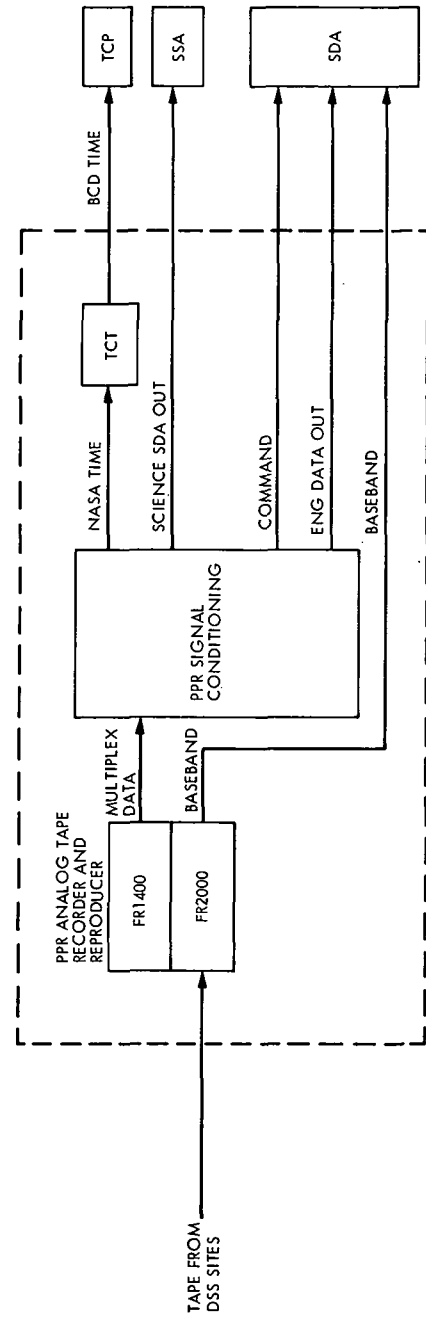


Fig. 1. Block diagram of PPR Subsystem

Performance Capabilities of the Data Decoder Assembly Through the Viking Era

C. R. Grauling and N. J. Jones
DSIF Digital Systems Development Section

The Data Decoder Assembly will be performing several different telemetry processing functions at various antenna type sites through the Mariner Venus-Mercury 1973, Helios, and Viking eras. These include sequential decoding block decoding and high-rate formatting of telemetry data. This article is a description of how these functions have been implemented by either test or operational software.

I. Introduction

The Data Decoder Assembly (DDA) is a recent addition to the DSIF Telemetry and Command Subsystem and is capable of performing medium rate sequential decoding, medium rate block decoding, and high-rate formatting of telemetry data with simultaneous original data record generation and transmission on the wide-band data line. (See Ref. 1 for a general description of the DDA.)

The medium rate block decoding will be performed at 26-meter-antenna sites in support of the *Mariner Venus-Mercury 1973* (MVM 73) and *Viking* Projects. The high-rate formatting function will be performed at 64-meter sites in support of MVM 73 and *Viking* missions. Sequential decoding is required by the *Pioneer 10*, *Pioneer G*, and *Helios* Projects. The hardware capability to meet these

requirements already exists in the current configuration of the DDA, although some of the required equipment has not yet been delivered to the antenna sites. A multi-mission program is currently under development and will be available for MVM 73. Preliminary analysis of the requirements and DDA hardware capabilities has been done in order to verify that project requirements can in fact be met. The results of this analysis are the subject of this article.

II. Sequential Decoding

The sequential decoding function is already implemented in the DSIF and is currently being used to support *Pioneer 10*. The decoding algorithm is implemented as a microprogram, i.e., there is an instruction in the DDA

Central Processing Unit (CPU) instruction repertoire which performs the sequential decoding algorithm on an entire frame of convolutionally encoded data.

The monitoring and control of the decoder and data handling is a software function implemented in the DDA resident software portion of the *Pioneer* Operational Program DOI-5035-OP (see Ref. 1). The sequential decoding portion of the operational program for the 1973-1975 era will differ only slightly from DOI-5035-OP. The major difference between DOI-5035-OP and the implementation of sequential decoding for the 1973-1975 era will be in the area of received data buffer management. The new program will have a slightly different data buffer allocation algorithm which will enable the DDA to handle the large frames for the *Helios* Project.

III. Block Decoding

The DDA will perform block decoding of medium rate (less than 2500 bps) block coded data. The data flow in this case is the same as in the sequential decode case, i.e., the received channel symbols are input to the DDA from the Symbol Synchronizer Assembly (SSA) coupler via a direct memory access channel. The decoding is performed by the DDA CPU. The decoded data plus time and status information are transferred to the Telemetry and Command Processor (TCP) via direct memory access through a Decoded Data Buffer which performs a data packing function in hardware.

The decoding algorithm is a hybrid firmware-software implementation. The repetitive functions of the block decoding algorithm are done via the execution of a set of special block decoding instructions. There are three special instructions used in block decoding. A typical block of received data (e.g., 32/6 comma-free, biorthogonal block coded data) is decoded using the following procedure.

Step 1. The comma-free vector is added to the received block using an EXCLUSIVE OR memory-to-memory instruction. (A received data block in this case is a set of 32 contiguous halfwords of memory, each halfword corresponding to a received channel symbol.)

Step 2. A set of 32 sums and differences by pairs is computed and stored in a temporary buffer using another special block decoding instruction. This step is repeated five times exchanging input and output pointers between executions. The final result is the set of correlations of the received data with the 32-word code dictionary.

Step 3. The correlation set is searched for the location which contains the correlation with maximum absolute value. This search operation is also implemented in firmware as a single instruction. The address of maximum correlation value provides five bits of the decoder output. The sixth bit is determined by the sign of the correlation value which is maximum in absolute value.

A test program has been written which implements this procedure. At 2500 bps, the block decoding function consumes 85% of the available processor time. The test program has the capability of comparing the decoded data with the actual transmitted data and compiling word error rate statistics. The word error rates obtained by the DDA have been observed to be the same as those obtained by the Block Decoder Assembly when both devices are decoding the same data stream.

IV. High-Rate Formatting

Wide-band formatting and transmission is done at 64-m stations which have DDAs configured with wide-band data line input/output (I/O) assemblies and magnetic tape recorders (Configuration II DDAs). This channel is referred to in Telemetry and Command Data Handling Subsystem (TCD) multi-mission terminology as the high-rate telemetry channel. A diagram of the data flow of such a DDA is found in Fig. 1.

The DDA has high-speed interfaces with the Block Decoder Assembly (BDA), the Symbol Synchronizer Assembly (SSA), and the High-Speed (HS) and Wide-Band Data Lines (WBDL). High-rate decoded or uncoded telemetry data are input through one of these channels and formatted by the DDA into 1200- or 4800-bit GCF blocks, based on configuration and standards and limits values received from the TCP. These blocks are then sent to the HS/WB unit for transmission to the Network Control System (NCS) and Mission Control and Computing Center (MCCC) via the GCF lines. The line rate used is 4800 bps for high-speed data and 28.5 kbps for wide band. An original data record (ODR) is simultaneously recorded on the 9-track magnetic tape recorders.

A detailed timing study has been done to determine the capability of the DDA to perform its function on the high-rate channel. This study used the MVM 73 maximum rates of 22.05 kbps for logging and transmission and 117.6 kbps for logging only. These rates remain the maximum required rates for all missions through the *Viking* era. Partial results of that study follow.

A. The 22.05-kbps Rate

Telemetry data input, processing, and output functions all impose timing requirements on the high-rate channel software implementation. The input constraint consists of meeting the interrupt response time of 3.27 ms imposed by the direct memory access channel on the SSA. Meeting an interrupt response time in the DDA depends on the delaying effects of the existence of higher priority external interrupts and the execution times of their interrupt processors, on the CPU time taken up by the priority interrupt firmware, and on the presence of long un interruptable assembly language instructions. The maximum time taken up by these delaying processes is 490 μ s which shows that the input restriction is satisfied.

At this rate, magnetic tape recording can be done in either background or main program routines, and does not present restrictions on the software design. The outputting of data on the Wide-Band Data Lines, however, must adhere to the timing constraints of the WB unit. This minimum interrupt response time of 860 μ s is associated with a maximum delaying process time of 290 μ s and, thus, can be met.

The processing of data is done in various background routines. Test software was written to closely resemble an operational program by simulating all anticipated external stimuli and internal responses. Using this test program the main program's executive loop was shown to contain 40%

unused CPU time which would be available for features not incorporated into the test program.

Thus, at 22.05 kbps, the DDA has been shown to perform its wide-band transmission and ODR recording functions within a 60% margin of the most severe timing constraint.

B. The 117.6-kbps Rate

The procedures for the processing of data at this rate are identical to those at the 22.05-kbps rate. However, since output is restricted to the generation of ODRs, the amount of time available for background execution is larger than at the lower rate. This will ensure the processing of input telemetry data.

Data input restrictions correspond to an interrupt response time of 418 μ s. Delaying processes, though, are a maximum of 290 μ s, since the interrupt of the SSA direct memory access channel now is of highest priority within the program. Therefore, the interrupt will be met within the time constraint specified.

Even at this highest rate, data output can be done in background routines. Based on timing calculations and the performance of a similar tape-logging program, real-time recording, including a rewrite capability, is ensured. Thus, at 117.6 kbps, the DDA performs its high-rate logging function within a 30% margin.

Reference

1. Grauling, C. R., "Data Decoder Assembly," in *The Deep Space Network Progress Report*, Technical Report 32-1526, Vol. IV, pp. 170-176. Jet Propulsion Laboratory, Pasadena, Calif., Aug. 15, 1971.

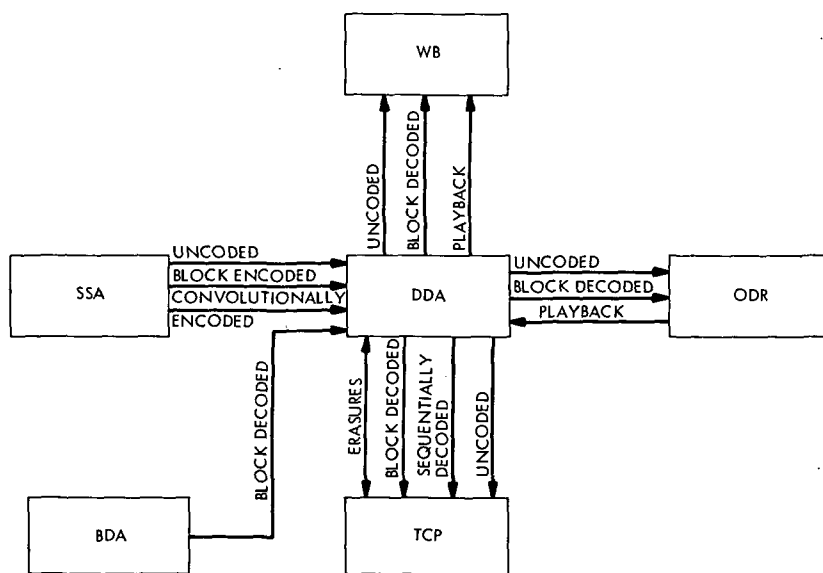


Fig. 1. Telemetry data flow at a Configuration II DDA

S-Band Receiver Third-Order Loop Demonstration

R. B. Crow

R.F. Systems Development Section

In mid-April 1972, the Mariner Mars 1971 spacecraft began encountering high doppler rates under weak signal conditions. The Block III receiver was dropping lock, resulting in lost data. This article describes a third-order tracking filter which was designed for the Block III receiver and successfully demonstrated at DSS 14.

I. Introduction

The *Mariner Mars 1971* spacecraft has pushed the DSIF tracking system into a new era. Currently, the mission dynamics are such that S-band doppler rates of 25 Hz/s and doppler acceleration as high as 0.16 Hz/s have been experienced. The Block III DSIF receiver cannot track doppler rates greater than 10 Hz/s with the current signal margin (8 dB).

It was decided to design and build a third-order loop filter for the Block III DSIF receiver. The receiver using the third-order loop has two bandwidths (5 and 10 Hz) and is capable of tracking doppler rates in excess of 1000 Hz/s and will stay locked with doppler acceleration as high as 3.8 Hz/s² as demonstrated by tests at CTA 21 (see Fig. 1).

The immediate response from DSS 14 operations was that the third-order loop solved the tracking problem. It was noted, however, that the initial frequency acquisition was more difficult. A trip was made by the designer to DSS 14 to watch an operational acquisition of the *Mariner Mars 1971* spacecraft with the third-order loop. It was

apparent that part of the problem was the operator's continuous tuning of the voltage-controlled oscillator (VCO). While this procedure has worked well for the second-order loops, it is inappropriate for the third-order loop due to the added "memory" inherent in the added integrator.

It was found that when the third-order loop was within 200 Hz (at S-band) that loop would acquire within 60 seconds. When frequency predicts were used, acquisition occurred within 15 seconds.

Acquisition with the high doppler rates (i.e., 30 Hz/s present when the uplink is being swept) is a more difficult problem. This appears to be too great a doppler rate for an unassisted acquisition, even for a third-order loop. This presents a problem since the receiver operator has no good indicators of when he is "oversteering" the third-order loop, and acquisition under these conditions seems unreliable.

The answer to the problem seems to be a *hybrid loop*—a device that can acquire as a second-order loop and automatically switch to the third-order configuration to track. A filter of this type has been designed and tested at CTA 21 (see Fig. 2).

II. Design Approach

A. Third-Order Loop Filter

The open-loop transfer of the third-order loop filter (see Fig. 1) is

$$H(s) = \left[\frac{R_2 + R_3}{R_1} \left(\frac{1 + SC \frac{R_2 R_3}{R_2 + R_3}}{1 + SC R_3} \right) \right]^2$$

$$\approx \left[\frac{R_2 + R_3}{R_1} \left(\frac{1 + SC R_2}{1 + SC R_3} \right) \right]^2$$

$$= \left(K_1 \frac{(1 + T_2 S)}{1 + T_1 S} \right)^2$$

The design approach has been to select the design that satisfied the doppler and doppler rate input with the minimum time constant T_1 .

Define

$$q = \alpha A K_d (\text{volts/deg}) K_v (\text{Hz/volt}) K_m$$

$$\times 360 \times \left(\frac{K_1}{T_1} \right)^2 T_2^3 = K K_1^2 \frac{T_2^3}{T_1^2} = G \frac{T_2^3}{T_1^2}$$

$$q_0 = 6.75$$

$$W_{L_0} = \frac{4.455}{T_2}$$

$$W_L = \frac{q(2q + 3)}{2T_2(2q - 1)}$$

$$\phi_{ss} (\text{deg}) = \frac{360(\Omega_0 + \Delta t)}{G} + \frac{720\Delta T_1}{G} + \frac{360\Delta T_1^2}{G}$$

Let

$$a = \frac{360 T_2^3}{q}$$

so that

$$T_1 = \frac{a \Delta}{\phi_{ss}} + \left(\left(\frac{a \Delta}{\phi_{ss}} \right)^2 + \frac{a(\Omega_0 + \Delta t)}{\phi_{ss}} \right)^{1/2} = R_3 C$$

$$T_2 = \frac{4.455}{W_{L_0}} = R_2 C$$

$$R_1 = R_2 \left(\frac{R_2 + R_3}{R_3} \right) \frac{\sqrt{K T_2}}{q}$$

B. Second-Order Hybrid Filter

Design for the hybrid loop was implemented by leaving the second integrator (see Fig. 2) as designed for the third-order loop (since this integrator stores the frequency offset control voltage to the VCO). The first integrator was modified to be a simple gain stage so that the second-order loop would have the same bandwidth as the third-order loop. The second-order loop is overdamped (i.e., $r_0 = 7.91$).

For second-order hybrid design,

$$H(s) = \frac{R_4}{R_1} \times \frac{R_2 + R_3}{R_1} \left(\frac{1 + \frac{R_2 R_3}{R_2 + R_3} SC}{1 + SC R_3} \right)$$

$$\approx \frac{R_4}{R_1} \times \frac{R_2 + R_3}{R_1} \left(\frac{1 + SC R_2}{1 + SC R_3} \right)$$

$$= K_1 K_2 \left(\frac{1 + T_2 S}{1 + T_1 S} \right)$$

$$r = 360 K_D (\text{volts/deg}) K_v (\text{Hz/volt}) K_m \alpha K_1 K_2 \frac{T_2^2}{T_1}$$

$$= G K_1 K_2 \frac{T_2^2}{T_1}$$

$$K_1 = \frac{2T_2 \times W_{L_0} - 1}{G \times \frac{R_2}{R_1} \times T_2}$$

but

$$R_1 = R_2 \left(\frac{R_2 + R_3}{R_2} \right) \frac{\sqrt{K T_2}}{q} \text{ (same as standard third-order loop design)}$$

$$R_4 = R_1 K_1$$

Whenever $R_2 \ll R_3$,

$$r = G K_1 \frac{R_2 + R_3}{R_1} \times \frac{R_2 C}{R_3 C} \times T_2 \approx G K_1 \frac{R_2}{R_1} T_2$$

and

$$W_{L_0} = \frac{r + 1}{2T_2}$$

so that

Computer programs have been written for both of the above designs utilizing the PDP-11 BASIC language.

III. Future Effort

Theoretically the acquisition characteristics for the third-order loop are much superior to the second-order

loop (and may well prove to be the case when computer-controlled acquisition is available). However, in the present DSS 14 environment, it appears the hybrid loop is a better approach since it allows past experience and procedures to be used during difficult manual acquisition

and then automatic switching (activated by the lock detector circuit) to use the superior tracking performance of the third-order filter. Theoretical studies are currently underway to predict the loop performance to an arbitrary forcing function.

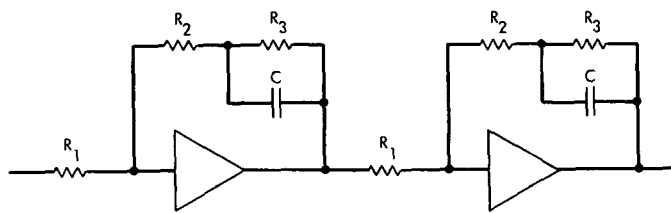


Fig. 1. Third-order filter

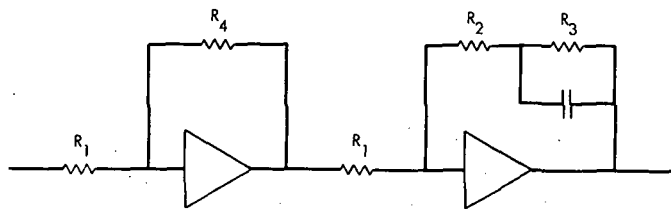


Fig. 2. Second-order hybrid filter

Novel 70-MHz Limiting Amplifier

J. G. Leflang and R. N. MacClellan
R.F. Systems Development Section

A high-speed digital differential comparator has been successfully utilized as the limiting element in an RF module operating in the VHF region. The device exhibits good amplitude and phase characteristics. This article describes the design and test results of the device, which uses emitter-coupled logic as a limiting amplifier.

I. Introduction

At various DSIF stations, both the receiver/exciter and the antenna microwave subsystems utilize RF modules which are electrically connected but are physically separated from each other. This occurs because some modules must be located in a control room area while others must be installed in antenna-mounted assemblies. Separation distance depends upon the particular station, and may vary from approximately 100 to 500 meters. In the frequency range used, 40 to 100 MHz, the corresponding insertion loss of the RF cables connecting the modules varies from 3 to 10 dB or more depending on the type of cable used.

It is desirable to design the modules involved to accept, without realignment, input power variations associated with the different cable losses at each station. This article describes the design and test results of a broadband wide range limiter which uses emitter-coupled logic (ECL) as a limiting amplifier.

II. Design Requirements

To accommodate all installations, the limiter must operate with an input power variation of at least 15 dB. The limiter output power must not vary more than 0.5 dB over the 15-dB input power range, and the input range must be compatible with the maximum output power capabilities of most modules, namely +10 dBmW maximum. In addition, the phase delay of the limiter must not change more than a few degrees per dB input change over the power range. Finally, the above performance must be obtained over the frequency range of 40 to 100 MHz.

III. Design Concept

Within the digital logic families are differential comparators which offer an effective limiting function because the two levels associated with the output states are dependent upon the relative logical condition of the inputs and not upon the absolute level of the input signal. High-speed comparators are available and can operate easily

in the 100-MHz region. In fact, ECL devices typically exhibit sub-nanosecond switching times.

There are several lines of ECL which are suitable for this application. While not necessarily the best choice for all applications, the design of the limiter tested and reported here utilizes an MC1650, MECL III comparator.

IV. Configuration

Figure 1 shows the configuration which was tested at 40, 70, and 100 MHz. Because of the low output impedance of the MECL comparator, no matching was used between the comparator and the single stage, class A output amplifier. The amplifier offered enough harmonic rejection to make the output waveform essentially sinusoidal without additional filtering.

V. Results

ECL limiter performance at 70 MHz is presented in Fig. 2. Temperature effects are not plotted, but produce a shift in the power curve of less than 0.02 dB per degree

centigrade. The temperature effect on phase is approximately 0.2 degrees per degree centigrade. Curves at 40 and 100 MHz are not presented because they are essentially identical to the curves shown.

VI. Conclusions

The amplitude curve in Fig. 2 clearly shows a device with excellent limiting characteristics over a dynamic range greater than 20 dB. Low level leakage and a region of linear operation are also apparent in the curve, but these areas are well outside of the operating region.

The phase slope is smooth in the operating region, and has a slope less than 3 degrees per dB at the worst point. The phase exhibits some wildness when the input is overloaded, but this point can be controlled by changing the input attenuator.

The device meets the requirements set forth and provides a simple means of obtaining a good limiter in the VHF region.

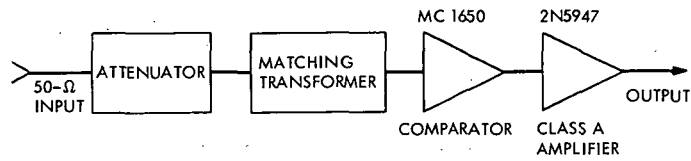


Fig. 1. Limiter configuration

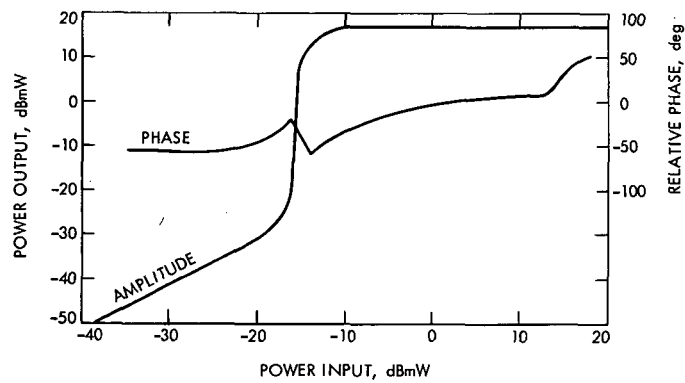


Fig. 2. Limiting amplifier performance at 70 MHz

Block IV Receiver Development

C. E. Johns

R.F. Systems Development Section

This article describes a digital control assembly developed for use in controlling the frequency of a Dana Laboratory Digiphase synthesizer, Model 7010-S-179. The control assembly allows the synthesizer to be used as the oscillator within a phase-locked loop. A brief analysis using the synthesizer control assembly in a third-order loop is included.

I. Introduction

In the original Block IV analog loop design (Ref. 1), a crystal voltage-controlled oscillator (VCO) is combined with a programmed oscillator to provide both frequency agility and the capability of programming the local oscillator frequency to track the doppler. The programmed oscillator used in Block IV contains a Dana Laboratory Digiphase synthesizer (Ref. 2), essentially a number-controlled oscillator that can readily be adapted to function as a loop-controlled oscillator. This can be accomplished by digitizing the loop error signal and processing this digital information to control the synthesizer. In such a configuration, the VCO is eliminated and the frequency tracking range is no longer limited by the VCO frequency range. There are the added advantages of: (1) eliminating crystal oscillator drifts that offset the local oscillator frequency during acquisition, and (2) eliminating the need to combine two signals (VCO and synthesizer), which inherently introduces unwanted intermodulation products.

The type of loop design that would be most effective in tracking future spacecraft is being investigated. The use of a synthesizer as the loop-controlled oscillator still leaves

open the option of using either a second- or third-order loop or modifications of these designs. Until now, the doppler rates and accelerations of spacecraft were not significant. Recently, however, during the extended-mission phase of the *Mariner* Mars 1971 mission, these rates became factors at low signal levels and exceeded the tracking capability of the second-order loop being used. In future probes, these rates will increase and become more significant at stronger signal levels, which will result in excessive tracking errors in second-order ground receivers. For this reason, a third-order loop using the synthesizer as the loop-controlled oscillator is being investigated to provide tracking capability without the need to program the synthesizer.

II. Loop Design

As mentioned previously, in the present Block IV receiver, the output from the Dana synthesizer is combined with a VCO to yield a sum frequency, which is subsequently multiplied to generate the local oscillator. The VCO is controlled by the loop and is used to track the phase of the received signal, while the synthesizer is used for automatically sweeping the local oscillator around the

received signal (for signal acquisition purposes) and for tracking the doppler of the received signal. To control the synthesizer in this configuration, a Programmed Oscillator Control Assembly (POCA) is used (Ref. 2).

To utilize the synthesizer as a loop-controlled oscillator, it is necessary to convert the loop phase error into the format required to control the synthesizer. This is done in the Receiver Loop Phase Control Assembly (RLPCA). The RLPCA is an extension of the POCA (Fig. 1), incrementing or decrementing the input to the synthesizer from the POCA. Designing the RLPCA to generate a synthesizer output frequency rate proportional to the polarity and magnitude of the loop phase error provides a third-order loop. Third-order loops in sensitive phase-lock receivers have been extensively analyzed (Ref. 3). In the following, the designs of both the RLPCA and the third-order loop for this application are presented.

III. RLPCA Design

Figure 2 is a simplified block diagram of the RLPCA. The receiver static-phase-error voltage is applied to the input of an absolute-value-plus-sign (AVS) module. The AVS module produces a unipolar output voltage proportional to a bipolar input and also a logic level (sign bit) to denote the input polarity. The need for the AVS module is predicated on the characteristics of the high-speed analog/digital (A/D) converter which it drives. The A/D converters available for this application accept unipolar voltages only.

The A/D converter driven by the AVS module provides a 12-bit binary output number proportional to the input voltage and can convert the analog voltage to this binary number in less than 4 μ sec. This allows the input static phase error to be sampled each 100-kHz clock period and to complete the conversion during the first half-period of the clock. This is necessary because the Dana synthesizer samples the binary-coded decimal (BCD) input during the second half-period of the clock.

The binary number from the A/D converter is converted to a serial pulse rate by the pulse rate generator. This pulse rate is then proportional to the static-phase-error voltage. The pulses and the AVS sign bit (and its complement) are applied to the inputs of two logic gating circuits, G2 and G3. The gate circuit outputs are connected to the count up/down terminals on the least-significant (10^{-4}) BCD counter. When the receiver control functions are in the mode for the RLPCA to control the synthesizer frequency, the pulses generated by the

pulse rate generator are coupled to the count up/down terminals of a BCD counter (10^{-4} -decade) through gate circuits G2 and G3. The sign bit supplied by the AVS module is also coupled to the inputs of G2 and G3, and it determines whether the pulses increment or decrement the number stored in the counter. The 10^{-4} -decade counter is cascaded with 11 similar BCD counters, which store the control numbers up to the 10^7 -decade of the synthesizer. The BCD numbers at the counter outputs are fed directly to the synthesizer frequency control inputs.

Twelve BCD control numbers from the POCA are applied to the parallel inputs of the BCD counters. When the receiver status is such that the synthesizer is to be controlled by the POCA, the receiver status signal disables gates G2 and G3 and enables gate G1. Enabling G1 allows the BCD numbers from the POCA to be loaded into the up/down counters each clock cycle, and the counter output numbers then track the POCA. When the receiver status changes so that again the receiver phase is to be controlled by the RLPCA, gate circuit G1 is disabled and G2 and G3 are enabled. Thus, the number stored in the BCD counters is the last number supplied by the POCA plus or minus (depending on the AVS sign bit polarity) the accumulation of the pulses applied to the up/down counter terminals of the 10^{-4} decade. The synthesizer output frequency then varies at a rate proportional to the static-phase-error voltage.

The combination of the RLPCA and the Dana synthesizer (neglecting the numerical resolution of the A/D converter) has a frequency transfer function of

$$\frac{dw}{dt} = KE_i(t) \text{ rad/sec}^2 \quad (1)$$

where K is the sensitivity constant in $\text{rad/sec}^2/\text{V}$. In Laplace notation, Eq. (1) becomes

$$s^2 \phi(s) = KE_i(s)$$

or

$$\phi(s) = \frac{KE_i(s)}{s^2} \quad (2)$$

IV. Third-Order Loop Design

A basic mathematical block diagram of the receiver loop is shown in Fig. 3. The design criteria for the receiver loop parameters adhere closely to those in Ref. 3 and some unpublished notes on cascade design of third-order loops by R. C. Tausworthe and R. B. Crow. Setting

$$G = AK$$

where A is the rms signal input voltage, and K is the total open-loop gain, the linear transfer function becomes

$$L(s) = \frac{G(\tau_2 s + 1)^2}{\tau_1 s^3 + (G\tau_2 + 1)s^2 + 2G\tau_2 s + G} \quad (3)$$

Setting

$$q = \frac{G\tau_2^3}{\tau_1}$$

Eq. (3) becomes

$$L(s) = \frac{q(\tau_2 s + 1)^2}{s^3 + \frac{q}{\tau_2} s^2 + \frac{2q}{\tau_2^2} s + \frac{q}{\tau_2^3}} \quad (4)$$

Testing the denominator of Eq. (4) for critical damping and solving for q ,

$$q = 27/4 \text{ at critical damping} \quad (5)$$

Setting $s = j\omega$ in Eq. (4) and taking the squared absolute value,

$$|L(j\omega)|^2 = \frac{q^2(\tau_2^4 \omega^4 + 2\tau_2 \omega^2 + 1)}{\omega^6 + \frac{q}{\tau_2^2}(q - 4)\omega^4 + \frac{2q^2}{\tau_2^4}\omega^2 + \frac{q^2}{\tau_2^6}} \quad (6)$$

Integration of Eq. (6) over all frequencies yields the loop noise bandwidth:

$$w_L = \frac{q}{2\tau_2} \left(\frac{2q + 3}{2q - 1} \right) \quad (7)$$

The loop parameters are selected such that the loop is never underdamped (pp. 9-12, Ref. 3). This is accomplished by letting the design point q in Eq. (5) be

$$q_0 = \frac{G_0 \tau_2^3}{\tau_1} = 27/4 \quad (8)$$

where G_0 is the design point open-loop gain. The lead time constant τ_2 then is derived from Eq. (7) by

$$w_{L,0} = \frac{q_0}{2\tau_2} \left(\frac{2q_0 + 3}{2q_0 - 1} \right) = \frac{4.455}{\tau_2} \text{ Hz} \quad (9)$$

or

$$\tau_2 = \frac{4.455}{w_{L,0}} \text{ sec}$$

Tracking errors due to input phase transients, $\phi_i(s)$, can be calculated by

$$\epsilon\phi(s) = \phi_i(s) [1 - L(s)] \quad (10)$$

and the steady-state tracking error, ϕ_{ss} , by

$$\phi_{ss} = \lim_{s \rightarrow 0} s\phi_i(s) [1 - L(s)] \quad (11)$$

The $1 - L(s)$ term in Eq. (11) is obtained from Eq. (3):

$$1 - L(s) = \frac{\tau_1 s^3 + s^2}{\tau_1 s^3 + (G\tau_2^2 + 1)s^2 + 2G\tau_2 s + G} \quad (12)$$

The steady-state tracking error due to an initial offset phase ϕ_0 , an initial offset frequency $\Omega_0 t$, and a doppler rate $\Lambda_0 t^2/2$ is calculated by Eqs. (11) and (12):

$$\phi_{ss} = \lim_{s \rightarrow 0} \frac{\left(\frac{\phi_0}{s} + \frac{\Omega_0}{s^2} + \frac{\Lambda_0}{s^3} \right) s^3 (\tau_1 s + 1)}{\tau_1 s^3 + (G\tau_2^2 + 1)s^2 + 2G\tau_2 s + G} \quad (13)$$

$$\phi_{ss} = \frac{\Lambda_0}{G} \text{ rad} \quad (14)$$

To calculate the value of τ_1 , Eq. (8) is solved for G_0 and substituted in Eq. (14):

$$\phi_{ss} = \frac{\Lambda_0}{G_0} = \frac{\Lambda_0 \tau_2^3}{\tau_1 q_0}$$

from which

$$\tau_1 = \frac{\tau_2^3 G_0}{q_0} \text{ sec} \quad (15)$$

A typical design example would be as follows:

$$\begin{aligned} G_0 &= K_D G_A K_V K_M \times 360 \alpha_0 \\ &= \frac{5}{57.3} \text{ (V/deg)} \times 100 \text{ (V/V)} \\ &\quad \times 2 \text{ (Hz/sec/V)} \times 40 \times 360 \times 0.06 \\ &= 1.5079 \times 10^4 \end{aligned}$$

$$w_{L,0} = 3 \text{ Hz}$$

$$\Lambda_0 = 200 \text{ Hz/sec at S-band}$$

$$\tau_2 = \frac{4.455}{3} = 1.485 \text{ sec (from Eq. 10)}$$

$$\tau_1 = \frac{(1.485)^3 \times 1.5079 \times 10^4}{6.75}$$

$$= 7.316 \times 10^3 \text{ sec (from Eq. 15)}$$

$$\phi_{ss} = \frac{360 \times 200}{1.5079 \times 10^4} = 4.4775 \text{ deg (from Eq. 14)}$$

V. Concluding Remarks

The circuit design of the Receiver Loop Phase Control Assembly has been accomplished, and a breadboard

model of the circuit is currently under construction. The design will be evaluated in the engineering model of the Block IV receiver.

References

1. Donnelly, H., Shallbetter, A. C., and Weller, R. E., "Block IV Receiver-Exciter Development," in *The Deep Space Network*, Space Programs Summary 37-66, Vol. II, pp. 115-124, Jet Propulsion Laboratory, Pasadena, Calif., Nov. 30, 1970.
2. Wick, M. R., "DSN Programmed Oscillator Development," in *The Deep Space Network Progress Report for January and February 1972*, Technical Report 32-1526, Vol. VIII, pp. 111-124, Jet Propulsion Laboratory, Pasadena, Calif., Apr. 15, 1972.
3. Tausworthe, R. C., "Practical Design of Third-Order Phase-Locked Loops," Report 900-450, Apr. 27, 1971 (JPL internal document).

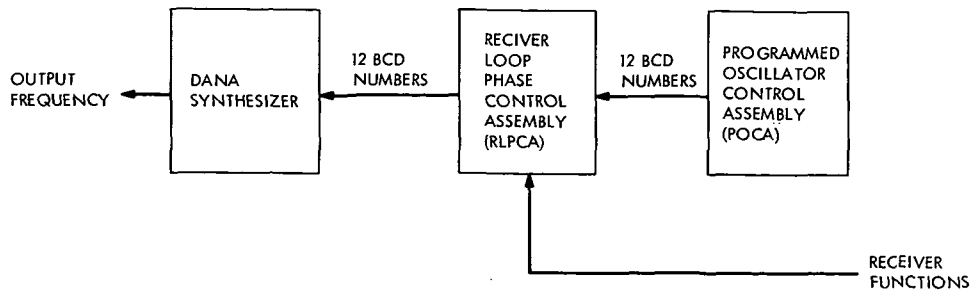


Fig. 1. Receiver Loop Phase Control Assembly application

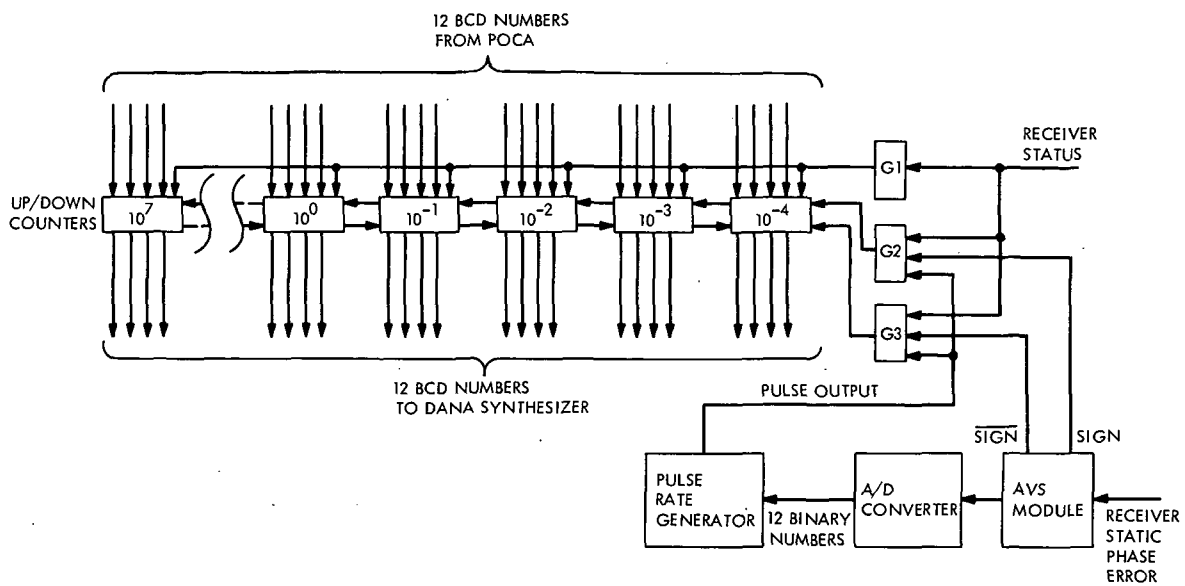


Fig. 2. Block diagram of Receiver Loop Phase Control Assembly

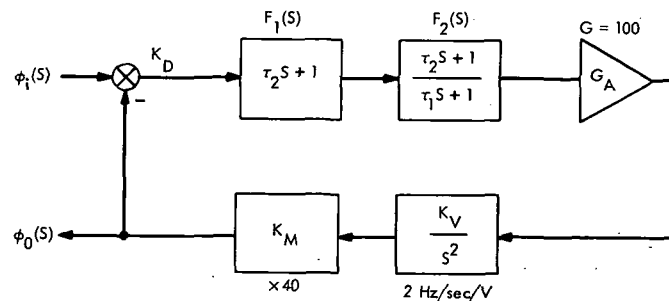


Fig. 3. Receiver loop block diagram

Programmed Oscillator Development

H. Donnelly and M. R. Wick
R.F. Systems Development Section

This article describes the addition of programmed oscillators in the Block III receiver/exciter subsystems at DSS 14 and DSS 43 for Pioneer 10 support during Jupiter flyby. A brief description of the tracking requirements of the mission and the subsystem modifications to incorporate the programmed oscillators is given.

I. Introduction

Programmed oscillator development for the Block IV receiver/exciter and the time sync exciter has been discussed in previous progress reports (Refs. 1 and 2). However, before the Block IV becomes available in the network, there will be a need for a programmed oscillator, the first requirement being to track *Pioneer 10* during Jupiter flyby. To meet this requirement, the programmed oscillator is being adapted to the Block III receiver/exciter subsystems at DSSs 14 and 43 to support tracking until Block IV subsystems become available.

II. Pioneer 10 Tracking Requirements

Before discussing the adaptation of the Block IV programmed oscillator to the Block III receiver/exciter, the Jupiter flyby doppler ranges, rates, and accelerations are presented and a plan for tracking during this period discussed.

Figure 1 shows typical plots of doppler ranges, rates, and accelerations expected during the flyby period. With these expected ranges a large frequency offset is developed in the probe receiver during each pass. It is desirable to reduce this frequency offset prior to handover

from one station to the next to minimize the phase error in the probe receiver and thereby increase the probability of transfer without loss of lock. This is significant at Jupiter distances since loss of lock would not be detected until 100 minutes later (two-way transmission time). The offset in the probe receiver can be minimized by linearly ramping the frequency of the uplink transmitter with the exciter programmed oscillator.

The frequency profile during flyby while using the technique of ramping the exciter programmed oscillator at DSSs 14 and 43 is shown in Fig. 2. Details during the occultation period of Jupiter and its Moons have been omitted—one-way tracking during this period has been assumed. Since the exciter is programmed at a linear rate, knowing the frequency rate, the starting time, and the rest frequency at the end of the program makes it very likely that doppler data can be obtained during this period.

Estimated maximum significant positive and negative errors that will occur during the flyby period resulting from doppler are shown in Table 1. Errors resulting from linear programming are not included. This rate can be selected so that it does not produce a significant error. The estimated maximum error in the probe is approxi-

mately 10 degrees; this error will cause no significant degradation in the command link. The DSS receivers, however, do accumulate significant errors which can be reduced to approximately 10 degrees by programming either the receiver or exciter or a combination of both. A third-order loop design would also reduce these errors, and such a design has been used to track *Mariner* Mars 1971 at DSS 14 on an R&D basis. The third-order loop, however, is being investigated for use in the Block IV receiver.

III. Block III Programmed Oscillator Modifications

The frequency range of the Block IV programmed oscillator does not permit its use directly in the Block III exciter and receiver. The Block III modifications required to accommodate the Block IV programmed oscillator are discussed in the following.

A. Exciter

The existing and modified block diagrams are shown in Fig. 3. The programmed oscillator must be inserted into the exciter ahead of the phase modulator at 22 MHz. Since the Dana synthesizer output frequency range is 40 to 51 MHz, it is necessary to convert the Dana synthesizer output frequency to 22 MHz by mixing with a standard frequency. 25 MHz was selected as the standard to minimize interference from intermodulation products resulting in the mixer.

B. Receiver

The existing and modified block diagrams are shown in Fig. 4. The programmed oscillator can be inserted into the receiver at 69 MHz after the $\times 3$ frequency multiplier. The Dana synthesizer's output of 48 MHz is mixed with a voltage-controlled oscillator (VCO) operating at 21 MHz. A VCO gain of 1200 Hz/volt at 21 MHz is used to maintain the existing loop gain.

C. Programmed Oscillator

The programmed oscillator described in Ref. 2 will have additional *manual* (operator control) capability so that it can be used without a computer in this application. Additional storage will be incorporated to provide for programming the frequency sweep to begin at a specified GMT and stop at a predetermined handover frequency. A sweep rate and corresponding start time will be entered manually by the operator and easily verified with a front panel digital display. With this added feature, sweep rates can be stored well in advance of the time at which the sweep is to occur. The control assembly will have the capability of storing up to four sweep rates (with corresponding start times). The frequency sweeps required for the complete pass can then be programmed in advance, and no adjustments would be required during tracking.

Initial receiver acquisition will be similar to the present method, using existing predict formats, and the acquisition procedure will be based on monitoring the doppler. Adjustment of the receiver frequency to obtain lock will be accomplished with the present acquisition control knob or by manual programming of the synthesizer. Exciter and receiver monitoring will be the same as in the present Block IIIC configuration.

IV. Concluding Remarks

Programming the Block IIIC exciter and receiver during the Jupiter flyby will minimize the probe receiver and ground receiver loop phase error. This will increase the probability of maintaining two-way lock during handover and also provide the possibility of obtaining two-way doppler data during this period.

The Block IV programmed oscillator design is being adapted to the Block IIIC Receiver/Exciter Subsystem for installation at DSS 14 and DSS 43 and will contain additional manual control capabilities to enable the operator to manually preset the program prior to the tracking period.

References

1. Wick, M. R., "Programmed Oscillator Development," in *The Deep Space Network*, Space Programs Summary 37-66, Vol. II, pp. 127-132. Jet Propulsion Laboratory, Pasadena, Calif., Nov. 30, 1970.
2. Wick, M. R., "DSN Programmed Oscillator Development," in *The Deep Space Network Progress Report*, Technical Report 32-1526, Vol. VIII, pp. 111-124. Jet Propulsion Laboratory, Pasadena, Calif., Apr. 15, 1972.

Table 1. Doppler phase error^a

DSS	43	63	14 and 43	43
Track	Pre-periapsis	Pre-periapsis	Periapsis	Post-periapsis
DSS receiver $2B_{L_0}$	12	12	48	48
Probe receiver doppler:				
Range	-3	-4	-5	+7
Rate	-5	-3	+5	+6
Acceleration	-3	-1	-3	+6
Estimated maximum total	-11	-8	+7	-3
			+9	+10
DSS receiver doppler:				
Range	-8	-13	-15	+23
Rate	-4	-10	-16	+25
Acceleration	-6	-3	+23	+8
Estimated maximum total	-18	-26	-31	+56
DSS receiver noise error (degrees rms)	12	12	17	17

^aIn degrees pK.

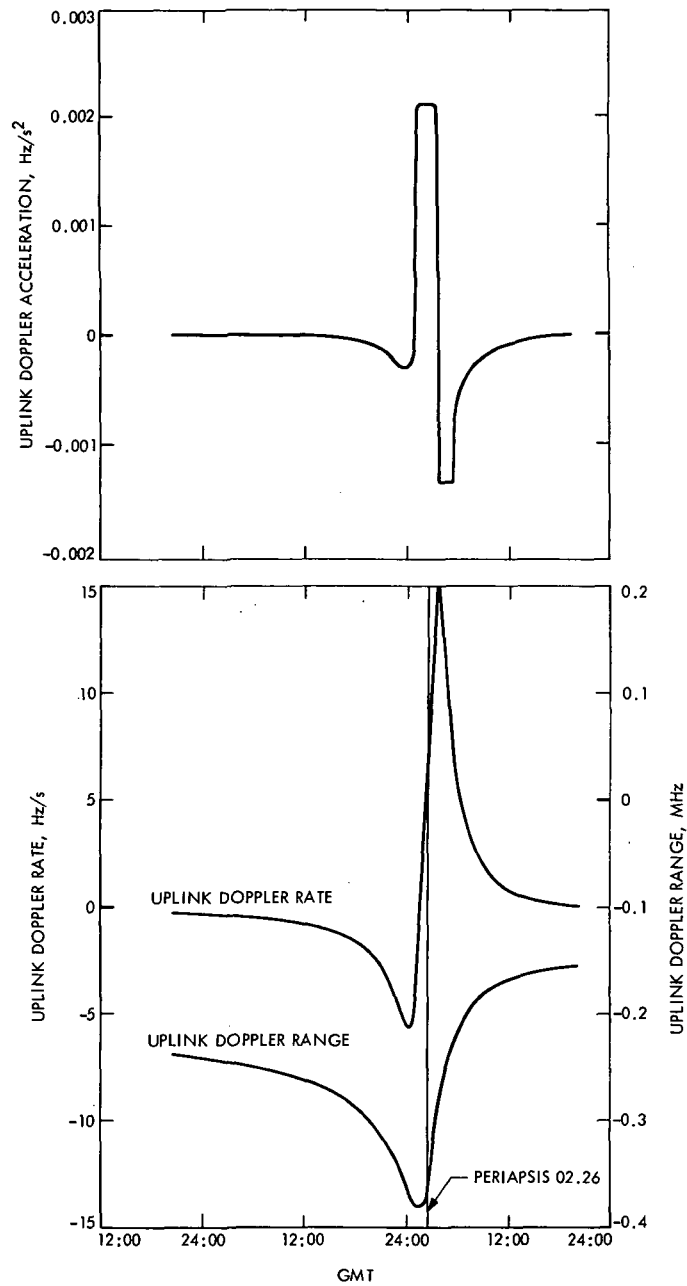


Fig. 1. Jupiter flyby doppler

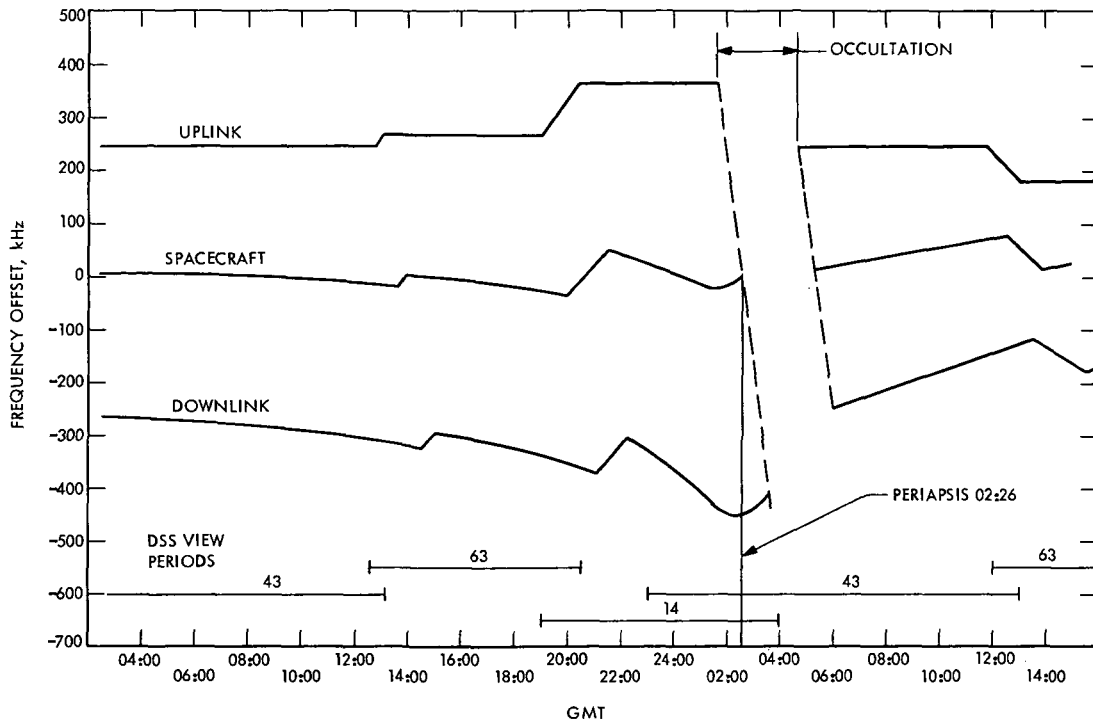


Fig. 2. Jupiter flyby frequency profile

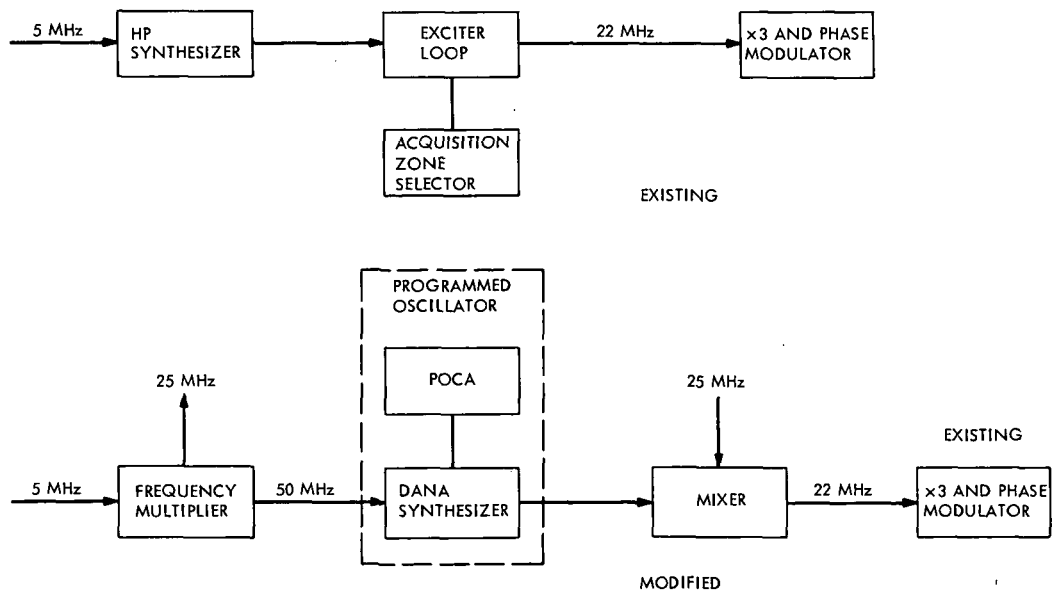


Fig. 3. Exciter block diagram

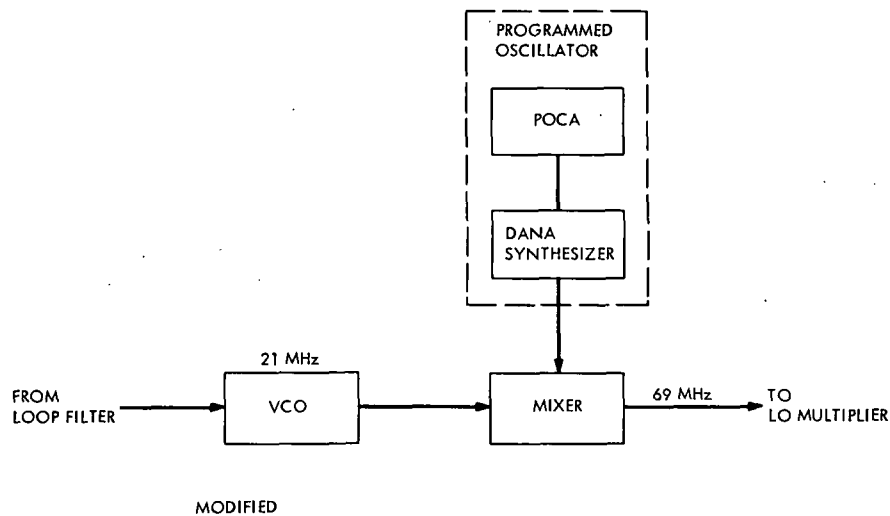
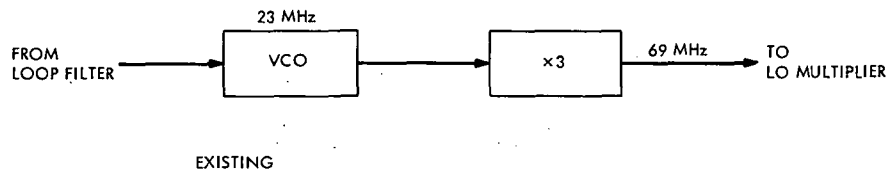


Fig. 4. Receiver block diagram

Experimental S- and X-Band Feed System Ellipsoid Reflector

H. R. Hoggan and W. J. Kissane
DSIF Engineering Section

To support the Mariner 1973 X-band experiment, the S/X feed system has been designed and is currently under fabrication for installation on the DSS 14 64-m-diameter antenna. The system will allow both S- and X-band signals to be received along the same bore sight direction. Basic elements of the system are the ellipsoid reflector over the S-band horn and a dichroic reflector plate over the X-band cone. The first parts to be manufactured are the ellipsoid reflector and its backup structure. This article describes the ellipsoid reflector, the method used to form it, the measured accuracy of the finished part, and its connection to the backup structure.

I. Introduction

To receive S-band and X-band radio-frequency signals along the same bore sight direction on the 64-m-diameter antenna (Refs. 1, 2, and 3), two essential elements are required: a dichroic plate and an ellipsoid reflector. The dichroic plate is mounted at an angle over the X-band horn and reflects S-band signals while allowing the X-band signal to pass through the plate with no change in direction. The reflected S-band signal is then directed toward the ellipsoid reflector. This reflector is positioned over the S-band horn in such a way as to direct the signal down the axis of the horn. The system has been designed to allow both elements to be retracted so that individual horns can be used in a normal manner.

This article describes the fabrication of the ellipsoid reflector and its connection to the backup structure.

These are the first pieces of hardware to be manufactured. As additional pieces are fabricated, they will be described in future articles. Figures 1 thru 4 are photographs of the eggcrate surface template, the completed ellipsoid reflector, the backup structure resting on the reflector, and one of the flexures mounted to the backup structure.

II. Ellipsoid Reflector

The reflector is a segment of an ellipsoid whose semi-major axis is 2.3 m (90.928 in.) and the semi-minor axis is 1.88 m (73.993 in.). The edge of the reflector is described by the intersection of a cone with the ellipsoid. The surface is approximately 2.33 m (88 in.) long, 2.00 m (79 in.) wide, and 0.3 m (12 in.) deep and in plan is heart-shaped.

An investigation into the methods of forming such a dish surface was made during the initial stages of the project. Five methods were found that could be used and still meet the specified accuracy:

- (1) Drop hammer method.
- (2) Explosive forming.
- (3) Stretch forming.
- (4) Secret process (believed to be membrane forming).
- (5) Yoder hammer.

Methods (1), (2), and (3) require an expensive forming die. For method (4), being secret, the requirements were not known and the process is expensive. Using the yoder hammer, parts are relatively inexpensive to form, but accuracy is highly dependent on the operator's skill. The yoder hammer method was selected for three reasons:

- (1) A company was found that had the necessary operator skills.
- (2) It was the most economical method.
- (3) It had the shortest delivery time (important in meeting the schedule).

A surface template was required during the forming process to check progress, to use as a final checking template, and to hold the dish to the contour during the mounting of the flexures. First a female mold was made using a sweep template rotating on the axis of the ellipsoid. From this mold an eggcrate surface template was cast using wood intercostals and an epoxy surface (see Fig. 1). The accuracy of the template is within 0.25 mm (0.010 in.) of the theoretical surface. On the template is scribed the RF center (point I), the X and Y centerlines, and the reflector edge trim line.

Upon completion of the checking template, fabrication of the ellipsoid was commenced. The material selected was 1100-H14 aluminum. It was selected for its high electrical conductivity which causes less RF heating of the surface and thus less heat distortion. The material is 3.2

mm (0.125 in.) thick. The yoder hammer is a cam-operated power hammer operating at about 120 blows per minute. The forming anvil used was about 40 mm (1.5 in.) in diameter.

For ease of fabrication, two 1.22-m (48-in.)-wide sheets were used to form the two halves of the ellipsoid. They were welded together with 1100 filler metal after both halves were shaped as close as possible to the eggcrate surface. Little welding distortion was noted but some rework of the surface was necessary to bring the completed part into acceptable tolerance. Figure 2 shows the completed ellipsoid on its checking template.

Inspection of the completed part was made using back lighting and a feeler gage. The piece was resting on the surface template unrestrained. Measurements were made on 130 points of the surface. The specified surface tolerance was ± 1.5 mm (± 0.060 in.). The maximum point was 2.3 mm (0.09 in.) at two locations. Ninety-three percent of all points measured fell within 0.8 mm (± 0.030 in.) making the rms of the surface better than 0.6 mm (0.023 in.). The completed reflector unit mounted on the backup structure has a specified rms less than 1.5 mm (0.060 in.).

Figure 3 shows the backup structure resting on the ellipsoid. Currently in progress is the attachment of the backup structure to the dish. The connection is through nine flexures. Each flexure is 1.5 mm (0.06 in.) thick and has holes that keep the flexure stiffness constant even though the length of the flexures varies. (see Fig. 4 for photograph of one flexure). Bracket clips at short intervals attach the flexure to the ellipsoid reflector. This method of attachment will allow for thermal expansion of the dish and minimize thermal distortion.

III. Future Work

As fabrication continues on the ellipsoid assembly, future articles will describe the retraction mechanism and the space structure. Fabrication of the dichroic plate and support will start shortly. Future articles will describe the plate and its support structure.

References

1. Katow, M., "S- and X-Band RF Feed System," in *The Deep Space Network Progress Report*, Technical Report 32-1526, Vol. VI, pp. 139-141. Jet Propulsion Laboratory, Pasadena, Calif., Dec. 15, 1971.
2. Potter, P. D., "S- and X-Band RF Feed System," in *The Deep Space Network Progress Report*, Technical Report 32-1526, Vol. VIII, pp. 53-60. Jet Propulsion Laboratory, Pasadena, Calif., Apr. 15, 1972.
3. Katow, M. S., and Hoggan, H. R., "Prototype S- and X-Band Feed System Hardware," in *The Deep Space Network Progress Report*, Technical Report 32-1526, Vol. IX, pp. 185-187. Jet Propulsion Laboratory, Pasadena, Calif., June 15, 1972.

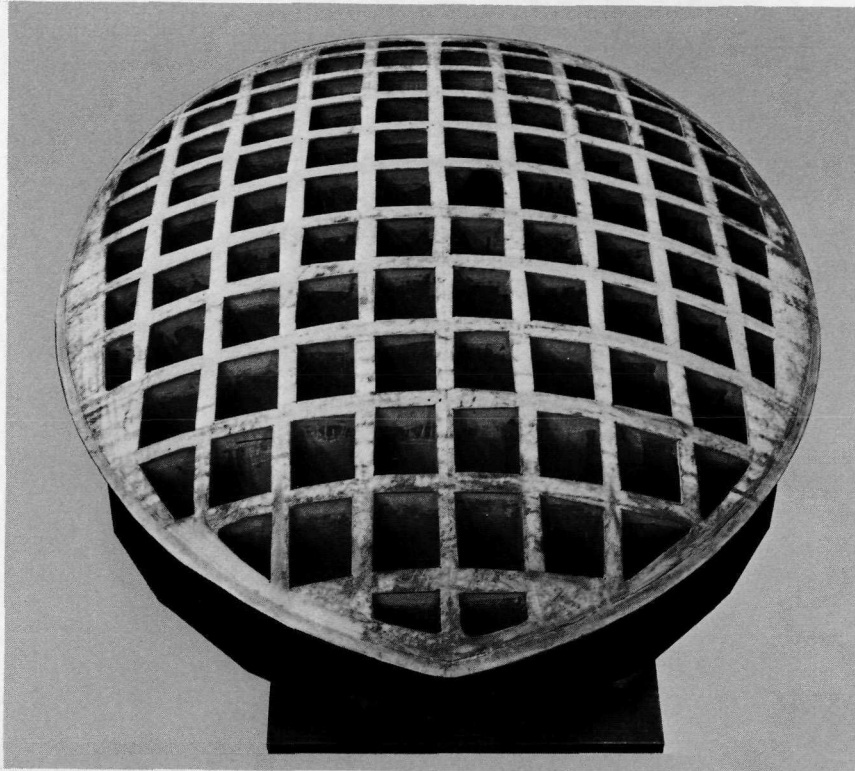


Fig. 1. Eggcrate surface template

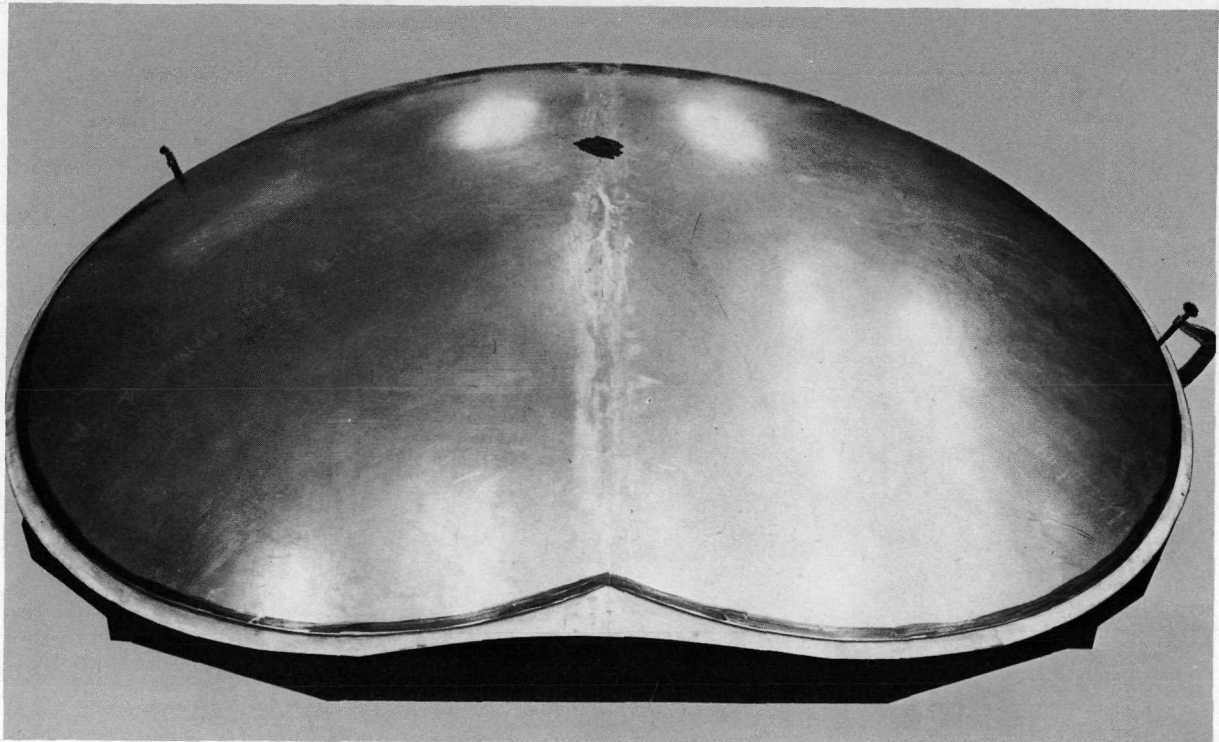


Fig. 2. Completed ellipsoid reflector

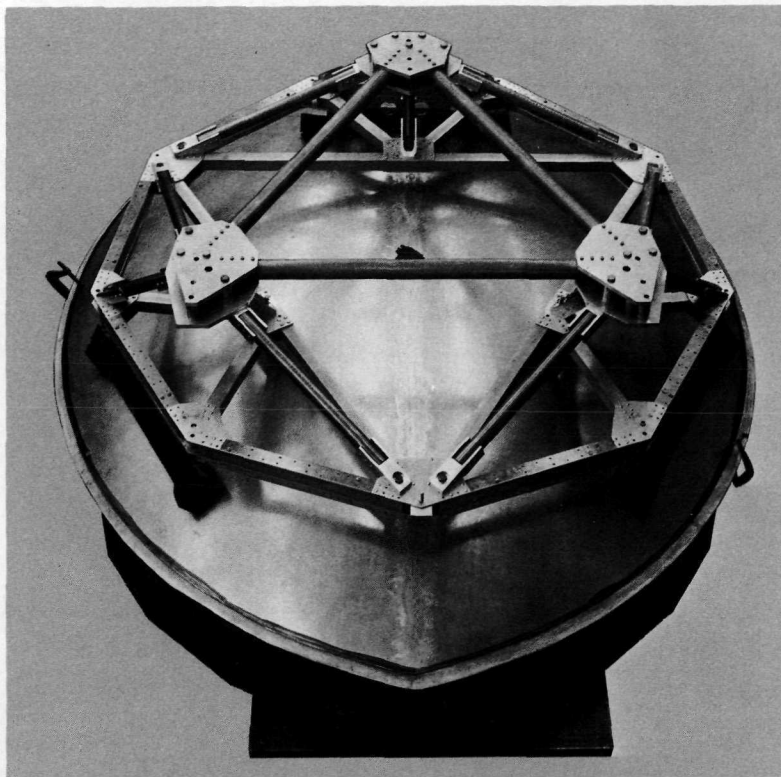


Fig. 3. Backup structure resting on ellipsoid reflector

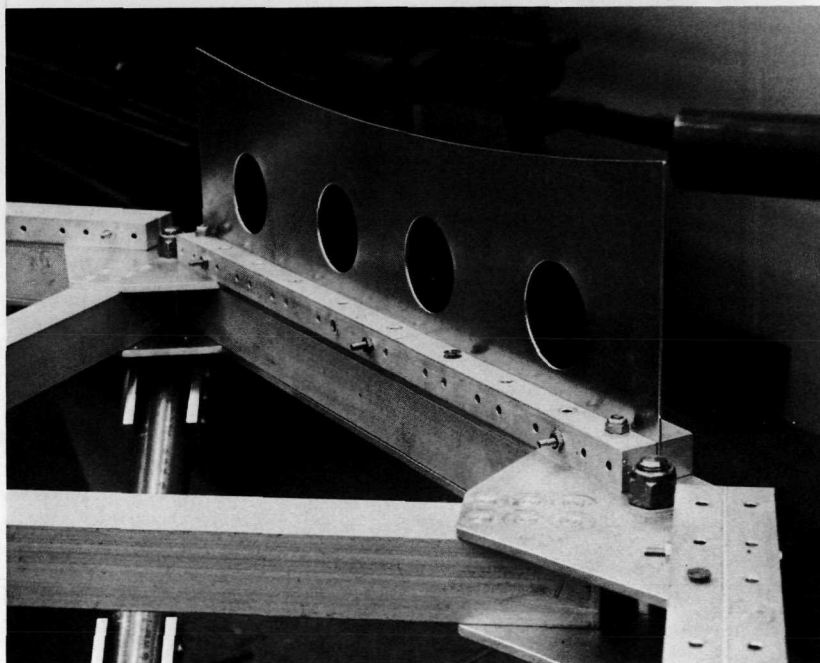


Fig. 4. Flexure mounted on backup structure

Improvements to Angle Data System Autocollimators

R. A. Zanteson
DSIF Engineering Section

The Angle Data System of the 64-m-diameter antenna utilizes two-axis autocollimators as the optical link between the precision instrument mount and the intermediate reference optical assembly. The accuracy, resolution and stability of these instruments directly affects the pointing accuracy of the antennas. With an accuracy and resolution of better than one arc second, great care must be taken in each phase of the design and construction.

The Angle Data System of the 64-m-diameter antenna utilizes two-axis automatic autocollimators as the optical link between the precision instrument mount, located at the intersection of the antenna axis, and the intermediate reference optical assembly.

The autocollimators currently in use at DSS 14 represent the state of the art at the time of their purchase (1965). The trend toward higher operating frequencies of the 64-m subnet, with attendant narrower beamwidths, places an emphasis on the need for higher overall accuracy of the Angle Data System. In the procurement of the autocollimators for the overseas 64-m antennas, the work which has been done in order to meet these needs includes the areas of higher resolution, accuracy, and long-term stability. A simplified schematic of the new design is included as Fig. 1.

The autocollimators must maintain their full accuracy and null stability while moving through all attitudes, with respect to gravity. During the design, particular emphasis was placed on the structural rigidity of each component, both singly and as it relates to the entire assembly.

One source of attitude instability has been the tungsten filament lamp, which is the primary illumination source. In the previous design, a broad filament lamp was mounted in the autocollimator housing to illuminate the 0.94-millimeter square source stop, with a pair of unsymmetrical condensor lenses interposed to concentrate and diffuse the lamp filament image. The gravity deflection of the filament contributed five-arc second error. It was not practical to make the filament and its supports

sufficiently stiff to avoid degrading the uniformity of illumination across the source stop as they deflect due to gravity.

In the design of the new units, a more conventional lamp is used which satisfies the dual need for radiation in the visual spectrum, and a peak output compatible with the 900-nm peak of the silicon detector used in the primary system. This lamp is now housed separately from the optical sensing head. This basic change in design incorporates many advantages. The removal of the lamp as a heat source from the basic cast instrument housing gives benefit in terms of output stability and long electronic component life. With the increased ease of convective cooling, the lamp may be made larger and allowed to operate at higher envelope temperatures.

The lamp housing is connected to the autocollimator optical system by means of an incoherent fiber optic bundle, which accomplishes excellent integration of the source stop illumination. This integration makes the system insensitive to lamp alignment and allows the lamp filament to move with thermal deflection or gravity loading. Also it allows the lamp to be replaced in the field without a tedious realignment procedure. The fiber optic bundle also may be replaced in the field without any adjustment or alignment.

Long-term stability of the electrical null is particularly important in order to maintain the basic angle reference. The stability has been enhanced by using selected integrated circuits with low temperature drift, metal film resistors with low temperature coefficients, as well as zener-regulated power supplies to drive the operational amplifiers. Redesign of the demodulator circuitry to employ solid-state switches, instead of electro-mechanical units, will further enhance the reliability and temperature stability of the instrument.

Resolution has been improved by removing or modifying sources of noise in the optical train. In the new design the resolution has been improved from greater than one

arc second to less than one-half arc second. The secondary source stop consists of a 0.94-millimeter square aperture and means of evenly illuminating the aperture. In the previous design the aperture was produced photographically on a glass plate, but this suffers from internal reflections between the surfaces of the relatively thick plate, which detracts from aperture uniformity. The stop used in the new instrument is a physical aperture, photochemically etched in a very thin metal plate. The photo-detector assembly stop is now made in the same configuration, and is physically against the face of the detector, avoiding problems of spurious light leaking between source and detector. This arrangement also has excellent mechanical stability.

The beamsplitter which divides the incoming and outgoing legs of the optical train was, in the previous design, a solid prism. The prism beamsplitter was found to introduce secondary reflections which prevented a uniform wavefront, thereby increasing optical noise. Tests of intensity distribution across the light beam were run with and without the prism in the path. The distribution was also found to be sensitive to prism alignment.

To reduce optical noise in the new design, a thin Mylar membrane commonly known as a pellicle will be used, instead, as the normal mode beamsplitter. The pellicle, being only on the order of 0.0025 millimeter thick, is essentially free of ghost reflections attendant on a plate or prism beamsplitter.

Also, to reduce noise, great care has been taken to minimize internal reflections within the autocollimator, both by internal baffling and by the application of nonreflective coatings to all surfaces adjacent to the optical path. The objective lens design is unchanged, but it is now narrow band coated with magnesium-fluoride for maximum transmission efficiency at 900 nanometers.

The changes brought about in the new generation of instruments should improve the stability, reliability, and accuracy of the Angle Data System.

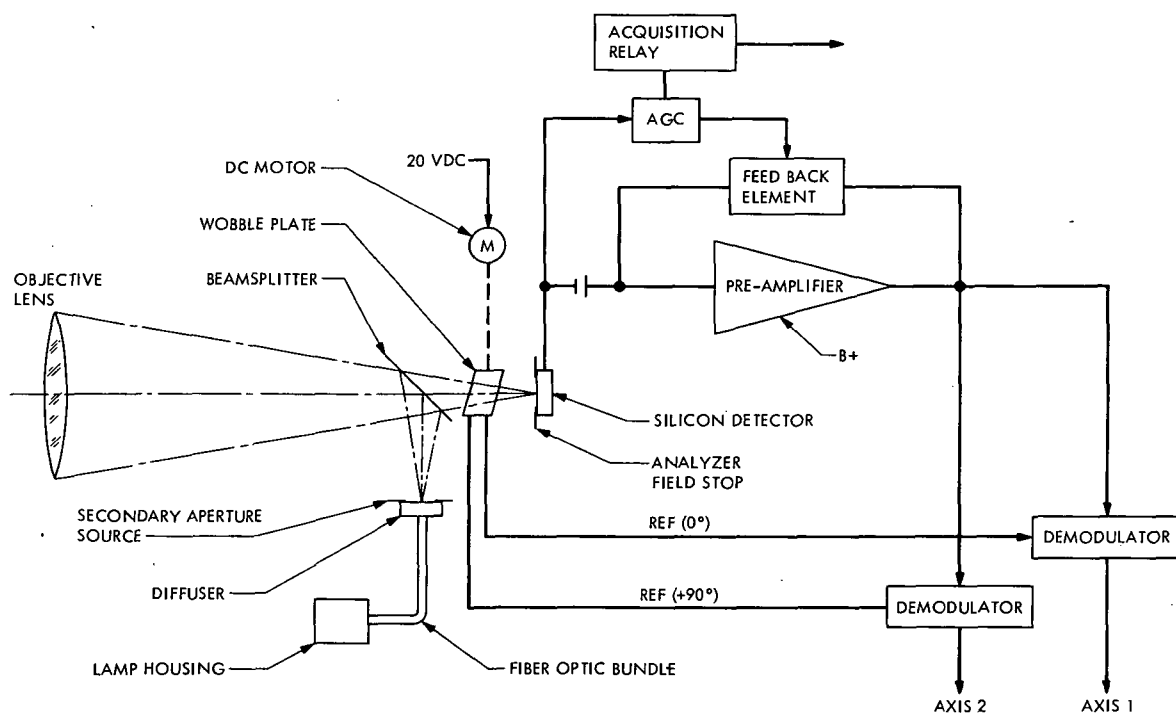


Fig. 1. Two-axis autocollimator block diagram

New Probes for Tracing Electrical Noise

C. Lundy
DSIF Engineering Section

Stations of the DSN are vulnerable to many kinds of noise. To discover and measure potentially harmful noise, three new designs of probes are described. The article also suggests design practices that defend the station against noise.

Electrical noise is any signal-like disturbance capable of obscuring information. The most perfect timing pattern in a station would be noise if it merged into a computer input. Since the receivers, transmitters, and control rooms contain hundreds of signal circuits capable of inadvertent mutual coupling, there is a constant danger of noise interference. Further, the sudden or gradual deterioration of electrical devices and power distribution systems endangers proper operation of the rest of the station. Prevention, measurement, and cure of noise is a paramount concern.

Some noise is distributed on the primary power wires. Once introduced into the power system, the noise may travel throughout the station. Other noise is coupled from rack to rack over defective cables or on cables which are imperfectly coupled to the chassis.

The ideal signal cable would carry a current from source to load without radiating any part of it, and would be able to pass through a noisy environment without picking up any noise. Actual cables generally are very close to the ideal. In the DSIF stations, there are hun-

dreds of signal paths that usually have no evidence of any undesired coupling.

Most of the signals are low impedance, with currents typically tens of milliamperes. These currents travel in circuits, going out from the source on one conductor and returning to the source on a second. Sometimes the return path is poorly defined. This is a serious oversight; the return path requires the same attention as the signal lead. Noise problems nearly always come from separation of the two signal paths.

Whenever the current in a conductor changes, the magnetic field around it also changes. Every signal, therefore, sets up a varying magnetic field around each of the two conductors in which it flows. If the two conductors are very close to each other, the currents flowing in opposite directions almost perfectly cancel each other's magnetic fields. In this case, little power is radiated. But if the two branches of the circuit are separated, they both become radiators.

Not only do these separated paths radiate signals along the way, they at the same time become susceptible to

noise from other sources. The converse is also true; a circuit that cannot radiate is immune to pickup.

A properly made coaxial cable, properly used, demonstrates the principle of balancing the signal and its return. The cable has no external field at all, and external fields do not induce signals into the cable. (Some coaxial cables sacrifice a little quality to improve mechanical flexibility or to reduce cost, but even they come close to the ideal.) The coaxial cable must have all of its return signal in the shield. If any of the current escapes to some other path, the cable loses its effectiveness. This can result from poor equipment design that allows alternate paths for part of the signal circuit. It can also come from a termination that has a bad connection to either one lead of the cable or to the mating connector.

In a multiconductor cable it is best to use a separate return lead for each signal circuit. For best isolation the pair of leads should be twisted together. Telephone cables are outstanding in the use of careful twisting of pairs of wires. Crosstalk is usually negligible even with miles of cables containing many circuits.

To measure noise currents in cables and ground buses, three convenient probes have been developed. The first is a modified clip-on ammeter. It can be snapped over any cable up to 2.8 cm in diameter and is useful over a frequency range of 30 Hz to 400 kHz. The second is insensitive to low frequencies, but has high output from about 5 kHz to nearly 1 MHz. The third is useful from 300 kHz to 10 MHz. Each probe is used as a current-to-voltage transducer, usually with an oscilloscope as a readout. Each reads only the unbalanced component in a cable or group of cables, without disconnecting the cable. These probes are sensitive enough to read any potentially harmful currents. They can be used without disturbing any of the equipment. Using an oscilloscope to show the waveform and frequency of signals makes it easy to identify and trace the noise paths.

The first probe, useful for low-frequency currents from 1 milliamperes to 100 amperes, is modified from an RS-1 Amprobe ammeter. As supplied by Amprobe, the clip-on ammeter has provision for reading voltage with a pair of leads attachable to the bottom. The lead terminals are used to connect a cable to the oscilloscope, and, inside the instrument, a jumper is added from one terminal to one end of the pickup coil. The other end of the coil already has a lead to the second terminal. Modification steps are as follows:

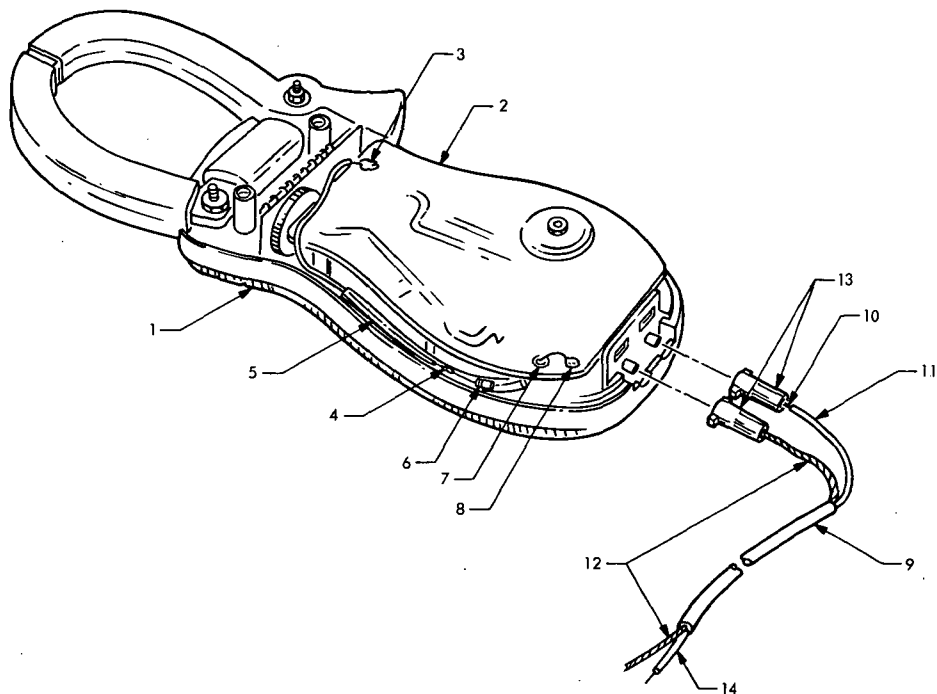
- (1) Remove the instrument rear cover. A special deep socket wrench must be used.
- (2) With the back off, add the jumper (5) and resistor (6) as shown in Fig. 1. The 100-ohm $\frac{1}{8}$ -watt resistor is included as a fuse. (The voltmeter is still good to about 40 volts.)
- (3) When replacing the back, it is safer to use the plastic screws to prevent high-voltage shock.
- (4) Label the instrument to indicate that it should not be used for reading line voltages. Its usefulness as a normal clip-on ammeter is not affected.
- (5) Cut the two connectors from the voltage leads that came with the instrument. Attach them to the center conductor and shield respectively of a coax or shielded cable.
- (6) The instrument is now usable, but the frequency response shows a gradual rise to about 700 Hz, and a gradual decline to 10 kHz. A pad has been added on the far end of the cable. This pad adjusts the output to the characteristics shown on Fig. 2. The pad schematic is Fig. 3. The pad has a J. W. Miller 70F223A1 subminiature 2.2-mH choke, a 470-ohm 1-watt resistor, and a 5- μ F capacitor in series.

To make a higher frequency probe, use a core of a single piece of nickel alloy foil 2×12 cm. It is insulated and cushioned with a wrap of polyolefin shrink tubing; then 1000 turns of No. 34 AWG wire are bank-wound in one pass around the middle of the core. A 1000-ohm resistor shunts the coil, and a coaxial cable connects it to the oscilloscope. The probe is bent into a U-shape and an outer jacket added. The construction of this probe is described more completely in DSIF-STD-00006 (Ref. 1). Figure 4 shows a typical calibration curve. Several were also made with an outer shield covering the exterior bend of the U. These probes respond only to cables within the curve, not those on the outside. The response curve has somewhat better high-frequency output than Fig. 4 shows. If the central core is made from tinned soft steel, the output is low at frequencies below 10 kHz. If aluminum is used for the core, there is little response below 100 kHz.

To trace leakage signals above 300 kHz, there are excellent pickups available at radio parts stores. The ferrite core antennas used in miniature broadcast receivers have high sensitivity from 0.3 to 10 MHz. Those intended to be tuned by 365-pF capacitors are best. The response should be flattened by a 1000-ohm shunt, and a pair of short leads used to connect to an oscilloscope or RF voltmeter.

Reference

1. *DSIF Standard Grounding System Requirements for Deep Space Stations*, DSIF-STD-00006, June 6, 1972 (JPL internal document).



- | | |
|---|---|
| 1. AMPROBE MODEL RS-1 | 8. SOLDER RESISTOR LEAD TO LOWER LEFT-HAND PAD OF PRINTED-CIRCUIT BOARD |
| 2. PRINTED-CIRCUIT BOARD | 9. CUT COAXIAL CABLE RG-1808/U TO 3-m LENGTH |
| 3. SOLDER ONE END OF 24 AWG WIRE TO UPPER RIGHT-HAND PAD OF PRINTED-CIRCUIT BOARD | 10. CENTER CONDUCTOR |
| 4. SOLDER RESISTOR LEAD TO INSULATED 24 AWG WIRE | 11. INSULATION |
| 5. INSTALL TEFLON SLEEVE | 12. SHIELD |
| 6. INSTALL RESISTOR | 13. SOLDER CONNECTOR SUPPLIES WITH AMPROBE MODEL RF-1 TO COAXIAL CABLE |
| 7. ROUTE RESISTOR LEAD THROUGH INSULATED EYELET IN PRINTED-CIRCUIT BOARD | 14. STRIP AND TIN COAXIAL FOR OUTPUT SIGNAL TO OSCILLOSCOPE |

Fig. 1. Field modification of Amprobe Model RS-1

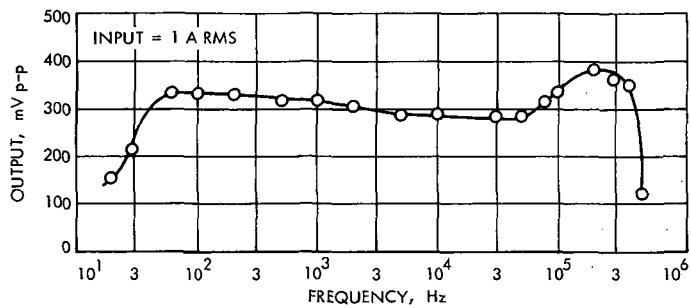


Fig. 2. Calibration curve of low-frequency probe

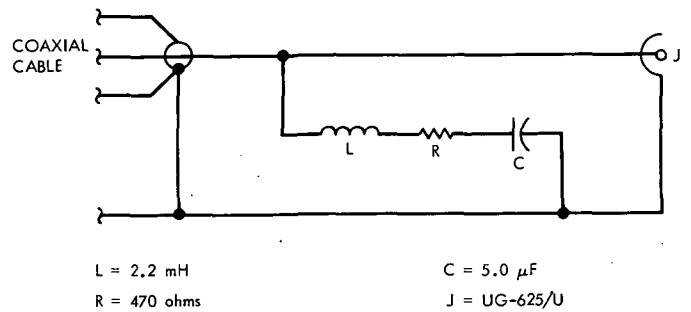


Fig. 3. Pad for low-frequency probe

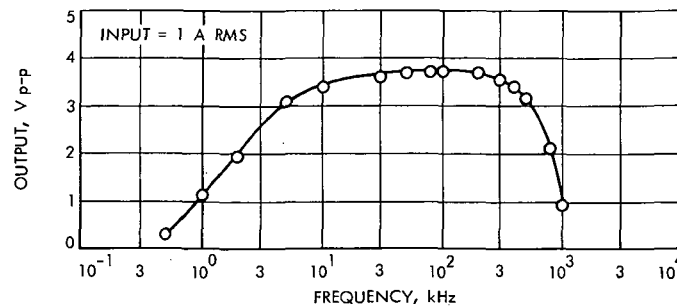


Fig. 4. Calibration curve of high-frequency probe

Repositioning of Parabolic Antenna Panels Onto a Shaped Surface

R. Levy
DSIF Engineering Section

Optimal parameters for shifting existing parabolic reflector surface panels for re-use within shaped antenna configurations are determined from theory and equations given in this article. The panels are reset to minimize the rms half-pathlength differences between their surface and the ideal, shaped surface. Input, output, and results are described for a computer program that implements the equations. Results for typical 26- and 64-m antennas indicate that, if all or most of the existing parabolic panels are re-used and repositioned according to the procedure, the consequent rms differences will be small.

I. Introduction

Gain enhancement for existing parabolic antenna reflectors has been discussed by Ludwig (Ref. 1) and Potter¹. One improvement is to modify the hyperbolic subreflector and parabolic main reflector surfaces with slightly different, "shaped" surfaces, which can provide nearly uniform aperture illumination. To do this, completely new subreflectors are anticipated, because the usual subreflector structural configurations are not readily adaptable to surface and envelope changes. However, the main reflector surface typically is formed from many individual panels that can be repositioned to provide a good approximation to the new shaped surface. The approximation depends, of course, upon how closely the original para-

bolic surface within each panel approaches the shaped contour. These errors tend to be small near the center of the antenna and increase towards the rim.

This article presents the geometrical and mathematical relationships used in a computer program that generates optimal new coordinates for repositioning parabolic panels for a shaped surface reflector. These coordinates are selected to minimize differences of the RF energy beam from the path that would be provided by the ideal shaped surface.

II. Approach

Figure 1a shows a radial section of a typical antenna. The solid curve represents the original parabolic surface, and the broken curve represents the desired new shaped

¹"Antenna Study: Performance Enhancement" by P. D. Potter in this issue.

surface. The actual distances between the two curves are exaggerated for clarity. As an example, for the 64-m antenna at the Mars DSS (DSS 14), the maximum distance in the focal direction is only about 2 cm.

Figure 1b shows a typical panel that has been shifted towards the shaped surface. The shifted panel maintains the original curvature, but, because of the inner and outer edge translations, distances from the shaped surface are significantly reduced.

The procedure that will be given here is used to define new edge translations that minimize the weighted rms pathlength deviations from the shaped surface for a discrete set of points distributed over each panel. Since the objective of surface shaping is to provide uniform aperture illumination, the weighting factors are the aperture areas tributary to each of the points. The set of points used in the procedure is the set defined for the shaped surface generated by the computer program Dual Reflector Antenna System Design (DAR) (Ref. 2). This program generates focal-axis shaped coordinates and the angle at the surface between incident and emergent rays for a closely spaced discrete set of points spaced, for example, on an average of about 15 cm in the radial direction for the 64-m antenna.

All relationships developed are based upon a linearization of the actual geometry. In this, the surface between two points closely spaced in the radial direction is approximated by the tangent to the surface at either point. This is reasonable because curvatures are relatively flat and do not have rapid local changes. Furthermore, in developing the parameters for shifting the parabolic panels, it is noted that the shifts are of differential magnitude with respect to the overall geometry, and that the sines and cosines of associated angles of rotation can be replaced by the angle and by unity, respectively. It can be confirmed by calculation that the related approximations in these linearizations are of higher order than the pathlength deviations and shift dimensions.

III. Pathlength Difference Geometry

Figure 2 shows a typical incident ray at radius r that would be reflected towards the subreflector at the angle β after impinging on the shaped surface at point a . Points b and c are, respectively, points on a parabolic panel at the same radius before and after shifting the panel. Points d and e are auxiliary points used to define distances associated with pathlength differences. Expressions will be given for the difference in the path of a ray reflected by a

parabolic panel with respect to the path of a ray reflected by a point on the shaped surface.

Before shifting the panel, the initial difference in pathlength is

$$\underline{DP} = \overline{ad} + \overline{ae} \quad (1)$$

To evaluate \underline{DP} in terms of the parameters of the shaped and parabolic surfaces, let the parabolic curve, with focal length f , be defined in terms of the focal-axis coordinate z and the radial coordinate r as

$$z - r^2/4f = 0 \quad (2)$$

and let the slope be defined as

$$ZP = \frac{dz}{dr} = r/2f \quad (3)$$

Let $DZ = \overline{ab}$ = original difference in the z coordinate between the panel and shaped surfaces. Then, from Fig. 2,

$$\overline{bd} = \overline{de} \cdot ZP \quad (4)$$

$$\overline{de} = \overline{ad} \cdot \tan \beta \quad (5)$$

$$\begin{aligned} \overline{ad} &= DZ - \overline{bd} \\ &= DZ - \overline{ad} \cdot ZP \cdot \tan \beta \end{aligned} \quad (6)$$

Solving Eq. (5) for \overline{ad} ,

$$\overline{ad} = DZ / (1 + ZP \cdot \tan \beta) \quad (7)$$

Also,

$$\overline{ae} = \overline{ad} \sec \beta \quad (8)$$

Therefore, substituting Eqs. (7) and (8) in Eq. (1),

$$\underline{DP} = DZ \cdot S \quad (9)$$

where

$$S = (1 + \sec \beta) / (1 + ZP \cdot \tan \beta) \quad (10)$$

After shifting the panel through an amount $DELZ$ at radius r , the difference in the z coordinate from the panel to the shaped surface is $DZ + DELZ$. Therefore, by analogy with Eq. (9), the pathlength difference, DP , for the shifted panel is

$$DP = (DZ + DELZ) \cdot S \quad (11)$$

Except for *DELZ*, all terms in Eq. (11) are obtained from either the original parabolic geometry or the output of the DAR program. In the following, *DELZ* will be expressed in terms of two shift parameters for each panel: a rigid body z direction shift, H , and a rotation angle, ϕ . The shift parameters are then chosen to minimize the sums of the weighted pathlength deviations for the set of points for which new shaped coordinates are supplied by the DAR program.

IV. Computation of Weighting Factors

The weighting factor based upon the aperture area tributary to the p th radius within the k th panel will be derived with reference to Fig. 3. According to the figure, let R_A and R_B be the inner and outer boundary radii, respectively, for this panel, and let n be the number of radii for which shaped surface coordinates are defined; assume temporarily that all of the panels (with various boundary radii) have a common central sector angle θ .

Then, an appropriate weighting factor, W_p , for a typical interior radius, r_p , of this panel is

$$W_p = [(r_p + r_{p+1})^2 - (r_p + r_{p-1})^2]/4 \quad (12)$$

The weighting factor for the first point in this panel (at radius r_1) is

$$W_1 = [(r_1 + r_2)^2 - 4R_A^2]/4 \quad (13)$$

The weighting factor for the last point in this panel (at radius r_n) is

$$W_n = [4R_B^2 - (r_n + r_{n-1})^2]/4 \quad (14)$$

The weighting factors are normalized so that the sum of these factors at all radii is equal to the number of DAR points for the entire aperture. The corresponding normalization factor F is

$$F = NT/(R_{\max}^2 - R_{\min}^2) \quad (15)$$

where

$$NT = \sum_{k=1}^m n_k \quad (16)$$

in which m is the number of panel rings; n_k is the number of radii in the k th panel; and R_{\max} and R_{\min} are, respectively, the maximum and minimum radii for the aperture.

The pathlength differences are computed within an antenna aperture sector defined by the central angle θ ,

which is taken as the central angle for the innermost panel. At each panel, this sector can be further subdivided for pathlength computations into J sections in the circumferential direction. Then, letting J_k = number of circumferential sections for the k th panel, a second set of weighting factors equal to $1/J_k$ is defined for each panel, and the weighting factor previously derived for the p th radius within the panel is multiplied by $1/J_k$ for the J_k points that are considered at this radius.

V. Computation of Pathlength Difference for Panel Shift Parameters

This computation requires that the focal-axis coordinate change term, *DELZ* according to Eq. (11), which is the sum of a panel rigid body shift, H , plus components caused by the rotation, ϕ . The rotation components can be derived in terms of ϕ from the original parabolic geometry shown in Fig. 4. In Fig. 4a, a typical parabolic panel, which subtends central angle TR , is shown projected on a plane parallel to and above the aperture plane. The panel projection consists of the radial lines, \overline{bd} and \overline{ce} , and the chords, \overline{bc} and \overline{de} . In Fig. 4b, the height, Z_A , of the projection plane above the aperture plane is

$$Z_A = [RA \cdot \cos (TR/2)]^2/4f \quad (17)$$

A local coordinate system is defined by the V axis, to give the distance above the projection plane, and the X axis, which is taken along the panel centerline and represents the distance measured outward from a plane parallel to the Z axis and containing \overline{bc} . The axis of rotation is parallel to \overline{bc} and intersects the origin of the local coordinate system. Rotations are measured positive counterclockwise, as shown. Point p , with coordinates V_p and X_p , is on the parabolic panel before rotation and is located at radius R_p with respect to the focal axis, and at angle TS_c from the panel centerline. For J_k = the number of central angle subdivisions for this panel, TS_c is determined from

$$TS_c = C \cdot TR/J_k, \quad C = 1/2, 3/2, \dots, (J_k - 1)/2 \quad (18)$$

Rotation has two effects on *DELZ*. The first is to bring p' , originally at radius $R_p + \Delta R_p$, inwards by ΔX_p and directly over p . The second is the change in the V coordinate due to rotation, which is approximately the same for p and p' . The rotation component of *DELZ*, which is the distance pp'' , is the sum of these two effects. This sum is approximately

$$DELZ = \Delta R_p \cdot ZP + \phi \cdot (X_p + \Delta X_p) \quad (19)$$

However,

$$\Delta R_p \simeq \Delta X_p \cdot \cos TS_c \quad (20)$$

$$\Delta X_p \simeq \phi (V_p + \Delta R_p \cdot ZP) \quad (21)$$

Substituting Eqs. (20) and (21) in Eq. (19) and neglecting quadratic and higher-order terms in ϕ and ΔX_p leads to the rotation component:

$$DELZ = \phi \cdot (V_p \cdot \cos TS_c \cdot ZP + X_p) \quad (22)$$

Adding the rigid body shift H , the total focal-axis shift at the original point p becomes

$$DELZ = H + \phi \cdot T_c \quad (23)$$

where

$$T_c = V_p \cdot \cos TS_c \cdot ZP + X_p \quad (24)$$

Therefore, the pathlength difference is given in terms of ϕ and H for points in this panel as

$$DP = (DZ + H + \phi \cdot T_c) \cdot S \quad (25)$$

VI. Computation of Shift Parameters

The sum of the weighted squared pathlength differences, $(DP)_p^2$, for all points at R_p in Fig. 4 is (see Eqs. 12-14, 18, 24, 25)

$$(DP)_p^2 = W_p \sum_{c=1}^{J_k} \frac{1}{J_k} S_p^2 \cdot (DZ_p + H + \phi \cdot T_c)^2 \quad (26)$$

where the subscript "p" on the right-hand side is appended to indicate terms depending on R_p and not on the summation parameter "c." By defining

$$T_p = \frac{1}{J_k} \sum_{c=1}^{J_k} T_c \quad (27)$$

$$T2_p = \frac{1}{J_k} \sum_{c=1}^{J_k} T_c^2 \quad (28)$$

Eq. (26) becomes, upon expanding,

$$(DP)_p^2 = W_p \cdot S_p^2 \cdot (DZ_p^2 + H^2 + \phi^2 \cdot T2_p + 2DZ_p \cdot H + 2H \cdot \phi \cdot T_p + 2DZ_p \cdot \phi \cdot T_p) \quad (29)$$

The weighted sum of the squared differences for all $(J_k \cdot n_k)$ points in this k th panel is

$$SS = \sum_{p=1}^{n_k} (DP)_p^2 \quad (30)$$

Taking the partial derivatives of SS with respect to H and ϕ leads to the following normal equations, which can be solved for the shift parameters that minimize Eq. (30) for this panel:

$$\begin{bmatrix} A & B \\ B & C \end{bmatrix} \begin{pmatrix} H \\ \phi \end{pmatrix} = \begin{pmatrix} D \\ E \end{pmatrix} \quad (31)$$

in which

$$A = \sum W_p \cdot S_p^2 \quad (32)$$

$$B = \sum W_p \cdot S_p^2 \cdot T_p \quad (33)$$

$$C = \sum W_p \cdot S_p^2 \cdot T_p^2 \quad (34)$$

$$D = -\sum W_p \cdot S_p^2 \cdot DZ_p \quad (35)$$

$$E = -\sum W_p \cdot S_p^2 \cdot DZ_p \cdot T_p \quad (36)$$

and the summations in Eqs. (32-36) are taken over the n_k radii defined for this panel.

Once H and ϕ are determined from Eq. (31), Eqs. (26) and (30) are used to obtain the weighted sum of squared differences. The minimized rms difference in half pathlength is then obtained from

$$\text{rms} = \frac{1}{2} (SS/n_k)^{1/2} \quad (37)$$

VII. Non-optimum End-Match Shift Parameters

For comparison, it is informative to perform a relatively simple computation to determine the difference in pathlength for a corner-match, non-minimum rms shift of the panel. In this case, the corners b, c, d, e of the parabolic panel are brought to the shaped surface without considering distances from the interior panel points to the shaped surface. To determine the corresponding values of H and ϕ , the sum $DZ + DELZ$ is set equal to zero for the panel corners. Therefore, in Eq. (24), let

$$T_A = V_A \cdot \cos \langle TR/2 \rangle \cdot R_A/2f \quad (38)$$

$$T_B = V_B \cdot \cos \langle TR/2 \rangle \cdot R_B/2f + (R_B - R_A) \cdot \cos \langle TR/2 \rangle \quad (39)$$

where

$$V_A = R_A^2 [1 - \cos^2 \langle TR/2 \rangle]/4f \quad (40)$$

$$V_B = R_B^2 [1 - \cos^2 \langle TR/2 \rangle]/4f \quad (41)$$

Consequently, the non-optimum shift parameters can be found from (see Eq. 23)

$$\begin{bmatrix} 1 & T_A \\ 1 & T_B \end{bmatrix} \begin{pmatrix} H \\ \phi \end{pmatrix} = \begin{pmatrix} DZA \\ DZB \end{pmatrix} \quad (42)$$

where DZA and DZB are the central focal-axis coordinate distances from the shaped to the parabolic panel surfaces.

In practice, the foregoing equations are adjusted to reflect the first and last radii defined for the panel by the DAR program, because it is unlikely that shaped surface coordinates will be supplied exactly at R_A and R_B .

VIII. Computer Program and Results

A computer program has been written to perform the calculations described. Input to the program consists of the focal length of the parabolic surface, the number of panel rings, the central sector angle of the innermost panel, the boundary radii for each panel ring, the number of panels in each ring that fit into the central sector, and the punched card output from the DAR program giving radius, focal-axis coordinate, and β angle.

Output from the program is sequential, beginning with the innermost panel rings and proceeding to the rim. For each panel, the output consists of the rms half-pathlength difference before and after shifting, coordinates, the shift parameters, original and new pathlength differences for points along the panel edges and centerline, and a summary designed to expedite field resetting of the panel that contains focal-axis and radial shift dimensions for panel corners. After all panel rings are processed, summary data for panel edges at R_A and R_B are combined in a single table. This table makes it convenient to determine

focal and radial coordinate gaps and approaches between adjacent panel edges, which are not constrained during the fitting procedure. The current experience is that these gaps tend to be small; for the 64-m antenna, the maximum gap in the focal direction is about 1.5 mm, and the maximum approach in the radial direction is about 3 mm. The average gaps and approaches are considerably less. The radial approaches can either be contained within existing clearance spaces between adjacent panels or be accommodated by minor field trimming.

Both before and after fitting, the inner panel rings exhibit generally smaller pathlength differences than the outer rings. Therefore, if an extremely close fit to the shaped surface is required, it could be advisable to replace some of the outer panel rings with new panels contoured to the shaped surface. Consequently, a final tabulation that is output is the weighted half-pathlength differences for the reflector surface, considering the alternatives of retaining 1, 2, \dots , m existing panel rings and providing $m - 1$, $m - 2$, \dots , 0 new rings.

Table 1 shows a summary of the rms differences for each panel ring for the Mars DSS (DSS 14) 64-m antenna ($m = 9$) and the Venus DSS (DSS 13) 26-m antenna ($m = 7$) before and after fitting. Table 2 contains a summary of the reflector rms differences for various alternatives of retaining existing and supplying new panel rings. Data from Table 2 are plotted in Figs. 5 and 6. In Fig. 5, the broken line is for the alternative of reworking the last panel ring for the DSS 14 antenna by subdividing the existing ring into two rings with independent shift parameters. Figs. 5 and 6 show that, for either of these antennas, the rms differences resulting from best-fit rms shifts of the existing panels are small; therefore, it is appropriate to re-use most or all of the existing panels. The figures also show that the non-optimum corner match fit results in about double the foregoing differences.

References

1. Ludwig, A. C., "Antennas for Space Communications: 1. Shaped Reflector Cassegrain Antennas," in *Supporting Research and Advanced Development*, Space Programs Summary 37-35, Vol. IV, pp. 266-268. Jet Propulsion Laboratory, Pasadena, Calif., Oct. 31, 1965.
2. Jarvie, P., and Gerritson, R., *Dual Reflector Antenna System Design Program*, Document TR-66-700-13-2, Oct. 12, 1966 (JPL internal document).

Table 1. Individual panel ring differences

Panel numbers (in order of increasing radius)	Half-pathlength rms, mm					
	DSS 14 64-m antenna			DSS 13 26-m antenna		
	Before fit	rms fit	Corner fit	Before fit	rms fit	Corner fit
1	0.93	0.10	0.32	0.35	0.13	0.44
2	0.49	0.04	0.09	2.55	0.05	0.10
3	2.55	0.07	0.14	5.43	0.03	0.06
4	7.15	0.03	0.08	7.13	0.05	0.09
5	11.71	0.01	0.02	7.17	0.09	0.20
6	15.60	0.07	0.16	4.83	0.19	0.41
7	17.86	0.15	0.31	2.84	0.37	0.91
8	15.10	0.49	1.18	—	—	—
9	7.17	1.41	3.59	—	—	—

Table 2. Alternatives for retained parabolic vs new panel rings

Combined reflector half-pathlength rms differences, mm							
DSS 14 64-m antenna				DSS 13 26-m antenna			
Panel rings		rms fit	Corner fit	Panel rings		rms fit	Corner fit
Retained	New			Retained	New		
1	8	0.01	0.03	1	6	0.03	0.10
2	7	0.01	0.03	2	5	0.04	0.11
3	6	0.02	0.05	3	4	0.04	0.11
4	5	0.02	0.05	4	3	0.04	0.12
5	4	0.02	0.05	5	2	0.06	0.15
6	3	0.04	0.08	6	1	0.10	0.23
7	2	0.07	0.15	7	0	0.17	0.41
8	1	0.24	0.57	—	—	—	—
9	0	0.69	1.73	—	—	—	—

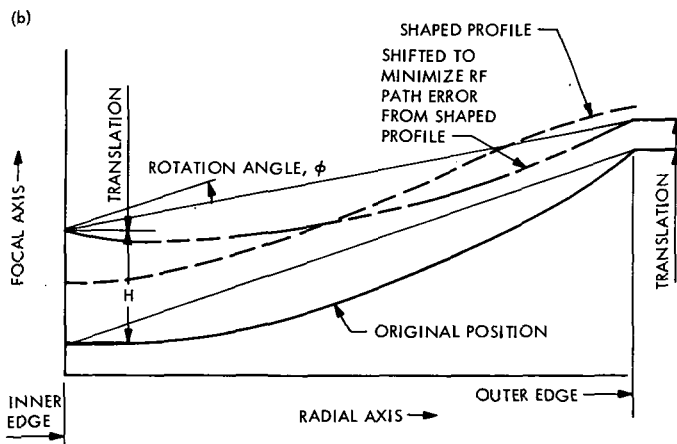
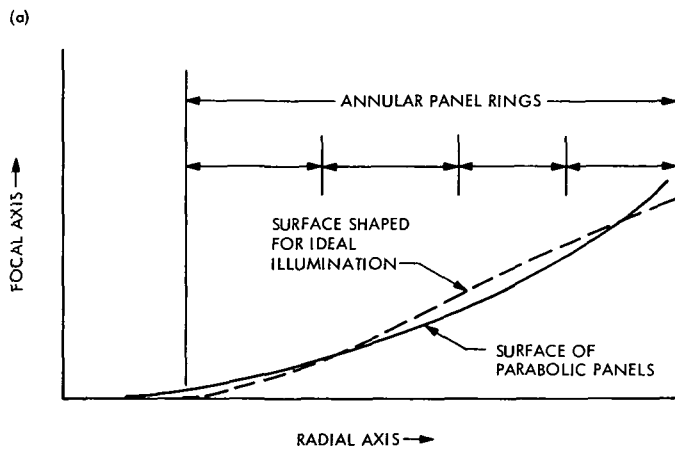


Fig. 1. Parabolic panels for shaped-surface reflector: (a) profile view of shaped vs parabolic surfaces, (b) resetting of typical parabolic panel

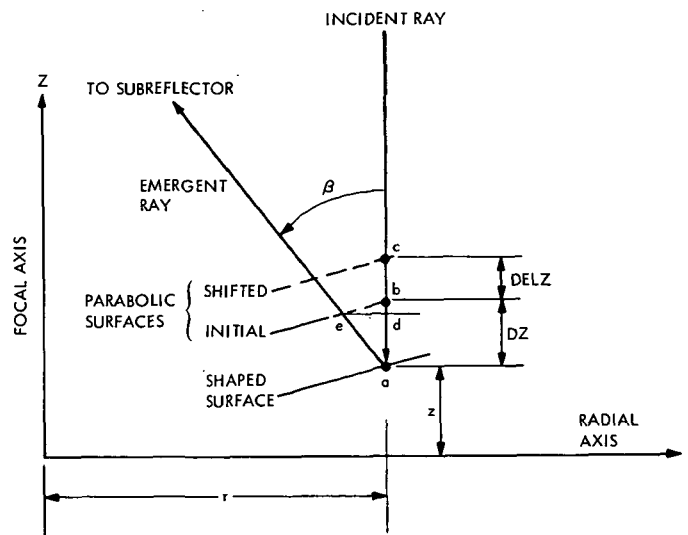


Fig. 2. Pathlength geometry

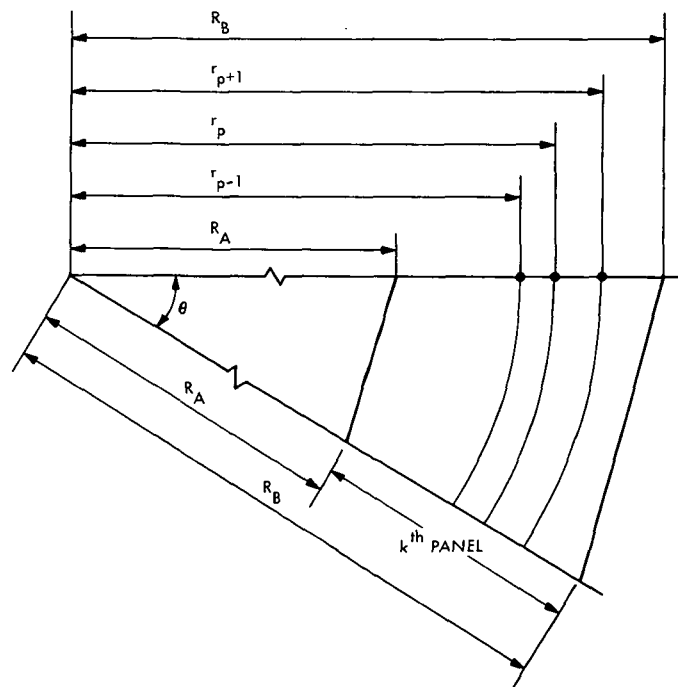


Fig. 3. Weighting factor geometry

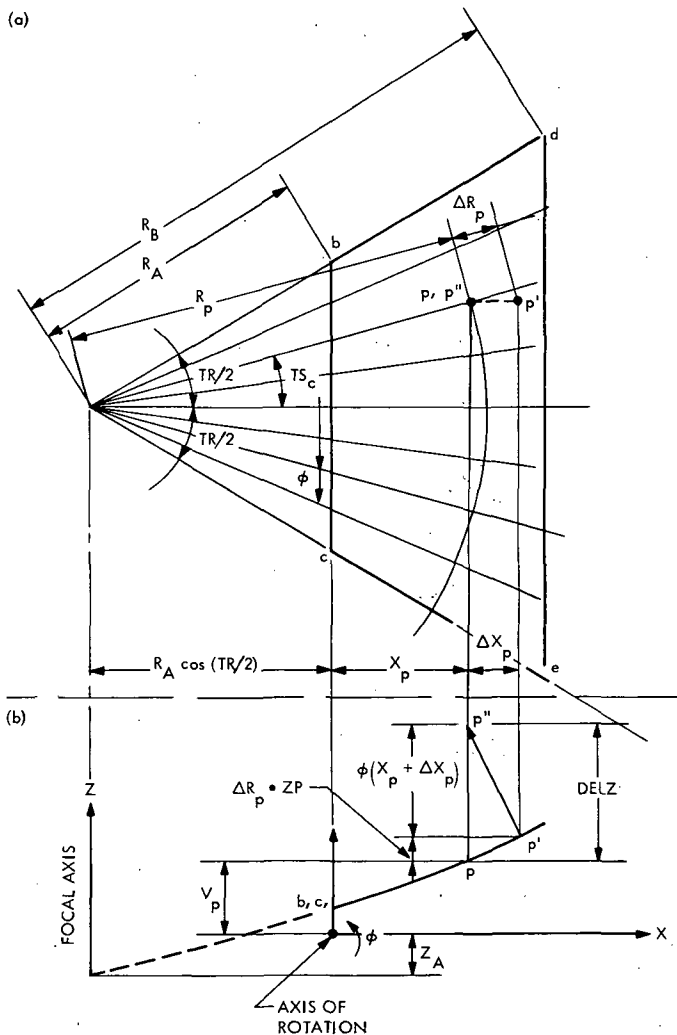


Fig. 4. Focal-axis coordinate shift for panel rotation: (a) panel projection on aperture plane, (b) side view of panel

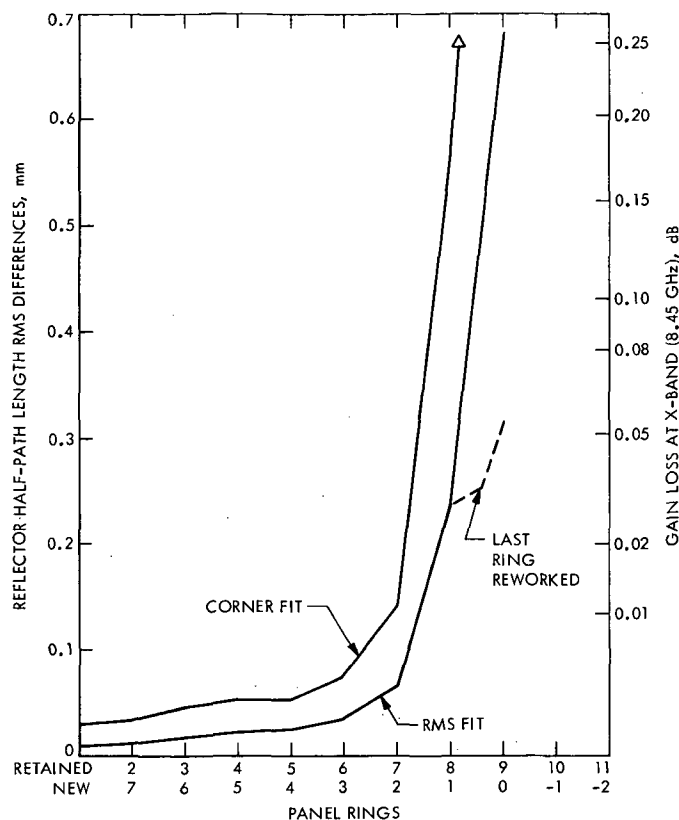


Fig. 5. Alternatives for retained vs new panel rings: DSS 14 antenna

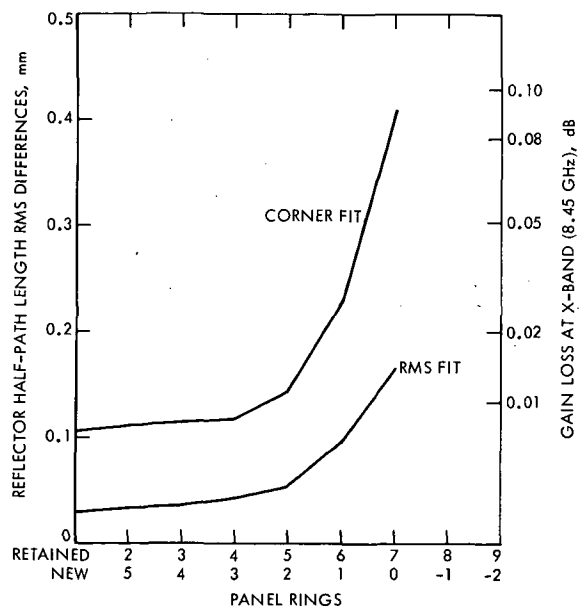


Fig. 6. Alternatives for retained vs new panel rings: DSS 13 antenna

DSN System Testing: A Critical Review of the Pioneer 10 Test Program

C. K. Stein

DSN Engineering and Operations Office

The Pioneer 10 test program was unique since the majority of DSN testing was conducted during the Mariner 9 encounter and orbiting. The importance of both programs to the NASA effort required special emphasis to assure that successful programs can be supported simultaneously. This critique lists the major problems encountered and the solutions used for a successful Pioneer 10 launch, while fully supporting all Mariner Mars 1971 requirements.

I. Introduction

This article covers the DSN test activities from the start of DSN system testing through the launch attempts (three aborts due to adverse weather conditions at Kennedy Space Center), launch, spacecraft ΔV and Conscan activation and the first midcourse correction. The bar chart in Fig. 1 illustrates the test activities during this period. The test span covered 81 calendar days or 55 normal 24-hour working days and 26 days of Sundays and holidays. Of the total available test time (81 24-hour days), 46.5% was used for *Pioneer 10* testing while maintaining the multi-mission DSN capability of supporting the high-activity *Mariner Mars 1971* mission with no degradation. The difficulty in the performance of this type of a compressed program is:

- (1) The usual pre-test and post-test activities are curtailed due to the requirement to test and train.

- (2) New changes in software are implemented prior to adequate pre-test.
- (3) Configuration control is difficult to maintain due to the discovery of new problems requiring immediate solutions.

The success of the program may be measured by a successful launch and the ability to track and control the spacecraft within the required accuracy. However, this approach must be analyzed to determine how to perform these tasks better, more efficiently, and during the normal working periods.

Figure 1 does not show the pre- and post-test activities accompanying the testing. There were very limited pre-test meetings and post-test critiques because of the concentration of test and training during the final 81 days.

Quick Look Reports were limited and often not very "quick" due to the continued pressure of testing, test support, training, scheduling, and retesting modified configurations.

II. Test Problems

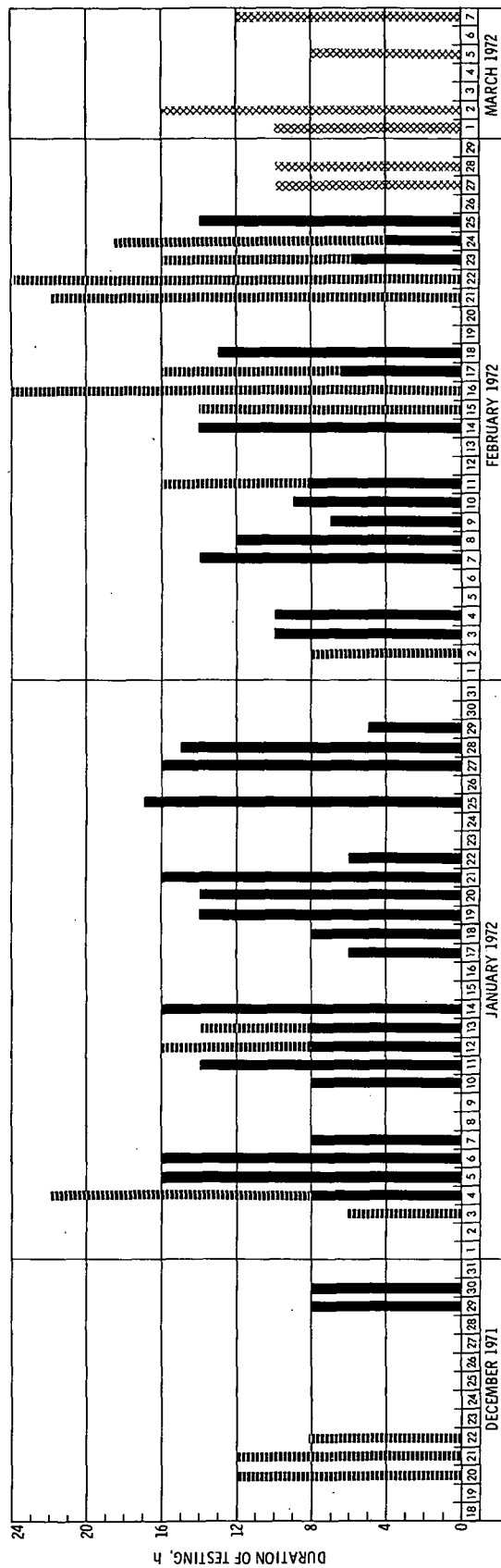
The major problems encountered during this program were as follows:

- (1) The DSN and Project documentation required for preparation of detailed test planning was not available with sufficient lead time.
- (2) The final launch support configuration was not available at the start of system testing. Formal configuration control was not implemented until about 30 days before the planned launch. These two conditions led to inconclusive testing until the system was frozen and tightly controlled.
- (3) Although early Project and DSN requirements were established, late software programming changes negated much of this planning. These changes included different display requirements and over-complicated software solutions.
- (4) An idealized test program was planned instead of recognizing the lateness of support documentation and the absolute requirement for supporting *Mariner*.

- (5) The simulation mathematical model occupied an excessive amount of core storage in the assigned computer causing many unnecessary scheduling problems and computer downtime.
- (6) Knowledgeable project personnel were not always available to support on-the-spot decision making. This was further complicated by the physical distance between NASA centers.

III. Plans for Future DSN Multi-mission System Test and Operational Training Support

- (1) Systems test and operational training documentation integrating multi-mission requirements is being prepared and will support concurrent programs.
- (2) Systems Engineering is preparing and maintaining network test schedules integrating total program requirements. Problems that could arise from overlapping project testing will be reduced due to the improved visibility.
- (3) Configuration control of both software and hardware will be implemented prior to systems testing.
- (4) DSN Systems Engineering and DSN Operations are documenting the methodology and standard test and training procedures which will eliminate or greatly reduce the test problems encountered with *Pioneer 10*.



ACTUAL LAUNCH WAS ON MARCH 2. THREE PRIOR ATTEMPTS WERE MADE ON FEBRUARY 27, 28, AND MARCH 1 AND TERMINATED DUE TO ADVERSE WEATHER AT THE KENNEDY SPACE CENTER.

Fig. 1. Pioneer 10 DSN test and test support summary

DSN Telemetry Predicts Generation and Distribution

C. W. Harris and E. S. Burke
DSN Engineering and Operations Office

The DSN Telemetry System Analysis Group is responsible for generating and/or disseminating the predicted uplink signal levels at the spacecraft, and the predicted downlink signal levels at the Deep Space Stations. Also included in the predictions are the telemetry signal-to-noise ratios. Two different Univac 1108 programs are used to generate these data. The JPL spacecraft-oriented predicts are generated by the Telecommunications Prediction and Analysis Program. The non-JPL spacecraft-oriented predicts are generated by the DSN Telecommunications Prediction Program which is operated by the Telemetry Group of the Network Analysis Team (NAT TEL). These predicts are distributed throughout the DSN and to specified project personnel.

I. Introduction

The generation and distribution of telemetry signal-to-noise ratio (SNR) and signal-level predictions are handled by nonreal-time analysts in the NAT TEL Group. These predicts are generated in the Univac 1108 computer by use of station, spacecraft, trajectory, and range parameters. The predicts are distributed to all interested parties on a scheduled basis.

II. Usage

The real-time analysts in NAT TEL modify the predicts to conform to any change in the spacecraft or DSN configuration/parameters, and use them to calculate the residual signal levels and SNRs of the station which is being operated. From these residuals the analysts can determine if the tracking station is within a specified

tolerance, and can perform troubleshooting analysis where required.

The nonreal-time analysts in NAT TEL use the predicts and residuals to perform long-term trend analysis. The residuals are compiled and various measures of statistical variation are computed by another Univac 1108 computer program developed by the NAT TEL Group.

All active tracking stations are on distribution. The station personnel use the predicts to help determine the accuracy and performance of their systems.

The Operations and Engineering Groups of the Deep Space Instrumentation Facility (DSIF) use the predicts for long-term trend analysis work to enhance the performance of the tracking stations.

The DSN Project Managers are on distribution in order to perform quick-look analyses.

Project personnel are also on distribution to help determine the health of their spacecraft, the mission operational limitations, and spacecraft mode feasibilities.

III. Generation

The JPL spacecraft-oriented predicts are received from Project personnel and are modified, as required, by NAT TEL. They are then distributed by standard teletype (TTY) methods.

For non-JPL spacecraft, the Receiver and Telemetry SNR Predictions Program has been updated and changed to the DSN Telecommunications Prediction Program and is now being used for *Pioneers 6* through *10*. With slight modifications and Project-supplied parameters, this program can be used for any mission.

The following information shows the different parameters and computations that are used to generate the DSN Telecommunications Prediction Program.

A. Identification Input

The ID card provides the following inputs:

- (1) Modulation index
- (2) System noise temperature
- (3) Receiver bandwidth
- (4) Polarizer in or out
- (5) 26- or 64-meter network
- (6) Spacecraft number
- (7) Month to start predicts
- (8) Year to start predicts
- (9) Pass number to start predicts
- (10) Number of days to run predicts
- (11) Mission [Ground Operational Equipment (GOE) or Multiple-Mission Telemetry (MMT)]

(12) Cone in use [S-Band Cassegrain Monopulse (SCM), Polarization Diversity S-Band (PDS), S-Band Megawatt Transmit (SMT) or S-Band Polar Ultra (SPU)]

(13) Transmitter power

(14) Downlink bias

(15) Uplink bias

B. Data Input

Data input is by cards providing day of year and spacecraft range in kilometers. The range data are obtained from the spacecraft trajectory printout [Double-Precision Trajectory Program (DPTRAG)].

C. N and FIN Card Input

The N card provides the number of range values to be input to the program. The FIN card is used to signal a new run or termination of the program.

D. Range Interpolation

The program uses a four-point Lagrange interpolation routine. The day of year and spacecraft range are input to the program and interpolated to provide range for daily computations. The program will take up to 99 inputs and can compute predicts for 999 days.

E. Prediction Computations

The equation for free-space loss is

$$L_{fs} = 92.45 + 20 \log(f) + 20 \log(d)$$

where

L_{fs} = free space loss in decibels

f = received frequency in GHz

d = spacecraft range in kilometers

The predicted received signal strength is computed as follows:

$$SS = (\text{spacecraft gain}) + (\text{ground antenna gain}) - (\text{modulation loss}) - L_{fs} - (\text{antenna pointing loss} = 0.5 \text{ dB})$$

where

Spacecraft gain for:

$$\text{Pioneer 6} = +48.9 \text{ dB}$$

$$\text{Pioneer 7} = +48.2 \text{ dB}$$

$$\text{Pioneer 8} = +49.1 \text{ dB}$$

$$\text{Pioneer 9} = +49.1 \text{ dB}$$

$$\text{Pioneer 10} = +70.4 \text{ dB}$$

Ground antenna gain for:

$$26\text{-m antenna} = +53.3 \text{ dB}$$

$$64\text{-m antenna} = +61.4 \text{ dB}$$

Modulation loss is $20 \log \cos$ (modulation index)

Modulation index for PN 6 through 9 = 51.6 deg or 0.9 rad

Modulation index for PN 10 = 63.03 deg or 1.1 rad

The receiver margin is computed by

$$M = SS - 10 \log T_s - 10 \log BW + 198.6$$

The ST_b/N_o of the telemetry is computed by

$$DPWR = \text{total gain} - L_{fs} + 20 \log \sin (\text{modulation index})$$

$$SNR = DPWR - 10 \log T_s - 10 \log BR - \text{loss} + 198.6$$

where

M = receiver margin in dB

$DPWR$ = telemetry data power in dB

SS = predicted receiver signal strength in dBm

SNR = telemetry ST_b/N_o

K = Boltzman constant (-198.6 dBm)

BR = bit rate

T_s = system noise temperature in kelvin

BW = receiver bandwidth in hertz

Loss = fixed system loss depending on bit rate and mode (MMT or GOE)

The predicted uplink signal strength is computed as follows:

$$UL = P_{\text{out}} + \text{spacecraft gain} + \text{ground antenna gain} - L_{fs}$$

where

Spacecraft gain for:

$$\text{Pioneer 6} = -8.6 \text{ dB}$$

$$\text{Pioneer 7} = +9.2 \text{ dB}$$

$$\text{Pioneer 8} = +9.9 \text{ dB}$$

$$\text{Pioneer 9} = +8.6 \text{ dB}$$

$$\text{Pioneer 10} = +9.1 \text{ dB (medium gain)}$$

$$\text{Pioneer 10} = +28.5 \text{ dB (high gain)}$$

Ground antenna gain for:

$$26\text{-m antenna} = +51.8 \text{ dB}$$

$$64\text{-m antenna} = +60.5 \text{ dB}$$

$$P_{\text{out}} = 10 \log (TXP / 0.001)$$

TXP = ground transmitter power

IV. Future Methods

At this time the only method of transmitting telemetry predicts is via teletype (TTY). In the near future capability will exist for all JPL spacecraft-oriented predicts to be transmitted via High-Speed Data Line (HSDL) as well as TTY. This will be done by using a different Univac 1108 computer program, which will format a magnetic tape to be used on the IBM 360/75. The 360/75 will transmit the predicts to the stations and other specified areas by use of the on-line operational program.

DSN Command System Performance Evaluation

W. G. Stinnett

DSN Engineering and Operations Office

This article presents a general performance description of the DSN Command System as configured for support of the Mariner Mars 1971 and Pioneer 10 missions. Included are statistics related to system reliability and availability. A comparison of command activity is presented for previous Mariner- and Pioneer-type missions.

I. Introduction

The DSN Multiple-Mission Command System has now been utilized for significant periods of the *Mariner Mars 1971 (Mariner 9)* and *Pioneer 10* missions. There exists enough operational experience that a performance evaluation can be made on this system. The system has been utilized in support of *Mariner 9* and *Pioneer 10* for over a year. In comparison with past missions of similar length, a significant increase in the number of commands transmitted has been realized.

II. Performance Evaluation

A. Operational Characteristics

The primary characteristic of the DSN Multiple-Mission Command System, as configured for support of the *Mariner 9* and *Pioneer 10* missions, has been the automatic control of the Deep Space Station (DSS) Command Subsystem from the Space Flight Operations Facility (SFOF). This control is established via a standard high-speed data system interface between the SFOF and a DSS. Both Project and DSN personnel are responsible for

transmitting high-speed data blocks to the DSS. Table 1 describes these operational functions. Both the DSN and the flight projects have benefited from the existence of the present command system.

The DSN has realized the following operational improvements from the present command system:

- (1) Command system operations procedures are almost entirely mission-independent.
- (2) A major portion of the operations functions is performed from the SFOF, requiring fewer DSS personnel.
- (3) Excessive verbal communication with DSS/Projects is not required for command system operations.
- (4) Project-dependent personnel or mission-dependent equipment is not required at DSSs.
- (5) Command entry is entirely the responsibility of Project personnel (except for infrequent manual entry at a DSS).
- (6) Command data interface is standard with both projects.

The flight projects (*Mariner 9* and *Pioneer 10*) have realized the following operational benefits from the present command system:

- (1) Volume of commands per given time period has increased.
- (2) Less verbal coordination with DSN/DSS personnel has been required.
- (3) System is more responsive to real-time decisions/changes. Verbal communication with DSN/DSS is minimal.

B. Highlights of Command Activity

The present DSN Command System has been utilized in support of the *Mariner 9* and *Pioneer 10* launch phases, trajectory correction maneuvers, and cruise periods. *Mariner 9* was supported during Mars orbit insertion and orbit sequences. The best test of the system has been its use in updating the *Mariner 9* on-board computer in support of picture-taking sequences. Large volumes of commands in a relatively short period of time have been transmitted to *Mariner* on a day-to-day basis.

C. Volume of Commands

By the end of May 1972, over 37,000 commands to *Mariner 9* and over 4000 commands to *Pioneer 10* had been transmitted. Figure 1 shows the DSN command history of the *Pioneer*- and *Mariner*-type missions. As can be seen, a significant increase in DSN command activity has occurred in support of the *Mariner 9* and *Pioneer 10* missions. This level of command activity is expected to be sustained in support of the present missions, plus *Pioneer G*, *Mariner Venus-Mercury*, *Helios*, and *Viking* missions. A DSN Command System, with minor modifications, is planned for use by these future missions.

D. Performance

A measure of the performance of the DSN Command System for support of the *Mariner 9* and *Pioneer 10* missions is shown in Table 2. As can be seen, the total system

has been available to the projects between 96 and 98% of the time. The majority of the outages has been due to the failures of the Space Flight Operations Facility (SFOF) IBM 360-75 computer. Backup commanding via manual means at a DSS would bring a "command capability" percentage to greater than 99%. The failures in the IBM 360-75 computer have been almost entirely caused by problems outside the command system, e.g., other system processing failures, analysis program failures, computer system failures. The net result of these failures from whatever source is the unavailability of the "complete" DSN Command System.

Problems and anomalies have occurred in the use of the command system. In the first versions of the "systems" for use by the *Mariner 9* and *Pioneer 10* missions, failures in the command system caused interruption in project command sequences. The "final" version of the software utilized for *Mariner 9* support has been in use for approximately seven months. This version has the following performance record:

Commands transmitted: >36,000

Commands aborted: 3

Abort rate: 0.008%

Recent fixes to problems associated with the system utilized for support of the *Pioneer 10* mission have been implemented. This new version has not been in use long enough to gather statistics similar to those above.

III. Conclusions

The use of the DSN Command System in support of the *Mariner 9* and *Pioneer 10* missions has proven to be a very valuable tool. Increased command activity requirements of the present and future missions have outdated former modes of command operations. The automatic operation of the DSN Command System from the SFOF has proven to be a reliable and efficient means to provide the support necessary for these increased command activity requirements.

Table 1. DSN Command System high-speed data control from the SFOF to a DSS

High-speed block type	Purpose	Responsibility for transmission
Configuration message	To establish the correct mission configuration of the multiple-mission hardware at the DSS	DSN
Standards and limits message	To establish the appropriate alarm and abort conditions of the DSS command subsystem	DSN
Test command message	To test the command system end-to-end prior to flight project use	DSN
Recall request message	To recall data from the DSS concerning commands, configuration, and standards and limits	DSN and Project
Command message	To transmit commands from the SFOF to a DSS	Project
Command enable/disable message	To allow transmission of a command from the DSS to the spacecraft; to delete a command from the DSS command subsystem	Project

Table 2. DSN Command System: Command activity and percentage down

Activity	Deep Space Station							
	11	12	14	41	42	51	61	62
Commands to <i>Mariner 9</i>	—	3303	1041	3359	65	109	—	29621
Commands to <i>Pioneer 10</i>	334	274	—	1409	1265	639	495	—
Percent down ^a — <i>Mariner 9</i>	—	3.9	3.8	3.2	2.4	4.0	—	4.0
Percent down ^a — <i>Pioneer 10</i>	5.1	2.5	—	2.2	2.6	3.3	3.8	—

^aPercent down calculation: Time total system unavailable for project use divided by DSS track time.
Time system unavailable includes SFOF IBM 360/75, HSDL, and DSS command subsystem outages.

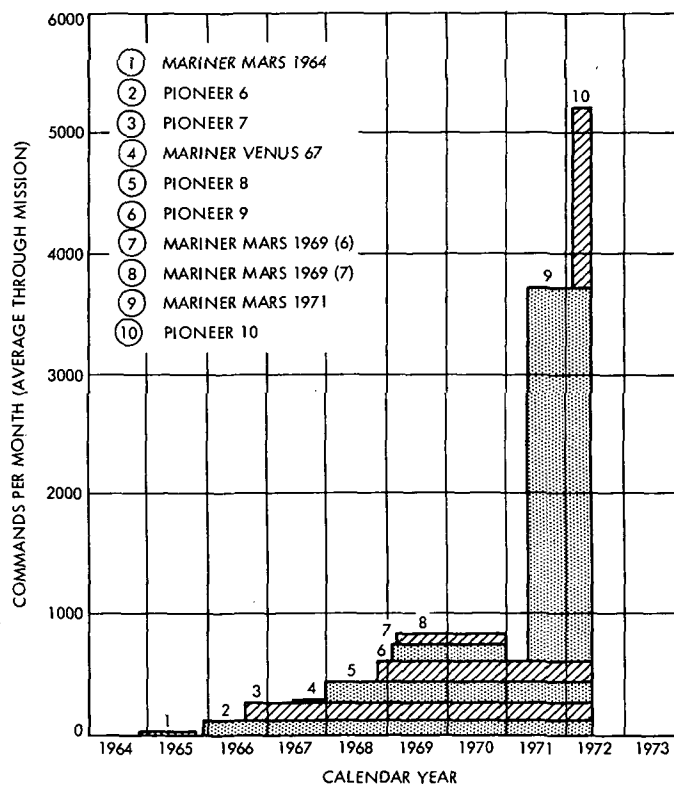


Fig. 1. DSN command history

Accuracy of the Signal-to-Noise Ratio Estimator

J. R. Lesh
DSIF Operations Section

In this article the effects of external and internal noise, finite sample size, and transition estimation errors are included in an analysis of the signal-to-noise ratio estimator used in the symbol synchronizer assembly. Expressions for the estimator mean and variance are developed, from which their dependence on the above effects are determined. The results of this study show that the estimator mean depends almost entirely on the external and internal signal-to-noise ratios while the estimator variance depends almost exclusively on the sample size.

I. Introduction

The statistics of the signal-to-noise ratio (SNR) estimation algorithm have been the target of several noteworthy analyses over the past eight years. The first of these was performed by Gilchriest (Ref. 1) in 1964 and resulted in an expression for the probability density function for the estimator. Gilchriest, however, did not take into consideration the tails of the noise distribution, which rendered his result valid for only high signal-to-noise ratios. Two years later Boyd (Refs. 2 and 3) extended Gilchriest's result to a more computable expression and included some additional error sources, but he still retained Gilchriest's basic assumption.

In 1967 Layland (Ref. 4) derived the expression for the mean SNR estimate with the effects of the noise distribution tails included. From this expression he found a significant bias in the estimator at low signal-to-noise ratios from which a set of correction expressions were determined. Layland's result, however, disregarded the effects of symbol transition estimation errors and was only true

asymptotically with the sample size. Layland later revised his result (Ref. 5) to include the effects of transition estimation errors, but his resulting expressions (even when a uniform error distribution was assumed) required numerical integration for evaluation.

With this history in mind we shall develop in this article the expressions for the mean and variance of the SNR estimator used in conjunction with the Symbol Synchronizer Assembly (SSA) with the effects of (1) input noise distribution tails, (2) finite sample size, (3) gaussian distributed transition estimation errors, (4) quantization errors, and (5) internal equipment noise all included. Upon evaluation of these equations we will find that the estimator mean depends heavily on the input noise and internally generated noise but is relatively insensitive to changes in the sample size. The variance of the estimator, on the other hand, will be found to be strongly dependent on the sample size and relatively independent of the noise sources.

Before proceeding it is necessary to make a comment regarding notation. In this analysis extensive use of the

error function and its complement is necessary. However, one often finds in the literature two definitions of the error function. For this reason the error function recognized by the National Bureau of Standards will be denoted by $\widetilde{\text{erf}}$ and is defined by

$$\widetilde{\text{erf}}(x) = \frac{2}{\sqrt{\pi}} \int_0^x e^{-t^2} dt$$

The other error function (sometimes called the Q-function) will not contain the tilde and is defined by

$$\text{erf}(x) = \frac{1}{\sqrt{2\pi}} \int_{-\infty}^x e^{-\frac{1}{2}t^2} dt$$

The associated complementary error functions will similarly be denoted.

II. Mean and Variance of the SNR Estimator

Consider the model of the SSA and estimator algorithm shown in Fig. 1. The input data signal $V(t)$ is a binary signal taking on either of the values $+V$ or $-V$ in the intervals t_k to t_{k+1} , $k = 1, 2, \dots$. This signal is corrupted by additive white gaussian noise $n(t)$ having a zero mean and two-sided spectral density $N_0/2$. The Symbol Transition Estimator uses this composite signal to estimate the values of t_k and t_{k+1} . Using these estimates (\hat{t}_k and \hat{t}_{k+1}) the received signal is integrated over the expected symbol duration. After removing the algebraic sign from the integral, the resulting quantity is quantized to produce the random sequence y_k . $\{y_k\}$ is assumed to be an independent sequence.

Two noise sequences, the quantizer noise $n_q(k)$ and the internal equipment noise $n_e(k)$ (produced from crosstalk, computational inaccuracies, etc.), are then added to y_k to produce the sequence Z_k . It is assumed that $n_q(k)$ and $n_e(k)$ are independent zero mean white gaussian sequences having variances σ_q^2 and σ_e^2 , respectively. Finally, Z_k and its square are transferred to the SNR estimator where the estimate \hat{R} is produced.

Let us for the moment assume that the first four moments of y_k are known. For notational simplicity, define $E\{y_k\} = \mu$ and $E\{(y_k - \mu)^2\} = \sigma^2$. Then we know that

$$E\{Z_k\} = \mu \quad (1)$$

and

$$\text{var}\{Z_k\} = \sigma^2 + \sigma_q^2 + \sigma_e^2 \triangleq \sigma_z^2 \quad (2)$$

Next, note that the SNR algorithm is the square of the sample mean divided by twice the sample variance. Both the sample mean and variance are random variables depending on the statistics of Z_k . Then, if the sample size (N) is large enough ($N \geq 20$ should suffice), we can use the Central Limit Theorem to express the estimated SNR by

$$\hat{R} = \frac{(\mu + \sqrt{\sigma_M^2} \xi)^2}{2(\sigma_z^2 + \sqrt{\sigma_{SV}^2} \psi)} \quad (3)$$

where ξ and ψ are independent zero mean gaussian random variables with unit variances, σ_M^2 is the variance of the sample mean given by

$$\sigma_M^2 = \frac{1}{N} \sigma_z^2 \quad (4)$$

and σ_{SV}^2 is the variance of the sample variance. The variance of a sample variance is derived in Appendix A and with the help of Eqs. (1) and (2) can be expressed as

$$\begin{aligned} \sigma_{SV}^2 = & \frac{1}{N} E\{y^4\} - \frac{4}{N} E\{y^3\} \mu + \frac{3}{N} [E\{y^2\}]^2 \\ & - \frac{2(2N-3)}{N(N-1)} \sigma^4 + \frac{2}{N-1} (\sigma_q^2 + \sigma_e^2) (\sigma_q^2 + \sigma_e^2 + 2\sigma^2) \end{aligned} \quad (5)$$

where y represents any of the y_k 's.

Returning now to Eq. (3) and expanding the denominator in a geometric series gives

$$\hat{R} = \frac{\mu^2}{2\sigma_z^2} \left(1 + \frac{\sqrt{\sigma_M^2}}{\mu} \xi\right)^2 \left(1 - \frac{\sqrt{\sigma_{SV}^2}}{\sigma_z^2} \psi + \frac{\sigma_{SV}^2}{\sigma_z^4} \psi^2 - \dots\right) \quad (6)$$

However, if the sample variance is a reasonably accurate estimator for the variance, then $\sqrt{\sigma_{SV}^2}/\sigma_z^2 \ll 1$ so that we can neglect the higher order terms, and

$$\hat{R} = \frac{\mu^2}{2\sigma_z^2} \left(1 + \frac{\sqrt{\sigma_M^2}}{\mu} \xi\right)^2 \left(1 - \frac{\sqrt{\sigma_{SV}^2}}{\sigma_z^2} \psi + \frac{\sigma_{SV}^2}{\sigma_z^4} \psi^2\right) \quad (7)$$

Now, by using the independence of ξ and ψ , we have that the mean SNR estimate is

$$E\{\hat{R}\} = \frac{1}{2NA} (1+A)(1+B) \quad (8)$$

where

$$A = \frac{\sigma_M^2}{\mu^2} \quad (9)$$

$$B = \frac{\sigma_{SV}^2}{\sigma_Z^4} \quad (10)$$

Similarly we find that the variance of the estimator is given by

$$\begin{aligned} \text{var} \{\hat{R}\} &= \frac{1}{4N^2 A^2} \{B(1+B)(1+A)^2 \\ &\quad + 2A(2+A)(1+B)^2 \\ &\quad + 2AB(2+A)(1+2B)\} \end{aligned} \quad (11)$$

Equations (8) and (11) are the desired equations for the mean and variance of \hat{R} in terms of the expressions given in Eqs. (1), (2), (4), (5), (9), and (10). However, when all of these equations are substituted into Eqs. (8) and (11), we find that the results depend only on N (the sample size), σ_q^2 , σ_b^2 , and the first four moments of y . We will now consider these quantities.

III. The First Moment of y

Referring again to Fig. 1, we see that y_k is given by

$$y_k = \left| \int_{\hat{t}_k}^{\hat{t}_{k+1}} [V(t) + n(t)] dt \right| \quad (12)$$

We shall assume that \hat{t}_k differs from t_k by an amount Δ , which is zero mean gaussian random variable having a variance σ_Δ^2 . Furthermore, if we assume that the transition estimator loop is in lock and has a sufficiently narrow bandwidth, then the duration of the symbol integration will be the symbol period T ($T = t_{k+1} - t_k$). Thus, we can express Eq. (12) as

$$y_k = \left| \int_{t_k+\Delta}^{t_k+\Delta+T} [V(t) + n(t)] dt \right| \quad (13)$$

In order to evaluate the mean of y_k , we must condition on the random variable Δ . However, since the sign of Δ will determine which symbols are integrated during the k th estimated interval, we must also condition on $\Delta \geq 0$ or $\Delta < 0$. Thus, the expected value of y_k can be expressed as

$$\begin{aligned} E\{y_k\} &= \int_0^\infty E\{y_k/\Delta, \Delta \geq 0\} f_\Delta d\Delta \\ &\quad + \int_{-\infty}^0 E\{y_k/\Delta, \Delta < 0\} f_\Delta d\Delta \end{aligned} \quad (14)$$

where f_Δ is the probability density function of Δ and is given by

$$f_\Delta(\Delta) = \frac{1}{\sqrt{2\pi}\sigma_\Delta} \exp\left[-\frac{\Delta^2}{2\sigma_\Delta^2}\right] \quad (15)$$

Now by evaluating the symbol integrals under the appropriate errors (Δ) allows Eq. (14) to be expressed as

$$\begin{aligned} E\{y_k\} &= \int_0^\infty E\{|V_k T + (V_{k+1} - V_k)\Delta + n'|/\Delta, \Delta \geq 0\} f_\Delta d\Delta \\ &\quad + \int_{-\infty}^0 E\{|V_k T + (V_{k-1} - V_k)\Delta + n'|/\Delta, \Delta < 0\} f_\Delta d\Delta \end{aligned} \quad (16)$$

where n' is a zero mean gaussian random variable having a variance $N_0 T/2$.

The conditional expectations in the integrands can be further simplified by noting that

$$E\{g(V_k, V_{k+1})/\Delta, \Delta \geq 0\} = \sum_{V_k} \sum_{V_{k+1}} E\{g(V_k, V_{k+1})/V_k, V_{k+1}, \Delta, \Delta \geq 0\} P\{V_k, V_{k+1}/\Delta, \Delta \geq 0\} \quad (17)$$

However, $P\{V_k, V_{k+1}/\Delta, \Delta \geq 0\} = P\{V_k, V_{k+1}\}$ since the transition estimates do not affect the value of the incoming signal. Recalling now that the V_k 's are independent and equally likely to be $+V$ or $-V$ allows us to express Eq. (16) as

$$\begin{aligned} E\{y_k\} &= \frac{1}{4} \sqrt{\frac{N_0 T}{2}} \int_0^\infty \sum_{V_k} \sum_{V_{k+1}} E\left\{ \left| \text{sgn}(V_k) \sqrt{2R} + \text{sgn}(V_{k+1} - V_k) \frac{2\Delta}{T} \sqrt{2R} + n'' \right| \middle| V_k, V_{k+1}, \Delta, \Delta \geq 0 \right\} f_\Delta d\Delta \\ &\quad + \frac{1}{4} \sqrt{\frac{N_0 T}{2}} \int_{-\infty}^0 \sum_{V_k} \sum_{V_{k-1}} E\left\{ \left| \text{sgn}(V_k) \sqrt{2R} + \text{sgn}(V_{k-1} - V_k) \frac{2\Delta}{T} \sqrt{2R} + n'' \right| \middle| V_k, V_{k-1}, \Delta, \Delta < 0 \right\} f_\Delta d\Delta \end{aligned} \quad (18)$$

where R is the actual signal-to-noise ratio $R = V^2 T / N_0$, n'' is a unit normal random variable ($\mathcal{N}(0, 1)$) and $\text{sgn}(x)$ is defined by

$$\text{sgn}(x) = \begin{cases} +1, & \text{if } x > 0 \\ 0, & \text{if } x = 0 \\ -1, & \text{if } x < 0 \end{cases}$$

In Appendix B it is shown that if x is a unit normal random variable and α is a constant, then

$$E\{|x + \alpha|\} = \frac{2}{\sqrt{2\pi}} \exp\left[-\frac{\alpha^2}{2}\right] + \alpha \widetilde{\text{erf}}\left(\frac{\alpha}{\sqrt{2}}\right) \quad (19)$$

Using this relationship the expectations in the integrands of Eq. (18) can be evaluated yielding

$$\begin{aligned} E\{y_k\} = & \frac{1}{4} \sqrt{\frac{N_0 T}{2}} \int_0^\infty \sum_{V_k} \sum_{V_{k+1}} \left\{ \frac{2 \exp\left\{-R \left[\text{sgn}(V_k) + \text{sgn}(V_{k+1} - V_k) \frac{2\Delta}{T}\right]^2\right\}}{\sqrt{2\pi}} \right. \\ & \left. + \sqrt{2R} \left[\text{sgn}(V_k) + \text{sgn}(V_{k+1} - V_k) \frac{2\Delta}{T} \right] \widetilde{\text{erf}}\left(\sqrt{R} \left[\text{sgn}(V_k) + \text{sgn}(V_{k+1} - V_k) \frac{2\Delta}{T} \right]\right) \right\} f_\Delta d\Delta \\ & + \frac{1}{4} \sqrt{\frac{N_0 T}{2}} \int_{-\infty}^0 \sum_{V_k} \sum_{V_{k-1}} \left\{ \frac{2 \exp\left\{-R \left[\text{sgn}(V_k) + \text{sgn}(V_{k-1} - V_k) \frac{2\Delta}{T}\right]^2\right\}}{\sqrt{2\pi}} \right. \\ & \left. + \sqrt{2R} \left[\text{sgn}(V_k) + \text{sgn}(V_{k-1} - V_k) \frac{2\Delta}{T} \right] \widetilde{\text{erf}}\left(\sqrt{R} \left[\text{sgn}(V_k) + \text{sgn}(V_{k-1} - V_k) \frac{2\Delta}{T} \right]\right) \right\} f_\Delta d\Delta \quad (20) \end{aligned}$$

Now, by summing over the possible values of the V_k 's we find that the two integrands are equal and the above expression becomes

$$\begin{aligned} E\{y_k\} = & \frac{1}{4} \sqrt{\frac{N_0 T}{2}} \int_{-\infty}^\infty \left\{ \frac{4}{\sqrt{2\pi}} \exp[-R] + \frac{4}{\sqrt{2\pi}} \exp\left[-R \left(1 - \frac{2\Delta}{T}\right)^2\right] + 2\sqrt{2R} \widetilde{\text{erf}}(\sqrt{R}) \right. \\ & \left. + 2\sqrt{2R} \left(1 - \frac{2\Delta}{T}\right) \widetilde{\text{erf}}\left[\sqrt{R} \left(1 - \frac{2\Delta}{T}\right)\right] \right\} f_\Delta d\Delta \quad (21) \end{aligned}$$

By straightforward integration we obtain

$$\begin{aligned} E\{y_k\} = & \sqrt{\frac{N_0 T}{2}} \left\{ \frac{e^{-R}}{\sqrt{2\pi}} + \frac{T \exp\left[\frac{-RT^2}{8R\sigma_\Delta^2 + T^2}\right]}{\sqrt{2\pi}(8R\sigma_\Delta^2 + T^2)} + \sqrt{\frac{R}{2}} \widetilde{\text{erf}}(\sqrt{R}) \right. \\ & \left. + \sqrt{\frac{R}{2}} \int_{-\infty}^\infty \widetilde{\text{erf}}\left[\sqrt{R} \left(1 - \frac{2\Delta}{T}\right)\right] f_\Delta d\Delta - \frac{\sqrt{2R}}{T} \int_{-\infty}^\infty \Delta \widetilde{\text{erf}}\left[\sqrt{R} \left(1 - \frac{2\Delta}{T}\right)\right] f_\Delta d\Delta \right\} \quad (22) \end{aligned}$$

A closed form for the last integral can be obtained through integration by parts but the first integral is not quite as easy to evaluate. In Appendix C we prove the identity

$$\int_{-\infty}^\infty \frac{\widetilde{\text{erf}}(a + bx) \exp\left[-\frac{x^2}{2\sigma^2}\right]}{\sqrt{2\pi\sigma^2}} dx = \widetilde{\text{erf}}\left(\frac{a}{\sqrt{2b^2\sigma^2 + 1}}\right) \quad (23)$$

Using these results we have

$$E\{y_k\} = \sqrt{N_0 T} \left\{ \frac{e^{-R}}{2\sqrt{\pi}} + \frac{T \exp\left[\frac{-RT^2}{8R\sigma_\Delta^2 + T^2}\right]}{2\sqrt{\pi(8R\sigma_\Delta^2 + T^2)}} + \frac{\sqrt{R}}{2} \widetilde{\text{erf}}(\sqrt{R}) \right. \\ \left. + \frac{\sqrt{R}}{2} \widetilde{\text{erf}}\left(\sqrt{\frac{RT^2}{8R\sigma_\Delta^2 + T^2}}\right) + \frac{4R\sigma_\Delta^2}{T\sqrt{\pi(8R\sigma_\Delta^2 + T^2)}} \exp\left[-\frac{RT^2}{8R\sigma_\Delta^2 + T^2}\right] \right\} \quad (24)$$

It is quite often more practical to express these functions in terms of the variance of the SSA loop phase error (σ_ϕ^2) rather than the variance of the timing error (σ_Δ^2). Since

$$\sigma_\Delta^2 = \frac{T^2 \sigma_\phi^2}{4\pi^2} \quad (25)$$

and if we simplify notation by using the substitution

$$D = \sqrt{2R\sigma_\phi^2 + \pi^2} \quad (26)$$

then Eq. (24) becomes

$$E\{y_k\} = \sqrt{N_0 T} \left\{ \frac{e^{-R}}{2\sqrt{\pi}} + \frac{D \exp\left[-\frac{R\pi^2}{D^2}\right]}{2\pi\sqrt{\pi}} + \frac{\sqrt{R}}{2} \left[\widetilde{\text{erf}}(\sqrt{R}) + \widetilde{\text{erf}}\left(\frac{\pi\sqrt{R}}{D}\right) \right] \right\} \quad (27)$$

Equation (27) is the desired expression for the first moment of y . To verify this equation, note that as $\sigma_\phi^2 \rightarrow 0$, then D goes to π . Making this substitution yields

$$\lim_{\sigma_\phi^2 \rightarrow 0} E\{y_k\} = \sqrt{N_0 T} \left\{ \frac{e^{-R}}{\sqrt{\pi}} + \sqrt{R} \widetilde{\text{erf}}(\sqrt{R}) \right\} \\ = \sqrt{N_0 T} \left\{ \frac{e^{-R}}{\sqrt{\pi}} + \sqrt{R} [1 - 2 \text{erfc}(\sqrt{2R})] \right\}$$

which is precisely Layland's result (Ref. 4).

As a further comment, Anderson and Hurd (Ref. 6) have shown that the SSA loop phase error is given by

$$\sigma_\phi^2 = \frac{\pi^2 \omega_L t_s}{2R \widetilde{\text{erf}}(\sqrt{R})} \quad (28)$$

where $\omega_L t_s$ is the fractional loop bandwidth. Thus, if we know the value of $\omega_L t_s$, then Eq. (27) depends only on the actual signal-to-noise ratio R and the noise factor $\sqrt{N_0 T}$. However, in the SNR algorithm the factors containing $\sqrt{N_0 T}$ all cancel, leaving the resulting expressions functions of only R .

IV. The Second Moment of y

Determination of the second moment is much simpler than the first since the absolute value is absorbed by the square. We have, therefore,

$$E\{y_k^2\} = \int_0^\infty E \left\{ \left| \int_{t_k+\Delta}^{t_k+T+\Delta} [V(t) + n(t)] dt \right|^2 \middle| \Delta, \Delta \geq 0 \right\} f_\Delta d\Delta \\ + \int_{-\infty}^0 E \left\{ \left| \int_{t_k+\Delta}^{t_k+T+\Delta} [V(t) + n(t)] dt \right|^2 \middle| \Delta, \Delta < 0 \right\} f_\Delta d\Delta \quad (29)$$

which becomes

$$\begin{aligned}
E\{y_k^2\} &= \frac{1}{4} \int_0^\infty \sum_{V_k} \sum_{V_{k+1}} [V_k T + (V_{k+1} - V_k) \Delta]^2 f_\Delta d\Delta \\
&\quad + \frac{1}{4} \int_{-\infty}^0 \sum_{V_k} \sum_{V_{k-1}} [V_k T + (V_{k-1} - V_k) \Delta]^2 f_\Delta d\Delta + \frac{N_0 T}{2}
\end{aligned} \tag{30}$$

Again we find that the integrands are the same so that

$$\begin{aligned}
E\{y_k^2\} &= \int_{-\infty}^\infty (2V\Delta^2 - 2V^2 T \Delta + V^2 T^2) f_\Delta d\Delta + \frac{N_0 T}{2} \\
&= V^2 T^2 + 2V^2 \sigma_\Delta^2 + \frac{N_0 T}{2}
\end{aligned} \tag{31}$$

Now, if we use the relationships given in Eq. (25) and the definition of R , we obtain

$$E\{y_k^2\} = N_0 T \left(R + \frac{R \sigma_\Phi^2}{2\pi^2} + \frac{1}{2} \right) \tag{32}$$

Again we see that, when σ_Φ^2 goes to zero, Eq. (32) reduces to Layland's result (Ref. 4).

V. The Third Moment of y

Using the same procedure as in Section III, we can express the third moment of y_k by

$$\begin{aligned}
E\{y_k^3\} &= \frac{1}{4} \left(\sqrt{\frac{N_0 T}{2}} \right)^3 \int_0^\infty \sum_{V_k} \sum_{V_{k+1}} E \left\{ \left| \left[\operatorname{sgn}(V_k) + \operatorname{sgn}(V_{k+1} - V_k) \frac{2\Delta}{T} \right] \sqrt{2R} + n'' \right|^3 \middle| \Delta, \Delta \geq 0 \right\} f_\Delta d\Delta \\
&\quad + \frac{1}{4} \left(\sqrt{\frac{N_0 T}{2}} \right)^3 \int_{-\infty}^0 \sum_{V_k} \sum_{V_{k-1}} E \left\{ \left| \left[\operatorname{sgn}(V_k) + \operatorname{sgn}(V_{k-1} - V_k) \frac{2\Delta}{T} \right] \sqrt{2R} + n'' \right|^3 \middle| \Delta, \Delta < 0 \right\} f_\Delta d\Delta
\end{aligned} \tag{33}$$

In Appendix D we use the properties of the characteristic function to prove the identity

$$E\{|x + \alpha|^3\} = \frac{\sqrt{2}(\alpha^2 + 2)}{\sqrt{\pi}} \exp\left[-\frac{\alpha^2}{2}\right] + \alpha(\alpha^2 + 3) \operatorname{erf}\left(\frac{\alpha}{\sqrt{2}}\right) \tag{34}$$

whenever x is a unit normal random variable ($\mathcal{N}(0, 1)$) and α is a constant. With this result Eq. (33) becomes

$$\begin{aligned}
E\{y_k^3\} &= \frac{1}{4} \left(\frac{N_0 T}{2} \right)^{3/2} \int_0^\infty \sum_{V_k} \sum_{V_{k+1}} \left\{ \left(2R \left[\operatorname{sgn}(V_k) + \operatorname{sgn}(V_{k+1} - V_k) \frac{2\Delta}{T} \right]^2 + 2 \right) \frac{\sqrt{2}}{\sqrt{\pi}} \right. \\
&\quad \times \exp \left\{ -R \left[\operatorname{sgn}(V_k) + \operatorname{sgn}(V_{k+1} - V_k) \frac{2\Delta}{T} \right]^2 \right\} \\
&\quad + \left(2R \left[\operatorname{sgn}(V_k) + \operatorname{sgn}(V_{k+1} - V_k) \frac{2\Delta}{T} \right]^2 + 3 \right) \left(\sqrt{2R} \left[\operatorname{sgn}(V_k) + \operatorname{sgn}(V_{k+1} - V_k) \frac{2\Delta}{T} \right] \right) \\
&\quad \times \operatorname{erf} \left(\sqrt{R} \left[\operatorname{sgn}(V_k) + \operatorname{sgn}(V_{k+1} - V_k) \frac{2\Delta}{T} \right] \right) \left. \right\} f_\Delta d\Delta
\end{aligned}$$

$$\begin{aligned}
& + \frac{1}{4} \left(\frac{N_0 T}{2} \right)^{\frac{3}{2}} \int_{-\infty}^0 \sum_{V_k} \sum_{V_{k-1}} \left\{ \left(2R \left[\operatorname{sgn}(V_k) + \operatorname{sgn}(V_{k-1} - V_k) \frac{2\Delta}{T} \right]^2 + 2 \right) \frac{\sqrt{2}}{\sqrt{\pi}} \right. \\
& \times \exp \left\{ -R \left[\operatorname{sgn}(V_k) + \operatorname{sgn}(V_{k-1} - V_k) \frac{2\Delta}{T} \right]^2 \right\} \\
& + \left(2R \left[\operatorname{sgn}(V_k) + \operatorname{sgn}(V_{k-1} - V_k) \frac{2\Delta}{T} \right]^2 + 3 \right) \left(\sqrt{2R} \left[\operatorname{sgn}(V_k) + \operatorname{sgn}(V_{k-1} - V_k) \frac{2\Delta}{T} \right] \right) \\
& \times \widetilde{\operatorname{erf}} \left(\sqrt{R} \left[\operatorname{sgn}(V_k) + \operatorname{sgn}(V_{k-1} - V_k) \frac{2\Delta}{T} \right] \right) \left. \right\} f_{\Delta} d\Delta
\end{aligned} \tag{35}$$

As before, by carrying out the summations, we find that the integrands are the same, producing

$$\begin{aligned}
E \{y_k^3\} &= \left(\frac{N_0 T}{2} \right)^{\frac{3}{2}} \left\{ \frac{2R+2}{\sqrt{2\pi}} e^{-R} + \frac{(2R+3)\sqrt{R}}{\sqrt{2}} \widetilde{\operatorname{erf}}(\sqrt{R}) \right. \\
&+ \frac{\sqrt{2}}{\sqrt{\pi}} \int_{-\infty}^{\infty} \left(R+1 - \frac{4R\Delta}{T} + \frac{4R\Delta^2}{T^2} \right) \exp \left[-R \left(1 - \frac{2\Delta}{T} \right)^2 \right] f_{\Delta} d\Delta \\
&+ \left. \sqrt{2R} \int_{-\infty}^{\infty} \left[R + \frac{3}{2} - \frac{3}{T} (2R+1)\Delta + \frac{12R\Delta^2}{T^2} - \frac{8R\Delta^3}{T^3} \right] \widetilde{\operatorname{erf}} \left[\sqrt{R} \left(1 - \frac{2\Delta}{T} \right) \right] f_{\Delta} d\Delta \right\}
\end{aligned} \tag{36}$$

The first integral of this expression can be evaluated using straightforward techniques. The second integral involves error functions and is of the form

$$\sum_{n=0}^3 \int_{-\infty}^{\infty} a_n \Delta^n \widetilde{\operatorname{erf}} \left[\sqrt{R} \left(1 - \frac{2\Delta}{T} \right) \right] f_{\Delta} d\Delta$$

For $n=0$, we can use the result of Appendix C. For $n=1, 2, 3$, we can with some effort use integration by parts. After performing these operations and using Eqs. (25) and (26), we finally arrive at

$$\begin{aligned}
E \{y_k^3\} &= (N_0 T)^{\frac{3}{2}} \left\{ \frac{(R+1)}{2\sqrt{\pi}} e^{-R} + \frac{(2R+3)\sqrt{R}}{4} \widetilde{\operatorname{erf}}(\sqrt{R}) \right. \\
&+ \frac{1}{2} \sqrt{R} \left(R + \frac{3D^2}{2\pi^2} \right) \widetilde{\operatorname{erf}} \left(\frac{\pi\sqrt{R}}{D} \right) + \frac{D \exp \left[-\frac{R\pi^2}{D^2} \right]}{2\pi\sqrt{\pi}} \left(R + \frac{D^2}{\pi^2} \right) \left. \right\}
\end{aligned} \tag{37}$$

VI. The Fourth Moment of y

The fourth moment of y_k is found by the same procedure used to determine the second moment. After conditioning on Δ and evaluating the integrands one obtains

$$\begin{aligned}
E \{y_k^4\} &= \int_{-\infty}^{\infty} \left\{ V^4 T^4 + 3V^2 T^3 N_0 + \frac{3N_0^2 T^2}{4} \right. \\
&- 2V^2 T^2 (2V^2 T + 3N_0) \Delta \\
&+ 6V^2 T (2V^2 T + N_0) \Delta^2 \\
&- \left. 16V^4 T \Delta^3 + 8V^4 \Delta^4 \right\} f_{\Delta} d\Delta
\end{aligned} \tag{38}$$

which, after using the previously used substitutions, becomes

$$\begin{aligned}
E \{y_k^4\} &= \\
& N_0^2 T^2 \left[R^2 + 3R + \frac{3}{4} + \frac{3R\sigma_{\phi}^2}{\pi^2} \left(R + \frac{1}{2} \right) + \frac{3R^2 \sigma_{\phi}^4}{2\pi^4} \right]
\end{aligned} \tag{39}$$

VII. Quantizing and Internal Noise Variances

In this section we shall consider both the quantizing error variance and the internal equipment noise variance.

These are considered together since in practice one would measure the effect of both simultaneously.

The quantizing errors result from the SSA analog-to-digital converters, which are 12-bit converters having a dynamic range of ± 5 volts. The least-significant digit, therefore, corresponds to ± 2.44 mV. However, the nominal integrated symbol voltage is 1.1 volts. Thus, if we let δ_v represent the quantizing step size, then

$$\delta_v = \frac{VT}{450} \quad (40)$$

Now, from Panter (Ref. 7), we know that for equal quantizing intervals the variance of the quantizing error is given by

$$\sigma_q^2 = \frac{(\delta_v)^2}{12} \quad (41)$$

Therefore, the desired quantizing error variance is

$$\sigma_q^2 = \frac{N_o TR}{2.43 \times 10^6} \quad (42)$$

For the internal noise variance, let us assume that the internal noise causes the equipment to have an internal signal-to-noise ratio of γ dB. Also recall that the signal voltage (after the integrator and quantizer) is VT . Then, if we let \tilde{N}_o represent the internal noise one-sided spectral density, then

$$\tilde{N}_o = VT^2 (10^{-\gamma/10}) \quad (43)$$

However, the desired variance is the two-sided noise density, so that

$$\sigma_B^2 = \frac{\tilde{N}_o}{2} = \frac{1}{2} N_o TR (10^{-\gamma/10}) \quad (44)$$

VIII. Evaluation Results

A computer program was written to evaluate the mean (Eq. 8) and the variance (Eq. 11) of the SNR estimator using the appropriate substitutions from Section II, the expressions for the first four moments (Sections III-VI), and the equations for the internal error variances. The program was designed to compute the mean and variance over the range of input SNRs (R) from -7 dB to $+42$ dB for specified values of sample size (N), fractional loop bandwidth ($\omega_L t_s$), and equipment SNR (γ). By holding any

two of these parameters constant, the dependence on the third quantity could be determined.

When the mean of the estimator was evaluated, it was found to depend heavily on both the input and internal signal-to-noise ratios. At low input SNRs, the estimator behaved essentially as predicted by Layland. However, as the input SNR was raised, the estimator became limited by the internal SNR and asymptotically approached that internal quantity. This effect is illustrated in Fig. 2.

The dependence of the mean on the sample size or the loop bandwidth, however, was found to be much less pronounced. As the sample size was varied, the estimator mean was found to be virtually insensitive to these variations except at extremely low input SNRs. When the fractional loop bandwidth was varied, no significant change in the mean was detected until the bandwidth was made much larger than the values presently available in the SSA.

These effects are illustrated in Figs. 3 and 4. Figure 3 shows the manner in which the mean approaches Layland's asymptotic value of -0.363 dB as the sample size increases and the input SNR is fixed at -7 dB. Figure 4 illustrates the decrease in the estimator mean as the fractional loop bandwidth is increased.

Unlike the mean, the estimator variance was found to depend quite heavily on the sample size and was essentially independent of variations in the signal-to-noise ratio or loop bandwidth. Figure 5 illustrates the dependence of the $1-\sigma$ estimation error on the sample size. In Figure 6 we see the dependence of the $1-\sigma$ error on the input SNR. Note that as the input SNR varies over five orders of magnitude, the $1-\sigma$ error varies only about 30%.

IX. Conclusions

In this article the effects of input and internal noise, transition estimation errors, and finite sample size were considered to derive expressions for the mean and variance of the SNR estimation algorithm of the SSA. These quantities were found to depend on the first four moments of the absolute symbol integrals which in turn were derived. When these expressions were evaluated, we found that the estimator mean depended heavily on the input and internal signal-to-noise ratios, but was virtually insensitive to changes in the sample size or fractional loop bandwidth. The estimator variance, on the other hand, was found to be essentially independent of the signal-to-noise ratios and the loop bandwidths and to vary appreciably only with changes in the sample size.

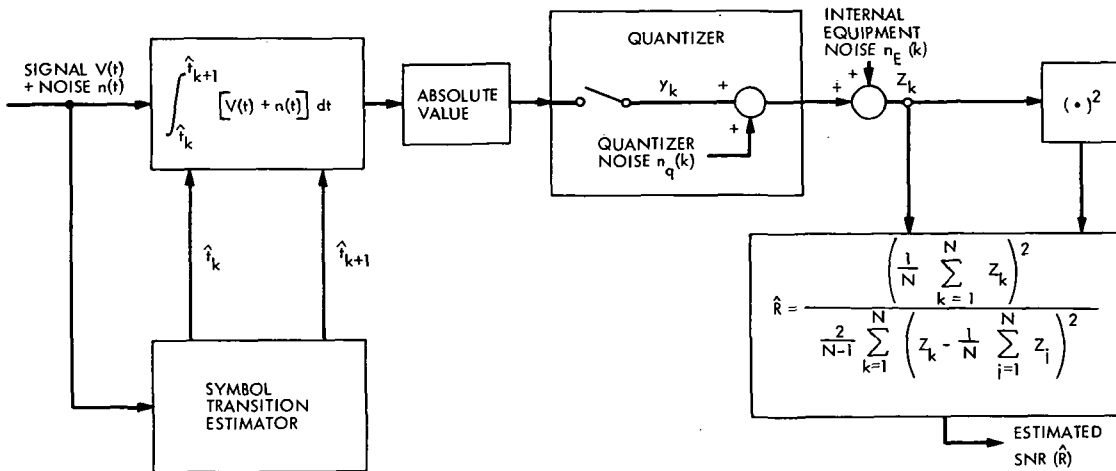


Fig. 1. Model of the SNR estimation process

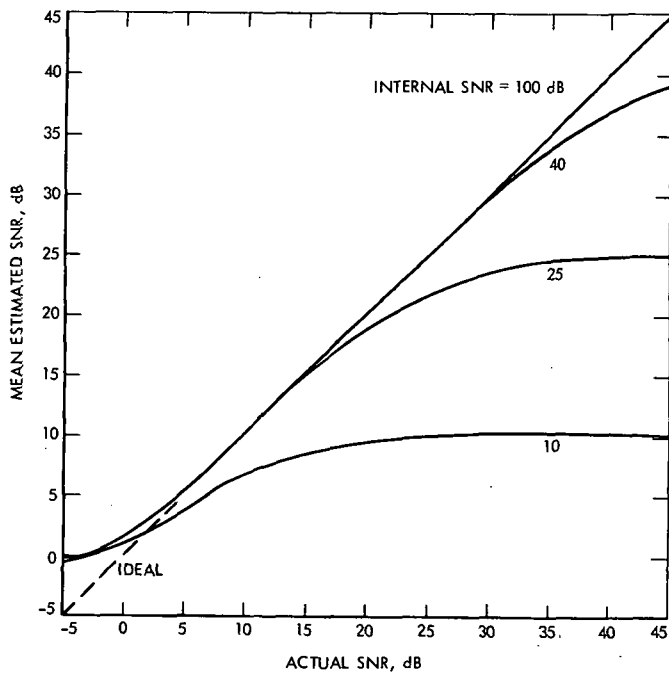


Fig. 2. Mean estimated SNR vs actual SNR

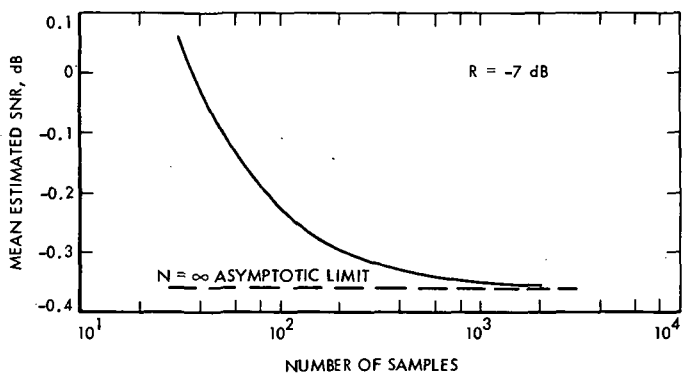


Fig. 3. Dependence of estimator mean on the sample size

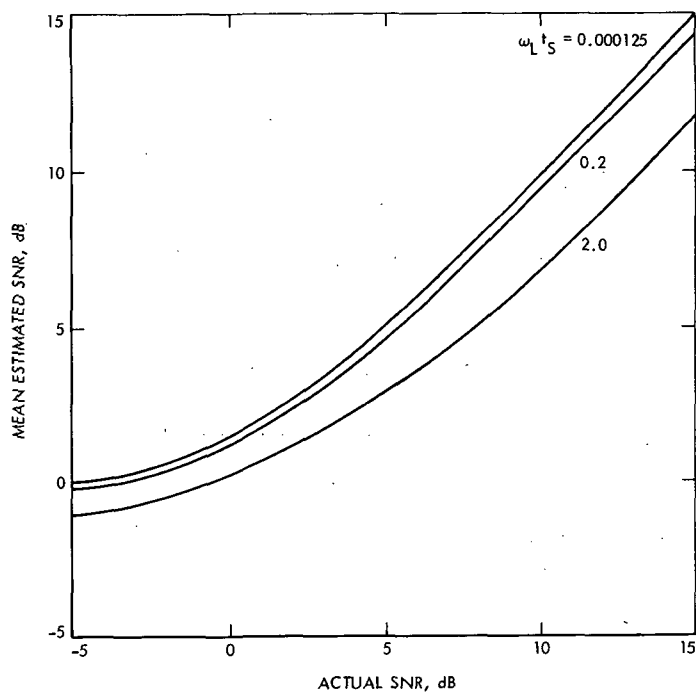


Fig. 4. Dependence of estimator mean on fractional loop bandwidth

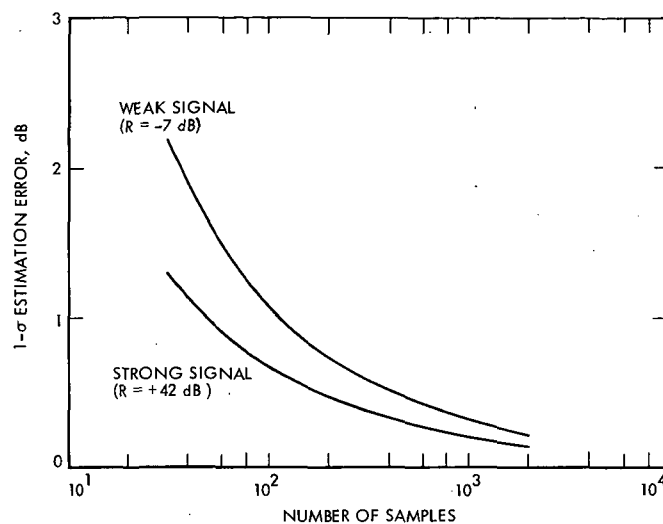


Fig. 5. Dependence of 1-σ estimation error on sample size

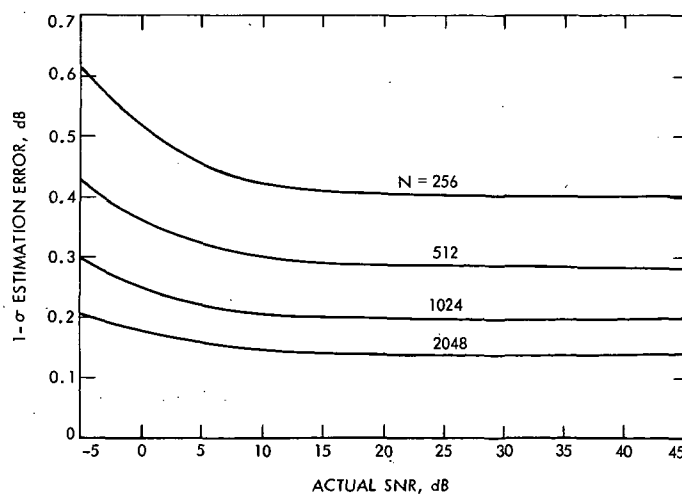


Fig. 6. Dependence of 1-σ estimation error on input SNR for various sample sizes

Appendix A

The Variance of a Sample Variance

Assume we are given a sequence of random variables $\{y_i\}$, which are taken independently from a stationary random process having some arbitrary probability distribution. Assume also that the first four moments of y_i are finite and that the mean and variance of y_i are denoted μ and σ^2 , respectively. We form the unbiased variance estimator (W) defined by

$$W = \frac{1}{N-1} \sum_{i=1}^N \left(y_i - \frac{1}{N} \sum_{j=1}^N y_j \right)^2 \quad (\text{A-1})$$

where N is the number of samples ($N \geq 2$). We desire to determine the variance of W .

First we note that since W is an unbiased estimator

$$E\{W\} = \sigma^2 \quad (\text{A-2})$$

Now, let us consider

$$E\{W^2\} = E \left\{ \left[\frac{1}{N-1} \sum_{i=1}^N \left(y_i - \frac{1}{N} \sum_{j=1}^N y_j \right)^2 \right]^2 \right\} \quad (\text{A-3})$$

If we expand the inner square, we have

$$E\{W^2\} = \left(\frac{1}{N-1} \right)^2 E \left\{ \left(\sum_{i=1}^N y_i^2 \right)^2 - \frac{2}{N} \sum_{i=1}^N y_i^2 \left(\sum_{j=1}^N y_j \right)^2 + \frac{1}{N^2} \left(\sum_{j=1}^N y_j \right)^4 \right\} \quad (\text{A-4})$$

Now, by expanding the summations and using the independence of the y_i 's, the first expectation becomes

$$E \left\{ \left(\sum_{i=1}^N y_i^2 \right)^2 \right\} = NE\{y^4\} + N(N-1)[E\{y^2\}]^2 \quad (\text{A-5})$$

where y corresponds to any one of the samples. Likewise, the second expectation becomes

$$\begin{aligned} E \left\{ \sum_{i=1}^N y_i^2 \left(\sum_{j=1}^N y_j \right)^2 \right\} &= NE\{y^4\} + 2N(N-1)E\{y^3\}\mu \\ &+ N(N-1)[E\{y^2\}]^2 \\ &+ N(N-1)(N-2)E\{y^2\}\mu^2 \end{aligned} \quad (\text{A-6})$$

The third expectation is somewhat more complex. However, by considering the fourth power of the summation as the square of the summations squared, we can decompose this expectation into the previously evaluated expectation plus an expectation involving the cross-product terms. The resulting expression is

$$\begin{aligned} E \left\{ \left(\sum_{i=1}^N y_i \right)^4 \right\} &= NE\{y^4\} + 4N(N-1)E\{y^3\}\mu \\ &+ 3N(N-1)[E\{y^2\}]^2 \\ &+ 6N(N-1)(N-2)E\{y^2\}\mu^2 \\ &+ N(N-1)(N-2)(N-3)\mu^4 \end{aligned} \quad (\text{A-7})$$

Combining these results and using the definition of the variance yields

$$\begin{aligned} E\{W^2\} &= \frac{E\{y^4\}}{N} - \frac{4E\{y^3\}\mu}{N} + \frac{3[E\{y^2\}]^2}{N} \\ &+ \frac{(N-2)(N-3)\sigma^4}{N(N-1)} \end{aligned} \quad (\text{A-8})$$

Finally, we have that the variance of the sample variance is given by

$$\begin{aligned} \text{var}\{W\} &= \frac{1}{N}E\{y^4\} - \frac{4}{N}E\{y^3\}\mu \\ &+ \frac{3}{N}[E\{y^2\}]^2 - \frac{2(2N-3)\sigma^4}{N(N-1)} \end{aligned} \quad (\text{A-9})$$

In deriving Eq. (A-9), no properties of the probability distribution of y were used. Consequently, the result will remain valid for any distribution (symmetrical or not) provided that the samples are taken independently.

One additional simplification of Eq. (A-9) can be obtained if one is willing to compute centralized moments instead of ordinary moments. This can be accomplished by making the substitution $y = x + \mu$, where x is a zero

mean random variable with the appropriate distribution. After substitution and simplification, one obtains

$$\text{var } \{W\} = \frac{1}{N} E \{x^4\} - \frac{(N-3)}{N(N-1)} \sigma^4 \quad (\text{A-10})$$

or equivalently

$$\text{var } \{W\} = \frac{1}{N} E \{(y - \mu)^4\} - \frac{(N-3)}{N(N-1)} \sigma^4 \quad (\text{A-10a})$$

As an example of the use of this result let us assume that y is a zero mean gaussian random variable having a variance σ^2 . It is a well-known result that for this case the sample variance given by Eq. (A-1) is an \mathcal{C} -square distributed random variable with $(N-1)$ degrees of freedom. Since

$$E \{(y - \mu)^4\} = E \{y^4\} = 3\sigma^4 \quad (\text{A-11})$$

then we have from Eq. (A-10a)

$$\text{var } \{W\} = \frac{2}{N-1} \sigma^4 \quad (\text{A-12})$$

which is precisely the variance of the associated \mathcal{C} -square distribution (Ref. 8).

Finally, for the sake of completeness, we should verify that our result (Eq. A-9 or A-10) is indeed a candidate solution for a variance (i.e., it produces a nonnegative variance). This can be easily verified by noting from Eq. (A-10) that

$$N \text{var } \{W\} \geq E \{x^4\} - \sigma^4 \quad (\text{A-13})$$

However, the right-hand side of expression (A-13) is by definition the variance of $\lambda = x^2$. Therefore,

$$\text{var } \{W\} \geq 0 \quad (\text{A-14})$$

Appendix B

Evaluation of $E\{|x + \alpha|\}$

In this appendix we desire to establish the identity

$$E\{|x + \alpha|\} = \frac{2}{\sqrt{2\pi}} \exp\left[-\frac{\alpha^2}{2}\right] + \alpha \widetilde{\text{erf}}\left(\frac{\alpha}{\sqrt{2}}\right) \quad (\text{B-1})$$

whenever x is a unit normal ($\mathcal{N}(0, 1)$) random variable and α is a constant. To establish this result, let

$$y = |z| \quad (\text{B-2})$$

where $z = x + \alpha$. The probability density function for z is then

$$f_z(z) = \frac{1}{\sqrt{2\pi}} \exp\left[-\frac{(z - \alpha)^2}{2}\right] \quad (\text{B-3})$$

From Papoulis (Ref. 9) the density function for y is

$$f_y(y) = [f_z(y) + f_z(-y)] U(y) \quad (\text{B-4})$$

where $U(y)$ is the unit step function. Then, the expected

value of y is expressed by

$$E\{y\} = \frac{1}{\sqrt{2\pi}} \int_0^\infty y \exp\left[-\frac{(y - \alpha)^2}{2}\right] dy + \frac{1}{\sqrt{2\pi}} \int_0^\infty y \exp\left[-\frac{(y + \alpha)^2}{2}\right] dy \quad (\text{B-5})$$

After a change of variables and integrating, we obtain

$$E\{y\} = \frac{2}{\sqrt{2\pi}} \exp\left[-\frac{\alpha^2}{2}\right] + \alpha \text{erf}(\alpha) - \alpha \text{erfc}(\alpha) \quad (\text{B-6})$$

And, finally, with a trivial identity for error functions, we have

$$\begin{aligned} E\{y\} &= E\{|x + \alpha|\} \\ &= \frac{2}{\sqrt{2\pi}} \exp\left[-\frac{\alpha^2}{2}\right] + \alpha \widetilde{\text{erf}}\left(\frac{\alpha}{\sqrt{2}}\right) \end{aligned} \quad (\text{B-7})$$

which is the desired result.

Appendix C

Evaluation of $\int_{-\infty}^{\infty} \widetilde{\text{erf}}(a + bx) \frac{\exp\left[-\frac{x^2}{2\sigma^2}\right]}{\sqrt{2\pi\sigma^2}} dx$

Consider the integral

$$I = \int_{-\infty}^{\infty} \widetilde{\text{erf}}(a + bx) \frac{\exp\left[-\frac{x^2}{2\sigma^2}\right]}{\sqrt{2\pi\sigma^2}} dx \quad (\text{C-1})$$

By changing to the nonstandard error function, Eq. (C-1) can be expressed as

$$I = 1 - 2 \int_{-\infty}^{\infty} \text{erfc}(a\sqrt{2} + b\sqrt{2}x) \frac{\exp\left[-\frac{x^2}{2\sigma^2}\right]}{\sqrt{2\pi\sigma^2}} dx \quad (\text{C-2})$$

Now, for notational simplicity, let $I = 1 - 2I'$, $a' = a\sqrt{2}$ and $b' = b\sqrt{2}$. Then, using the definition of the complementary error function, we have

$$I' = \frac{1}{2\pi\sqrt{\sigma^2}} \int_{-\infty}^{\infty} \int_{a'+b'x}^{\infty} \exp\left[-\frac{u^2}{2} - \frac{x^2}{2\sigma^2}\right] du dx \quad (\text{C-3})$$

This expression is a double integration of the exponential function over the (x, u) plane such that x varies over the entire real line and u is restricted to be above the line $u = a' + b'x$ as shown in Fig. C-1. This strongly suggests that a rotation of coordinates could simplify the integration. If we let θ represent the angle between the line $u = a' + b'x$ and the positive x -axis, then we can define a new coordinate system (x', u') by the transformations

$$\left. \begin{aligned} x &= x' \cos \theta - u' \sin \theta \\ u &= x' \sin \theta + u' \cos \theta \end{aligned} \right\} \quad (\text{C-4})$$

as shown in Fig. C-2.

Now, recall that if a function $\phi(x, u)$ is to be integrated over a region A and if we define the transformations

$$\left. \begin{aligned} x &= f(x', u') \\ u &= g(x', u') \end{aligned} \right\} \quad (\text{C-5})$$

then (Ref. 10)

$$\iint_A \phi(x, u) dx du = \iint_B \phi[f(x', u'), g(x', u')] |J| dx' du' \quad (\text{C-6})$$

where $|J|$ is the Jacobian

$$|J| = \det \begin{bmatrix} \frac{\partial x}{\partial x'} & \frac{\partial x}{\partial u'} \\ \frac{\partial u}{\partial x'} & \frac{\partial u}{\partial u'} \end{bmatrix} \quad (\text{C-7})$$

and the region B is the region which results from mapping the region A through the transformations $x = f(x', u')$ and $y = g(x', u')$. In our problem (see Fig. C-2)

$$B = \{(x', u') : -\infty \leq x' \leq \infty, u' \geq c\}$$

where c can be determined from the Law of Sines and the fact that

$$\theta = \tan^{-1}(b') \quad (\text{C-8})$$

Thus we have that

$$c = \frac{a'}{\sqrt{(b')^2 + 1}} \quad (\text{C-9})$$

Using these results and the fact that for a rotation of coordinates the Jacobian equals 1, we can express Eq. (C-3) as

$$I' = \frac{1}{2\pi\sqrt{\sigma^2}} \int_{-\infty}^{\infty} \int_{a'/\sqrt{(b')^2+1}}^{\infty} \exp\left[-\frac{1}{2\sigma^2} \{ (x')^2 [(b')^2 \sigma^2 + 1] - 2x'u'b'(1 - \sigma^2) + (u')^2 [\sigma^2 + (b')^2] \} \right] du' dx' \quad (\text{C-10})$$

Now, if we interchange the order of integration, complete the square on the variable x' in the exponent, and use the properties of the gaussian density function, we obtain

$$I' = \frac{1}{\sqrt{2\pi}} \sqrt{\frac{(b')^2 + 1}{(b')^2 \sigma^2 + 1}} \int_{a'/\sqrt{(b')^2 + 1}}^{\infty} \exp \left\{ -\frac{1}{2} \left[\frac{(b')^2 + 1}{(b')^2 \sigma^2 + 1} \right] (u')^2 \right\} du' \quad (C-11)$$

Now using the substitution

$$\lambda = \sqrt{\frac{(b')^2 + 1}{(b')^2 \sigma^2 + 1}} u' \quad (C-12)$$

we obtain

$$\begin{aligned} I' &= \frac{1}{\sqrt{2\pi}} \int_{a'/\sqrt{(b')^2 + 1}}^{\infty} \exp \left[-\frac{\lambda^2}{2} \right] d\lambda \\ &= \operatorname{erfc} \left(\frac{a'}{\sqrt{(b')^2 \sigma^2 + 1}} \right) \end{aligned} \quad (C-13)$$

Returning now to Eq. (C-2) with the substitutions for the

unprimed values of a and b , we have

$$I = 1 - 2 \operatorname{erfc} \left(\frac{a \sqrt{2}}{\sqrt{2b^2 \sigma^2 + 1}} \right) \quad (C-14)$$

so that we arrive at the result

$$\begin{aligned} I &= \int_{-\infty}^{\infty} \widetilde{\operatorname{erf}}(a + bx) \frac{\exp \left[-\frac{x^2}{2\sigma^2} \right]}{\sqrt{2\pi\sigma^2}} dx \\ &= \widetilde{\operatorname{erf}} \left(\frac{a}{\sqrt{2b^2 \sigma^2 + 1}} \right) \end{aligned} \quad (C-15)$$

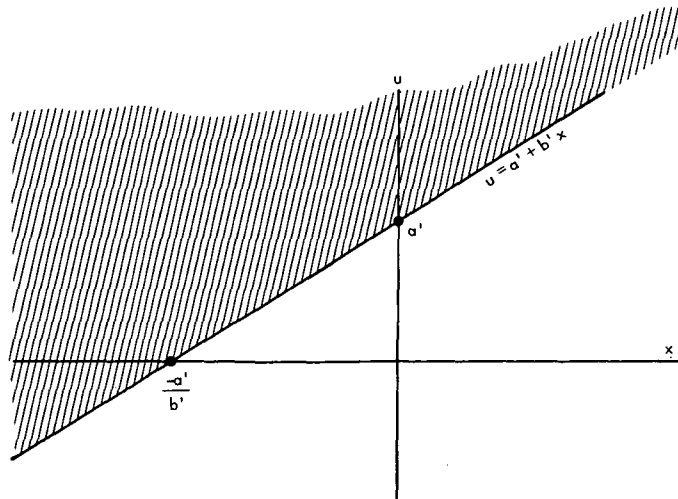


Fig. C-1. Domain of integration for I' (shaded area)

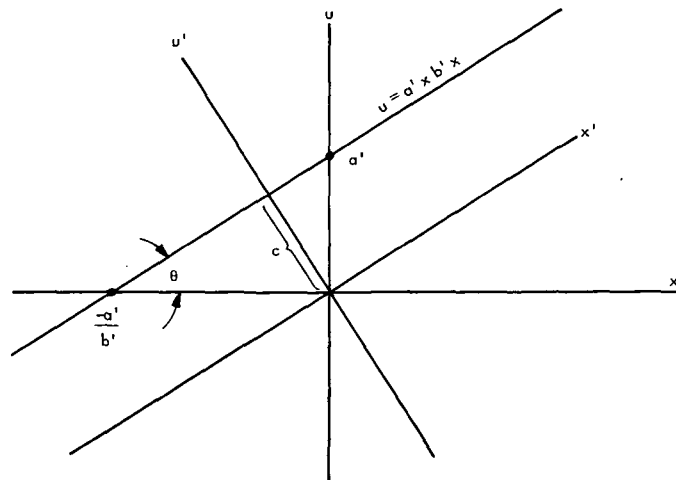


Fig. C-2. Rotated coordinate system

Appendix D

Evaluation of $E\{|x + \mu|^3\}$

Let

$$y = |x + \mu| \quad (D-1)$$

where x is a unit normal random variable ($\mathcal{N}(0, 1)$) and μ is a constant. We wish to compute $E\{y^3\}$.

From Appendix A we found that the probability density function of y was given by

$$f_Y(y) = \frac{1}{\sqrt{2\pi}} \left\{ \exp\left[-\frac{(y-\mu)^2}{2}\right] + \exp\left[-\frac{(y+\mu)^2}{2}\right] \right\} U(y) \quad (D-2)$$

where $U(y)$ is the unit step function. Then, the characteristic function of y ($\phi_Y(\cdot)$) is given by

$$\begin{aligned} \phi_Y(\omega) &= E\{\exp[i\omega y]\} \\ &= \frac{1}{\sqrt{2\pi}} \int_0^\infty \exp\left[-\frac{(y-\mu)^2}{2}\right] (\cos \omega y + i \sin \omega y) dy \\ &\quad + \frac{1}{\sqrt{2\pi}} \int_0^\infty \exp\left[-\frac{(y+\mu)^2}{2}\right] (\cos \omega y + i \sin \omega y) dy \end{aligned} \quad (D-3)$$

From Erdelyi, et al. (Ref. 11), Eq. (D-3) can be expressed as

$$\begin{aligned} \phi_Y(\omega) &= \frac{\exp\left[-\frac{\omega^2}{2}\right]}{2} \left\{ \exp[i\mu\omega] \widetilde{\text{erfc}}\left[-\frac{\sqrt{2}}{2}(\mu + i\omega)\right] \right. \\ &\quad \left. + \exp[-i\mu\omega] \widetilde{\text{erfc}}\left[\frac{\sqrt{2}}{2}(\mu - i\omega)\right] \right\} \end{aligned} \quad (D-4)$$

Since we now have the characteristic function, we can determine the moments of y by successive differentiation. Differentiating once we obtain

$$\begin{aligned} \frac{\partial \phi_Y(\omega)}{\partial \omega} &= i \sqrt{\frac{2}{\pi}} \exp\left[-\frac{\mu^2}{2}\right] + \frac{(i\mu - \omega)}{2} \exp\left[-\frac{\omega^2}{2} + i\mu\omega\right] \widetilde{\text{erfc}}\left[-\frac{\sqrt{2}}{2}(\mu + i\omega)\right] \\ &\quad - \frac{(i\mu + \omega)}{2} \exp\left[-\frac{\omega^2}{2} - i\mu\omega\right] \widetilde{\text{erfc}}\left[\frac{\sqrt{2}}{2}(\mu - i\omega)\right] \end{aligned} \quad (D-5)$$

Differentiating again we have

$$\begin{aligned} \frac{\partial^2 \phi_Y(\omega)}{\partial \omega^2} &= \frac{-2i\omega}{\sqrt{2\pi}} \exp\left[-\frac{\mu^2}{2}\right] \\ &\quad + \frac{(\omega^2 - 2i\mu\omega - \mu^2 - 1)}{2} \exp\left[-\frac{\omega^2}{2} + i\mu\omega\right] \widetilde{\text{erfc}}\left[-\frac{\sqrt{2}}{2}(\mu + i\omega)\right] \\ &\quad + \frac{(\omega^2 + 2i\mu\omega - \mu^2 - 1)}{2} \exp\left[-\frac{\omega^2}{2} - i\mu\omega\right] \widetilde{\text{erfc}}\left[\frac{\sqrt{2}}{2}(\mu - i\omega)\right] \end{aligned} \quad (D-6)$$

Finally, a third differentiation yields

$$\begin{aligned}
\frac{\partial^3 \phi_Y(\omega)}{\partial \omega^3} = & \frac{1}{2} \left\{ \frac{-2i\sqrt{2}}{\sqrt{\pi}} \exp\left[-\frac{\mu^2}{2}\right] + 2(\omega^2 - \mu^2 - 1)i\sqrt{\frac{2}{\pi}} \exp\left[-\frac{\mu^2}{2}\right] \right\} \\
& + \left\{ \frac{-\omega^3 - 3i\mu\omega^2 + 3\omega\mu^2 + 3\omega + 3i\mu + i\mu^3}{2} \right\} \exp\left[-\frac{\omega^2}{2} - i\mu\omega\right] \widetilde{\text{erfc}}\left[\frac{\sqrt{2}}{2}(\mu - i\omega)\right] \\
& + \left\{ \frac{-\omega^3 + 3i\mu\omega^2 + 3\omega\mu^2 + 3\omega - 3i\mu - i\mu^3}{2} \right\} \exp\left[-\frac{\omega^2}{2} + i\mu\omega\right] \widetilde{\text{erfc}}\left[\frac{-\sqrt{2}}{2}(\mu + i\omega)\right]
\end{aligned} \tag{D-7}$$

and, since

$$\left. \frac{\partial^3 \phi_Y(\omega)}{\partial \omega^3} \right|_{\omega=0} = -iE\{y^3\} \tag{D-8}$$

we have the result

$$\begin{aligned}
E\{y^3\} &= E\{|x + \mu|^3\} \\
&= (\mu^2 + 2)\sqrt{\frac{2}{\pi}} \exp\left[-\frac{\mu^2}{2}\right] + (\mu^2 + 3)\mu \widetilde{\text{erf}}\left(\frac{\mu}{\sqrt{2}}\right)
\end{aligned} \tag{D-9}$$

References

1. Gilchrist, C. E., "Signal-to-Noise Monitoring," in *Supporting Research and Advanced Development*, Space Programs Summary 37-27, Vol. IV, pp. 169-184. Jet Propulsion Laboratory, Pasadena, Calif., June 30, 1964.
2. Boyd, D. W., "Signal-to-Noise Ratio Monitoring: Calculation of an Important Probability Density Function," in *Supporting Research and Advanced Development*, Space Programs Summary 37-37, Vol. IV, pp. 259-261. Jet Propulsion Laboratory, Pasadena, Calif., Feb. 28, 1966.
3. Boyd, D. W., "Signal-to-Noise Ratio Monitoring: Error Analysis of the Signal-to-Noise Ratio Estimator," in *Supporting Research and Advanced Development*, Space Programs Summary 37-39, Vol. IV, pp. 172-179. Jet Propulsion Laboratory, Pasadena, Calif., June 30, 1966.
4. Layland, J. W., "On S/N Estimation," in *Supporting Research and Advanced Development*, Space Programs Summary 37-48, Vol. III, pp. 209-212. Jet Propulsion Laboratory, Pasadena, Calif., Dec. 31, 1967.
5. Layland, J. W., Burow, N. A., and Vaisnys, A., "MMTS: Bit-Sync Loop Lock Detector," in *The Deep Space Network*, Space Programs Summary 37-52, Vol. II, pp. 121-124. Jet Propulsion Laboratory, Pasadena, Calif., July 31, 1968.
6. Anderson, T. O., and Hurd, W. J., "Symbol Synchronizer for Low Signal-to-Noise Ratio Coded Systems," in *The Deep Space Network*, Space Programs Summary 37-53, Vol. II, pp. 51-63. Jet Propulsion Laboratory, Pasadena, Calif., Sept. 30, 1968.
7. Panter, P. F., *Modulation, Noise, and Spectral Analysis*, p. 635. McGraw-Hill Book Co., Inc., New York, 1965.
8. Hogg, R. V., and Craig, A. T., *Introduction to Mathematical Statistics*, Problem 6.5. The Macmillan Co., New York, 1958.
9. Papoulis, A., *Probability, Random Variables, and Stochastic Processes*, p. 131. McGraw-Hill Book Co., Inc., New York, 1965.
10. Thomas, G. B., Jr., *Calculus and Analytic Geometry*, 3rd Edition, p. 743. Addison-Wesley Publishing Co., Inc., Reading, Mass., 1962.
11. Erdelyi, A., Magnus, W., Oberhettinger, F., and Tricomi, F. G., *Tables of Integral Transforms*, Vol. 1, pp. 15 and 74. McGraw-Hill Book Co., Inc., New York, 1954.

Initial Acquisition Planning

W. G. Meeks
DSIF Operations Section

Each spacecraft supported by the DSN must be acquired and tracked by a deep space station (DSS). The first acquisition, generally referred to as initial acquisition, is unique for each spacecraft and presents problems that must be recognized and resolved long before a launch actually takes place. This article tells how plans are developed and implemented to ensure the successful beginning of DSN tracking support.

I. Introduction

A. Definition of Initial Acquisition Phase

For any mission, the initial acquisition phase is defined as the period of time starting at liftoff of the spacecraft booster and ending when a selected DSIF station has:

- (1) RF acquisition and has auto-tracked the spacecraft using the Acquisition Aid Antenna (SAA).
- (2) Transferred auto-track to the main 26-m dish feed (SCM).
- (3) Established a coherent RF link, up and down, between the spacecraft and the DSIF station, if applicable.
- (4) Obtained a specified continuous period of angular position and two-way doppler data.

Before a DSIF station can be designated an initial acquisition station, it must be capable of accomplishing all of these items. The criteria to accomplish items 1 and 2

are outlined in paragraph B below, item 3 is discussed in paragraph C, and item 4 is outlined in paragraph D.

B. Criteria for RF and Auto-Track Acquisition

- (1) The station designated as an initial acquisition station must be equipped with an SAA antenna system.
- (2) The spacecraft's elevation angle must be higher than 10 deg above the local land mask *for a minimum of 20 min* and within antenna mechanical limits.
- (3) Initial auto-track attempts must be on the SAA antenna system, but auto-tracking may not begin until the spacecraft's elevation angle is 10 deg above the local land mask and within antenna mechanical limits.
- (4) Angular tracking rates, except during the period specified in item 5, must not exceed 0.5 deg/sec in the HA or Dec axis.

- (5) Switch from SAA auto-track to SCM auto-track cannot be made until the angular tracking rates are equal to or less than 0.25 deg/sec in both axes.
- (6) The phase error, due to the doppler rate, in the selected loop bandwidth of the DSIF receiver shall not exceed 30 deg rms during the acquisition period.
- (7) The carrier level, based on SAA antenna gain, must not drop below -135 dBm during the period specified in item 2.

C. Station Status After Completion of Paragraph B

At the end of the 20-min period specified in item B.2, the initial acquisition station will be in two-way lock, furnishing good angle, doppler, and telemetry data. Also, the station will be available for sending commands to the spacecraft.

D. Data Requirements

After a coherent uplink and downlink have been established, the spacecraft will be auto-tracked for at least 10 min to furnish precision angle and doppler information for use in orbit determination calculations.

II. Initial Acquisition Study

An initial acquisition study must be conducted to determine if the DSIF can meet the requirements to acquire the spacecraft and provide data to the Flight Project. The study consists of analyzing the probable spacecraft trajectories to determine if initial acquisition criteria are violated; analyzing Flight Project data requirements, plans, and operating modes; and analyzing DSIF capabilities.

The Flight Project selects a group of trajectories based on mission objectives, range safety requirements, tracking and data acquisition requirements, and many other variables affecting the final decision. Each trajectory presents a different set of problems to DSIF planners. Station view periods vary, doppler and angle rates vary, and the launch window itself is another factor to be considered. Since the cost of analyzing all the variables existing in all possible trajectories would be prohibitive, representative conditions are chosen for the first and last days of the window and for one day near the middle. For each day chosen, there may be a substantial variation in launch time; therefore, it is generally necessary to perform a detailed analysis of doppler and angle rates

and data system performance margins for three launch times on three different dates, resulting in nine cases being considered.

There are usually some special requirements for the launch phase that specify that telemetry data must be continuous, uplink signal level must not exceed some specified maximum level, and/or command readiness must be achieved by a certain time. These requirements must be given consideration during the acquisition study.

Capabilities of the DSIF stations are given in Ref. 1. That document is the primary reference for determining whether Project requirements have exceeded DSIF capabilities.

The results of the acquisition study are presented in mission-dependent documentation for the use of the initial acquisition station. Examples of these documents are Refs. 2 and 3.

Figure 1 shows an example of a downlink signal level plot, Fig. 2 shows an example of a plot of angle rates, and Fig. 3 depicts a plot of doppler rates.

III. Operations Plan

A. Station Countdown

In preparation for launch, the initial acquisition station must perform a countdown which takes 8 hr, on the average, and consists of a comprehensive check of all station equipment committed for support of the Flight Project. Both primary and backup systems are checked in all configurations in accordance with Ref. 4.

At the conclusion of the countdown, the station must interface with the rest of the DSN to ensure that simulated spacecraft data will properly flow through the entire integrated system, from input at the DSIF station to output on control center displays at JPL.

B. Predicts Strategy

1. *Preflight nominal tracking predicts.* The day before a scheduled launch, three (window open, mid-window and window close) sets of nominal trajectory predicts containing doppler, angle, and range information are generated and transmitted to the initial acquisition station(s). Telemetry performance predicts containing uplink and downlink signal level and signal-to-noise ratio (SNR) information are also transmitted.

2. Launch predicts. The Real Time Computing System (RTCS), a JPL-manned facility located at the Air Force Eastern Test Range (AFETR) in Florida, generates and transmits predicts to the initial acquisition station 1 hr before launch as a backup to the JPL-Pasadena predicts. The RTCS normally transmits two sets of predicts after spacecraft launch, based on C-band metric data received from near-Earth-phase tracking stations.

C. Sky Coverage Strategy

To prepare for possible azimuth anomalies in the spacecraft trajectory, sky search patterns are generated and transmitted 1 day before a scheduled launch. The basic pattern places the antenna 10 deg above the local horizon (in observance of the constraint levied in paragraph I.B.3) at spacecraft rise. If the spacecraft does not come into view at the expected time, a ± 8 deg azimuth search (SAA antenna beamwidth = 16 deg) is commenced at a predetermined time. Procedures for use of the sky coverage pattern are documented in Ref. 5. Figure 4 is a sample sky coverage plot.

D. Initial Acquisition Sequence

The initial acquisition configuration and nominal procedures are presented in mission-dependent documentation that is provided to the station(s) several months before launch. The final sequence is documented in the Mission Sequence of Events (SOE), distributed a few days before launch. Table 1 is an example of the sequence that would be followed at a station.

IV. Training

A. Station On-Site Training

The Station Director is responsible for conducting on-site training using the documented results of the acquisition study. The training normally involves conferences and airplane tracks at the signal levels and rates approximating those expected during the actual launch phase.

Coordination on details continues between JPL planners and station personnel until launch time.

B. DSIF Control Team Training

Several conference-type sessions are held at JPL between planners and the DSIF Operations Control Team (OCT) to develop a clear understanding of acquisition conditions and to refine plans.

C. Operations Verification Tests (OVTs)

OVTs are conducted to verify that personnel, procedures, and equipment configurations are adequate to accomplish the job. These tests employ the services of the DSN Simulation Center, which provides simulation of a launch environment; the DSN Network Analysis Team, which provides predictions and system performance analysis; and the DSN Operations Control Team (OCT), which supervises operations. These tests are obviously conducted under conditions as close to the actual event as possible.

D. Operations Readiness Tests (ORTs)

ORTs are Flight Project tests that serve as full-dress rehearsals for launch. It is intended that any holes or pitfalls not previously recognized will surface during this period. These tests are supported by all committed DSN facilities.

V. Launch Phase Operations

Launch phase operations are the culmination of years of planning, training, and testing. DSN operations are under the control of the DSN OCT, which is supported, in an advisory role, by those who have planned the DSN support of the mission. All actions and events related to this mission phase are documented in the DSN SOE, which is in the hands of all participants.

VI. Summary

The techniques described herein have evolved from approximately 14 years of experience with tracking operations at JPL. To date, the DSN record for performing initial acquisitions is perfect, with no spacecraft having been lost as a result of DSN anomalies.

References

1. *DSN/Flight Project Interface Design Handbook*, Document 810-5 (JPL internal document).
2. *DSN Operations Plan for Pioneer F Mission*, Document 616-26, Vol. VIII (JPL internal document).
3. *DSN Operations Plan for Mariner Mars 1971 Mission*, Document 610-84, Vol. VIII (JPL internal document).
4. *DSN Standard Test/Training Plan and Procedures*, 853-series Documents (JPL internal documents).
5. *Standard DSN Operations Plan and Procedures*, 843-series Documents (JPL internal documents).

Table 1. Initial acquisition procedure

Step	Time from launch (TFL)	Event
1	L - 50 min	TRAKON specifies predicts to use
2	L - 30 min	Confirm SEARCH PATTERNS
3	L - 10 min	Verify ETR prelaunch predicts
4		Verify JPL prelaunch predicts
5	L	LIFTOFF: : : Z
6	L + 10 min	Complete preacquisition checkout
7	L + 15 min	ANTENNA to Point A (Fig. 4)
8	L + 18 min	Recorders ON, TDH sampling
9	L + 19 min	Commence RCV search
10		Signals heard. If no signals heard by Point A, go to Step 27
11		RCV 2 in lock
12		RCV 1 in lock
13		Point A: SAA/AUTO
14		SCM/AUTO
15		SDA 1 in lock
16		Frame in lock
17		Bit lock
18	L + 23 min	TRAKON confirms TXR ON time and EXC VCO setting XA at (time to be supplied in DSN SOE).
19	L + (per SOE)	TXR ON-1kw-SAA.
20	TXR ON + 1½ min	RCV out of lock, CMD MOD ON (If RCVs do not drop lock by turn-on + 3 min or TXR switch-on is delayed, go to Step 29.)
21		RCV 1 in lock
22		RCV 2 in lock
23		AUTO SCM
24		Frame in lock
25		Bit in lock
26	TXR ON + 2 min	TRAKON confirms 2-way
27		No signals heard at Point A EXECUTE SKY SEARCH PROCEDURES. If spacecraft is acquired, return to Step 11
28		If spacecraft is not acquired: (a) Return to predictions (b) Reset TXR to 10 kw SAA (c) Await instructions from TRACK CHIEF
29	TXR ON + 3 min	Tune EXC VCO per real-time input from NAT TRK

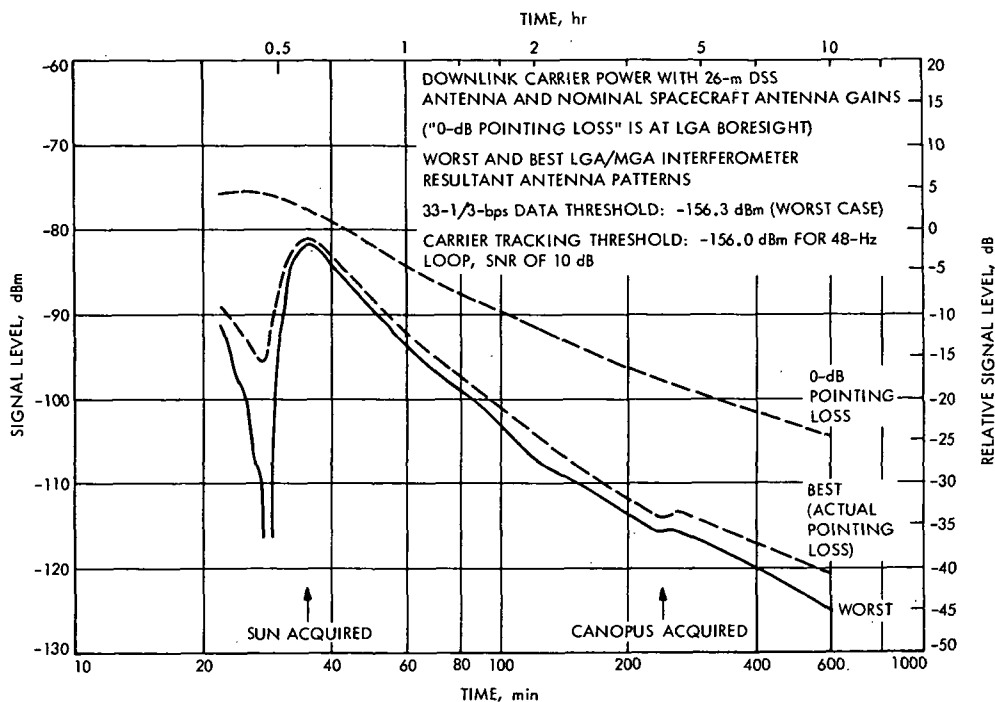


Fig. 1. Johannesburg nominal Mission A downlink power with interferometer effect

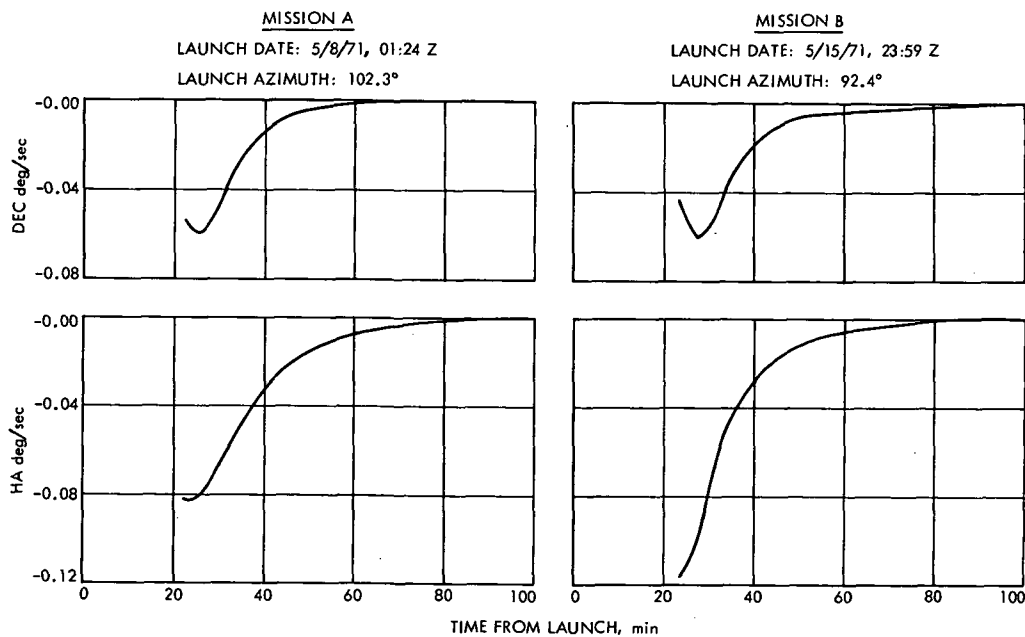


Fig. 2. DSS 51 angle rates vs TFL (window open, Missions A and B)

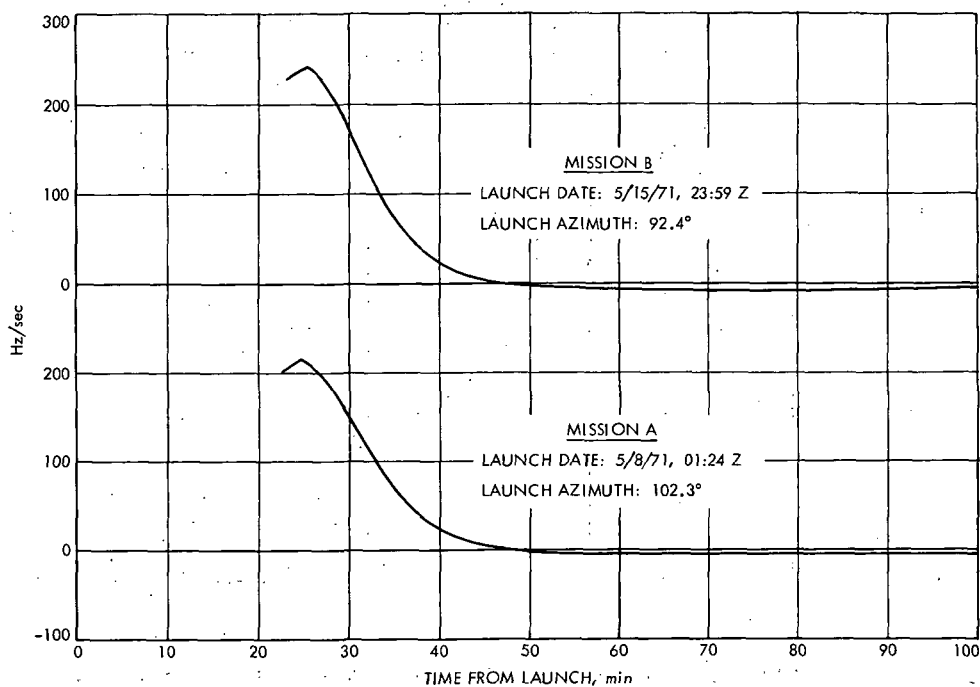


Fig. 3. DSS 51 two-way doppler rates vs TFL (window open, Missions A and B)

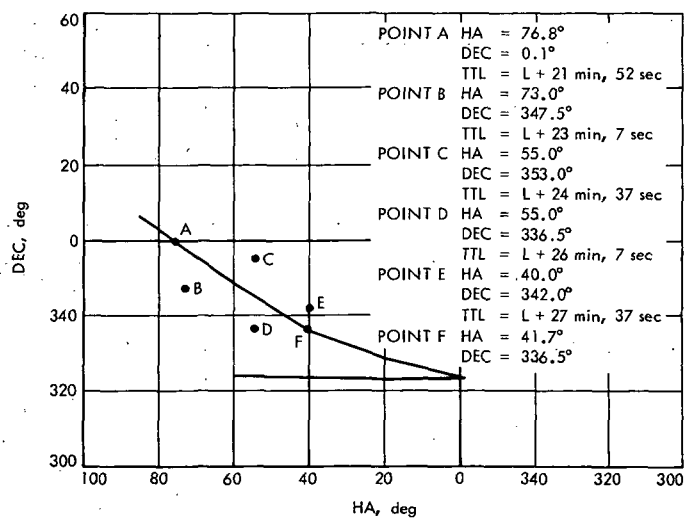


Fig. 4. DSS 51 sky coverage plot for 3/19/72 launch

Bibliography

- Anderson, J. D., *Determination of the Masses of the Moon and Venus and the Astronomical Unit from Radio Tracking Data of the Mariner II Spacecraft*. Technical Report 32-816. Jet Propulsion Laboratory, Pasadena, Calif., July 1, 1967.
- Anderson, J. D., et al., "The Radius of Venus as Determined by Planetary Radar and Mariner V Radio Tracking Data," *J. Atmos. Sci.*, pp. 1171-1174, Sept. 25, 1968.
- Berman, A. L., *Tracking System Data Analysis Report, Ranger VII Final Report*, Technical Report 32-719, Jet Propulsion Laboratory, Pasadena, Calif., June 1, 1965.
- Berman, A. L., *ABTRAJ—On-Site Tracking Prediction Program for Planetary Spacecraft*, Technical Memorandum 33-391. Jet Propulsion Laboratory, Pasadena, Calif., Aug. 15, 1968.
- Cain, D. L., and Hamilton, T. W., *Determination of Tracking Station Locations by Doppler and Range Measurements to an Earth Satellite*, Technical Report 32-534. Jet Propulsion Laboratory, Pasadena, Calif., Feb. 1, 1964.
- Carey, C. N., and Sjogren, W. L., "Gravitational Inconsistency, in the Lunar Theory: Confirmation by Radio Tracking," *Science*, Vol. 160, pp. 875, 876, Apr.-June 1968.
- Curkendall, D. W., and Stephenson, R. R., "Earthbased Tracking and Orbit Determination—Backbone of the Planetary Navigation System," *Astronaut. Aeronaut.*, Vol. 7, May 1970.
- Curkendall, D. W., "Planetary Navigation: The New Challenges," *Astronaut. Aeronaut.*, Vol. 7, May 1970.
- Efron, L., and Solloway, C. B., *Proceedings of the Conference on Scientific Applications of Radio and Radar Tracking in the Space Program*, Technical Report 32-1475. Jet Propulsion Laboratory, Pasadena, Calif., July 1970.
- Flanagan, F. M., et al., *Deep Space Network Support of the Manned Space Flight Network for Apollo: 1962-1968*, Technical Memorandum 33-452, Vol. I. Jet Propulsion Laboratory, Pasadena, Calif., July 1970.
- Flanagan, F. M., et al., *Deep Space Network Support of the Manned Space Flight Network for Apollo: 1969-1970*, Technical Memorandum 33-452, Vol. II. Jet Propulsion Laboratory, Pasadena, Calif., May 1, 1971.
- Fjeldbo, G., and Eshleman, V. R., "Radio Occultation Measurements and Interpretations," in *The Atmospheres of Venus and Mars*, p. 225. Gordon and Breach, Science Publishers, Inc., New York, N.Y.
- Georgevick, R. M., "Mathematical Model of the Solar Radiation Force and Torques Acting on the Components of a Spacecraft," Technical Memorandum 33-494. Jet Propulsion Laboratory, Pasadena, Calif., Oct. 1, 1971.
- Goldstein, R. M., "Radar Time-of-Flight Measurements to Venus," *Astron. J.*, Vol. 73, No. 9, Aug. 1968.
- Goldstein, R. M., and Rumsey, H., Jr., "A Radar Snapshot of Venus," *Science*, Vol. 169, Sept. 1970.

Bibliography (contd)

- Gordon, H. J., et al., *The Mariner 6 and 7 Flight Paths and Their Determination From Tracking Data*, Technical Memorandum 33-469, Jet Propulsion Laboratory, Pasadena, Calif., Dec. 1, 1970.
- Hamilton, T. W., et al., *The Ranger IV Flight Path and Its Determination From Tracking Data*, Technical Report 32-345, Jet Propulsion Laboratory, Pasadena, Calif., Sept. 15, 1962.
- Kellermann, K. I., et al., "High Resolution Observations of Compact Radio Sources at 13 Centimeters," *Astrophys. J.*, Vol. 161, pp. 803-809, Sept. 1970.
- Kliore, A., "Radio Occultation Measurements of the Atmospheres of Mars and Venus," in *The Atmospheres of Venus and Mars*, p. 205. Gordon and Breach Science Publishers, Inc., New York, N. Y.
- Labrum, R. G., Wong, S. K., and Reynolds, G. W., *The Surveyor V, VI, and VII Flight Paths and Their Determination from Tracking Data*, Technical Report 32-1302, Jet Propulsion Laboratory, Pasadena, Calif., Dec. 1, 1968.
- Lieske, J. H., and Null, G. W., "Icarus and the Determination of Astronomical Constants," *Astron. J.*, Vol. 74, No. 2, Mar. 1969.
- Lorell, J., and Sjogren, W. L., *Lunar Orbiter Data Analysis*, Technical Report 32-1220, Jet Propulsion Laboratory, Pasadena, Calif., Nov. 15, 1967.
- Lorell, J., *Lunar Orbiter Gravity Analysis*, Technical Report 32-1387, Jet Propulsion Laboratory, Pasadena, Calif., June 15, 1969.
- Lorell, J., et al., "Celestial Mechanics Experiment for Mariner," *Icarus*, Vol. 12, Jan. 1970.
- McNeal, C. E., *Ranger V Tracking Systems Data Analysis Final Report*, Technical Report 32-702, Jet Propulsion Laboratory, Pasadena, Calif., Apr. 15, 1965.
- Melbourne, W. G., et al., *Constants and Related Information for Astrodynamical Calculations*, Technical Report 32-1306, Jet Propulsion Laboratory, Pasadena, Calif., July 15, 1968.
- Melbourne, W. G., "Planetary Ephemerides," *Astronaut. Aeronaut.*, Vol. 7, May 1970.
- Miller, L., et al., *The Atlas-Centaur VI Flight Path and Its Determination from Tracking Data*, Technical Report 32-911, Jet Propulsion Laboratory, Pasadena, Calif., Apr. 15, 1966.
- Moyer, T. D., "Mathematical Formulation of the Double-Precision Orbit Determination Program (DPODP)," Technical Report 32-1527, Jet Propulsion Laboratory, Pasadena, Calif., May 17, 1971.
- Mulhall, B. D., et al., *Tracking System Analytic Calibration Activities for the Mariner Mars 1969 Mission*, Technical Report 32-1499, Jet Propulsion Laboratory, Pasadena, Calif., Nov. 15, 1970.
- Mulholland, J. D., and Sjogren, W. L., *Lunar Orbiter Ranging Data*, Technical Report 32-1087, Jet Propulsion Laboratory, Pasadena, Calif., Jan. 6, 1967.

Bibliography (contd)

- Mulholland, J. D., *Proceedings of the Symposium on Observation, Analysis, and Space Research Applications of the Lunar Motion*, Technical Report 32-1386. Jet Propulsion Laboratory, Pasadena, Calif., Apr. 1969.
- Muller, P. M., and Sjogren, W. L., *Consistency of Lunar Orbiter Residuals With Trajectory and Local Gravity Effects*, Technical Report 32-1307. Jet Propulsion Laboratory, Pasadena, Calif., Sept. 1, 1968.
- Muller, P. M., and Sjogren, W. L., *Lunar Mass Concentrations*, Technical Report 32-1339. Jet Propulsion Laboratory, Pasadena, Calif., Aug. 16, 1968.
- Null, G. W., Gordon, H. J., and Tito, D. A., *Mariner IV Flight Path and Its Determination From Tracking Data*, Technical Report 32-1108. Jet Propulsion Laboratory, Pasadena, Calif., Aug. 1, 1967.
- O'Neil, W. J., et al., *The Surveyor III and Surveyor IV Flight Paths and Their Determination From Tracking Data*, Technical Report 32-1292. Jet Propulsion Laboratory, Pasadena, Calif., Aug. 15, 1968.
- Pease, G. E., et al., *The Mariner V Flight Path and Its Determination From Tracking Data*, Technical Report 32-1363. Jet Propulsion Laboratory, Pasadena, Calif., July 1, 1969.
- Renzetti, N. A., *Tracking and Data Acquisition for Ranger Missions I-V*, Technical Memorandum 33-174. Jet Propulsion Laboratory, Pasadena, Calif., July 1, 1964.
- Renzetti, N. A., *Tracking and Data Acquisition for Ranger Missions VI-IX*, Technical Memorandum 33-275. Jet Propulsion Laboratory, Pasadena, Calif., Sept. 15, 1966.
- Renzetti, N. A., *Tracking and Data Acquisition Support for the Mariner Venus 1962 Mission*, Technical Memorandum 33-212. Jet Propulsion Laboratory, Pasadena, Calif., July 1, 1965.
- Renzetti, N. A., *Tracking and Data Acquisition Report, Mariner Mars 1964 Mission: Near-Earth Trajectory Phase*, Technical Memorandum 33-239, Vol. I. Jet Propulsion Laboratory, Pasadena, Calif., Jan. 1, 1965.
- Renzetti, N. A., *Tracking and Data Acquisition Report, Mariner Mars 1964 Mission: Cruise to Post-Encounter Phase*, Technical Memorandum 33-239, Vol. II. Jet Propulsion Laboratory, Pasadena, Calif., Oct. 1, 1967.
- Renzetti, N. A., *Tracking and Data Acquisition Report, Mariner Mars 1964 Mission: Extended Mission*, Technical Memorandum 33-239, Vol. III. Jet Propulsion Laboratory, Pasadena, Calif., Dec. 1, 1968.
- Renzetti, N. A., *Tracking and Data System Support for Surveyor: Missions I and II*, Technical Memorandum 33-301, Vol. I. Jet Propulsion Laboratory, Pasadena, Calif., July 15, 1969.
- Renzetti, N. A., *Tracking and Data System Support for Surveyor: Missions III and IV*, Technical Memorandum 33-301, Vol. II. Jet Propulsion Laboratory, Pasadena, Calif., Sept. 1, 1969.
- Renzetti, N. A., *Tracking and Data System Support for Surveyor: Mission V*, Technical Memorandum 33-301, Vol. III. Jet Propulsion Laboratory, Pasadena, Calif., Dec. 1, 1969.

Bibliography (contd)

- Renzetti, N. A., *Tracking and Data System Support for Surveyor: Mission VI*, Technical Memorandum 33-301, Vol. IV. Jet Propulsion Laboratory, Pasadena, Calif., Dec. 1, 1969.
- Renzetti, N. A., *Tracking and Data System Support for Surveyor: Mission VII*, Technical Memorandum 33-301, Vol. V. Jet Propulsion Laboratory, Pasadena, Calif., Dec. 1, 1969.
- Renzetti, N. A., *Tracking and Data System Support for the Mariner Venus 67 Mission: Planning Phase Through Midcourse Maneuver*, Technical Memorandum 33-385, Vol. I. Jet Propulsion Laboratory, Pasadena, Calif., Sept. 1, 1969.
- Renzetti, N. A., *Tracking and Data System Support for the Mariner Venus 67 Mission: Midcourse Maneuver Through End of Mission*, Technical Memorandum 33-385, Vol. II. Jet Propulsion Laboratory, Pasadena, Calif., Sept. 1, 1969.
- Renzetti, N. A., *Tracking and Data System Support for the Pioneer Project. Pioneer VI. Prelaunch to End of Nominal Mission*, Technical Memorandum 33-426, Vol. I. Jet Propulsion Laboratory, Pasadena, Calif., Feb. 1, 1970.
- Renzetti, N. A., *Tracking and Data System Support for the Pioneer Project. Pioneer VII. Prelaunch to End of Nominal Mission*, Technical Memorandum 33-426, Vol. II. Jet Propulsion Laboratory, Pasadena, Calif., Apr. 15, 1970.
- Renzetti, N. A., *Tracking and Data System Support for the Pioneer Project. Pioneer VIII. Prelaunch Through May 1968*, Technical Memorandum 33-426, Vol. III. Jet Propulsion Laboratory, Pasadena, Calif., July 15, 1970.
- Renzetti, N. A., *Tracking and Data System Support for the Pioneer Project. Pioneer IX. Prelaunch Through June 1969*, Technical Memorandum 33-426, Vol. IV. Jet Propulsion Laboratory, Pasadena, Calif., Nov. 15, 1970.
- Renzetti, N. A., *Tracking and Data System Support for the Pioneer Project. Pioneer VI. Extended Mission: July 1, 1966-July 1, 1969*, Technical Memorandum 33-426, Vol. V. Jet Propulsion Laboratory, Pasadena, Calif., Feb. 1, 1971.
- Renzetti, N. A., *Tracking and Data System Support for the Pioneer Project. Pioneer VII. Extended Mission: February 24, 1967-July 1, 1968*, Technical Memorandum 33-426, Vol. VI. Jet Propulsion Laboratory, Pasadena, Calif., Apr. 15, 1971.
- Renzetti, N. A., *Tracking and Data System Support for the Pioneer Project. Pioneer VII. Extended Mission: July 1, 1968-July 1, 1969*, Technical Memorandum 33-426, Vol. VII. Jet Propulsion Laboratory, Pasadena, Calif., Apr. 15, 1971.
- Renzetti, N. A., *Tracking and Data System Support for the Pioneer Project. Pioneer VIII. Extended Mission: June 1, 1968-July 1, 1969*, Technical Memorandum 33-426, Vol. VIII. Jet Propulsion Laboratory, Pasadena, Calif., May 1, 1971.
- Renzetti, N. A., *Tracking and Data System Support for the Pioneer Project. Pioneers VI-IX. Extended Missions: July 1, 1969-July 1, 1970*. Technical Memorandum 33-426, Vol. IX. Jet Propulsion Laboratory, Pasadena, Calif., Aug. 15, 1971.
- Sjogren, W. L., *The Ranger III Flight Path and Its Determination From Tracking Data*, Technical Report 32-563. Jet Propulsion Laboratory, Pasadena, Calif., Sept. 15, 1965.

Bibliography (contd)

- Sjogren, W. L., et al., *The Ranger V Flight Path and Its Determination From Tracking Data*, Technical Report 32-562. Jet Propulsion Laboratory, Pasadena, Calif., Dec. 6, 1963.
- Sjogren, W. L., et al., *The Ranger VI Flight Path and Its Determination From Tracking Data*, Technical Report 32-605. Jet Propulsion Laboratory, Pasadena, Calif., Dec. 15, 1964.
- Sjogren, W. L., et al., *Physical Constants as Determined From Radio Tracking of the Ranger Lunar Probes*, Technical Report 32-1057. Jet Propulsion Laboratory, Pasadena, Calif., Dec. 30, 1966.
- Sjogren, W. L., *Proceedings of the JPL Seminar on Uncertainties in the Lunar Ephemeris*, Technical Report 32-1247. Jet Propulsion Laboratory, Pasadena, Calif., May 1, 1968.
- Sjogren, W. L., "Lunar Gravity Estimate: Independent Confirmation," *J. Geophys. Res.*, Vol. 76, No. 29, Oct. 10, 1971.
- Spier, G. W., "Design and Implementation of Models for the Double Precision Trajectory Program (DPTRAJ)," Technical Memorandum 33-451, Jet Propulsion Laboratory, Pasadena, Calif., Apr. 15, 1971.
- Stelzried, C. T., *A Faraday Rotation Measurement of a 13-cm Signal in the Solar Corona*, Technical Report 32-1401. Jet Propulsion Laboratory, Pasadena, Calif., July 15, 1970.
- Stelzried, C. T., et al., "The Quasi-Stationary Coronal Magnetic Field and Electron Density as Determined From a Faraday Rotation Experiment," *Sol. Phys.*, Vol. 14, No. 2, pp. 440-456, Oct. 1970.
- Thornton, J. H., Jr., *The Surveyor I and Surveyor II Flight Paths and Their Determination From Tracking Data*, Technical Report 32-1285. Jet Propulsion Laboratory, Pasadena, Calif., Aug. 1, 1968.
- Vegos, C. J., et al., *The Ranger IX Flight Path and Its Determination From Tracking Data*, Technical Report 32-767. Jet Propulsion Laboratory, Pasadena, Calif., Nov. 1, 1968.
- Winn, F. B., *Selenographic Location of Surveyor VI, Surveyor VI Mission Report: Part II. Science Results*, Technical Report 32-1262. Jet Propulsion Laboratory, Pasadena, Calif., Jan. 10, 1968.
- Winn, F. B., "Post Landing Tracking Data Analysis," in *Surveyor VII Mission Report: Part II. Science Results*, Technical Report 32-1264. Jet Propulsion Laboratory, Pasadena, Calif., Mar. 15, 1968.
- Winn, F. B., "Post Lunar Touchdown Tracking Data Analysis," in *Surveyor Project Final Report: Part II. Science Results*, Technical Report 32-1265. Jet Propulsion Laboratory, Pasadena, Calif., June 15, 1968.
- Winn, F. B., *Surveyor Posttouchdown Analyses of Tracking Data*, NASA SP-184. National Aeronautics and Space Administration, Washington, D.C., p. 369.
- Wollenhaupt, W. R., et al., *The Ranger VII Flight Path and Its Determination From Tracking Data*, Technical Report 32-694. Jet Propulsion Laboratory, Pasadena, Calif., Dec. 15, 1964.